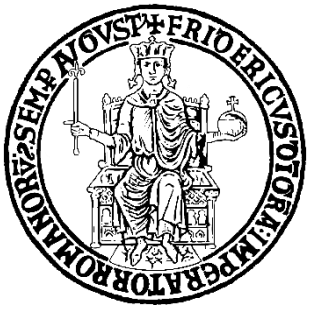

UNIVERSITY OF NAPLES FEDERICO II

DEPARTMENT OF INDUSTRIAL ENGINEERING

- MECHANIC AND ENERGETIC SECTION -

PH.D. SCHOOL IN INDUSTRIAL ENGINEERING –XXXIII CYCLE

NUMERICAL ANALYSES ON ULTRA-LEAN SI ENGINE INTEGRATED IN A HYBRID POWERTRAIN TO REDUCE NOXIOUS EMISSIONS

Doctoral Thesis

Ph.D. School Coordinator
Prof. Michele Grassi

Tutor
Prof. Fabio Bozza
Dr. Ing. Vincenzo De Bellis

Ph.D. Candidate
Enrica Malfi

Contents

List of figures

List of tables

Abbreviation and nomenclature

Acronyms

0D-1D-3D	Zero-One-Three-dimensional
A/F	Air-to-fuel ratio
AI	Auto Ignition
APR	Anti-Polishing Ring
ATDC	After firing top dead centre
Ba	Battery
BL	Boundary Layer
BMEP	Brake Mean Effective Pressure
BS	Brake specific
BSFC	Brake Specific Fuel Consumption
BTDC	Before top dead centre
BTE	Brake Thermal Efficiency
CAD	Crank angle degree
CCV	Cycle to cycle variation
CFD	Computational fluid dynamics
Cl	Clutch
CNG	Compressed Natural Gas
CO	Carbon monoxide
CO_2	Carbon dioxide
CoV	Coefficient of Variation
CSP	Conventional Spark Plug
DF	Dual Fuel
DI	Direct Injection
DP	Dynamic Programming
DSF	Dynamic Skip Fire
EATS	Exhaust After-Treatment System
ECU	Engine Control Unit
EG	Electric Generator

EGR	Exhaust Gas Recirculation
eEGR	External-Exhaust Gas Recirculation
EIVC	Early Intake Valve Closing
EM	Electric Motor
EML	Extreme Miller Lift
EMS	Energy Management Strategy
ETESS	Efficient Thermal Electric Skipping Strategy
EVC	Exhaust Valve Closure
EVO	Exhaust Valve Opening
EU	European Union
FL	Full Load
GB	Gear-Box
H_2	Hydrogen
HC	Hydrocarbon
HCCI	Homogeneous Charge Compression Ignition
HEV	Hybrid Electric Vehicle
HP	High pressure
HPC	High-Pressure Compressor
ICE	Internal Combustion Engine
IMEP	Indicated Mean Effective Pressure
IMPO	Integral of Modulus of Pressure Oscillations
ITE	Indicated Thermal Efficiency
IVC	Intake Valve Closure
IVO	Intake Valve Opening
IS	Indicated specific
LFS	Laminar Flame Speed
LIVC	Late Intake Valve Closing
LHV	Lower heating value
LP	Low pressure
LPC	Low-Pressure Compressor
LPT	Low-Pressure Turbine

MAPO	Maximum Amplitude of Pressure Oscillations
MC	Main-Chamber
MCE	Multi-Cylinder Engine
MFB	Mass fraction burned
MON	Motor octane number
NOx	Nitrogen oxides
OBTE	Overall Brake Thermal Efficiency
PC	Pre-Chamber
PID	Proportional integral derivative controller
PFI	Port Fuel Injection
PHEV	Plug-in Hybrid Electric Vehicle
PM	Particle Matter
PMP	Pontryagin minimum principle
PO	Post-oxidation
PS	Power-split
RANS	Reynolds averaged Navier-Stokes
RNG	Re-normalization group
RON	Research octane number
RMSE	Root Mean Squared Error
SA	Spark Advance
SACI	Spark Assisted Compression Ignition
SCE	Single Cylinder Engine
SI	Spark Ignition
SML	Standard Miller Lift
SoC	State of Charge
TC	Turbochargers
TDC	Top dead centre
TRF	Toluene reference fuel
TSCR	Two-Stage Compression Ratio
uHC	Unburned hydrocarbon
UNVS	UniNa Vehicle Simulation

VCR	Variable Compression Ratio
VVA/L/T	Variable Valve Actuation / Lift / Timing
WI	Water Injection
WLTC	Worldwide harmonized Light-Duty vehicles Test Cycle

Latin Symbols

A/a	Reaction rate parameter for iso-octane / air and methane / air mixtures
A_L, A_T A_w A_{tot}	Laminar / turbulent / wet / total flame area
b	Reaction rate parameter for iso-octane/air and methane / air mixtures
B	Bore
BB	Base Boost
B_m, B_ϕ	Metghalchi correlation coefficients
c_0	Tuning constant for the ETESS model
c_d	Discharge coefficient
c_{fd0}, c_{fdm}	Tuning constants of tumble decay function
c_{jet}	Fresh charge entrainment multiplier
c_{Kin0}	Tuning constant of inlet flow coefficient
c_p	Specific heat at constant pressure
c_{PKk}	Tuning constant of turbulence Production
c_q	Quenching tuning constant
c_{rT0}, c_{rTm}	Parameters for tumble radius adjustment
c_{Tin0}	Tuning constant of tumble flow coefficient
c_{trans}	Laminar turbulent transition multiplier
c_{wc}	Wall combustion tuning multiplier
c_{wrk}	Wrinkling multiplier
D_3	Fractal dimension
E_a	Apparent activation energy
E/e	Energy
F/f	Force / Function
f_d	Decay function of tumble
fl	Flame

H/h	Hamiltonian / Enthalpy
H	Piston position referred to cylinder head
$\mathbf{I}$	Current
J	Performance index
k	Turbulent kinetic energy
$\mathbf{K}$	Constant
K	Mean flow kinetic energy
$\mathbf{k}$	Ratio of the specific heats
$\mathbb{K}$	Flame stretch rate
k_{oxid}	Post-oxidation tuning constant
K_s	Hydrodynamic strain
K_{pist}	Kinetic energy related to piston motion
K_T	Kinetic energy related to tumble motion
L	Markstein length / Cost function
$\mathbf{L_k}$	Kolmogorov length scale
L_M	Taylor length scale
L_t	Turbulence integral length scale
L_{min}, L_{max}	Minimum / maximum flame front wrinkling scale
M/m	Mass
n	Engine rotational speed / Gear Ratio
$\mathbf{p}$	Pressure
$\mathbf{p_{th}}$	Tolerance of the hyperbolic tangent function
P	Power
Pe	Peclet
$\mathbf{Q}$	Heat transfer
$\mathbf{Q_{nom}}$	Total Capacity
R	Gas constant
r_{crit}	PC critical radius for MC combustion start
$\mathbf{r_f}$	Flame radius
R_{int}	Internal Resistance
r_S	Swirl radius

r_T	Tumble radius
s_{corr}	Equivalence factor correction
S_d	Flame displacement speed
s_0	Equivalence factor
$S_{L/T}$	Laminar / Turbulent Flame Speed
T	Temperature /Torque / Tumble angular momentum
t	Time
t_{trans}	Characteristic time scale
u	Control variable, power-split
U	Variation range of the control variable
u'	Turbulence intensity
v	Velocity
V	Volume
V_{OC}	Voltage of open circuit
x	State variable
X	Variation range of the state variable
x_b	Burned gas fraction
x_r, $\tilde{x}_r$	Residual mass / molar fraction
Ze	Zel'dovich number

Greek symbols

α	Air to fuel ratio / Temperature exponent in S_L correlation
β	Pressure exponent in S_L correlation / Penalization factor
δ_L	Flame Thickness
ε	Dissipation rate
γ	Speed ratio fixed / Residuals exponent in S_L correlation
Γ_{max}	Maximum scale of flame front wrinkling
Γ_{min}	Minimum scale of flame front wrinkling
δ	Residuals multiplier in S_L correlation
δ_f	Flame front thickness

δ_{th}	Flame front thermal thickness
κ	Flame curvature
η	Efficiency
λ	Relative air / fuel equivalence ratio / Costate / Thermal conductivity
Λ_T	Taylor length scale
ν	Kinematic viscosity
ν_t	Turbulent viscosity
ρ	Density
Σ	Turbulence-induced flame wrinkling
σ	Thermal expansion parameter
τ	Entrainment characteristic time
τ_{AI}	Auto-ignition Time
ϕ, ϕ_m	Air-to-fuel equivalence ratio
ω	Rotational Speed

Subscripts

0	Initial
10 / 50 / 90	Referring to 10 / 50 / 90% of mass fraction burned
aero	Aerodynamic
b	Burned
batt	Battery
bl	Boundary Layer
coul	Coulomb
crev	Crevices
cyl	Related to the cylinder
D/d	Downstream / Derivative
dem	Demand
diff	Differential
el	Electric
entr	Entrainment

eq	Equivalent
ex	Exhaust
exp	Experimental
f	Oil friction / Adiabatic Flame
f/F	Final, fuel, Related to flame
fractal	Related to fractal approach
i	Integrative / Inertia
in	Incoming
inj	Injected
jet	Related to turbulent jet
k	Kolmogorov scale
L	Laminar
max	Maximum
min	Minimum
MC	Related to Main Camber
out	Outcoming
p	Proportional / Production
PC	Related to Pre-Chamber
pwt	Powertrain
q	Quenching
ref	Reference
roll	Rolling
st	Stoichiometric
T/t	Turbulent / integral scale
th	Thermal
tl	Top land
trac	Tractive
U	Unburned / Upstream
veh	Vehicle
w	Wall
wh	Wheel

wq	Wall Quenching

Superscripts

.	Temporal derivative
*****	Optimal

Abstract

The Internal Combustion Engine (ICE) is one of the technological solutions that has changed the world and the way of life. It is considered both as one of the greater sources of benefits and one of the main reasons for atmospheric pollution. The European Regulation 2019/631 sets new EU fleet-wide CO_2 emission targets for the years 2025 and 2030, both for newly registered passenger cars and vans. These targets, defined as percentage reductions from the 2021 CO_2 emission level, are respectively 15% by 2025 and 37.5% by 2030 for the first category, while for the second one of 15% by 2025 and 31% by 2030. The specific emission targets are based on the EU fleet-wide targets, considering the average test mass of a manufacturer's newly registered vehicles. Further concerning the pollutant emissions, the vehicle manufacturers have to comply with the EU Regulation 2018/985, named Euro 6d, which imposes stringent limitations on carbon monoxide, unburned hydrocarbon, nitrogen oxides, and particulate matters. Therefore, the engine design needs to be continuously improved and new components have been introduced, such as on-board sensors and additional sub-systems. The pollutant formation from the combustion depends, not only on the engine structure but also on the engine management system that is mainly responsible for the engine behaviour. Because of the introduction of new components, many of which are electronic devices, a relevant increase of the degrees of freedom available during the engine operations arises, resulting in a more complex and less intuitive engine optimization and management. Nowadays, the engine control system is a huge collection of tuning tables, including the ones related to new electronic components. Generally, this control structure is defined by trial-and-error approaches: during the calibration process, the main targets, such as fuel consumption, engine emission, performances of the vehicle, and so on, are transformed in control references to be followed by some engine and vehicle variables that can be measured. These targets are reached through proper closed-loop control strategies receiving measurements by sensors and actuators. It is well known that nowadays the ICE is the most widespread thermal machine in the world, playing a key role in several application fields: passenger cars, motorcycles and motorbikes, on-road commercial transport, boats and ships, off-road for industrial use, and power generation. In particular, the automotive sector is currently experiencing a significant evolution, developing alternative powertrains with the aim to achieve clean mobility. However, since probably the ICE will represent the powertrain solution for the majority of vehicles worldwide during the next decades, sided by hybridization and electrification, an optimized engine will be fundamental to guarantee low fuel consumption and CO_2 emissions, and near-zero pollutant emissions. Innovative combustion modes, together with synthetic fuels, turbocharging, and advanced after-treatment systems, will contribute to achieving these challenging targets. In this context,

investigating and comparing experimentally different technologies will imply huge costs and times. Hence, modeling techniques and simulation codes will be fundamental in studying and designing new vehicle concepts. Indeed, a virtual engine gives the opportunity to fast test different technical solutions and their effects on performances and emissions. During the last few decades, a significant research effort in the field of 0D/1D/3D (zero-dimensional / one-dimensional / three-dimensional) engine modeling has been carried out. This progress has allowed a further diffusion of simulation tools for the engine design process.

In the light of the above considerations, the topic of the research activity, presented in this Ph.D. thesis, is the numerical investigation, through a hierarchical simulation-level approach, of innovative SI engines, possibly suitable for hybrid powertrains and featured by a reduced CO_2 impact. For this purpose, firstly a conventional naturally aspirated small Spark Ignition (SI) engine has been analysed, assessing the model predictivity of engine performance, combustion, and pollutant emissions. In a second stage, several engine architectures working in ultra-lean conditions have been numerically investigated, with particular emphasis on unburned hydrocarbon emission estimation. Then, an innovative 4-cylinder SI engine, equipped with an active pre-chamber (PC) ignition system and operating with an ultra-lean mixture, has been studied. Finally, this last engine has been virtually embedded into a hybrid electric vehicle (HEV), belonging to the C segment, to estimate CO_2 and pollutant emissions along the worldwide harmonized light vehicles test cycle (WLTC) and Real Driving Emission (RDE)-compliant cycles and to verify the EU regulation fulfilment.

The above-described engine analyses have been carried out in a 0D/1D modelling environment, schematizing the whole engine system through a network of 1D pipes and 0D cylinders. To describe the in-cylinder phenomena in-house developed quasi-dimensional models have been employed. Concerning the description of the combustion phenomenon in the conventional engine, the well-assessed fractal combustion model, developed at the University of Naples Federico II, has been adopted. Regarding the pre-chamber engine, a new and innovative procedure has been developed, not being available well-assessed specific models in the current literature. In the first stage, the reliability of the phenomenological model was checked through a comparison with 3D calculations outcomes. Subsequently, the model has been tested and assessed through comparisons with various sets of experimental data. Once verified its accuracy, the model has been employed as a predictive tool to evaluate complete performance maps over the whole engine domain.

For this purpose, firstly, the optimal setting of main engine control parameters has been identified by coupling the 1D model to an external optimizer. Then, the optimization results have been applied

to define a number of heuristic rules, implemented within several PID (proportional/integral/derivative) controllers in the 1D model. Both optimized and rule-based (RB) calibration strategies were conceived to maximize the engine efficiency. Due to the faster execution, the RB control strategy has been employed to evaluate engine maps of performance and control parameters.

Finally, the engine maps have been embedded in a vehicle simulation with the aim of quantifying CO_2 and pollutant emissions over WLTC and RDE cycles. A novel Energy Management Strategy (EMS) for the HEV, named Efficient Thermal Electric Skipping Strategy (ETESS), has been developed. The ETESS was conceived to minimize the fuel consumption along a prescribed driving mission. The ETESS has been compared to the well-known Pontryagin minimum principle (PMP) and Equivalent Consumption Minimization Strategy (ECMS), giving fuel consumption values close to those reference control strategies, but providing a significant advantage in the computational effort.

The outcomes achieved during this research activity showed that the investigated innovative 4-cylinder PC engine, embedded in a C segment HEV gave a CO_2 emission of 85 g/km along the WLTC. The value is below the target imposed by the European Union for 2021 of 95 g/km but above the one for 2025, equal to about 81 g/km. Concerning the pollutant emission outcomes, without considering the potential abatement of an Exhaust After-Treatment System (EATS), the simulations have highlighted that the nitrogen oxides (NO_x) kilometric production was 0.02 g/km, hence within the Euro 6d limit of 0.06 g/km. Regarding the unburned hydrocarbons (uHC) emissions, they resulted of 0.87 g/km, and hence well above the Euro 6d limit of 0.10 g/km. This has evidenced the need for an oxidizing EATS for regulation compliance. Anyway, this technology at the current state-of-art is very robust, low-cost, and reliable, not representing a substantial challenge for a real on-vehicle application. The innovative engine here studied, coupled to powertrain hybridization, showed hence the capability for the compliance of the current EU regulation, while further advances are required for the fulfilment of regulation to come in the medium term.

1. Introduction

Nowadays, the internal combustion engine is the most common thermal machine in the world, counting every year about 230 million new engines built, considering all the application fields, namely passenger cars, motorcycles and motorbikes, on-road commercial transport, boats, and ships, off-road for industrial use, and power generation. The ICE has its roots at end of the nineteenth century, being almost immediately applied in the transport sector, reaching today about 90 million passenger cars produced every year. The forecasts on future trends in the automotive industry predict a growth of world production to about 150 million cars per year in 2030, most of which (about 80%) still powered by an ICE. *Figure 1-1* and *Figure 1-2(a)* represent a possible future context for the passenger car powertrains.

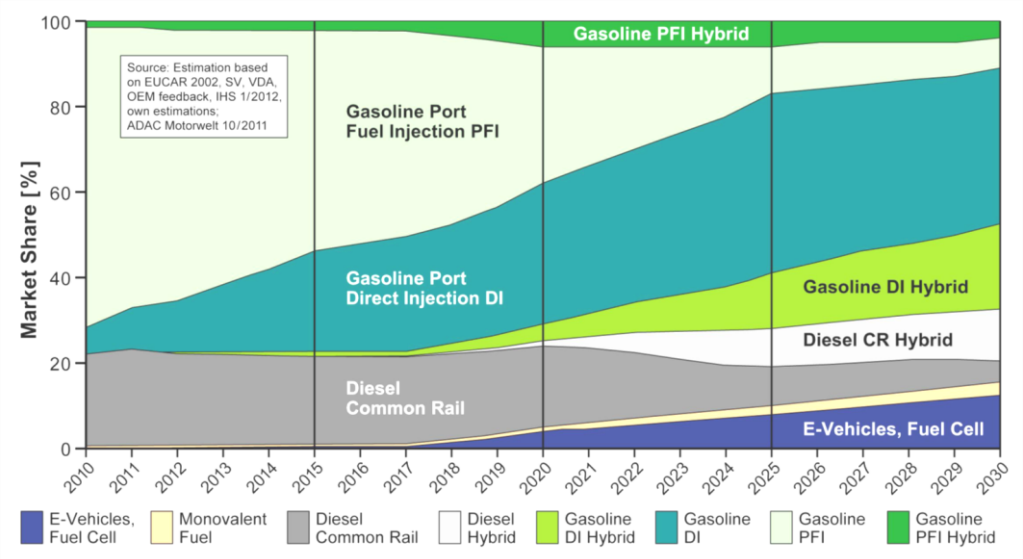

Figure 1-1 Assumption of future vehicle technologies global view [1].

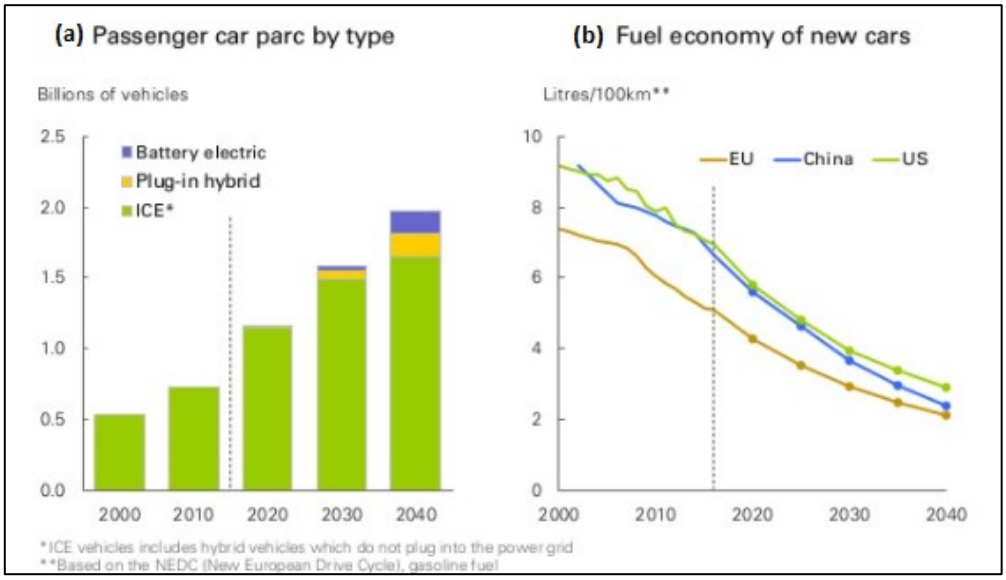

Figure 1-2 Passenger car parc by type (a) and fuel economy of new cars (b) scenarios (BP Energy Outlook 2018) [2].

Currently, because of the challenging and increasing development of alternative powertrains, especially in the automotive field, namely electric motors with batteries or fuel cells, the ICEs can be sometimes considered as an overcome technology, bound to disappear in the last few years. But, as all the other prime movers, the ICE represents a technology under continuous evolution, experiencing significant improvements and innovations, supported by the intense research activities in this field. Important efforts have been made to achieve enhancements in performance, fuel consumption (*Figure 1-2(b)*), and pollutant emissions. In this track, a constraint to consider is the compliance with the stringent limits imposed by the emission legislations executed in several countries (WLTP word wide, current Euro 6d in Europe, Tier 3 in the US, etc.), and with the introduction of the RDE procedure, as an additional assessment to get the vehicle homologation [3],[4]. With the aim to control the emissions in the road sector, a new emission limit for CO_2 was recently set by 2025 in the EU, fixing a target of 80 g/km as an average for all new passenger cars. Because of the introduction of this limitation combined with the ones related to the pollutant emissions, shown in *Figure 1-3*, the research processes are drawn towards innovative, clean, and more complex solutions to improve the fuel economy of the vehicle fleets. However, the debate about how to reach these ambitious targets is still open [3],[5].

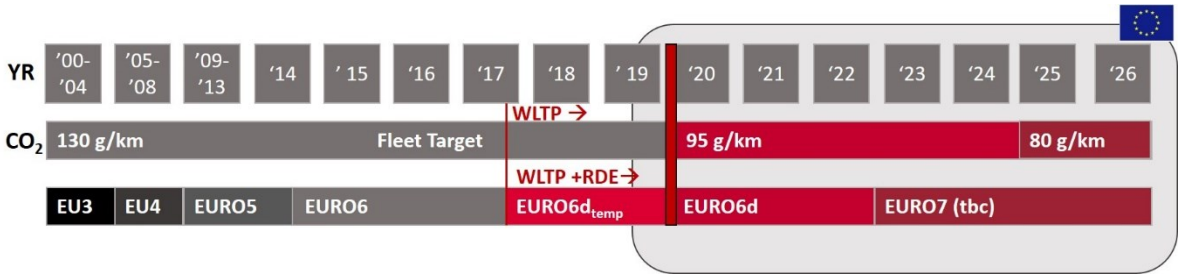

Figure 1-3 CO_2 and pollutant emissions limits roadmap

As said, the extremely low CO_2 target also plays a key role in guiding the advance of several new technologies, including vehicle electrification. Hence, several technologies are currently employed to achieve the required ICE performances.

As an example, the use of a Miller / Atkinson cycle [6],[7],[8] is quite common on new engines, allowing to reduce the effective engine compression ratio, using a shorter compression stroke, followed by a longer expansion stroke, resulting in higher thermodynamic efficiency. Further, a reduction of NO_x and knock propensity are achieved due to lower charge temperatures reached within the cylinder. Concerning the effective compression ratio reduction, it can be obtained as well by a late intake valve closure (LIVC) or an early intake valve closure (EIVC) [8],[9]. Moreover, another technique, nowadays considered as state of the art, is the adjustment of intake valve lifts and timings

realized by the introduction of variable valve actuation (VVA) [10] and variable valve timing (VVT) [11]. This technology not only allows to improve volumetric efficiency but also to manage the internal EGR. Concerning the charge ignition, an improvement can be reached through new ignition systems such as the "corona discharge" [12], allowing an enhanced combustion start, even in presence of lean or diluted mixtures. Since the knock phenomenon is one major critical issue of the turbocharged SI engine, it can be mitigated by the adoption of gasoline direct injection, Water Injection (WI) [13], cooled exhaust gas recirculation (EGR) [14],[15], variable compression ratio[16], and Miller cycle [8], as well. Most often the turbocharging is widely adopted to downsize the engine, keeping, or increasing performances, while reducing emissions and fuel consumption. Significant developments are continuously achieved in the field of exhaust after-treatment systems (EATS), one of the best measures to guarantee a notable reduction of pollutant emissions in the exhaust gas and to provide clean mobility. Regarding SI engines, research efforts are focused on the improvement of the next generation of the three-way and oxidation catalysts.

All the above-mentioned technologies are applied to SI ICEs working in stoichiometric condition, which, on one side, feature CO_2 emissions values higher than legislation limits, but, on the other side, present pollutant emissions below the limits thanks to the above-mentioned EATS. For this reason, in the very recent years, an innovative solution has arisen, i.e. the application of a combustion system that works with very lean air / fuel mixture, which showed the potential to further increase the engine efficiency and hence to reduce the CO_2 emission [17],[18],[19].

A new aspect to be considered is the new requirement for vehicle homologation, namely the RDE tests. Under these tests, the whole speed and load ranges of the ICE [20] is covered and hence need to be optimized [21]. During these tests, the pollutant emissions will be measured on-board, reproducing more consistently the operations in real driving conditions. Because of the evident trend towards vehicle electrification, the ICE requirements are changing in terms of performances, efficiency, and emissions. For hybrid powertrain, the ICE is usually featured by a more complex architecture, with high-boosting, EGR circuits, and advanced after-treatment technologies, and usually is coupled to several mechanical and electrical components of the driveline. In the light of such complexity, the optimization of a hybrid powertrain is a challenging objective, consisting of the optimal control of ICE, electric motor / generator, battery, cooling system, vehicle auxiliaries, etc., and having the aim of minimizing fuel consumption, pollutant emissions, CO_2 production, while maximizing power / torque performance. Therefore, the Energy Management Strategy becomes essential to get the above objective [22],[23]. Actually, the current competition between the internal combustion engine and alternative powertrains, namely the electric motor powered with batteries (full electric vehicle) [24] or the fuel cell (fed with hydrogen or hydrocarbons) [25], is undoubtedly helpful

to promote the further development and evolution of the ICE. The latter has to be evolved towards a sustainable mobility solution, contributing to reduce the environmental impact during the next decades.

This research activity aims to numerically investigate, by a hierarchical simulation-level approach, innovative SI engines, possibly suitable for hybrid powertrains, presenting a reduced CO_2 and pollutant emission impact. For this purpose, in the first stage, a conventional naturally aspirated stoichiometric small SI engine has been analysed. At this stage, the engine model reliability is assessed in terms of performances and emissions prediction. Hence, the models of several engine architectures, (two single cylinder pre-chamber engines and two large bore natural gas engines), all working in ultra-lean condition (relative Air / Fuel ratio $\lambda = \alpha/\alpha_{st}$ equal to 2) have been developed and validated. Finally, an innovative 4-cylinder SI engine, equipped with an active pre-chamber ignition system, has been numerically investigated. the latter engine has been virtually embedded into a HEV to perform vehicle simulations, assessing CO_2 and pollutant emissions along the WLTC and RDE cycles.

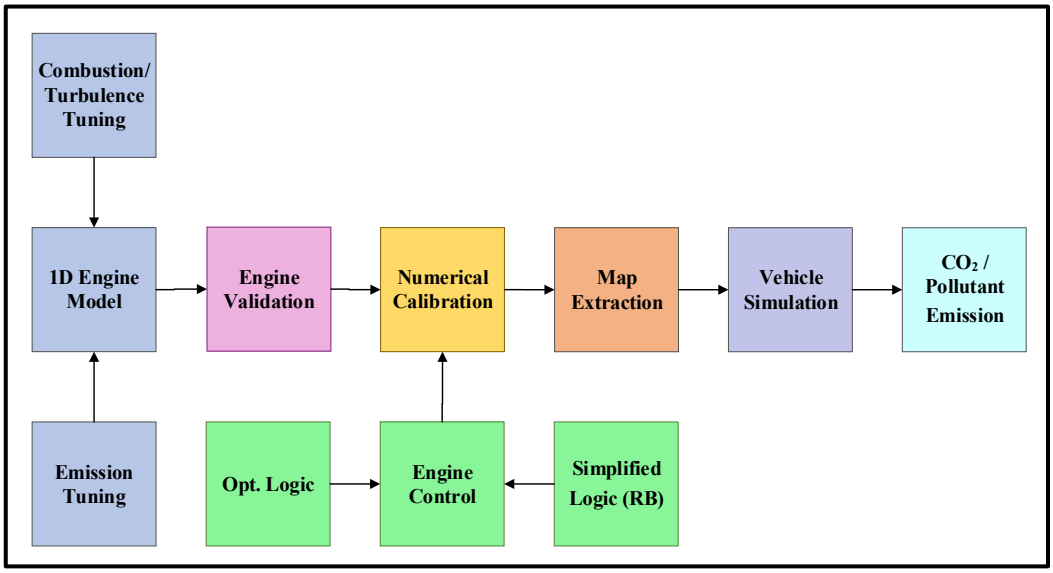

Figure 1-4 Main modelling steps of the research activity.

In *Figure 1-4* the methodology and main modelling steps followed during this research activity are reported. Firstly, the geometry of the tested engine is schematized in a commercial modelling framework, following a 1D description of the flow inside the intake and the exhaust pipes. Phenomenological 0D sub-models are used to reproduce in-cylinder phenomena such as turbulence, combustion, and heat transfer. Those are embedded in 1D code GT-Power through user routines Concerning the conventional engine, the fractal combustion model [26], developed at the University

of Naples Federico II [27],[28], is employed. The combustion simulation for the innovative pre-chamber engine architecture is modelled through a newly developed procedure. The original fractal model is adapted to describe all the phenomena occurring within an engine equipped by a PC, such as mixture preparation, turbulence evolution, flame area enhancement, burn rate development, jet entrainment, etc. This represents an important goal achieved during this research activity since, differently from conventional SI ICEs [27],[28],[29], only few predictive PC combustion models were available in the literature [30],[31],[32]. Further, emission models are developed as well. Specifically, the NO_x and CO are simulated recurring to conventional reduced chemical kinetics approaches, while for the uHC, an innovative phenomenological model is developed and implemented. The latter is able, not only to estimate the overall uHC production but also to distinguish the sources, namely accumulation / release from crevices and flame wall quenching. The above-mentioned sub-models are tuned and validated according to 3D calculations and experimental data, identifying a single set of tuning constants for a given engine architecture. For the conventional engine, a large validation data set is available, covering the whole engine operating domain. Concerning the large bore engines, numerical results are verified against a reduced number of operating conditions (load sweep at fixed rotational speed), but considering variations of ignition system, cylinder number, and combustion chamber geometry; considering the two prototype single-cylinder pre-chamber engines, numerical results are validated for different PC geometries and the fuel injection modalities; finally, the above single cylinder engines are used as starting point to define a 4-cylinder PC engine, whose model is used to explore the engine behaviour over the whole operating domain.

For this purpose, a Rule-Based (RB) calibration strategy is set up. It is preliminarily assessed against automatic optimizer outcomes. The performance and control maps of the 4-cylinder PC engine are computed based on the RB strategy and then are embedded in the vehicle model of a C segment HEV Simulations are performed to quantify the CO_2 and pollutant emission over the WLTC and RDE-compliant cycles and to verify the compliance with EU regulations. A novel EMS is here developed, able to minimize the fuel consumption and CO_2 emissions along the driving cycle.

The thesis is organized as follows. Firstly, a brief synopsis of internal combustion engine is reported, describing the most relevant physical phenomena occurring in the cylinder, i.e. turbulence, combustion, and knock. Then, the state of the art of technologies developed to improve the efficiency of the modern ICEs is presented. Among the proposed techniques, a deep insight is reported concerning the main features and benefits of the pre-chamber device. Then, the phenomenological sub-models to simulate engine behaviour are described in detail, focusing on in-cylinder processes.

The state of the art on vehicle simulation methods is reported, and a novel EMS, the ETEES, is presented. Engine simulation outcomes are shown, analysing the tuning procedure and the model validation. A numerical calibration approach is presented and then used to compute the maps of the 4-cylinder PC engine. Finally, the engine maps are used in the vehicle simulation, whose results are reported and discussed.

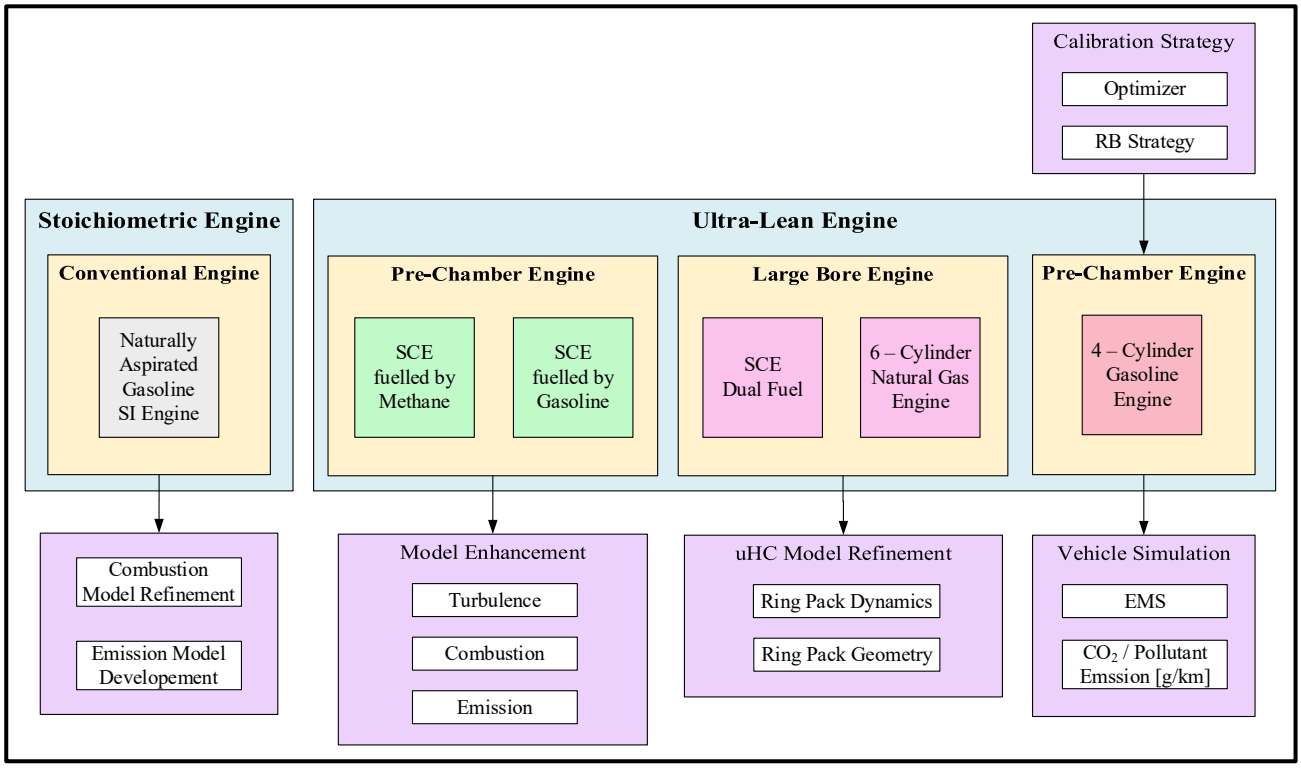

Figure 1-5 Main research activity steps highlighting the architectures analysed.

In *Figure 1-5* are schematized the above-described main steps of the research activity presented in this Ph.D. thesis, putting into evidence all the analysed engine architectures and the models enhanced / developed on the basis of each of them.

It is important to mention that the research work about the pre-chamber ultra-lean engine is realized in the framework of the European H2020 project EAGLE (*Efficient Additivated Gasoline Lean Engine*: https://h2020-eagle.eu/), having the objective to develop a prototype SI engine achieving 50% Brake Thermal Efficiency (BTE), and 50 g/km of CO_2 emissions along the WLTC. The research work related to the development of a model to predict the unburned hydrocarbon is carried out as a part of a cooperation with Wärtsilä Corporation, a Finnish company that produces power sources and equipment in marine and energy sectors.

Both research works integrate experimental and numerical activities, some of them reported in this thesis. The interest of international institutions and private companies, on one hand, highlights the

needing for further advancements in the field of ICE efficiency and pollutant abatement, and, on the other side, confirms the increasing relevance of the simulations in the engine / vehicle development process.

References

[1] Schöppe, D., Zhang, H., Kapphan, F., Schmidt, C., "Designing the Future with Clean Power Analysis and Strategic Solution Concepts on System Level," Aachener Kolloquium 2012 Continental AG 2012.

[2] https://www.bp.com/content/dam/bp/business-sites/en/global/corporate/pdfs/energy-economics/energy-outlook/bp-energy-outlook-2018.pdf

[3] Martin Weiss, P.B., Hummel, R., and Steininger, N., "A Complementary Emissions Test for Light-Duty Vehicles: Assessing the Technical Feasibility of Candidate Procedures," European Commission, Joint Research Centre, Institute for Energy and Transport (IET), 2013.

[4] Maschmeyer, H., Kluin, M., and Beidl, C., "Real Driving Emissions - A Paradigm Change for Development," MTZ Worldwide 76, no. 2 (2015): 16-21.

[5] Fontaras, G., Zacharof, N., Ciuffo, B., "Fuel consumption and CO_2 emissions from passenger cars in Europe–Laboratory versus real-world emissions," *Progress in Energy and Combustion Science* 60:97-131, 2017, doi: 10.1016/j.pecs.2016.12.004.

[6] Li, T., Gao, Y., Wang, J., and Chen, Z., "The Miller Cycle Effects on Improvement of Fuel Economy in a Highly Boosted, High Compression Ratio, Direct-Injection Gasoline Engine: EIVC vs. LIVC," Energy Convers. Manag. 79 (2014): 59-65, doi: 10.1016/j.enconman.2013.12.022.

[7] Okamoto, K., Zhang, F.-R., Shimogata, S., and Shoji, F., "Development of a Late Intake-Valve Closing (LIVC) Miller Cycle for Stationary Natural Gas Engines – Effect of EGR Utilization," SAE Technical Paper 972948, 1997, doi: 10.4271/972948.

[8] Luisi, S., Doria, V., Stroppiana, A., Millo, F. et al., "Experimental Investigation on Early and Late Intake Valve Closures for Knock Mitigation through Miller Cycle in a Downsized Turbocharged Engine," SAE Technical Paper 2015-01-0760, 2015, doi: 10.4271/2015-01-0760.

[9] Luo, X., Teng, H., Lin, Y., Li, B. et al., "A Comparative Study on Influence of EIVC and LIVC on Fuel Economy of a TGDI Engine Part II: Influences of Intake Event and Intake Valve Closing Timing on the Cylinder Charge Motion," SAE Technical Paper 2017-01-2246, 2017, doi: 10.4271/2017-01-2246

[10] Hara, S., Suga, S., Watanabe, S., Nakamura, M., "Variable valve actuation systems for environmentally friendly engines," Hitachi Review, 58(7), 319-324, 2009,

[11] Millo, F., Luisi, S., Stroppiana, A., and Borean, F., "Effects of Different Geometries of the Cylinder Head on the Combustion Characteristics of a VVA Gasoline Engine," SAE Technical Paper 2013-24-0057, 2013, doi: 10.4271/2013-24-0057.

[12] Pineda, D., Wolk, B., Chen, J., and Dibble, R., "Application of Corona Discharge Ignition in a Boosted Direct-Injection Single Cylinder Gasoline Engine: Effects on Combustion Phasing, Fuel Consumption, and Emissions," SAE Int. J. Engines 9, no. 3 (2016): 1970-1988, doi: 10.4271/2016-01-9045

[13] Hoppe, F., Thewes, M., Baumgarten, H., Dohmen, J., "Water injection for gasoline engines: Potentials, challenges, and solutions," *International J of Engine Research* 17(1):86-96, 2016, doi:10.1177/1468087415599867.

[14] Bozza, F., De Bellis, V., and Teodosio, L., "Potentials of Cooled EGR and Water Injection for Knock Resistance and Fuel Consumption Improvements of Gasoline Engines," Appl. Energy 169 (2016): 112-125, doi: 10.1016/j.apenergy.2016.01.129

[15] Francqueville, L., Michel, J., "On the Effects of EGR on Spark-Ignited Gasoline Combustion at High Load," *SAE Int J Engines* 7(4):1808-1823, 2014, doi:10.4271/2014-01-2628.

[16] Roberts, M., "Benefits and Challenges of Variable Compression Ratio (VCR)," SAE Technical Paper 2003-01-0398, 2003, doi:10.4271/2003-01-0398.

[17] Germane, G., Wood, C., Hess, C., "Lean Combustion in Spark-Ignited Internal Combustion Engines - A Review," SAE Technical Paper 831694, 1983, doi:10.4271/831694.

[18] Moriyoshi, Y., Kuboyama, T., Kaneko, M., Yamada, T., Sato, H., "Fuel Stratification Using Twin-Tumble Intake Flows to Extend Lean Limit in Super-Lean Gasoline Combustion," SAE Technical Paper 2018-01-1664, 2018, doi:10.4271/2018-01-1664.

[19] Ji, C. Wang, S., "Effect of hydrogen addition on combustion and emissions performance of a spark ignition gasoline engine at lean conditions," *International journal of hydrogen energy*, 34(18), pp.7823-7834, doi: 10.1016/j.ijhydene.2009.06.082.

[20] Bosteels, D., "Real Driving Emissions and Test Cycle Data from 4 Modern European Vehicles," IQPC 2nd International Conference Real Driving Emissions, Düsseldorf, 2014.

[21] Naber, D., Bareiss, S., Kufferath, A., Krüger, M. et al., Measures to Fulfill "Real Driving Emission (RDE)" with Diesel Passenger Cars," 18th Internationales Stuttgarter Symposium, March 2018.

[22] Serrao, L., Onori, S., Rizzoni, G., "A Comparative Analysis of Energy Management Strategies for Hybrid Electric Vehicles," ASME. J. Dyn. Sys., Meas., Control. 133(3):031012-031012-9, 2011, doi: 10.1115/1.40032607.

[23] Pisu, P. and Rizzoni, G., "A Comparative Study Of Supervisory Control Strategies for Hybrid Electric Vehicles," IEEE Transactions, 506-518, doi: 10.1109/TCST.2007.894649.

[24] Safari, M., "Battery Electric Vehicles: Looking behind to Move Forward," Energy Policy 115 (2018): 54-65, doi: 10.1016/j.enpol.2017.12.053.

[25] Walters, M., Wick, M., Pischinger, S., Ogrzewalla, J. et al., "Fuel Cell System Development: A Strong Influence on FCEV Performance," SAE Technical Paper 2018-01-1305, 2018, doi: 10.4271/2018-01-1305.

[26] Gouldin, F., "An application of Fractals to Modeling Premixed Turbulent Flames," *Combustion and Flame* 68(3):249-266, 1987, doi:10.1016/0010-2180(87)90003-4.

[27] De Bellis, V., Severi, E., Fontanesi, S., Bozza, F., "Hierarchical 1D/3D approach for the development of a turbulent combustion model applied to a VVA turbocharged engine. Part II: Combustion model", Energy Procedia 45: 1027-1036, 2014, doi: 10.1016/j.egypro.2014.01.108.

[28] De Bellis, V., Malfi, E., Teodosio, L., Giannattasio, P., Di Lenarda, F., "Novel Laminar Flame Speed Correlation for the Refinement of the Flame Front Description in a Phenomenological Combustion Model for Spark-Ignition Engines", *SAE International Journal of Engines*, 12(3): 251-270, 2019, doi: 10.4271/03-12-03-0018.

[29] Grill, M., Billinger, T. and Bargende, M., "Quasi-dimensional modeling of spark ignition engine combustion with variable valve train," SAE Technical Paper, 2006-01-1107, 2006, doi:10.4271/2006-01-1107.

[30] Demesoukas, S., Caillol, C., Higelin, P., Boiarciuc., "Zero-Dimensional Spark Ignition Combustion Modeling-A Comparison of Different Approaches," SAE Technical Paper, 2013-24-0022, 2013, doi:10.4271/2013-24-0022.

[31] Hiraoka, K., Nomura, K., Yuuki, A., Oda, Y. et al., "Phenomenological 0-Dimensional Combustion Model for Spark-Ignition Natural Gas Engine Equipped with Pre-Chamber," SAE Technical Paper 2016-01-0556, 2016, doi:10.4271/2016-01-0556.

[32] Shojaeefard, M. H., Keshavarz, M. "Flame propagation model for a rotary Atkinson cycle SI engine," International Journal of Automotive Technology, 19(1), 9-25, 2018, doi:10.1007/s12239-018-0002-7.

[33] https://arpa-e.energy.gov/?q=arpa-e-programs/nextcar.

2. Internal Combustion Engine Synopsis

The Internal Combustion Engine has the purpose to produce mechanical power starting from chemical energy stored in the fuel, which is burned releasing energy. The actual working fluids are the fuel-air mixture before combustion and the burned products after combustion. The requested power output is provided by the work transfer that occurs between the working fluid and the mechanical components of the engine. Nowadays the SI and Compression Ignition (CI) engines are the most common thermal machine in the world, playing a key role in several application fields: passenger cars, motorcycles and motorbikes, commercial transport, boats and ships, and power generation. This is due to their simplicity, ruggedness, and high power / weight ratio. In the last years, the automotive sector is experiencing a significant evolution, considering a wide range of alternative powertrains aiming at achieving clean mobility.

In this chapter, a brief recall of the SI engine for automotive application will be presented, since the thesis is mainly focused on this system. Particularly the greatest part of SI engines, for the above-mentioned application field, is featured by a four-stroke working cycle, in which each cylinder requires four strokes of the piston, two revolutions of the crankshaft, to realize the thermodynamic cycle [1].

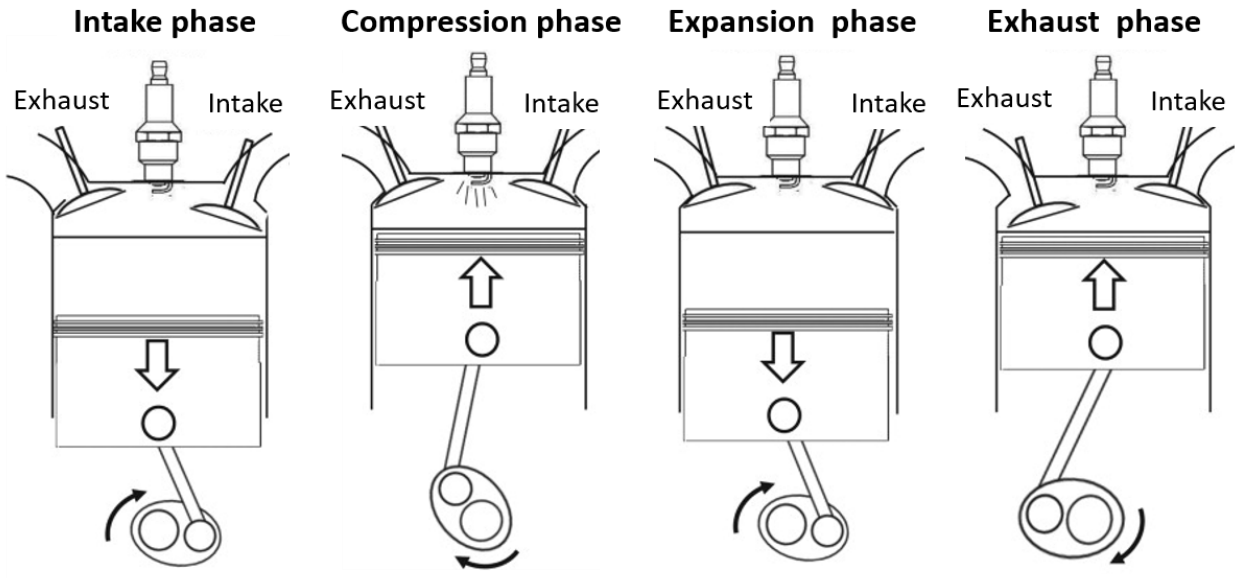

Figure 2-1 Four-stroke SI engine cycle.

The operating SI engine cycle and the related four phases are represented in *Figure 2-1*. The cycle phases can be described as follows:

1. *Intake phase*: it is mainly identified by the piston motion from top dead centre (TDC) to bottom dead centre (BDC) drawing fresh air or fuel-air mixture into the cylinder. Generally, with the aim to increase the mass introduced, optimizing the cylinder filling, the

intake valve opens before the TDC (0-40 CADs), while its closure is delayed of 40/50 CAD after the BDC. Hence, the intake phase is longer than the intake stroke, beginning at the Intake Valve Opening (IVO) and ending at the Intake Valve Closure (IVC).

2. *Compression phase*: conventionally it occurs once intake valves are closed and when the piston moves from BDC to TDC. The mixture inside the cylinder is compressed as a consequence of a volume reduction. When this phase is ending, the combustion starts, close to the TDC, rapidly causing an increment of pressure and temperature.
3. *Expansion phase*: it takes place with the piston at the TDC and concludes in correspondence to the exhaust valves opening (EVO). Realising this phase, thanks to the energy released by the combustion process, the piston receives the expansion work exerted by the gas.
4. *Exhaust phase*: here, two sub-phases can be identified: the spontaneous exhaust (from EVO to BDC) and forced one (from BDC to exhaust valves closure (EVC)). In the first stage, the cylinder pressure is higher than the exhaust manifold one, causing a natural escape of the burned gases from the cylinder to the exhaust pipes. Then, once the piston moves from the BDC to the TDC, volume reduction pushes the exhaust gases outside from the cylinder. Once the intake valves open, the engine cycle starts again.

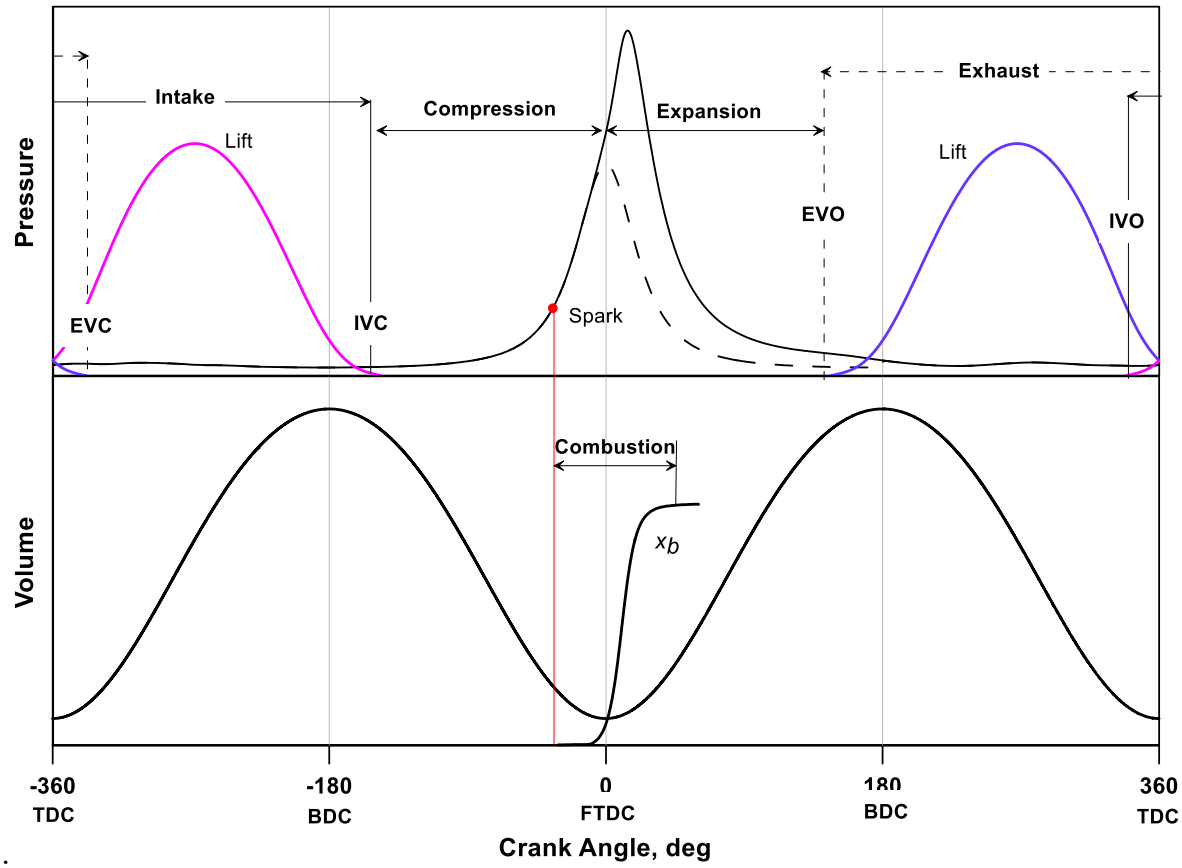

Figure 2-2 (top) Pressure traces and valve lift profiles in fired / motored conditions, (bottom) cylinder volume and mass fraction burned x_b as a function of the crank angle.

The events above described, for a conventional SI engine, are depicted in *Figure* 2-2. In addition, valves timing, volume, and pressure traces in motored (dashed line) and fired condition (continuous line) are reported against the crank angle. All phases contribute to the power and to the efficiency of the overall cycle. Further, to reach the prescribed load level, with the correct mixture proportion for the combustion, it is important to introduce in the cylinder the proper amount of air / fuel mixture.

On one hand, the air flow is regulated by the intake pipes geometry, the throttle valve, and the turbocharging system, if available, on the other, the fuel injection can be realized in two different ways, namely a Port Fuel Injection (PFI) or a Direct Injection (DI). The PFI is featured by a low-pressure system, injecting the fuel into the intake port, while the DI system directly provides the fuel into the cylinder at a higher pressure. Thanks to the high-pressure injection, the fuel diffusion and vaporization are improved. Although DI systems allow reducing the fuel consumption, in the case of fuel wall impingement Particle Matter (PM) increases, if compared with a PFI [2].

A proper flow motion inside the cylinder has to be ensured by the intake ports since it affects the combustion process, the heat transfer, and the air / fuel mixing. By varying intake ports orientation, valves geometry, and combustion chamber shape, three ordered flow motions, namely tumble, swirl, and squish can be generated. Particularly, the introduction of these motions into the combustion chambers aims to increase the combustion rate and/or to promote the mixing of the charge.

Once all the mixture is introduced in the combustion chamber, and the valves are closed, the electric discharge is realized across the spark plug, commonly in advance of the TDC, realizing the start of the combustion. A turbulent flame develops from the spark plug, propagating in the chamber, extinguishing once in contact with the walls. As can be seen in *Figure 2-2*, the combustion process, having a typical duration of about 40-60 CADs, causes the rapid increase of the in-cylinder pressure. Then, once the expansion ends, during the exhaust phase the cylinder scavenging process occurs, and subsequently the admission of the fresh charge for the next cycle.

With the aim to ensure the required load, depending on the engine architecture, the combustion process can be handled by varying its control parameters, e.g. Spark Advance (SA), valve timing, throttle position, or air / fuel ratio. It is worth remembering that, although not changing the control variables, two consecutive engine cycles are never equal. Indeed, due to the variations in local flow motion and turbulence levels into the cylinder, some differences arise in the mixture homogeneity and composition, especially near the spark plug, resulting in a phenomenon called Cycle to Cycle Variation (CCV). The CCV mainly causes fluctuations in the rate of heat release, hence in the amount of useful work done by a single combustion event, in the fuel consumption and emissions. Because of its erratic and stochastic character, it causes several problems to the development of optimal engine control systems.

2.1. Internal Cylinder Flow And Turbulence Development

One of the major factors controlling the combustion process in SI engine is the gas motion into the cylinder. The flow motion significantly affects the engine heat transfer, as well. The bulk gas motion and the flow turbulence characteristics are both important. The initial in-cylinder flow can be controlled and driven by the intake process. Then, during compression stroke, it significantly modifies. In the following sections the main features of gas motion into the cylinder, established by flows into and out of the cylinder through valves or ports, and by the piston motion will be detailed.

2.1.1. Intake Flows

The intake process controls many important aspects of the flow into the cylinder. For SI four-stroke cycle engines, due to the descending motion of the piston, the air is pulled into the cylinder. The intake flow velocities scale depends on the piston speed. During most of the intake phase, the gap between the intake valve head and the valve seat is the minimum cross-section for the flow, thus the gas velocities through this gap are the highest ones achieved in the cylinder flow field. The gas released within the cylinder from the valve opening results in an annular conical jet, while the radial and axial velocities in this jet have values about 10 times higher than the mean piston speed. Then, the jet separates from the valve seat and head, generating shear layers with large velocity gradients creating turbulence. This jet separation produces recirculation regions under the valve head and in the corner between the cylinder wall and cylinder head. Once the jet reaches the wall, the wall itself deflects most of the jet to the bottom toward the piston, nevertheless, a significant fraction flows up toward the cylinder head. The interaction between the jet with the wall produces large-scale rotating flow patterns into the cylinder. Such flows bring within the cylinder significant fluid kinetic energy and create shear, both of which can generate turbulence. Further, the intake valve and port geometries can be designed with the aim to increase these jet-created flows by producing large-scale in-cylinder rotating flows.

2.1.2. Mean Velocity and Turbulence

The charge motions into and within the engine cylinder are turbulent. In turbulent flows, if comparing the rates of transfer and mixing to the ones due to the molecular diffusion, the first are several times greater. This “turbulent diffusion” arises from the local fluctuations in the flow field, leading to increased rates of momentum, heat, and mass transfer, being essential to achieving satisfactory operation of SI engines. Turbulent flows are always dissipative. This is due to the viscous shear stresses that perform deformation work on the fluid, improving its internal energy at the expense

of its turbulent kinetic energy. The turbulence generation requires energy, indeed if this last is not supplied, the turbulence decays. So, for the turbulent velocity fluctuation, a common source of energy is shear in the mean flow structures. In particular, turbulence is rotational and characterized by high fluctuating vorticities, which persist only if the velocity fluctuations are three dimensional. Considering the engine cylinder, the flow is a combination of turbulent shear layers, recirculating regions, and boundary layers; further, it is unsteady and may exhibit substantial cycle-to-cycle fluctuations. In this case, both large-scale and small-scale turbulent motions are essential factors controlling the overall flow behaviour

It is worth underlining that, the application of these turbulence concepts to the engine field is complicated since the flow pattern into the cylinder varies during the engine cycle. Moreover, the mean flow can also change substantially from a cycle to the next one. Hence, cycle-to-cycle variations in the mean or bulk flow at any instant in the cycle occur together with turbulent fluctuations about that specific cycle's mean flow.

Since the turbulent flow is irregular or random, this phenomenon is often defined by applying statistical methods [1]. For an ICE, an ensemble-averaging approach is used, evaluating the main quantities at a fixed crank-angle θ, over many consecutive engine cycles. In this case, the typical approach for the flow characterization is the decomposition of the velocity components in the mean values $(\bar{u}, \bar{v}, \bar{w})$ and their turbulent components (u', v', w') according to:

$$u(\theta) = \bar{u}(\theta) + u'(\theta);\ v(\theta) = \bar{v}(\theta) + v'(\theta);\ w(\theta) = \bar{w}(\theta) + w'(\theta); \tag{2.1}$$

In turbulent flows, several length scales exist characterizing different aspects of the flow behaviour. In the following section, these scales will be recalled, whereas a brief description is provided here. The largest eddies in the flow are constrained in size by the system boundaries, while the smallest ones are limited by molecular diffusion. The three main length scales are qualitatively illustrated in *Figure 2-3* through the schematization of a jet entering the cylinder from the intake valve. Most of the turbulence production is due to the large eddies in the conical jet flow between the valve and seat. The largest scale structures in turbulent flow are measured by integral length scale l_t.

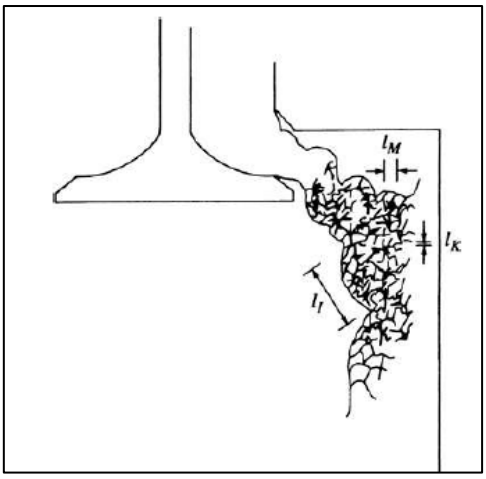

Figure 2-3 Schematic of jet created by the flow through the intake valve indicating its turbulent structure [1].

Over this scale, a smaller size eddies range is superimposed, fed by the continual breakdown of larger eddies. The dissipation of turbulence energy occurs in these smallest structures. In correspondence of this scale, named Kolmogorov scale l_k, the kinetic energy is dissipated via molecular viscosity into thermal energy. Finally, the last scale characterizing a turbulent flow is the microscale (Taylor microscale) l_M. It is defined by relating the fluctuating strain rate of the turbulent flow field to the turbulence intensity.

2.1.3. Swirl

The swirl phenomenon can be described as an organized rotation of the charge around the cylinder axis. It is created bringing the intake flow in the cylinder and promoting an initial angular momentum around the cylinder axis. Generally, the swirl generated at the intake carries on through compression, combustion, and expansion phases, occurring some decay because of friction during the engine cycle. Depending on the combustion chamber shape, the swirl can be controlled. As an example, in an engine featured by bowl-in-piston combustion chambers, the rotational motion imposed during intake undergoes a significant amplification during compression.

Usually, the swirl is applied in diesels and in some stratified-charge engine with the aim to favour a more rapid mixing between the air charge and the injected fuel. Further, this phenomenon is applied to accelerate the combustion process in spark-ignition engines. It is also used in pre-chamber engines, where swirl into the pre-combustion chamber is generated during compression properly orientating the PC holes. This aspect will be deepened in the following.

Since this phenomenon is beneficial, it is intentionally created during the induction process, with two general approaches. In the first one, the flow is released within the cylinder tangentially, being deflected laterally and to the bottom in a swirling motion. In the second one, the swirl is mainly

produced into the inlet port forcing the flow to rotate around the valve axis, before entering the cylinder.

To achieve the first motion type, the flow distribution around the circumference of the inlet valve is forced to be nonuniform leading to an intake flow characterized by a significant net angular momentum around the cylinder axis. In *Figure 2-4* directed port (*a*) and deflector wall port (*b*) are depicted, being the two common solutions to achieve this result.

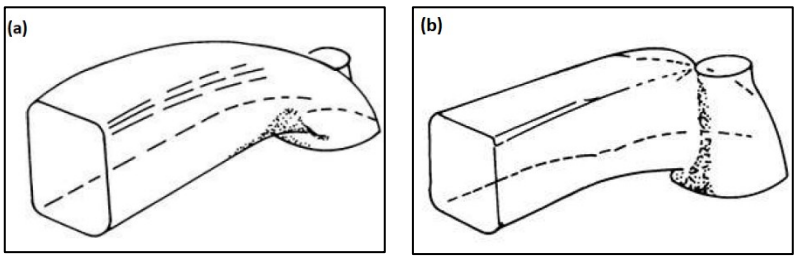

Figure 2-4 Different types of swirl-generating inlet ports: directed port (a) and deflector wall port [1].

The second approach above-described, is realized by employing helical ports, as shown in *Figure 2-5*. These ports are characterized by a higher flow discharge coefficient, obtaining equivalent swirl levels, because of more effective utilization of the whole periphery of the valve open area. This leads to higher volumetric efficiency.

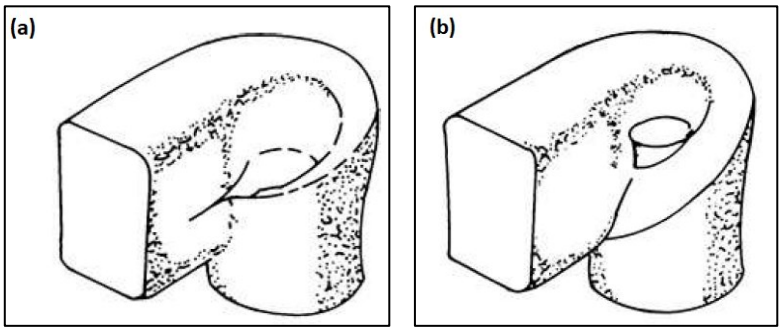

Figure 2-5 Different types of swirl-generating inlet ports: shallow ramp helical (a) and step ramp helical [1].

As said, once generated the swirl can be modified within the cylinder. The angular momentum of the air entering the cylinder incurs in a decay during the rest of the intake and the compression because of the friction at the walls and turbulent dissipation into the fluid. Nevertheless, during compression, the swirl velocities can be enhanced in the charge by a dedicated combustion chamber.

2.1.4. Tumble

Tumble phenomenon is generated within the cylinder of an SI engine with the aim to accelerate the combustion process. The tumble can be described as a charge rotation around an axis orthogonal to the cylinder axis. A typical combustion chamber featured by a tumble establishment, depicted in *Figure 2-6,* is the pent-roof one equipped with four valves with inclined valve stems. The tumble is

achieved by placing the intake ports so to bring the air flow into the cylinder through the upper portion of the open area between the valve head and valve seat. In such a way a transverse motion is imposed on the entering air. Then, the descending piston pulls the flow downwards, in the proximity of the liner on the opposite side of the intake valves. Subsequently, the flow goes back passing along the piston crown, moving upwards, again along the liner, completing its rotation, as shown in *Figure 2-6.* Since the intake-valve open area is not used uniformly, the transverse flow velocity beyond the valve is higher for a fixed piston speed, resulting in additional kinetic energy storage into this tumbling flow. It is worth underlining that, because of the inhomogeneous use of the valve open area, the flow resistance of the intake valve is higher, resulting in a lowering of the engine volumetric efficiency. Successively, during the compression process, the tumble flow is squashed due to the ascending piston and degrades in smaller-scale vortices producing turbulent kinetic energy which, after the spark event, enhances the mixture burning rate. Considering SI engines, the tumble phenomenon is usually exploited aiming at obtaining faster burn rates, especially to improve the part-load operating condition, accepting as a consequence a certain loss in engine breathing capacity at higher loads and speeds.

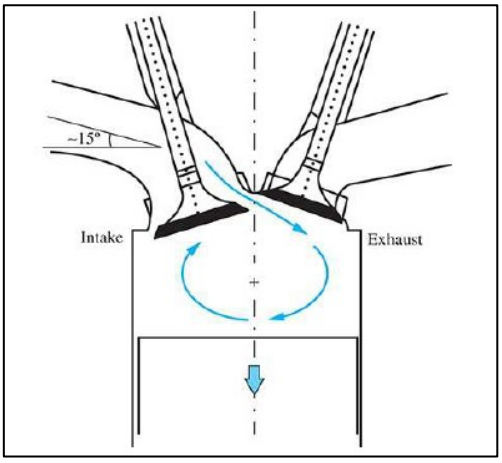

Figure 2-6 Schematic showing tumble generation [1].

Tumble flows are characterized and classified depending on their angular momentum. The first one is the tumble flow, depicted in *Figure 2-6*, representing the so-called *normal tumble*, featured by a flow rotation around the shown axis that is parallel to the ridge of the pent roof cylinder head. Instead, the second one, the *reverse tumble*, characterized by a flow rotating in the direction opposite to the one reported in *Figure 2-6*, (counter-clockwise), is created by using intake ports directed vertically downward the intake valve, instead of the one more inclined as in *Figure 2-6*. Finally, the third one, namely *cross tumble*, happens once tumble arises in the presence of swirl, resulting in a flow component in the plane at 90° to the one depicted in *Figure 2-6.*

The generation of more vigorous in-cylinder flows, such as swirl and tumble, leads to higher pressure losses and flow restrictions across the intake port, and the valve and seat opening, resulting in a lowering of the maximum air flow. For these reasons, the challenge is achieving the desired faster combustion rates produced by these higher kinetic energy flows, minimizing the loss in air flow, especially at the higher engine speeds and loads, where the combustion process is already fast. Therefore, adequate geometries of the cylinder-head, intake-port, and piston-crown have to be designed, aiming at improving the combustion and reducing the flow losses, depending on the engine characteristics.

2.1.5. Squish

If the cylinder head or piston crown surfaces are shaped (i.e., pent-roof cylinder heads in SI engines, or bowl-in-piston combustion chambers in CI engines) and not flat, the axial velocity generated by the piston during compression and expansion processes, creates transverse or radial flows because of the differences in the axial distance between the cylinder head and piston crown surfaces across the cylinder cross-section. This radial / transverse gas motion, named squish, occurs toward the end of the compression and during the first stage of expansion, when the piston face and cylinder head come closer, or move away, each other. Two examples representing how piston motion generates squish are reported in *Figure 2-7* depicting a wedge-shaped SI engine combustion chamber (*a*) and a bowl-in-piston CI engine combustion chamber (*b*). Hence, the gas motion generated by the squish results from employing a compact combustion chamber geometry.

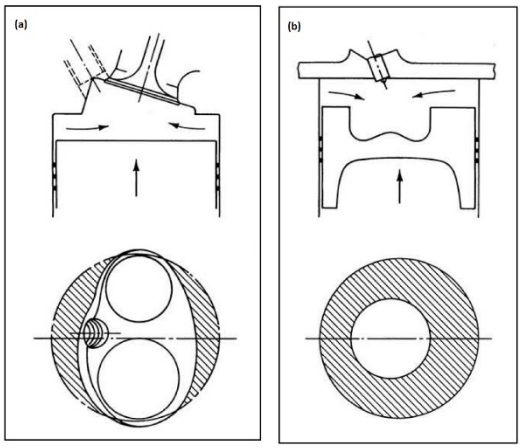

Figure 2-7 Schematics of squish generation: wedge-shaped SI engine combustion chamber (a) and bowl-in-piston direct-injection diesel combustion chamber (b) [1].

2.1.6. Pre-chamber Engine Flows

Engines concept equipped with a pre-chamber presents this auxiliary small chamber that is connected to the main one through nozzle, passageway, or one or more orifices. The high velocities in the PC at the time when the fuel-injection begins are due to the flow through this restriction, generated during the compression. For this reason, the fuel-air mixing rates are usually high. Depending on the dimension, numbers, and direction of the nozzles, the flow within the PC varies. As an example, two of the most common PC designs are the swirl pre-chamber, characterized by a flow entering the chamber tangentially, producing a rapid flow rotation, or the turbulent pre-chamber featured by more connecting orifices, which generate high turbulent flow. It is worth to underline that the most critical phase for the flow within the pre-chamber arises towards the end of compression. Indeed, in this phase, the velocity field is highly dependent on the characteristic of nozzles and pre-chamber geometry. Considering for instance a swirl pre-chamber, the flow through the nozzles generates a rotating flow into the chamber. Here, the velocities increase during the compression stroke. Then, once the piston reaches the TDC and the flow through the orifices decreases to zero, the vortex in the PC expands, filling the entire chamber and resulting in a mean velocities decay. The highest swirl rates can be achieved just before TDC, producing large centrifugal accelerations. Concerning the turbulent pre-chamber, a similar effect is achieved by a number of properly shaped holes, which guides the incoming flow during the compression phase. The interaction of the multiple flows determines an intense turbulence increase before the TDC, which favourite the combustion onset and its cyclic stability.

2.1.7. Crevices Flows and Blowby

The combustion chamber is connected to several small volumes named crevices, characterized by narrow entrances. During the engine cycle, due to the pressure and volume change of the cylinder, these crevices are filled / emptied by the gases. The main crevice is the one between the piston lands, piston rings, and liner. Further, some gas leaves these regions, through the ring gaps, flowing into the crankcase and generating a phenomenon called blowby. Other crevices minor in volume are the spark plug threads, the space between the plug centre-electrode-insulator and casing, volumes between the intake and exhaust valve heads and related seats, and the head gasket.

During the compression, since the cylinder volume decreases and pressure rises, unburned mixture is forced within crevice regions. Once the gas flows into the crevice, it cools due to the lower wall temperature. Then, during the combustion process, the pressure continues to increase, and unburned

mixture continues to fill the crevice volumes. Subsequently, the cylinder pressure starts decreasing, causing a gas flow back from the crevice in the cylinder.

The volumes between the piston, piston rings, and liner, as said, represent the main crevices. They consist of a series of volumes connected by restrictions such as the ring side clearance and ring gap. Due to the ring motion into the related groove, the crevice volumes vary. Further, the gas flow, pressure distribution, and ring motion are coupled. Generally, during compression and combustion, the rings are forced to the groove lower surfaces, and gas flow enters in the crevice volumes. The pressure above and behind the first ring is equal to the cylinder one. Once the pressure begins decreasing, gas flows out of the top crevice within the cylinder. During the expansion, the top ring moves up close to the upper groove surface. A percentage of about 5-10% of the total charge can be trapped in these regions in correspondence to the pressure peak. Most of the gas returns into the cylinder, continuing the expansion process, while the remaining part is discharged into the crankcase as blowby. In SI engines the return into the combustion chamber of the unburned gas from crevices represents one of the major contributors to unburned hydrocarbon emission. This leads to a loss in torque and efficiency because a portion of fuel does not take part in the combustion process.

Regarding the above-mentioned blowby phenomenon, it represents the gas flowing from the combustion chamber, through the piston rings, to the crankcase. If the contact between the rings and the liner, and between the rings and the related grooves is good, the sole leakage path is due to the ring gap. Due to the blowby of gases from the cylinder to the crankcase, gas is removed from these crevice regions avoiding a return of some gases into the cylinder. Nowadays, the crankcase is discharged within the intake system, recycling the blowby gases. Further, the blowby is mainly regulated by the highest flow resistance in the flow path, between the cylinder and crankcase, for fixed speed and load.

2.2. Turbulent combustion

The combustion process is an important part of the ICEs operating cycle, since it releases the chemical energy of the fuel in a short time period between the end of the compression process and expansion one, producing the high-pressure and temperature burned gases that expand into the cylinder transferring work to the piston. To achieve an efficient energy conversion process, the combustion has to last in a small fraction of the total cycle time.

The combustion process is mainly controlled by the interaction between the flame development and the turbulent flow. The flame generation is due to the electric discharge in the spark plug, while the flow field production occurs during the intake process, being modified along the compression stroke. In *Figure 2-8* 2D images of the flame evolution are reported with the aim to better describe

its development. These are outcomes from digital imaging of an optically accessible single cylinder PFI engine, realized in [3]. The flame development is reported at different crank angles, selected to describe the main phases of the combustion process. At 3 CAD BTDC the *spark ignition* occurs, while the first flame is visible at 2 CAD ATDC, having approximately a circular shape. During this initial phase, called *early flame development*, the flame mainly propagates in laminar conditions. At around 6 CAD ATDC, the flame shape becomes irregular, because of the turbulent flow interaction, causing wrinkles and corrugating the flame surface.

When this interaction happens, the burning rate is incremented, and the *turbulent flame propagation phase* starts. Around 16-16 CAD ATDC, once the flame reaches the cylinder walls, the combustion process ends, resulting in the *flame termination phase*.

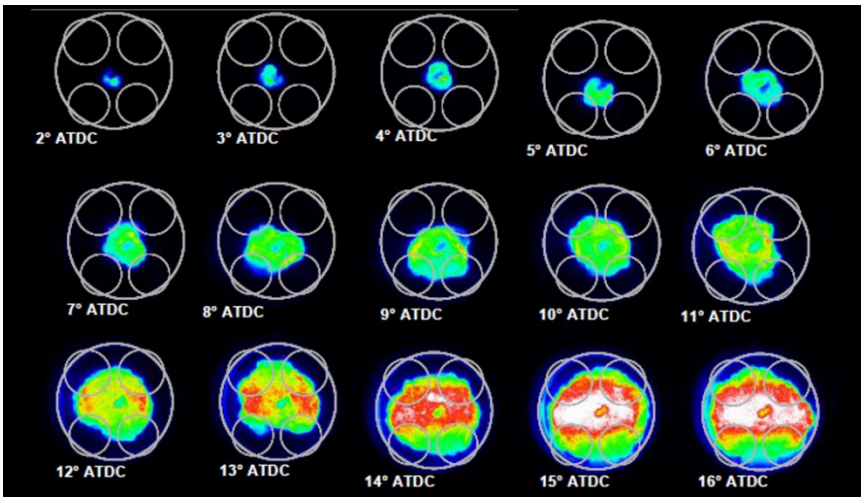

Figure 2-8 UV-visible digital images of the flame propagation [3], SA= 3 CAD.

Three of the main drivers, during the combustion process are the SA, the laminar flame speed, and the turbulent field into the cylinder.

Starting from the spark advance, it is important to underline that it has to be properly set to obtain the Maximum Brake Torque (MBT) and power. In *Figure 2-9(a)* the p-V diagram is reported, for three different spark timings. As can be noted, a very early start of combustion (blue line) increases the pressure peak during the compression stroke, resulting in a lower expansion work, while an extremely delayed spark timing (magenta line) leads to a late pressure peak along the expansion stroke, causing a reduction of the available work from the cycle. Therefore, the optimal SA is the one ensuring the biggest cycle area, which means available work (red line). Although the selection of SA value depends on engine design, operating conditions, air / fuel ratio, etc., generally, for a conventional SI engine, it is set aiming at burning the 50% of the mixture (50 % Mass Fraction Burned, MFB_{50}) at about 7-8 CAD ATDC [1]. However, if occurring an abnormal combustion

process (knock phenomenon), as better explained in the following, the SA is delayed with respect to the MBT value.

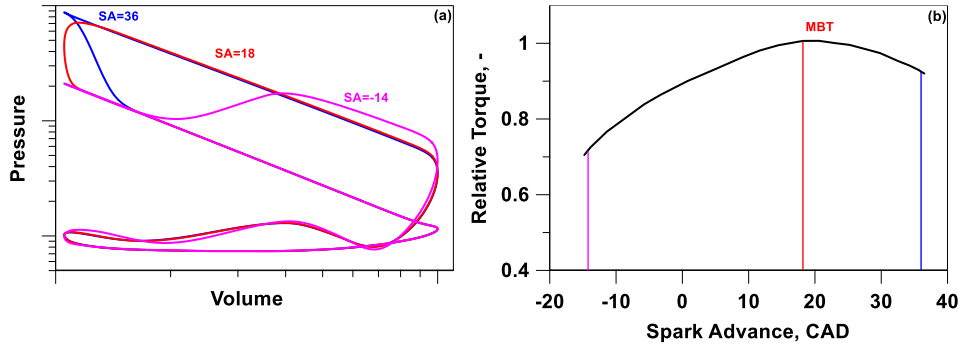

Figure 2-9 (a) Logarithmic p-V diagram for three different spark timing, (b) effect of spark advance on brake torque at a constant speed and air-fuel ratio.

After the spark event, a flame kernel is formed between the spark plug electrodes. In the first stage, a smooth quasi-laminar flame, with a reduced thickness δ_L, develops, with a characteristic speed, named laminar flame speed (LFS) and denoted with the symbol S_L. It is defined as the velocity of the unburned gases moving into a planar flame front under laminar flow conditions. Usually, LFS was experimentally derived [4],[5],[6],[7],[8],[9]. These investigations were mainly performed in preheated closed vessels with optical access, where the laminar burning speed of spherically expanding flames in premixed reactants was measured, resulting in different LFS correlations proposed for different blends of air and reference hydrocarbons. They arise from the analytical fitting of experimental data obtained for wide ranges of pressure, p, temperature, T, and composition (equivalence ratio, ϕ, and mixture dilution). The mathematical formulation of the pioneering correlations of Metghalchi and Keck [4] and Rhodes and Keck [5] is based on the so-called power-law formula. This formulation does not consider any cross-influences between p and T, and the exponents of the individual terms depend monotonically on the equivalence ratio. These oversimplifications were removed in novel formulations [6],[7]. Regardless of the mathematical expression for the LFS correlation, the application of an experimentally derived formulation may result in relevant uncertainties under typical engine-like operations. This is because the experimental tests could only be performed in a limited range of equivalence ratios and at low pressure and temperature (usually below 15 bar and 600 K, respectively), due to technical [8],[9] and ignitability [4][19] limitations. To overcome these limitations, alternative LFS models based on reaction kinetics calculations were developed [10],[11],[12]. These models allow extending the ranges of the independent variables, leading to more accurate LFS correlations for engine-like operating conditions. However, the accuracy and the computational burden of such models strongly depend on the number of species and reactions of the adopted kinetic scheme [13],[14],[15]. If the correlation aims to mimic the behaviour of commercial gasoline, the computations are usually carried out for a

surrogated fuel (a blend of reference primary fuels, such as n-heptane, iso-octane, toluene, and methanol). The composition of the surrogated fuel can influence significantly the LFS predictions, and its most appropriate selection remains an open issue.

The above-mentioned correlations, as said, are mainly based on the following power-law formula:

$$S_L = S_{L0} \cdot \left(\frac{T}{T_0}\right)^{\alpha} \left(\frac{p}{p_0}\right)^{\beta} \cdot EGR_{factor} \tag{2.2}$$

where S_{L0} is the flame speed at reference conditions $T=T_0$ and $p=p_0$ for given fuel type and equivalence ratio, exponents α and β depend only on ϕ, while EGR_{factor} is a LFS reduction term that accounts for the inert gases contained in the unburned mixture. In *Figure 2-10(a)*, the experimental $S_{L,0}$ is plotted for different fuels and equivalence ratios. The laminar flame speed presents a peak near stoichiometric or slightly rich air / fuel mixture for the most common hydrocarbons, justifying the need to always operate SI ICEs close to stoichiometric conditions. In *Figure 2-10(b-c),* the typical trends of S_L as a function of temperature, pressure are reported for various fuels used in SI engines. These two parameters have an opposite impact on the LFS, the higher the pressure (temperature), the lower (higher) S_L. Further, the EGR rate always causes, a substantial reduction in the laminar burning velocity.

The maximum LFS value, for typical conditions of an SI engine, is about 1 m/s. If the flame propagated in the combustion chamber having this velocity value, the combustion would not be completed in time, before exhaust valves opening. Therefore, the needing for a turbulent flow generation inside the combustion chamber arises to enhance the combustion velocity.

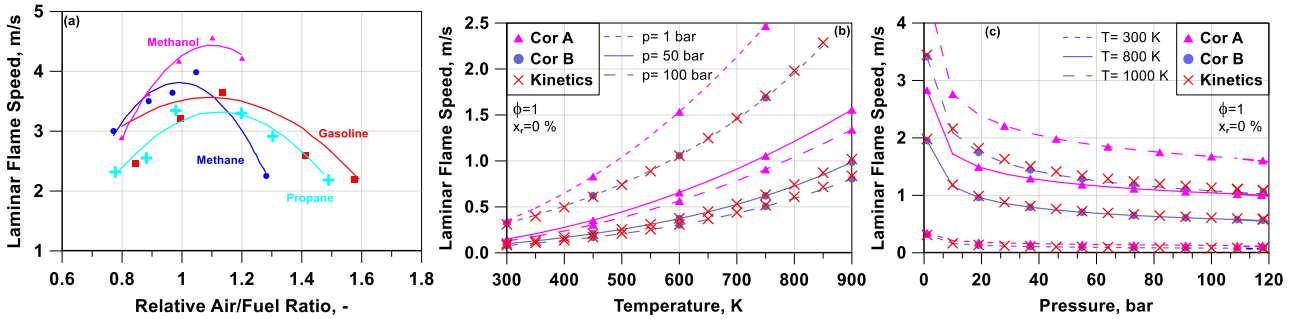

Figure 2-10 (a) Experimental $S_{L,0}$ and its polynomial fits for different fuels as a function of the relative air / fuel ratio at 1 atm and 300K, (b-c) gasoline laminar flame speed correlations cor. A [4] and cor. B [12] at different pressures, temperatures at stoichiometric conditions.

The turbulence phenomenon is a 3D unsteady, rotational, and highly diffusive flow, characterized by the presence of disordered eddies, ranging over a wide length scale interval. If the largest eddies are restricted in size by the system boundaries, the smallest ones are limited by the molecular

diffusion. Once eddies with different scales interact each other, an energy transfer sequentially occurs from the larger eddies gradually to the smaller ones, thanks to a process known as the turbulent energy cascade. In the turbulent field, two main length scales can be identified, associated with their characteristic time scales:

1. *Integral length scale* (L_t): is a measure of the largest scale structures in the turbulent flow, featured by low frequency and large fluctuation. It is defined as the integral of the autocorrelation coefficient of the fluctuating velocity at two adjacent points in the flow with respect to the variable distance between the points as shown in *Figure 2-11*.

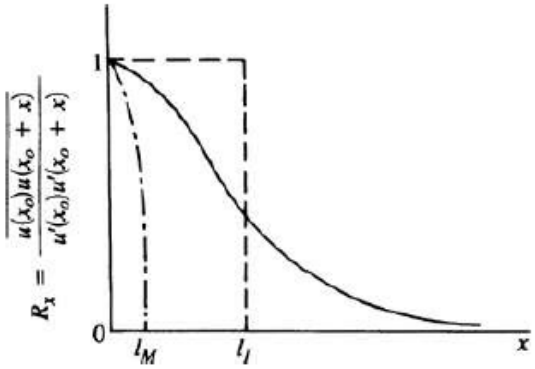

Figure 2-11 Spatial velocity autocorrelation R_x as a function of x, defining the integral length scale L_t and the micro length scale L_M [1].

$$L_t = \int_0^\infty R_x dx\,; \qquad R_x = \frac{1}{N_m - 1}\sum_{i=1}^{N_m} \frac{u(x_0)u(x+x_0)}{u'(x_0)u(x+x_0)} \tag{2.3}$$

where N_m is the number of measurements. This technique for determining the integral scale requires simultaneous measurements at two points. Due to the difficulty of applying this technique in engines, most efforts to determine length scales have first employed correlations to determine the integral time scale, τ_t.

2. *Taylor length scale* (L_M): is defined by relating the fluctuating strain rate of the turbulent flow field to the turbulence intensity, as expressed in eq. (2.4) and can be determined from the curvature of the spatial correlation curve at the origin, as shown in *Figure 2-11.*

$$\frac{\partial u}{\partial x} \approx \frac{u'}{L_M} \tag{2.4}$$

3. *Kolmogorov length scale* (L_k)*:* is the smallest scale of the turbulent motion, at which the kinetic energy is dissipated via molecular viscosity into thermal energy, expressed as:

$$L_k = \left(\frac{\nu^3}{\varepsilon}\right)^{3/4} \tag{2.5}$$

Depending on the interaction between the flame and the turbulent flow field, different combustion regimes can occur. Each regime is associated with a peculiar flame evolution and shape. Commonly the flame / turbulence interactions are classified on the basis of the comparison of the previously defined characteristic lengths / speeds and times, as summarized in *Table 2.1*.

Table 2.1 Characteristic speed, length, and time scales of the turbulent combustion.

Scale	Speed	Length	Time
Chemistry	S_L	δ_L	$\tau_L = \delta_L / S_L$
Kolmogorov	u_k	L_k	$\tau_k = L_k / u_k$
Integral	u'	L_t	$\tau_t = L_t / u'$

The above-mentioned comparisons can be easily represented in the Borghi diagram, shown in *Figure 2-12a*, with the aim to define all the possible combustion regimes that may occur in a premixed turbulent flame [16]. For this purpose, three dimensionless numbers have to be introduced:

1. *Turbulent Reynolds number*(Re) is the ratio between inertial forces related to turbulent flow motion and viscous forces, as defined in eq. (2.6). A turbulent flow is characterized by a Re number higher than the unit. The ratio between turbulent and chemistry speed scales can be derived, introducing the relationship between the flame thickness and the laminar flame speed ($\delta_L = \nu / S_L$).

$$Re = \frac{u' L_t}{\nu}; \qquad \rightarrow \quad \frac{u'}{S_L} = Re \left(\frac{L_t}{\delta_L}\right)^{-1} \tag{2.6}$$

2. *Damköhler number*(Da) is the ratio between the turbulence characteristic time at the integral length scale level and the chemical kinetics characteristic time. It is an inverse measure of the turbulent flow influence on the chemical processes occurring in the flame. A Da lower than 1 represents a condition such that the turbulence is faster than the chemistry, and the combustion is mainly regulated by chemical kinetics. On the contrary, once Da is higher than the unit, the combustion is characterized by very fast chemical kinetics if compared to the turbulent phenomena.

$$Da = \frac{\tau_t}{\tau_L} = \left(\frac{L_t}{u'}\right) / \left(\frac{\delta_L}{S_L}\right); \qquad \rightarrow \frac{u'}{S_L} = Da^{-1} \frac{L_t}{\delta_L} \tag{2.7}$$

3. *Karlovitz number*(Ka) represents the ratio between the chemical kinetics characteristic time and the turbulence characteristic time at the scale of the smallest turbulence eddies (Kolmogorov length scale). In the hypothesis of isotropic and homogeneous turbulence, the Reynolds Turbulent number can be expressed as $Re_t = (u'L_t)/(S_L\delta_L)$. This number can be correlated to the Kolmogorov length and speed as ${Re_t}^{1/4} = u'/u_k$ and ${Re_t}^{3/4} = L_t/L_k$. Hence, replacing in the second term of eq. (2.8) L_k and u_k from the above relations, the Ka can be expressed as the third form of the equation. If Ka is lower than 1, the chemical time scale is shorter than any turbulent scale and the flame thickness is smaller than the Kolmogorov scale, thus the chemical reactions inside the flame front are not affected by turbulent filed. When Ka becomes higher than the unit, the turbulent eddies penetrate the reactive zone of the flame.

$$Ka = \frac{\tau_L}{\tau_k} = \left(\frac{\delta_L}{S_L}\right) / \left(\frac{L_k}{u_k}\right) = \left(\frac{L_t}{\delta_L}\right)^{-\frac{1}{2}} / \left(\frac{u'}{S_L}\right)^{\frac{3}{2}} = \left(\frac{\delta_L}{L_k}\right)^2 \rightarrow \frac{u'}{S_L} = Ka^{2/3}\left(\frac{L_t}{\delta_L}\right)^{2/3} \qquad (2.8)$$

Equating the numbers above introduced to the unity, 5 different combustion regimes zones can be identified into the Borghi diagram, which reports the ratio $\frac{u'}{S_L}$ against $\frac{L_t}{\delta_L}$ in a logarithmic scale. The combustion regime regions on the Borghi diagram are represented in *Figure 2-12(a)* and summarized in *Figure 2-12(b)*, the related flame morphologies are shown. The main characteristic of the *wrinkled flamelets* zone is a laminar flame speed greater than the turbulence intensity, which implies that the flame front cannot be corrugated by the turbulence. Furthermore, since the Ka is lower than 1, the turbulence presence does not affect the chemical kinetics. Consequently, since the smallest eddies are bigger than the flame thickness, they are not able to enter the flame front. Once the turbulent intensity grows, becoming higher than the laminar speed, the combustion regime changes entering the *corrugated flamelets region*.

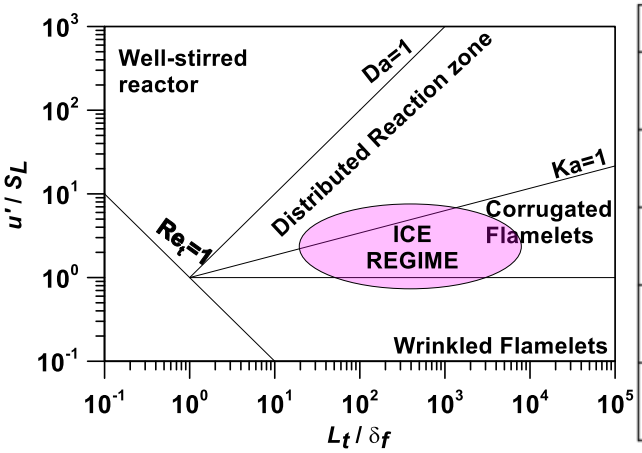

Regime	Re	Da	Ka	U'/SL	Flame
Wrinkled flamelets	>1	>1	<1	<1	
Corrugated flamelets	>1	>1	<1	>1	
Distribuited reaction zone	>1	>1	>1	>1	
Well-stirred reactor	>1	>1	>1	>1	
Broken reaction zone	>1	<1	>1	>1	

Figure 2-12 Borghi diagram (a) and list of the turbulent premixed combustion regimes (b).

This zone is featured by turbulence able, not only to corrugate the flame front, but also sometimes to create pockets of burnt gases inside the fresh gases zone. The Ka is still lower than one, hence the turbulence does not affect the flame structure. Passing to the *Distributed reactions zone*, since Ka becomes higher than the unit, the smallest eddies enter the pre-heat zone of the flame, not being able to penetrate the reaction zone; in other words, their dimension is still greater than the thickness of the reaction zone (*Figure 2-13).*

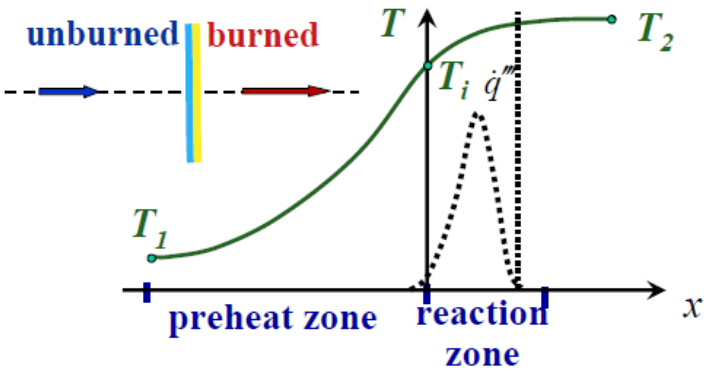

Figure 2-13 Structure of 1D pre-mixed flame.

As a consequence of the eddies entering the pre-heat zone, the turbulence convection accelerates both heat and mass transfer mechanisms. Once Da achieves values lower than 1, the chemical kinetics control the combustion, determining the *well stirred reaction regime*. Here the turbulence is intense enough to create a perfect stirring between the reactants and the products of the combustion, avoiding the establishment of a flame front. The last regime zone, not visible in the Borghi diagram, is the *broken reaction*, characterized by a Ka >>100. In this zone, the turbulent eddies enter the reaction zone, for this reason, the flame extinguishes. On the basis of experimental observations emerged that

the ICEs mainly work in the wrinkled and corrugated zone, magenta circle in *Figure 2-12*, In those regimes, the turbulence does not affect the chemistry kinetics and the reaction speed can be synthetized by the laminar flame speed.

2.2.1. Flame Stretch

As above discussed, the premixed combustion in a turbulent flow field is a very complex process, based on the interaction of different phenomena influencing the turbulent flame dynamics. As said, combustion in a SI engine principally occurs in the "corrugated flamelet" regime, where turbulence does not affect the inner flame structure, having the LFS as a parameter to describe the chemical reactions and molecular diffusion processes into the flame. Generally, the turbulence effect is to wrinkle and distort an essentially laminar flame front, strongly increasing the burning rate. However various instabilities may appear associated with the molecular diffusion of radical species and heat ahead of the flame front, even in a laminar flame. These instabilities are responsible for flame deformation and displacement, hence modifying the LFS. Moreover, since in a SI engine the flame propagates in a quasi-spherical shape, the flame stretch phenomenon occurs, leading to local variations, in terms of geometry and dynamics, of the flame speed.

The flame stretch phenomenon affects the combustion evolution, especially in its early stage of quasi-laminar flame propagation. It is a measure of the flame surface distortion that arises from its motion and the underlying flow field. Further, this phenomenon consists of local modifications of the flame speed caused by two effects: the preferential diffusion, which results in local variations of flame temperature and burning rate (depending on the effective Lewis number), and the flow divergence, which causes an increase in the flame speed at the upstream boundary of the preheat zone with respect to the speed of the reaction zone [17],[18]. The speed of a stretched flame can be related to the one of a planar flame introducing a flame-thickness-dependent coefficient accounting for the effects of diffusion and chemical reactions in the flame zone. This coefficient, known as the Markstein length, L, depends on fuel type and reactivity, and mixture composition [19]. This phenomenological parameter was introduced to describe the dependence of the flame speed on the local curvature. In these studies, the whole flame, including both preheat and reaction zones, was considered as a surface distinguishing the fresh unburned mixture from the hot combustion products. Recently, asymptotic approaches were used, suppling a more rigorous foundation for the flame stretch problem [20]. Using the asymptotic approaches to represent the flame, its speed can be considered as a linear function of the local stretch rate, $\mathbb{K}$. The flame stretch has been widely studied from an experimental point of view and, as an example, measurements of flame stretch for various Lewis numbers, equivalence ratios, and fuels have been performed [17]. All the theoretical and experimental studies have

highlighted the LFS variations induced by the flame stretch, which can affect the progress of combustion in typical SI engine operations.

2.3. Knock phenomena

One of the most critical abnormal combustion affecting SI engines is the knock phenomenon. Knock is the name given to the noise transmitted through the engine structure once the spontaneous ignition of a large fraction of the end-gas occurs. Usually, when this abnormal combustion process arises, a sudden release of chemical energy in the end-gas occurs, resulting in very high local pressures and in the propagation of pressure waves across the combustion chamber, characterized by significant amplitude. The main reasons to avoid this undesired event can be described as follows. Firstly, since the pressure oscillations promote the heat transfer, the thermal losses increase leading to a reduction of the available work. Then, due to the pressure wave reflections, the lubricant film separating the piston from the cylinder walls can be removed, reflecting into an engine seizure. Finally, if the knock intensity becomes quite huge, an irreparable damage of the cylinder may occur, as shown in representative cases of *Figure 2-14*. This is due to the heavy knock occurrence that causes the transfer of heat to the combustion chamber walls, leading to the overheat of the cylinder head and piston.

Figure 2-14 Example of engine piston damaged by heavy knock.

Different methods to measure and characterize the knock intensity are proposed in the literature [21]. The analysis of the in-cylinder pressure signals, through a pressure traducer flush-mounted in the combustion chamber, is the method more widely adopted. for knock estimation, the pressure trace is collected and then processed using a band-pass filter in a range of 4-20 kHz. The low cut-off is used to filter the regular combustion noise (low frequencies), whereas high cut-off is necessary to remove the signal disturbance given by the sensor resonances. The magnitude of the knock phenomenon can be quantified through a knock index. Two of the most frequently used [22] indices

are the Integral of Modulus of Pressure Oscillations (IMPO) and Maximum Amplitude of Pressure Oscillations (MAPO). Knock indices are estimated for each cycle, in a fixed crank angle window, commonly 40-60 CAD starting from the spark event. Once detected, MAPO and IMPO are averaged over various consecutive cycles, at least 100. So, the indexes are monitored to prevent the knock event through the adjustment of the spark timing. Indeed, delaying the spark timing allows decreasing the knock intensity, whereas an advanced spark causes an increase of the knock probability. Hence, during the engine calibration, under knock-limited operations, the SA is selected with the aim to maintain the knock indices around a predefined threshold level. This threshold is defined to preserve the engine safety and usually is variable with the engine speed.

In *Figure 2-15(a)* a typical measured pressure trace is represented in knock conditions, with the related signal detected by an accelerometer mounted on the cylinder block. The time delay between the two signals is due to the pressure oscillations propagation through the engine block. The difference in the pressure cycle behaviour under various knocking intensities is highlighted in *Figure 2-15(b),* where three pressures signals are reported, under different engine speeds and spark advances. The green line represents a cycle with incipient knock (#137), while the red line depicts a heavy knock condition occurs (#63), both for a speed of 4000 rpm. Instead, an acceptable very soft knocking cycle (#95) is reported in blue, corresponding to a lower engine speed (3000 rpm).

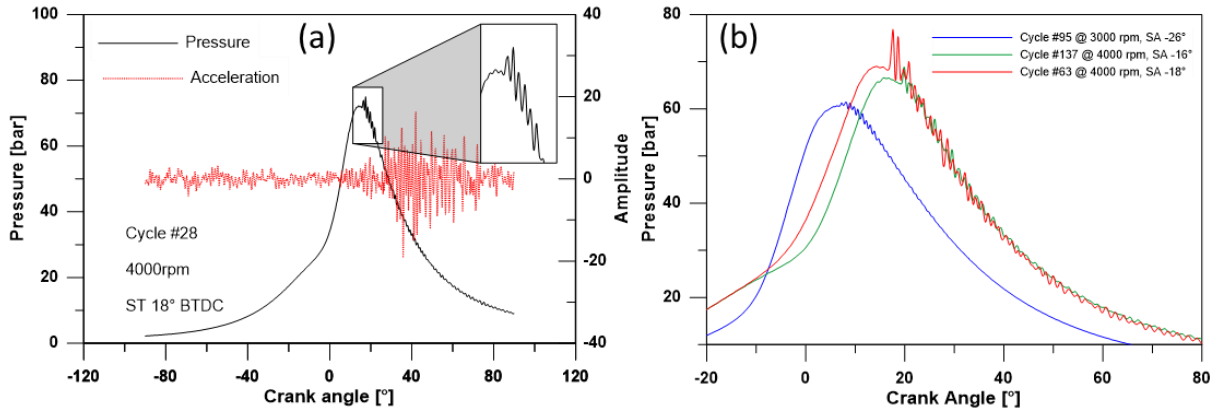

Figure 2-15 (a) Pressure trace and amplitudes detected by the accelerometer referring to the at 4000 rpm, WOT and SA=18° ATDC, (b) pressure traces for different spark advances at 4000 and 3000 rpm, WOT [23].

2.4. Cycle-to-Cycle variation

Another common phenomenon affecting the combustion of SI ICE is the cycle-to-cycle variation. Since the in-cylinder pressure variation alters the brake torque stability, directly influencing the vehicle drivability, the CCV should be limited. If compared to the knock phenomenon, the CCV is not totally eliminable but can be limited through a proper combustion parameter optimization. The main causes of CCV are to be found in the variations between consecutive cycles, not only in the air and fuel flow but also in the mixing of fresh charge and residual gas, mainly near the spark plug.

From several experimental campaigns, it turns out that the most critical combustion phase for the CCV is the early stage of flame development. A higher probability to have a combustion characterized by cyclic variation arises if the combustion itself begins slowly, for example in presence of air excess or high fraction of residual gas.

The optimal spark timing selection, for a train of pressure cycle at fixed operating conditions, is made with reference to the average cycle. However, the extreme cycles have to be monitored with special attention, since these can limit the engine operation. Under knock limited operations, in fact, the fastest cycles are characterized by higher values of pressure and temperature, for which is higher the probability of knocking combustion is higher. Instead, in the case of lean combustion, the cycles needing a monitoring are the slowest ones since they are characterized by the highest probability to have an incomplete combustion. The CCV intensity is usually based on the acquisition and the post-process of consecutive pressure traces (300-500), and then on the analysis of the Coefficient of Variation (CoV) for some fundamental parameter related to in-cylinder pressure, burning process, or engine performance. The two most commonly adopted CoV parameters are the ones related to the Indicated Mean Effective Pressure (IMEP) and to the in-cylinder peak pressure. The first parameter relates to the engine drivability and has to be limited below 2-3%. The second one more directly affects the knock onset, commonly assuming values higher than the CoV of the IMEP.

2.5. State of art of technologies

Nowadays the research on ICEs is focused on the improvement of efficiency combined with the reduction of pollutant emissions. Several methods have been investigated during the last years aiming at improving the efficiency of the SI engines. Among the technologies currently well assessed, the engine downsizing coupled to VVA proved efficiency improvements [24]. Combining numerical and experimental activities, it has been demonstrated the possibility to enhance the engine efficiency using different Variable Compression Ratio (VCR) concepts, including Two-Stage systems (TSCR) and continuously variable devices [25]. Another system employed to reduce the Brake Specific Fuel Consumption (BSFC) levels is the implementation of external cooled EGR. By using this technique, depending on the load level, a reduction of pumping losses, knock tendency and mixture over-fuelling emerged [26]. With the aim to suppress the knock, a beneficial solution is the liquid WI realised within the cylinder or at the intake port [27], showing significant efficiency improvements, of about 16%, at low speed and high load.

2.5.1. Variable Valve Actuation

The VVA system is employed to actuate a simultaneous variation of the lift, duration, and phase for intake and/or exhaust valves. The two main types of this technology are VVT and Variable Valve Lift (VVL). Both systems allow regulating the air flow and the turbulent field into the combustion chamber, providing an improvement of fuel consumption and/or engine performance. The valves' profiles can be varied through different mechanisms, which are a simple mechanical device, an electro-hydraulic / mechanical system, or a cam-less system [28]. One system widely used in the automotive field is the electro-hydraulic / mechanical device, representing a good compromise between control flexibility and cost. Actually, the main reasons why the cam-less system is not yet common in passenger cars are its high cost and difficulties in the control [28].

As an example, a comparison between a VVA system, commercially known as “Multi-Air” [29], employed for a conventional SI engine, and a VVT one, used for a pre-chamber engine, is reported in *Figure 2-16*. Both the technologies, as shown, realize an Early Intake Valve Closing. If considering the VVT, the early closure is achieved through a rigid shift of the intake valve profile, while for the VVA, the valve lift is modified, without changing the IVO. Commonly, the EIVC strategy is used at partial load, aiming at reducing the pumping losses. Moreover, shifting forward the IVC results also in knock mitigation, thanks to the reduction of the effective compression ratio. The main drawbacks of EIVC are the poor in-cylinder turbulence, especially at very low load, and the undesirable gas-dynamic noise with a fully opened throttle valve.

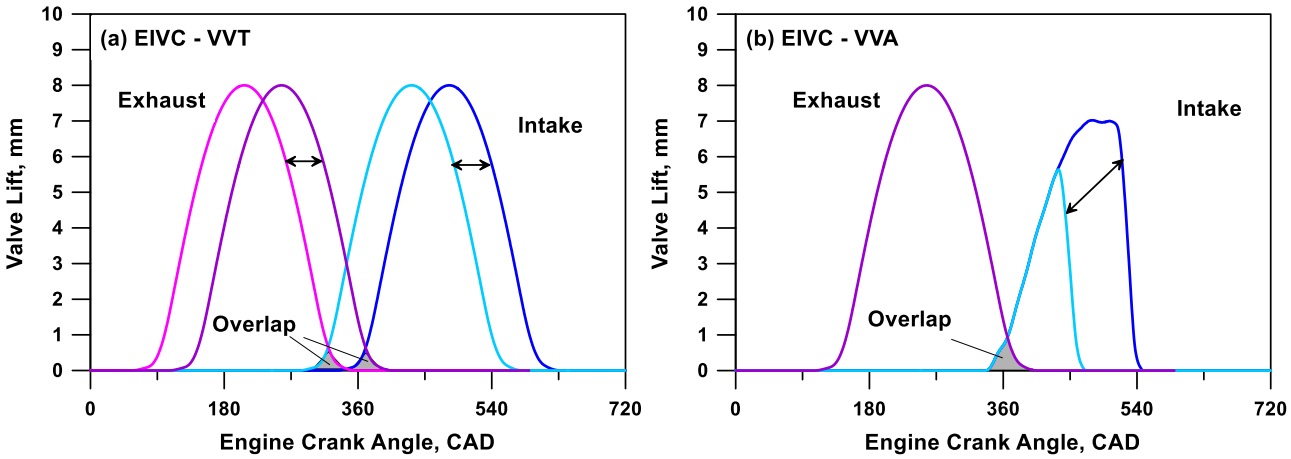

Figure 2-16 EIVC strategy in a VVT (a) and VVA(b) system.

Further, it is worth underlining that for described VVA system, the above-mentioned advantages can be achieved without changing exhaust valve phasing. On the contrary, for a VVT system applied in a PFI engine, a modification of the exhaust timing is mandatory in case of IVO advancement to avoid the scavenging phenomenon, which may lead to excessive fuel short-circuiting.

2.5.2. Variable Compression Ratio

A technique to improve the fuel consumption, under different load and speed conditions, is the variation of the engine geometrical compression ratio (CR). Commonly, for the SI engine, the compression ratio is limited at high load conditions, due to the high knock tendency. Nevertheless, at medium / low loads, a greater CR should be the more suitable, aiming at enhancing the thermodynamic efficiency. A variable compression ratio variation mechanism can be used to automatically modifies the compression ratio as a function of the engine load and speed. Despite the potential benefits, the VCR adoption is highly limited due to cost issues and to mechanical complexity [30].

2.5.1. Recirculating exhaust gas and Water Injection

The EGR technique was introduced in diesel engines to reduce NO_X emission through the limitation of the combustion temperature by the fresh gases dilution with a proper amount of recirculated exhaust gas. Subsequently, EGR application spread in SI engines, leading to different advantages depending on the operating condition. At part load, this technique is employed to decrease throttling losses. In fact, to keep a certain load, at increasing EGR, the throttle can be progressively opened, reducing the pumping loss. At high load, EGR allows achieving a NO_X emissions reduction, due to the in-cylinder temperature lowering [31]. Further, for this operating condition, a cooled exhaust gas recirculation can be employed to reduce the risk of knocking combustions.

The gas recirculation can be classed in internal EGR and external EGR. The first one is achieved by increasing the valve overlap. An advanced system to rapidly change the valve timing is required to realize the internal EGR. Considering the external EGR, the exhaust gases are subtracted from the exhaust line and then reintroduced into the cylinder through the inlet line by an external circuit, also including an EGR-cooler. This system is quite low-cost, since needing only a dedicated EGR control valve and an EGR-cooler, to control the gas recirculated rate and temperature at changing working conditions [26].

The water injection concept was introduced in the aircraft field around the 40’ and, as the EGR technique, having a comeback with the introduction of downsized turbocharged SI engines. Known as anti-knocking injection, this system provides a combustion chamber cooling through the injection of liquid water inside the cylinder. The subtracted heat, due to the water evaporation, considerably decreases the gases temperature, allowing to mitigate the knock tendency. Considering a turbocharged engine, the WI enables the reduction of the over-fuelling, typically required at high speed to maintain the turbine inlet temperature below a safe temperature level (usually around 950

°C). By coupling a better combustion phasing, an over-fuelling reduction, and the possibility to increase the engine compression ratio, relevant improvements in the fuel consumption [32] can be achieved, especially at a high speed and load.

2.5.2. Dynamic skip firing

Dynamic Skip Firing (DSF) is an advanced technique able to independently control the firing decision of each cylinder for the engine. Using this system reflects in a significant reduction of the pumping losses and in a combustion efficiency improvement if compared with standard, throttled engine operation [33]. Hence, the part load conditions are here achieved by controlling the number of firing cylinders rather than the throttle position. Thereby, reducing the load, the number of the firing cylinders decreases, unless the torque request is zero in which all the cylinders are turned off. Nevertheless, the DSF has to comply with noise, vibration, and harshness issues, limiting the declared advantages.

2.6. Ultra-lean combustion

Considering the advantages achievable by using the above-described technologies, they highly depend on the engine operating condition. For instance, VVA / VVT leads to a reduction in the pumping losses and to an improvement in the fuel consumption at low load and provides an enhanced knock resistance at high load. Nevertheless, once knocking phenomena become more relevant, different solutions must be adopted, such as water injection or cooled external EGR.

Over recent years, car manufactures are heading towards innovative SI engine architectures featured by unconventional combustion concepts to obtain considerable advantages in the whole engine operating domain. Particularly, one of the most interesting concepts is a combustion system working with very lean air / fuel mixtures because of the possibility to simultaneously reduce NO_X raw emissions and fuel consumption. Indeed, a lean mixture reflects in lower combustion temperatures, allowing to reduce NO_X production [34], *Figure 2-17(b)*. Whereas fuel benefits mainly arise from a higher specific heats ratio, lower heat losses, and higher knock resistance, *Figure 2-17(a)*. Further, due to the excess air, a very lean air / fuel mixture ensures lower CO and HC raw emissions, *Figure 2-17(b)* [35]. However, flame-propagation-based SI engines can work with a small amount of excess air, limiting the advantage of this combustion concept. In fact, lean conditions reduce the laminar flame speed, leading to undesirable cyclic variability, misfire, and massive HC-CO formation [34], [1].

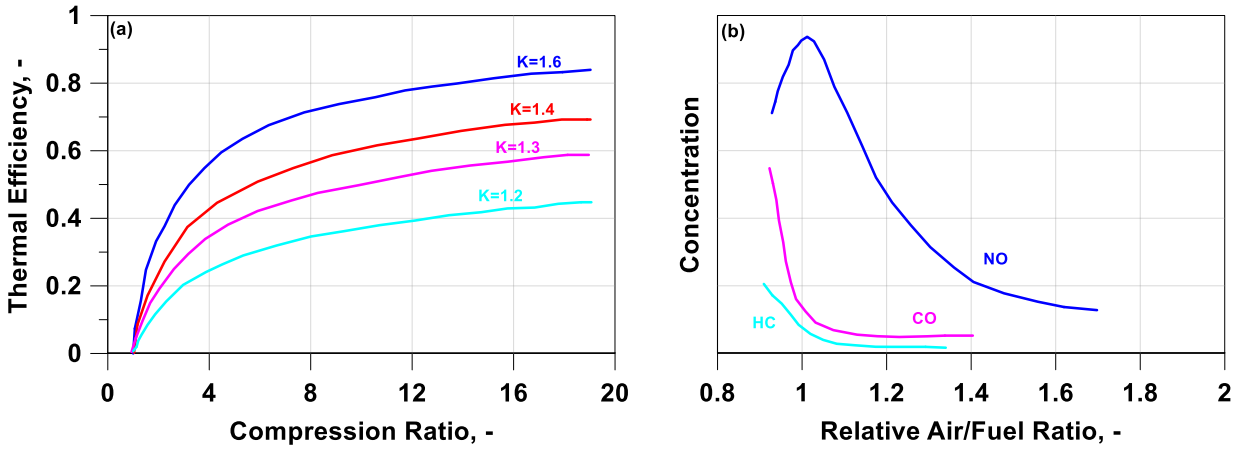

Figure 2-17 (a)Thermal efficiency as a function of the compression ratio for 4 different heat ratio, k, (b) NO, CO, HC concentration as a function of lambda for SI ICE.

Several solutions have been investigated over recent years to overcome these issues. One of the first techniques employed was the stratified lean combustion to realize a close-to-stoichiometric air / fuel ratio at the spark plug with various strategies, such as wall guided, flow guided or spray guided stratification, [36], [37]. Successively, the possibility to generate a slight vertical fuel stratification through twin-tumble intake flows has been introduced with the aim to reduce the cycle-to-cycle fluctuations [38]. Then, flame-less combustion concepts have been investigated, aiming at avoiding problems correlated to the extremely low flame speed at lean conditions, such as the Homogeneous Charge Compression Ignition (HCCI) [39]. However, HCCI revealed critical issues, not only to control the ignition timing but also due to limited power output and weak cold-start capability. Some variants of this method are still under investigation, such as the Spark-Assisted Compression Ignition (SACI) [40]. This combustion mode promotes a controlled auto-ignition of lean or diluted unburned mixtures by a spark-initiated flame propagation.

In recent years, a technical solution able to easily implement ultra-lean combustion is the Pre-Chamber ignition system, i.e. a small volume, housing the spark plug, connected to the Main Chamber (MC) through small orifices. The combustion process begins in the PC at the spark plug, then propagating in the MC as multiple turbulent jets of hot gas expelled from the pre-chamber. These jets penetrating the main-chamber, allow to increase the turbulence of the cylinder charge and to start the ignition establishing a stable flame propagation even under extremely lean mixtures [41], [42]. These engine architectures, although showing very promising potential, have some drawbacks principally associated with the precise control of the combustion development, and to the related emission formation. Indeed, more complex and innovative after-treatment systems are needed if compared to the conventional three-way catalysts.

Since two of the engines investigated in the following sections of this thesis are equipped with a pre-chamber system, more details on this novel architecture will be addressed below.

2.6.1. Pre-chamber engine

The Pre-chamber system is a well-assessed technology investigated since 1918 [43]. In compression ignition engines the PC, connected with the main combustion chamber through one or more nozzles, was largely utilized to properly mix the air / fuel charge, exploiting the turbulent flow generated during the compression phase. With the advent of a high-pressure electronic injection system, since the fuel vaporization and the mixture formation and homogenization were guaranteed by the high pressure of injection, this system was shelved.

In pioneer applications to SI engines, the pre-chamber system was supplied with a rich charge through a carburetor, introducing the sole air into the main chamber. The load control was achieved by adjusting the air-fuel ratio and the amount of the charge delivered in the pre-chamber. Due to some drawback observed at part load operations, regarding both performance and efficiency, this system was abandoned moving towards conventional spark plug engines.

Nevertheless, over the years, this technology was under study resulting in considerable improvements. In 1968, the jet ignition application, named as LAG-process (Lavinia Aktivatisia Gorenia or Avalanche Activated Combustion) was developed [44]. It was based on the "chain branching" theory developed by Semyonov. The aim was to exploit the active species and "chain carriers" produced in the PC, then ejected into the MC, to enhance the chemical process within the MC itself. Subsequently, the first concept introduced for SI engines was simplified removing the need for auxiliary pre-chamber fuelling. Indeed, the pre-chamber was directly filled with the main-chamber charge during the compression stroke. Then, the combustion started in the PC, through a spark plug, and due to the turbulence field, a mixture with a λ ratio equal to 1.3 was ignited [45]. Even these progresses in PC system allowed to foresee an improvement in engine efficiency, this technology was not diffused and employed through the car manufacturer because of the huge difficulties in controlling the combustion over the whole engine operating domain, further increased by the three-way catalyst inefficiency at lean condition.

Nowadays, this technology is applied in Formula-1 competition and in large stationary gas engines (heavy-duty for naval application). Considering the first application field, motorsport cars do not have to comply with stringent cost and pollutant limitations typical of passenger vehicles. For the second one, the stationary conditions allow to simply optimize the engine system due to the limited operating conditions to be cover.

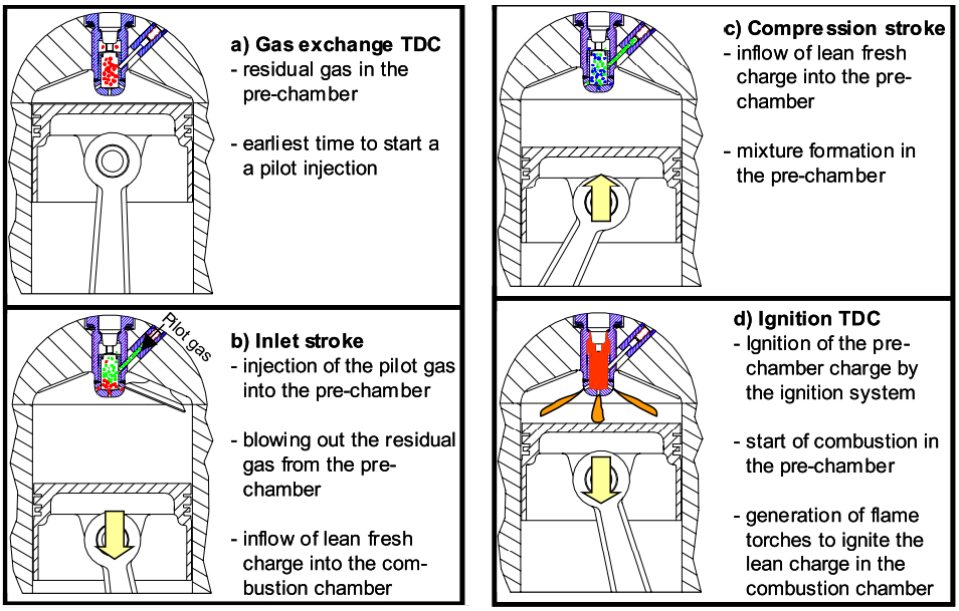

Figure 2-18 Principal phase of a pre-chamber spark plug with pilot injection [46].

A pre-chamber spark plug with a pilot injection, schematized in *Figure 2-18* was developed [46]. To overcome the problems due to insufficient residual gas scavenging in the PC, this technology used pilot injection during the intake stroke. For this application, the fuel injected into the PC was the hydrogen to extend the lean burn limit.

Then, in 2015, *MALHE* introduced the Turbulent Jet Igniter (TJI) system, declaring the possibility to extend the lean burn limit also using commercial fuels such as propane, gasoline, and natural gas. In *Figure 2-19* the schematization of the above-mentioned technology is shown. The TJI system consists of a pre-chamber, housing an injector and a spark plug, connected to the main chamber. The 2% of the fuel energy is provided to the PC, while the remaining energy is introduced by the MC, through a port fuelling.

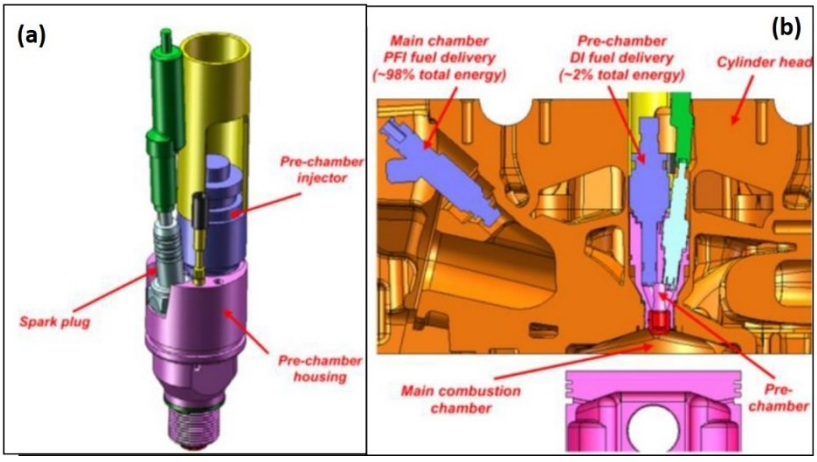

Figure 2-19. Pre-chamber (a) and overall engine scheme (b) for the TJI System [47].

Currently, as shown in *Figure 2-20*, the pre-chamber systems can be classified in two main categories: passive and active. The main characteristic of the first type is that the unburned air / fuel mixture around the spark has almost the same composition as the one inside the main chamber. The advantages are a low cost and engineering simplicity, but due to scavenging problems in the PC, the system is not able to work under extremely lean conditions. The second type of PC is featured by the presence of a fuel metering device, such as a fuel injector, integrated into the pre-chamber. This allows to have a stoichiometric or slightly rich mixture in the pre-chamber, not compromising the possibility to use lean mixture in the main chamber, also limiting the cyclic variations [48],[49]. In the last few years, several experimental activities were carried out on active pre-chambers [50], but the choice of the most suitable fuel to inject into the PC is still under studies. If gaseous fuels, such as methane [51] and hydrogen [52], or vaporized gasoline [53] guarantee a proper mixture homogenization before the spark event, liquid gasoline injection remains the most suitable option. Although its utilization can cause challenges regarding perfect mixture formation, this is due to the existing fuel supply infrastructure for passenger cars.

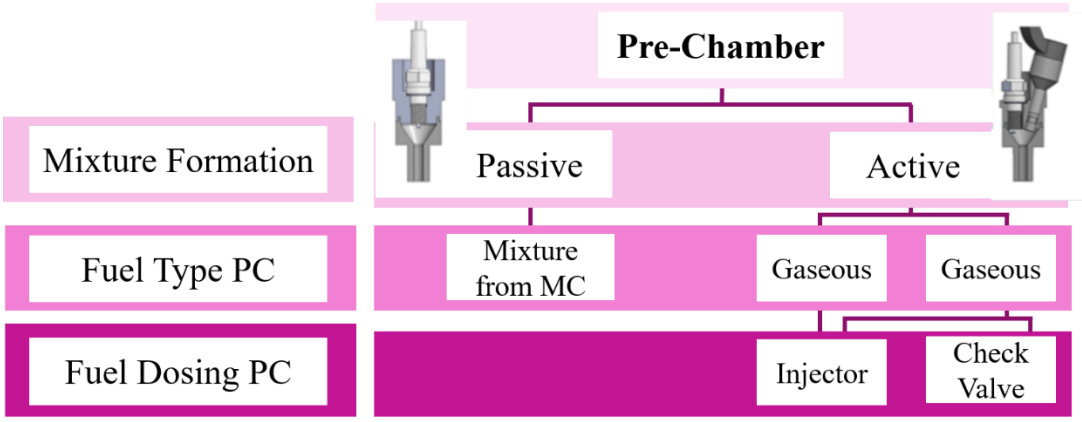

Figure 2-20 Classification of pre-chamber devices.

The combustion phenomena for an engine equipped with a PC engine can be described as follows. The spark plug located in the PC begins the combustions, releasing heat and leading to a pressure increment. As soon as the pre-chamber pressure exceeds the MC one, multiple turbulent jets of hot gas are expelled from the pre-chamber. These multiple jets start the ignition event in the MC, enhancing the first stage of the combustion development.

The combustion is highly sustained, even for very lean mixture, due to the combination of the high turbulent level of the jets with the establishment of multiple ignition sites [41]. In *Figure 2-21* a comparison between the ignition and flame propagation process for a Conventional Spark Plug (CSP) and a PC device, at the same engine speed and load, are reported from [41]. The images better illustrate the combustion enhancement due to the turbulent jets. In *Figure 2-21*, the flame imaging for three crank angle positions after the spark is depicted, considering t_0 as the crank angle of initial

flame detection. On the top is shown the full light spectrum, whereas on the bottom is reported a visualization based on the Otsu [54] method.

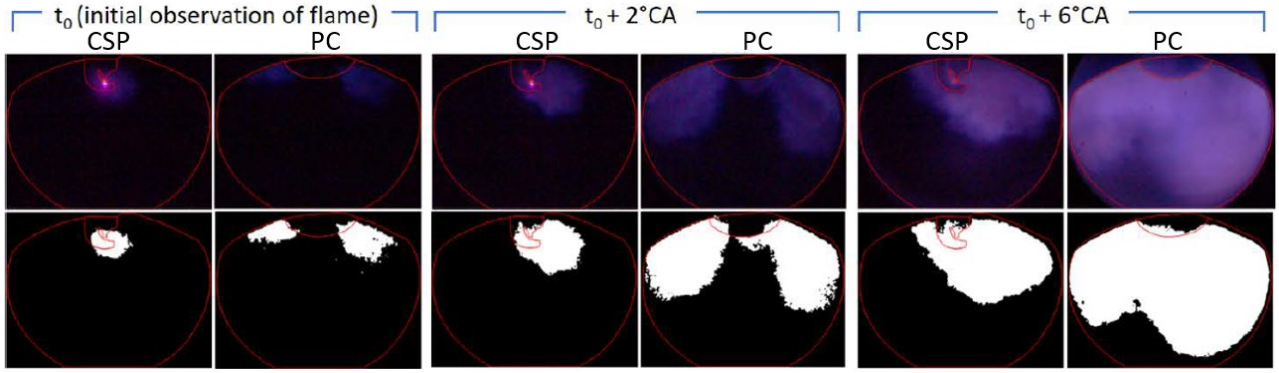

Figure 2-21 High-speed images of flame propagation comparing CSP and PC engine at n= 2000 rpm, BMEP= 16 bar [41].

The flame propagation in a PC engine, if compared to a CSP combustion, moves from the outer area of the cylinder toward the centre of the combustion chamber. Moreover, the multiple jets of hot gasses locally increase the turbulence, enhancing the combustion speed and reducing the knock tendency. Indeed, the flame fills faster the combustion chamber, especially its most knock-prone zones; in addition, since the combustion duration is reduced, this does not allow to reach the auto-ignition time of the end-gas. Therefore, the compression ratio can be increased, obtaining further efficiency improvements.

In *Figure 2-22* a representative comparison between spark ignition and jet ignition combustion systems at 1500rpm@3.3 IMEP is reported [47] to validate the above-described advantage. *Figure 2-22(a)* highlights the possibility of extending the lean limit up to 50% mass fraction diluent, still preserving an adequate combustion stability. Concerning the thermal efficiency, the maximum improvement is 18% if compared to a conventional stoichiometric SI engine for the considered operating condition. Moreover, as already mentioned, the combination of low temperature combustion with lean conditions leads to a strong reduction of NO_X emission.

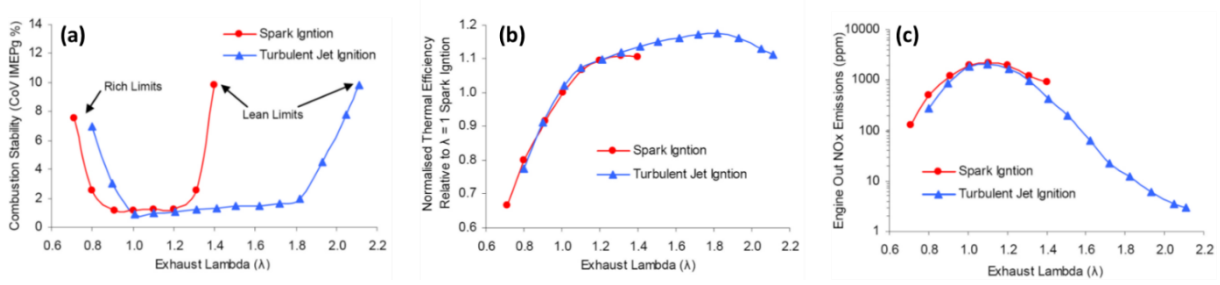

Figure 2-22 Comparison of spark ignition and jet ignition combustion systems with increased relative air / fuel ratio at 1500rpm@3.3 bar IMEP in terms of (a) combustion stability, (b) Normalized thermal efficiency, (c) NO_X emissions [47].

2.6.2. Hydrogen Injection

In recent years, due to an ever-increasing interest in lean combustion, different techniques have been investigated to enhance the combustion reactivity, aiming at ensuring a greater combustion stability. One of the methodologies examined is the addition of a small quantity of hydrogen (H_2) in the air / fuel mixture, since this can significantly expand the lean limit of the combustion. This is due to the higher laminar flame speed of the H_2 that supports both the ignition and the flame propagation, resulting in a significant reduction of the CCV fluctuations. Further, concerning the knock occurrence, although hydrogen addition reduces the mixture autoignition time, it also shortens the combustion duration, which may lead, in some conditions, to a reduced knock tendency. This also determines an increase in efficiency because of a better combustion phasing and thanks to the possibility to select a higher compression ratio. Moreover, H_2 presence promotes a lean operation, which helps in reducing the CO and HC emissions [55] and, for ultra-lean mixtures, in decreasing the NO_X formation, as well.

2.7. Pollutant Emission

The SI engine exhaust gases include nitrogen oxides (nitric oxide, NO, and small amounts of nitrogen dioxide, NO_2 - globally known as NOx), carbon monoxide (CO), and organic compounds, namely unreacted or partially reacted fuel hydrocarbons (HC). Although the relative amounts of the above-mentioned engine-out emissions depend on engine design and operating conditions, their characteristic values are about: NOx, 500 to 1000 ppm; CO, about 1%; HC, 2000 ppm (as C1). It is worth to underline that specific techniques are applied to abate other non-exhaust emissions of unburned hydrocarbons. As an example, the blowby gases are returned from the crankcase to the engine intake system, or the fuel tank is vented by using a vapor absorbing carbon canister. This last is purged with a fraction of the intake air during normal engine operation.

Considering diesel engine exhaust, the concentrations of NOx are similar to the ones from SI engines, while the CO ones are reduced. Concerning the hydrocarbon emissions, although they are significant, if compared to the typical levels of the SI engine, the exhaust concentrations result much lower. Further, CI engines are an important source of particulate emissions; between about 0.2 and 0.5% of the fuel mass is emitted as small (10 to 500 nm diameter) particles, consisting primarily of soot with additional hydrocarbon material.

Generally, the concentrations of the pollutant emissions in ICEs exhaust gases differ from the ones calculated at chemical equilibrium. Then, in determining emission levels, the detailed chemical mechanisms, describing the pollutant formations and the kinetics of these processes, are essential.

For example, for carbon monoxide, organic compounds, and particulates, the formation and destruction reactions are closely coupled with the primary fuel combustion process. Thus, the knowledge of combustion chemistry is fundamental in understanding the formation of these species. For nitrogen oxides and sulphur oxides, although the formation and destruction processes are not part of the fuel combustion process, since the reactions producing these species take place in an environment created by the combustion reactions, the two processes are still linked.

Substantial reductions in emissions can be achieved by removing pollutants from the exhaust gases in the exhaust system. Some of these devices are catalytic converters (oxidizing catalysts for HC and CO, reducing catalysts for NOx, and three-way catalysts for all three pollutants), and traps or filters for particulates. In SI engine exhausts, catalysts simultaneously removing CO, HC, and NOx are widely used, being highly effective. However, these three-way catalysts are only effective if the exhaust gas derives from a stoichiometric combustion. In CI engines, operating in lean conditions, NOx and particulates are the primary pollutants emitted. Oxidizing catalysts are frequently used to abate HC emissions, since, if not removed, higher molecular weight hydrocarbon can be absorbed later onto soot particles. It is worth to underline that for effective operation, these exhaust catalysts, both three-way and oxidizing ones, have to operate at an elevated temperature (few hundred of Celsius degrees) and with an exhaust gas flow rate and composition matched to the catalyst size and chemical conversion task. A joined design of the two interacting systems (catalyst and engine) is required, often including sensors and feedback loop. Moreover, the warm-up of the catalyst plays a key role, indeed the catalyst surface must reach a temperature of about 300°C to become effective.

Since one of the main topics of this thesis is pollutant emissions, in subsequent sections the basic formation mechanisms of each pollutant and the application of these mechanisms to SI engines will be examined.

2.7.1. Carbon Monoxide

Carbon monoxide forms during the combustion process. Having rich fuel-air mixtures results in insufficient oxygen to fully burn all the carbon in the fuel to CO_2, while, even with lean mixtures, the dissociation produces significant CO levels in the high-temperature products.

CO emissions from ICEs are controlled primarily by the relative air / fuel ratio or fuel / air equivalence ratio. If the mixture is fuel-rich, CO concentrations in the exhaust increase progressively at decreasing relative A/F ratio, with an increase of the amount of excess fuel. Whereas, if the mixtures are fuel-lean, CO concentrations in the exhaust vary slightly with relative A/F and are low in terms of mole fraction.

The CO levels in SI engine exhaust gases are lower than the maximum values measured inside the combustion chamber but are significantly higher than equilibrium values at the exhaust conditions. Hence, the processes governing CO exhaust levels are controlled by chemical kinetics. In a premixed hydrocarbon-air flame, the CO concentration increases rapidly in the flame zone, achieving a maximum value greater than the equilibrium one for the adiabatic combustion of the fuel-air mixture. CO formation is one of the principal reaction steps in the hydrocarbon combustion mechanism, summarized as:

$$RH \rightarrow R \rightarrow RO_2 \rightarrow RCHO \rightarrow RCO \rightarrow CO \tag{2.9}$$

where R is the hydrocarbon radical. The CO obtained during the combustion process is then oxidized to CO_2 with a slower rate. The main CO oxidation reaction in hydrocarbon-air flames is [56]:

$$CO + OH \rightarrow CO_2 + H \tag{2.10}$$

For the SI engines, in the post-flame combustion products, at conditions close to peak cycle pressures and temperatures, the carbon-oxygen-hydrogen system is in equilibrium. Therefore, it can be assumed that CO concentrations are close to equilibrium in the immediate post-flame burned gases. However, since during expansion and exhaust processes the burned gases cool down, because of temperature and cooling rate, the CO oxidation process eq. (2.10) may not remain locally equilibrated. This means that oxidation of CO in the exhaust system, without using a specific exhaust treatment device, does not occur intensely enough because of the low temperatures of exhaust gas.

2.7.2. Nitrogen Oxides

Nitric oxide and nitrogen dioxide are generally categorized together as NOx emissions, but in the engine cylinder, with fuel-rich mixtures, the predominant oxide of nitrogen is nitric oxide. The main source of NO is the oxidation of molecular nitrogen. In combustion of near-stoichiometric fuel-air mixtures, the principal reactions controlling the NO formation from nitrogen and its destruction are [56]:

$$\begin{cases} N_2 + O \rightarrow NO + N & (I) \\ N + O_2 \rightarrow NO + O & (II) \\ N + OH \rightarrow NO + H & (III) \end{cases} \tag{2.11}$$

NO forms in both the flame front and the post-flame gases. Since in engines the combustion occurs at high pressure, the flame reaction zone is very thin (~0.1 mm) resulting in a short residence time within this zone. Further, because of the cylinder pressure rising during most of the combustion process, the burned gases produced during its early stage are compressed achieving temperature higher than the ones reached immediately after combustion. Hence, the higher the burned gas temperature, the higher is the rate of formation of NO. Therefore, NO produced in the post-flame gases almost predominates the one produced within the flame front. It is worth underlining that the combustion chemistry and NO formation processes are decoupled. Further, since the burned gases cool during the expansion stroke, the reactions involving NO freeze, leaving NO concentrations well in excess of levels corresponding to equilibrium at exhaust conditions.

By chemical equilibrium considerations, it can be observed that, for burned gases at typical flame temperatures, NO_2/NO ratios should be negligible. This is true if considering near to stoichiometric SI engines, but in CI engines NO_2 can be 10 to 30% of the total oxides of nitrogen engine-out emissions [57]. A mechanism to describe the NO_2 persistence is the following: NO formed in the flame zone can be rapidly converted to NO_2 through the reaction:

$$NO + HO_2 \rightarrow NO_2 + OH \tag{2.12}$$

A subsequent conversion of this NO_2 to NO can occurs as:

$$NO_2 + O \rightarrow NO + O_2 \tag{2.13}$$

This happens when cooler regions, which could quench the conversion back to NO, are widespread.

Generally, the total oxides of nitrogen emissions, NO and NO_2, are measured by using a chemiluminescence analyser returning the NO_X combination.

The most important engine variables affecting NO emissions are the relative air / fuel ratio, the residual burned gas fraction, and spark timing. Fuel properties also affect burned gas composition. The effect of variations in these parameters can be explained with the NO formation mechanism above described: important factors are changes in the time history of temperature and oxygen concentration in the burned gases during the combustion process and early part of the expansion stroke.

2.7.3. Hydrocarbons

Hydrocarbons, or more properly organic emissions, are the consequence of an incomplete combustion of the hydrocarbon fuel. Specifically, engine-out hydrocarbon levels in the exhaust of a SI engine, under normal operating conditions, are usually in a range of about 1000 to 3000 ppm C_1. Typically, these HC emissions are between about 1-2% of the fuel flow into the engine. Unburned hydrocarbon (uHC) emissions rise in presence of mixtures richer than stoichiometric and stabilize with a λ value close to 0.87. In the case of very lean mixtures, since the combustion quality worsens, HC emissions increase because of the incomplete combustion or misfire in a fraction of the engine operating cycles.

Several sources contribute to engine HC emissions formation in SI engine, being summarized and shown in *Figure 2-23.* These uHCs formation mechanisms cause hydrocarbons escaping from the primary combustion process. All these formation processes together result in about 5-10% of the fuel not burned during the normal premixed-flame combustion process. Further, this causes a significant loss of torque and efficiency. Finally, some of these uHCs may fully or partly oxidize during the expansion and exhaust processes [58].

Summarizing the uHC sources, it is well known that during compression and combustion, the increasing cylinder pressure forces some of the in-cylinder gas into crevices—thin volumes connected to the combustion chamber. Most of this gas in the crevices is constituted by unburned fuel-air mixture, escaping combustion process since the flame is not able to enter inside the crevices. This gas, leaving the crevices during the expansion and exhaust processes, is the major HC source. An additional source is flame quenching on the combustion chamber walls. A quench layer incorporating unburned fuel-air mixture remains at the wall when the flame arrives since it extinguishes before reaching the wall itself. Then, depending on the operating conditions, the HC in these thin layers can burn up after flame quenching due to post-oxidation. Another source of HC is due to the presence of a thin oil film on the cylinder liner that absorbs and desorbs fuel hydrocarbon components, before and after combustion, respectively, allowing to hide a fraction of the fuel to the combustion. Below a description of uHC formation mechanisms will be described which constitute the theoretical basis of the pollutant emission model introduced in the following section.

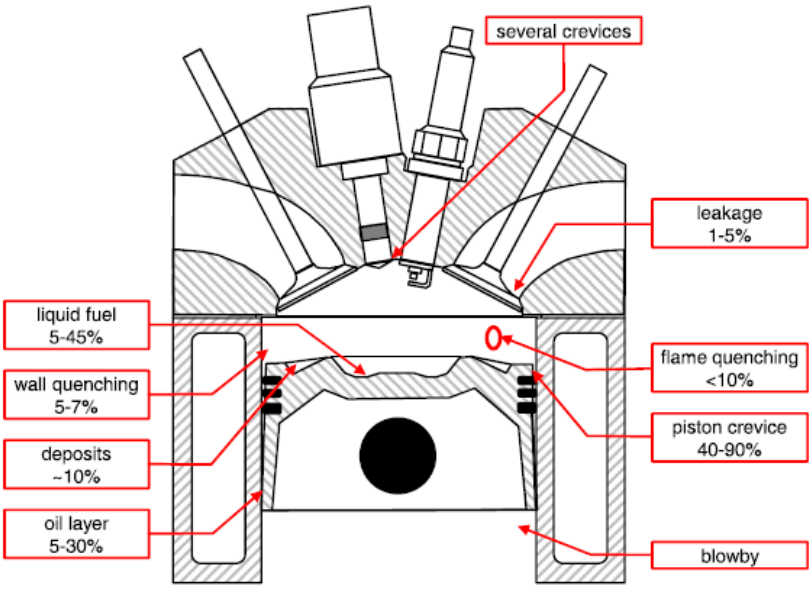

Figure 2-23 Possible formation mechanisms of engine-out HC emissions [58].

2.7.3.1 Crevices

One of the most significant processes that causes unburned HCs is the filling and emptying of the cylinder crevices. Crevices are narrow regions into the combustion chamber within which gas can flow in and out, generally not allowing flame entering. During the combustion process, an amount of unburned gas mixture remains inside these crevices avoiding burning and being discharged during the expansion and exhaust. In a combustion chamber, the possible crevices regions are several, such as cylinder head gasket, spark plug thread, valve seat, and piston ring pack [59]. The crevices depend on volumetric and geometric characteristics and on component temperature of the engine. The main crevice, due to its largest volume, is the region bordered by piston, compression ring, and liner, named top-land. Its contribution if compared to the total HC achieves values between 40% and 90% [59],[60],[61]. The fuel-air mixture, and residual gas, during the compression and combustion processes, are compressed into the top-land because of the rising pressure. As already said, since the access to this crevice is very thin, the flame is not able to enter it. Further, because of the coolest wall temperature, the trapped gas incurs in a temperature reduction. Then, during the expansion, once the piston moves down, the mass partially diffuses into the cylinder, finding burned mixture. The flows between the top and second lands (in correspondence of the second and third ring) including blowby effects are complex, due to pressure and temperature variation across the different ring regions [59]. Although the piston crevice geometrical volume is only 1–2% of the cylinder one, it potentially can trap 4–8% of the mixture mass because of the cold temperature in the crevice [62]. Finally, it is worth underlining that the influence of piston geometrical details affecting the volume of the piston crevice

and the texture of the edge at the piston crown are crucial aspects, contributing to the production of uHC from crevices.

2.7.3.2 Oil Layers

Another important mechanism for uHC formation is the absorption / desorption of fuel from the lubricating oil. The oil layer, coating the cylinder liner, when is uncovered by the piston, encounters the fuel-air mixture and residual gas. During this time, there is a fuel vapor transfer between the bulk gas and the oil / gas interface in both directions. When compression and combustion phases occur, the uHCs are absorbed into the oil layer, diffusing into it. While, during the expansion and exhaust, these unburned hydrocarbons are desorbed from the oil film into the cylinder, contributing to the engine-out emissions formation. The mechanism above described depends significantly on the characteristic of lubricating oil and on the cylinder wall temperatures. Further, the solubility characteristics of HCs in the oil, being the driver of this phenomenon, depend not only on cylinder pressure and temperature but also on the layer thicknesses and thermo-chemical affinity of oil and fuel.

2.7.3.3 Deposits

In the course of time, deposits accumulate into the combustion chamber, especially on the valves, piston crown, and walls of the cylinder head. The surfaces of these deposits are featured by many pores able to absorb / desorb fuel. [63]. This mechanism shows a strong dependency on the runtime and operation condition of the engine and the used fuel. Generally, it causes a small effect if compared to the total engine-out HC emission.

2.7.3.4 Wall and Flame Quenching

It is known that during combustion process in SI engines, the flame front extinguishes at a small distance from the cylinder walls because of their cooler temperatures. This leads to a thin layer formation close to the cylinder walls, called quench layer, containing unburned gas mixture. [64]. At warmed-up engine condition, the majority of the unburned mixture, diffusing into the cylinder, encounters hot burned gases and burns during expansion. At cold start operation, having a thicker quench layer, the completion of burning up is not ensured [59]. Concerning the flame quenching, as said, due to a prematurely flame extinguishment, the effects of partial burning leads to very high levels of uHCs emissions. This phenomenon occurs especially in presence of critical burning conditions, such as engine operation close to its dilution limits (high rate of residual gas) and lean mixture. If the fast-burn combustion system is well-designed, under normal steady-state engine

operating conditions, the flame-quenching phenomenon should not contribute substantially to HC emissions. Nevertheless, the combination of EGR high levels and retarded timing, during transients, requires special attention since the incomplete burning coupled with quench layers may contribute considerably to HC emission formation.

2.7.3.5 Liquid Fuel

Sometimes, especially in direct injection engines, the injected fuel can impact the cylinder walls and the piston crown. This effect can be compensated by adjusting the injection through pressure and time. The most critical phase is engine warm-up. Indeed, since the combustion chamber surfaces are still cold, only a fraction of the injected fuel will evaporate. In conditions, liquid fuel drops on the walls can be absorbed by the oil layer, deposits, or stored in crevices. Due to this phenomenon, to compensate the power losses, with the aim to obtain a stoichiometric air-fuel ratio in the exhaust gas, more fuel than normally required has to be injected. The fuel mass is corrected and scaled by the engine control unit (ECU) using a multiplier function of the engine temperature. The quantification of this source is quite difficult due to its combination with other storage mechanisms and due to its strong dependency on the used technologies of injection and charge motion.

2.7.3.6 Leakage

In older engines, another source of uHC emissions is the exhaust valve leakage. Indeed, unburned gas mixture had the possibility to flow into the exhaust manifold even the valves are closed. Usually, the amount of HCs is marginal (rates about 1–5%) and could be considered negligible. It is worth to underline that in modern engines, improved techniques allow narrow tolerances resulting in a fitting of the valves without leakage.

2.7.3.7 In-cylinder Oxidation

The oxidation process of uHCs has a considerable influence on the final amount of HC emissions. The unburned gas mixture can oxidize within the cylinder or in the exhaust manifold before arriving at the three-way catalyst. This phenomenon is primarily driven by the unburned gas temperature and by the amount of oxygen provided. Indeed, the HC emission can be significantly reduced in presence of a quite high temperature and with a sufficient oxygen quantity [59]. Generally, the oxidation rate can be of 40 % up to 70% [65]-[67]. Another aspect to consider, having a significant influence on the amount of oxidized, is the available time for the burn-up. Further, the oxidation also depends on the source of HC emissions [59]. Indeed, the crevices and quenching mechanisms, that produce unburned

fuel-air mixture, have higher oxidation rates if compared to oil layer or deposits, being sources that primarily store and emit fuel vapor.

2.7.4. Particulate Matter

Particulate emissions have long been an issue with CI engines. For these engines soot is formed during the fuel sprays evolution, and, while most of it burns up into the cylinder, a soot portion is directly exhausted. Hence, during the exhaust phase within the cylinder and during the scavenging through the exhaust pipe, the gases cool down, nucleate condense, and form small particles. Since hydrocarbons with higher molecular weight continue to condense, they are subsequently absorbed into the soot particles. Therefore, a particulate size distribution is established: the larger particles are categorized as accumulation mode, having a diameter in a range of 50 to 500 nm; the smaller particles constitute the nucleation mode, characterized by diameter below about 50 nm.

If compared to CI engines, the port-fuel-injection SI engines are featured by particulate emissions much lower, by a factor of about 70 on a mass basis. However, comparing direct-injection engine particulate emissions to the ones of port-fuel-injection equivalent engine, they are close to a factor of 10 times higher, again by mass.

Considering the particulate traps, they are located in the exhaust system of CI and direct-injection SI engines. These traps remove almost all the particulates from the exhaust gases by using a porous ceramic monolith as a filter. This filter, over time, must be regenerated by increasing its temperature so that the particulate layer created on the filter burns off.

In particular, considering the SI engines, traditionally, three classes of particulate emissions have been defined: inorganic particles (mainly lead compounds), organic particulates (including soot), and sulphates. On the basis of the sulphur contained in the fuel, sulphate emissions can occur with oxidation-catalyst equipped engines. Gasoline can contain a certain quantity of sulphur, depending on the extent of sulphur removed in the refinery, oxidized to sulphur dioxide within the engine cylinder. Then, SO_2 can be in turns oxidized to SO_3 by the exhaust catalyst. The sulphate emissions levels also depend on engine operating conditions and on the details of the catalyst system used. Further, the particulate emission rates are considerably higher when the engine is cold, following start-up. The exhaust temperature has a significant effect on emission levels.

Most of the particles are presumed to form and grow in the exhaust system because of vapor phase condensation. Some of these particles are directly emitted, without settling, while some others are deposited on the exhaust system walls. The majority of these last however is removed when the exhaust flow rate suddenly increases.

References

[1] Heywood, J., B., "Internal combustion engine fundamentals (2nd edit.)," New York: McGraw-Hill Education, 2018, ISBN: 978-1-26-011611-3.

[2] Chen, L., Liang, Z., Zhang, X. and Shuai, S., "Characterizing particulate matter emissions from GDI and PFI vehicles under transient and cold start conditions," *Fuel*, 189, pp.131-140, 2017, doi: 1016/j.fuel.2016.10.055.

[3] Bozza, F., Gimelli, A., Merola, S., S., Vaglieco, B., M., "Validation of a fractal combustion model through flame imaging," *SAE transactions*, pp. 973-987, 2005., doi: www.jstor.org/stable/44722057.

[4] Metghalchi, M., Keck, J., C., "Burning velocities of mixtures of air with methanol, isooctane, and indolene at high pressure and temperature", *Combustion and flame*, 48:191-210, 1982, doi: 10.1016/0010-2180(82)90127-4.

[5] Rhodes, D., B., Keck, J., C., "Laminar burning speed measurements of indolene-air-diluent mixtures at high pressures and temperatures, SAE Technical Paper 850047, 1985, doi: 10.4271/850047.

[6] Hara, T., Tanoue, K., Laminar flame speed of ethanol, n-heptane, iso-octane air mixtures. JSAE Paper Number 20068518, 2006.

[7] Liao, S., Y., Jiang, D., M., Cheng, Q., "Determination of laminar burning velocities for natural gas", *Fuel*, 83(9): 1247-1250, 2004, doi: 10.1016/j.fuel.2003.12.001.

[8] D. Bradley, R.A. Hicks, R.A. Lawes, C. Sheppard, R. Wolley, "The Measurement of Laminar Burning Velocities and Markstein Numbers for Iso-octane–Air and Iso-octane–nHeptane–Air Mixtures at Elevated Temperatures and Pressures in an Explosion Bomb", *Combust. Flame,* 115, 126–144, 1998, doi: 10.1016/S0010-2180(97)00349-0.

[9] Gülder, Ö., "Correlations of laminar combustion data for alternative SI engine fuels," SAE Technical Paper, No. 841000, 1984, doi:10.4271/841000.

[10] Bougrine, S., Richard, S., Nicolle, A., & Veynante, D., "Numerical study of laminar flame properties of diluted methane-hydrogen-air flames at high pressure and temperature using detailed chemistry", *International Journal of Hydrogen Energy*, 36(18), 12035-12047, 2011, doi: 10.1016/j.ijhydene.2011.06.053.

[11] Hann, S., Grill, M., Bargende, M., "Reaction Kinetics Calculations and Modeling of the Laminar Flame Speeds of Gasoline Fuels", SAE Technical Paper 2018-01-0857, 2018, doi: 10.4271/2018-01-0857.

[12] De Bellis, V., Malfi, E., Teodosio, L., Giannattasio, P., Di Lenarda, F., "Novel Laminar Flame Speed Correlation for the Refinement of the Flame Front Description in a Phenomenological

Combustion Model for Spark-Ignition Engines", *SAE International Journal of Engines*, 12(3): 251-270, 2019, doi: 10.4271/03-12-03-0018.

[13] Tanaka, S., Ayala, F., Keck, J.C., "A reduced chemical kinetic model for HCCI combustion of primary reference fuels in a rapid compression machine", *Combustion and Flame* 133(4): 467-481, 2003, doi: 10.1016/S0010-2180(03)00057-9.

[14] Liu, Y., Jia, M., Xie, M., Pang, B., "Development of a New Skeletal Chemical Kinetic Model of Toluene Reference Fuel with Application to Gasoline Surrogate Fuels for Computational Fluid Dynamics Engine Simulation", *Energy Fuels* 27(8):4899–4909, 2013, doi: 10.1021/ef4009955.

[15] Andrae, J., "Comprehensive chemical kinetic modeling of toluene reference fuels oxidation", *Fuel* 107:740–748, 2013, doi: 10.1016/j.fuel.2013.01.070

[16] Peters, N., "Laminar flamelet concepts in turbulent combustion", Symposium (International) on Combustion 21(1): 1231-1250, 1988, doi:10.1016/S0082-0784(88)80355-2.

[17] Wu, C., K., Law, C., K., "On the determination of laminar flame speed from stretched flames", Twentieth Symposium (International) on Combustion, 20(1): 1941-1949, 1985, doi: 10.1016/S0082-0784(85)80693-7.

[18] de Goey, L., P., H., ten Thije Boonkkamp, J., H., M., "A flamelet description of premixed laminar flames and the relation with flame stretch", Combustion and Flame 119(3): 253-271, 1999, doi: 10.1016/S0010-2180(99)00052-8.

[19] Markstein G., Nonsteady Flame Propagation, (McMillan Publication, New York, 1964).

[20] M. Matalon, B.J. Matkowsky, "Flames as gas-dynamic discontinuity", J. Fluid Mech. 124: 239–259, 1982, doi: 10.1017/S0022112082002481.

[21] Millo, F. and Ferraro, C., "Knock in S.I. Engines: A Comparison between Different Techniques for Detection and Control," SAE Technical Paper 982477, 1998, doi:10.4271/982477.

[22] Brecq G., Bellettre J., Tazerout M., "A New Indicator for Knock Detection in Gas SI Engines," *International Journal of Thermal Sciences*, 42, pp.523-532, doi: 10.1016/S1290-0729(02)00052-2.

[23] Siano, D., Bozza, F., D'Agostino, D. Panza, M.A., "The use of vibrational signals for on-board knock diagnostics supported by in-cylinder pressure analyses" SAE Technical Paper, 2014-32-0063, 2014, doi: 10.4271/2014-32-0063.

[24] Hara, S., Suga, S., Watanabe, S., Nakamura, M., "Variable valve actuation systems for environmentally friendly engines," *Hitachi Review*, 58(7), 319-324, 2009.

[25] Shaik, A., Moorthi, N., Rudramoorthy, R., "Variable Compression ratio engine: a future power plant for automobiles-an overview", *Proc. of the Institution of Mechanical Engineers* Part D: Journal of Aut. Eng. 221(9):1159-1168, 2007, doi: 10.1243:09544070JAUTO573

[26] Wei, H., Zhu, T., Shu, G., Tan, L., Wang, Y., "Gasoline engine exhaust gas recirculation–a review.," *Applied energy*, 99, 534-544, 2012, doi: apenergy.2012.05.011.

[27] Hoppe, F., Thewes, M., Baumgarten, H., Dohmen, J., "Water injection for gasoline engines: Potentials, challenges, and solutions," International J of Engine Research 17(1):86-96, 2016, doi:10.1177/1468087415599867.

[28] Ahmad, T., Theobald, M. A., "A survey of variable-valve-actuation technology," *SAE Transactions*, 1651-1677, 1989, doi: www.jstor.org/stable/44581049.

[29] Bernard, L., Ferrari, A., Micelli, D., Perotto, A., Rinolfi, R., Vattaneo, F., "Electro-hydraulic valve control with multiair technology," *MTZ worldwide*, 70(12), 4-10, 2009, doi:10.1007/bf03226988.

[30] Kleeberg, H., Tomazic, D., Dohmen, J., Wittek, K. and Balazs, A., "Increasing efficiency in gasoline powertrains with a two-stage variable compression ratio (VCR) system," SAE Technical Paper, 2013-01-0288, 2013, doi: 10.4271/2013-01-0288.

[31] Tabata, M., Yamamoto, T. Fukube, T., "Improving NO_x and fuel economy for mixture injected SI engine with EGR," SAE transactions, pp.1221-1230,1995.

[32] Bozza, F., De Bellis, V., Teodosio, L., "Potentials of cooled EGR and water injection for knock resistance and fuel consumption improvements of gasoline engines," Applied Energy, 169, 112-125, 2017, doi: j.apenergy.2016.01.129.

[33] Eisazadeh-Far, K., Younkins, M., "Fuel economy gains through dynamic-skip-fire in spark ignition engines, SAE Technical Paper 2016-01-0672, 2016, doi:10.4271/2016-01-0672.

[34] Rapp, V., Killingsworth, N., Therkelsen, P., et al., "Lean Combustion, 2nd Edition," *Lean-Burn Internal Combustion Engines*, Elsevier, 2016, 111-146, doi:10.1016/C2013-0-13446-0.

[35] Germane, G., Wood, C., Hess, C., "Lean Combustion in Spark-Ignited Internal Combustion Engines - A Review," SAE Technical Paper 831694, 1983, doi:10.4271/831694.

[36] Drake, M., Fansler, T Lippert, A, "Stratified-charge combustion: modeling and imaging of a spray-guided direct-injection spark-ignition engine," *Proceedings of the Combustion Institute*, 30(2), pp.2683-2691, 2005, doi: org/10.1016/j.proci.2004.07.028.

[37] Fajardo, C. Sick, V., "Flow field assessment in a fired spray-guided spark-ignition direct-injection engine based on UV particle image velocimetry with sub crank angle resolution," *Proceedings of the combustion institute*, 31(2), pp.3023-3031, 2007,

[38] Moriyoshi, Y., Kuboyama, T., Kaneko, M., Yamada, T., Sato, H., "Fuel Stratification Using Twin-Tumble Intake Flows to Extend Lean Limit in Super-Lean Gasoline Combustion," SAE Technical Paper 2018-01-1664, 2018, doi:10.4271/2018-01-1664.

[39] Stanglmaier, R., Roberts, C., "Homogeneous charge compression ignition (HCCI): benefits, compromises, and future engine applications," SAE *transactions*, pp.2138-2145,1999, doi: www.jstor.org/stable/44741335.

[40] Okita, R., "Mazda SKYACTIV-G Engine with New Boosting Technology," In Advanced Clean Cars Symposium: The Road Ahead, Air Resources Board, Sacramento, USA, 27th–28th September 2016

[41] Sens, M., Binder, E., Benz, A., Kramer, L., at all. "Pre-chamber ignition as a Key Technology for Highly Efficient SI Engines-New Approaches and Operating Strategies," 39th International Vienna Motor Symposium, Apr. 2018.

[42] Mueller, C., Morcinkowski, B., Habermann, K., Uhlmann, T., Schernus, C. "Development of a pre-chamber for spark ignition engines in vehicle applications," 4th International Conference on Ignition Systems for Gasoline Engines, Dec. 2018.

[43] Ricardo, H.R., Internal-combustion engine. 1918, Google Patents.

[44] Gussak, L., Karpov, V. Tikhonov, Y., "The application of lag-process in prechamber engines," *SAE Technical Paper*, 790692,1979, doi:10.4271/790692.

[45] Noguchi, M., Sanda, S. and Nakamura, "Development of Toyota lean burn engine," SAE Technical Paper, 760757, 1976, doi:10.4271/760757.

[46] Pape, J., Getzlaff, J., Gruenig, C., Kuhnert, D. and Latsch, R., "Investigations on Pre-Chamber Spark Plug with Pilot Injection," SAE Technical Paper 2007-01-0479, 2007, doi:10.4271/2007-01-0479.

[47] Attard, W.P., Fraser, N., Parsons, P. and Toulson, E., "A Turbulent Jet Ignition Pre-Chamber Combustion System for High Fuel Economy Improvements in a Modern Vehicle Powertrain," SAE Technical Paper 2010-01-1457, 2010, doi:10.4271/2010-01-1457.

[48] Roethlisberger, R., Favrat, D., "Comparison between direct and indirect (prechamber) spark ignition in the case of a cogeneration natural gas engine, part I: engine geometrical parameters," Applied Thermal Engineering, 22(11), 1217-1229, 2002, doi: 10.1016/S1359-4311(02)00040-6.

[49] Xu, G., Wright, Y., Schiliro, M., Boulouchos, K., "Characterization of combustion in a gas engine ignited using a small un-scavenged pre-chamber," International Journal of Engine Research, 2018, doi: 10.1177/1468087418798918.

[50] Jamrozik, A., "Lean combustion by a pre-chamber charge stratification in a stationary spark ignited engine," Journal of Mechanical Science and Technology, 29(5):2269-2278, 2015, doi:10.1007/s12206-015-0145-7.

[51] Toulson, E., Schock, H., Attard, W., "A Review of Pre-Chamber Initiated Jet Ignition Combustion Systems," SAE Technical Paper 2010-01-2263, 2010, doi:10.4271/2010-01-2263.

[52] Lumsden, G., Watson, H., "Optimum Control of an S.I. Engine with a λ=5 Capability," SAE Technical Paper 950689, 1995, doi:10.4271/950689.

[53] Schumacher, M., Wensing, M., "A Gasoline Fuelled Pre-Chamber Ignition System for Homogeneous Lean Combustion Processes," SAE Technical Paper 2016-01-2176, 2016, doi:10.4271/2016-01-2176.

[54] Otsu, N., "A Threshold Selection Method from Gray-Level Histograms," *IEEE Transactions on Systems*, Vol. SMC-9, No. 1, 1979.

[55] Iafrate, N., Matrat, M., & Zaccardi, J. M., "Numerical investigations on hydrogen-enhanced combustion in ultra-lean gasoline spark-ignition engines," *International Journal of Engine Research*, 1468087419870688, doi:10.1177/1468087419870688.

[56] Bowman, C., T., "Kinetics of Pollutant Formation and Destruction in Combustion," Progress in energy and combustion science, vol. 1, pp. 33–45, 1975.

[57] Hilliard, J. C, and Wheeler, R. W.: "Nitrogen Dioxide in Engine Exhaust," SAE paper 790691, SAE Trans., vol. 88, 1979.

[58] Dorsch M, Neumann J, Hasse C. Application of a phenomenological model for the engine-out emissions of unburned hydrocarbons in driving cycles. *J. Energy Resour. Technol.* 2016, 138(2): 022201-1-022201-10.

[59] Cheng, W. K., Hamrin, D., Heywood, J. B., Hochgreb, S., Min, K., and Norris, M., 1993, "An Overview of Hydrocarbon Emissions Mechanisms in Spark- Ignition Engines," SAE Paper No. 932708.

[60] Min, K., 1994, "The Effects of Crevices on the Engine-Out Hydrocarbon Emissions in Spark Ignition Engines," Ph.D. thesis, Massachusetts Institute of Technology, Cambridge, MA.

[61] Hochgreb, S., 1998, "Combustion-Related Emissions in SI Engines," Handbook of Air Pollution from Internal Combustion Engines: Pollutant Formation and Control, Academic, San Diego, CA.

[62] Huang, Z., Pan, K., Li, J., Zhou, L., and Jiang, D., 1996, "An Investigation on Simulation Models and Reduction Methods of Unburned Hydrocarbon Emissions in Spark Ignition Engines," Combust. Sci. Technol., 115(1–3), pp. 105–123.

[63] Sodre, J. R., 1998, "A Parametric Model for Spark Ignition Engine Turbulent Flame Speed," SAE Paper No. 982920.

[64] Hasse, C., Bollig, M., Peters, N., and Dwyer, H. A., 2000, "Quenching of Laminar Iso-Octane Flames at Cold Walls," Combust. Flame, 122(1–2), pp. 117–129.

[65] Schramm, J., and Sorenson, S. C., 1990, "A Model for Hydrocarbon Emissions From SI Engines," SAE Paper No. 902169.

[66] Trinker, F. H., Chen, J., and Davis, G. C., 1993, “A Feedgas HC Emission Model for SI Engines Including Partial Burn Effects,” SAE Paper No. 932705.

[67] Norris, M. G., and Hochgreb, S., 1996, “Extent of Oxidation from the Lubricant Oil Layer in Spark-Ignition Engines,” SAE Paper No. 960069.

3. Simulation of Internal Combustion Engine

The complex and challenging scenario for the internal combustion engine nowadays requires an advanced approach in the evaluation of the pros and cons of different technologies and integrated solutions, including new combustion modes, turbocharging and after-treatment systems, hybrid electric vehicle. Today, a key aspect in this context is the massive adoption of simulation codes, allowing to examine and compare new technical solutions with limited experimental support. The simulation tools currently available can provide useful and reliable results to guide the development of a new engine. Further, their application, aiming to the optimization of various technologies using a virtual engine, allows a cost-effective development process and a considerable reduction of the engine design duration [1].

The modelling of ICE involves different approaches, generally classified into four major categories, listed in *Table 3.1*, that differ in approximation level utilized. Both 0D/1D simulation and 3D computational fluid dynamic (CFD) approaches are currently applied to support the design process of ICE.

Table 3.1 Classification of the numerical approaches.

Model	Application Field
0D	Combustion
1D	Gas Exchange
Quasi-Dimensional	Combustion
3D	Flow Field, Combustion

A 0D model can solve mass and the energy conservation equations assuming that the thermodynamic properties are only time-dependent. Thus, any space dependency is neglected, and the working fluid is considered at rest. The main advantage of this model is the possibility to reproduce the in-cylinder processes of the whole engine in a reduced computational time. While a considerable limitation in predicting the volumetric efficiency is due to the lack of describing the pressure waves propagation in the pipes.

The utilization of a 1D approach allows overcoming the issue above described since it solves the unsteady flow equations in the pipes along the mean flow direction. In this modelling, all the thermo-fluid-dynamic properties are considered uniform over each pipe section. Commonly, 0D refined models (quasi-dimensional phenomenological sub-models) and 1D ones are combined to achieve an accurate and fast prediction of the engine behaviour. These coupled models are widely employed to predict and analyse the global engine performance and to support the engine optimization and calibration [2] because of a good compromise between accuracy and computational time.

3D approach, based on the integration of the Navier Stokes equations, are able to provide a detailed description of the thermo- and fluid-dynamics in complex 3D geometries. These models, requiring a significant computational effort, are applied to simulate unsteady mean and turbulent flow motion within a limited portion of the engine, usually combustion chamber, head ducts, turbocharger, intake air-box, after-treatment devices, for a reduced set of operating conditions.

For this Ph.D. research activity, phenomenological 0D sub-models have been employed to reproduce in-cylinder phenomena, whereas the flow inside the intake and the exhaust pipes has been described by a 1D approach. Nevertheless, 3D model outcomes have been also used, mainly to support the development and validation of a 0D turbulence sub-model.

3.1. 0D Model

As above-mentioned for a 0D model all the variables are time-dependent and uniform in the entire control volume. Therefore, the mass and energy conservation equations, eq. (3.1),(3.2), are solved. They are expressed as follows:

$$\frac{dm}{dt} = \dot{m}_{in} - \dot{m}_{out} + \dot{m}_{inj} \tag{3.1}$$

$$\frac{d(me)}{dt} = -p\frac{dV}{dt} - \frac{dQ_w}{dt} + \dot{m}_{in}h_{in} - \dot{m}_{out}h_{out} + \dot{m}_{inj}{h_f}^0 \tag{3.2}$$

On the right side of eq. (3.1), the first two terms represent the incoming and outcoming mass flow rate through the valves, respectively, while the last one is the injected fuel flow rate. Considering (3.2), the first term describes the mechanical power exchanged between fluid and piston, the second one represents the heat transfer rate through the combustion chamber walls, while the last three terms define the enthalpy fluxes associated with the mass exchanges through the control surface. eq. (3.2) can be reformulated making explicit the temperature derivative, reported in eq. (3.3), on the basis of the internal energy dependency on temperature and composition. Thereby, this reformulation presents explicitly a term representing the energy released by the combustion process depending on the burned gas fraction time derivative, from reactants to products, $\frac{dx_b}{dt}$.

$$\frac{dT}{dt} = \frac{1}{mc_v}\left(-p\frac{dV}{dt} - \frac{dQ_w}{dt} + \dot{m}_{in}h_{in} - \dot{m}_{ex}h_{ex} + \dot{m}_{inj}{h_f}^0 - e\frac{dm}{dt} - \frac{\partial e}{\partial x_b}\frac{dx_b}{dt}\right) \tag{3.3}$$

The modelling of the gas-cylinder wall heat transfer is achieved by employing different correlations, available in the current literature, and principally dependent on the in-cylinder thermodynamic state and on engine speed. The Woschni [3], Hohenberg [4], and Annand [5] correlations are the most widely used in ICE simulation. In this thesis, both an Hohenberg-like correlation and Woschini correlation, deeply described in the following section, have been applied.

Concerning the instantaneous flow through the valves, it is estimated by the equation of the isentropic flux, in subsonic, eq. (3.4), or sonic (3.5) conditions.

$$\frac{dm}{dt} = c_d A_{ref} P_1 \sqrt{\frac{2k}{k-1}\frac{1}{RT_1}\left[\left(\frac{p_2}{p_1}\right)^{\frac{2}{k}} - \left(\frac{p_2}{p_1}\right)^{\frac{k+1}{k}}\right]} \tag{3.4}$$

$$\frac{dm}{dt} = c_d A_{ref} P_1 \sqrt{\frac{k}{RT_1}\left[\left(\frac{2}{k+1}\right)^{k+1/k-1}\right]} \tag{3.5}$$

where p_1 and T_1 are respectively the pressure and temperature at the upstream flow conditions, while p_2 refers to the downstream pressure. k is the specific heat ratio, and A_{ref} is a reference area. c_d represent the discharge coefficient, being the ratio between the actual and the isentropic mass flow, evaluated under steady state conditions. This coefficient is a function of the valve geometry, lift and flow direction (direct / reverse).

The burning rate (dx_b/dt) can be imposed or can be estimated through predictive combustion models. In the first case, an "*experimental*" burning rate is needed, being extracted from the experimental pressure traces, through a single pressure analysis (SPA) or a three pressures analysis (TPA). Both require in-cylinder pressure measurement, but the TPA also needs the pressure traces at intake and exhaust ports. In both SPA and TPA cases, the burn rate derive is computed from (3.3), in the so-called inverse analysis. Differently, a Wiebe function is utilized assuming a predefined burned fraction profile in function of the crank angle.

The 0D models can be further classed in three different sub-categories, depending on the number of the thermodynamic zones in which the control volume is divided, namely single (*Figure 3-1(a)*), two-zone (*Figure 3-1(b)*), or multi-zone. In all cases, each zone is characterized by a distinct thermodynamic state, possibly considering energy and mass interactions. For each zone, the eq. (3.1) and (3.3) are solved at each time step. During the intake and exhaust strokes, a single zone approach is appropriated since the composition can be assumed uniform in the entire cylinder volume. During

combustion phase, the cylinder volume can be sub-divided into two zones, namely unburned and burned ones (two-zone approach), separated by a thin discontinuity surface that schematizes the flame front.

Finally, concerning the multi-zone approach, it is widely employed in predicting pollutant emissions, especially NO_x. The prediction of a temperature stratification in the burned gas is expected to improve the simulation of NO_x chemical kinetics. Another possible application of the multi-zone approach is HCCI and RCCI engines, where a temperature and composition stratification are expected.

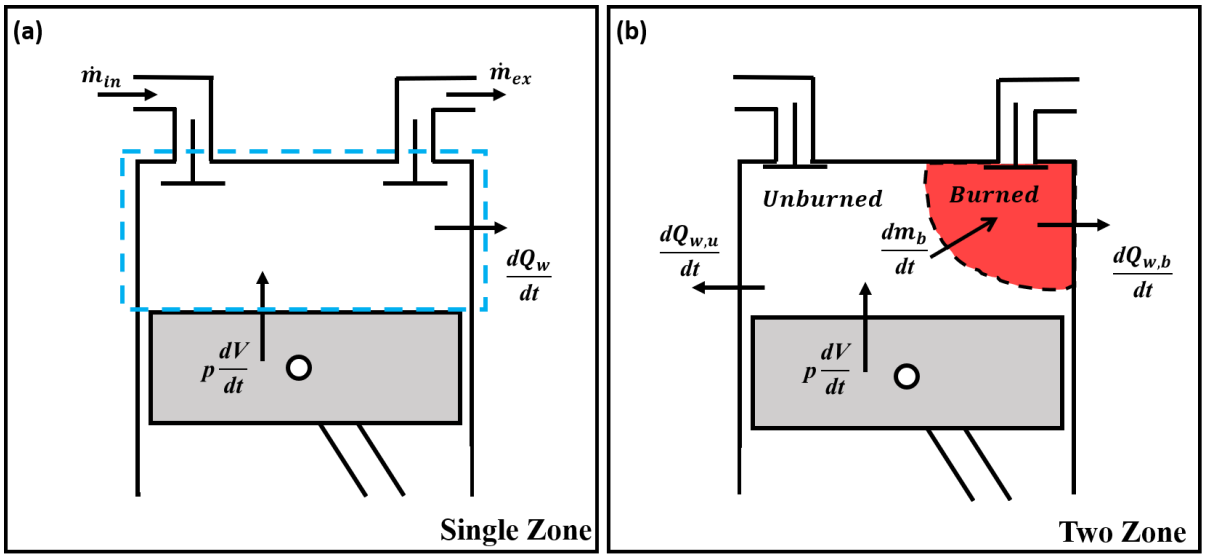

Figure 3-1 (a) Single zone combustion scheme, (b) two-zone combustion scheme.

During last years, several models to describe the combustion phenomenon in SI engines have been proposed, with the aim to physically assess the burning rate. They are all based on the widespread hypothesis of a combustion enhanced by turbulence phenomenon [6],[7],[8]. The main differences, distinguishing the models each other, are related to the description of the laminar-turbulent flame transition occurrence, and to the mechanism leading to the burn-rate enhancement due to the turbulence. Further, different approaches have been developed and used, as an example, the one introduced in [9], featured by a combustion chamber described as a stochastic reactor, where the combustion is modelled through probability density functions. The most widely employed combustion models are the eddy burn-up approach and the fractal one. The first outlines the flame entrainment and the subsequent combustion of unburned mixture, demonstrating to have a good agreement with the experimental burned mass fraction trends [10],[11]. Differently, the second aims to describes the enhancement of flame front surface, employing the concepts of fractal geometry [12],[13]. Numerous comparisons between these two approaches have been proposed in the current literature, coming to the conclusion that, if excluding the tuning efforts, both models can accurately reproduce the combustion phenomenon in conventional SI engines [6][14]. The chosen model, to

perform the simulations shown in the following of this work, is the fractal one. This because of its more consistent physical background, demonstrating the ability, once properly modified, to reproduce the behaviours of both conventional SI and pre-chamber engines.

3.2. 1D Models

The conservative form of the flow equations (continuity, energy, and momentum) under the hypothesis of an inviscid, adiabatic 1D flow schematization in a variable area pipe is reported through the system of partial differential equations in (3.6). It is worth to underline that all thermodynamic properties and the flow velocity, u, are space, x, and time, t dependent:

$$\begin{cases} \dfrac{\partial \rho}{\partial t} + \dfrac{\partial \rho u}{\partial x} + \rho u \left(\dfrac{1}{\Omega}\dfrac{d\Omega}{dx}\right) = \dfrac{\partial \rho}{\partial t} + \dfrac{\partial \rho u}{\partial x} + \rho u \alpha_A = 0 \\ \dfrac{\partial (\rho E)}{\partial t} + \dfrac{\partial (\rho u H)}{\partial x} + \rho u H \left(\dfrac{1}{\Omega}\dfrac{d\Omega}{dx}\right) = \dfrac{\partial (\rho E)}{\partial t} + \dfrac{\partial \rho u H}{\partial x} + \rho u H \alpha_A = 0 \\ \dfrac{\partial (\rho u)}{\partial t} + \dfrac{\partial (\rho u^2 + p)}{\partial x} + \rho u^2 \left(\dfrac{1}{\Omega}\dfrac{d\Omega}{dx}\right) = \dfrac{\partial (\rho u)}{\partial t} + \dfrac{\partial (\rho u^2 + p)}{\partial x} + \rho u^2 \alpha_A = 0 \end{cases} \tag{3.6}$$

In (3.7) the above equations are expressed in a more compact vectorial symbolisms, where U is the vector of the conservative variables, F is the flux vector and S represents the source term vector.

$$\frac{\partial U}{\partial t} + \frac{\partial F(U)}{\partial x} = S \quad U = \begin{Bmatrix} \rho \\ \rho u \\ \rho E \end{Bmatrix} ; \quad F = \begin{Bmatrix} \rho u \\ \rho u^2 + p \\ \rho u H \end{Bmatrix} \quad s = -\begin{Bmatrix} \rho u \alpha_A \\ \rho u^2 \alpha_A \\ \rho u H \alpha_A \end{Bmatrix} \tag{3.7}$$

The flow within the intake and the exhaust pipes of an ICE can be modelled considering additional terms, including the gas-wall friction, the heat exchange, and the scalar transport of injected fuel and residuals species. Then, adding these further terms, the system is rewritten as (3.8), having the last two equations respectively referred to the residual gases and vapour fuel fraction transport.

$$U = \begin{Bmatrix} \rho \\ \rho u \\ \rho E \\ \rho x_r \\ \rho x_f \end{Bmatrix} ; \quad F = \begin{Bmatrix} \rho u \\ \rho u^2 + p \\ \rho u H \\ \rho u x_r \\ \rho u x_f \end{Bmatrix} \quad S = -\begin{Bmatrix} \rho u \alpha_A \\ \rho u^2 \left(\alpha_A + \dfrac{2 f_a}{D}\dfrac{u}{|u|}\right) \\ \left(\rho u H \alpha_A - \dfrac{4q}{D}\right) \\ \rho u x_r \alpha_A \\ \rho u x_f \alpha_A \end{Bmatrix} \tag{3.8}$$

f_a is the friction coefficient evaluated by the Poiseuille or Blasius formula as a function of the velocity inside the pipes; x_r and x_f are the fractions of the residual gas and vapor fuel, expressed as

$$x_r = \frac{m_r}{m}; \quad x_f = \frac{m_f}{m}; \tag{3.9}$$

Finally, q symbolizes the heat flux through the pipe walls.

$$q = \frac{1}{2}\rho|u|f_a c_p(T_{wall} - T) \tag{3.10}$$

3.3. 3D Models

As known, 3D models solve the Navier-Stokes equations, resolving the mass, momentum, and energy equations as a function of time along the three space coordinates. These equations correspond to a non-linear system of partial differential equations, solved in a number of control volumes, schematized by a computational grid. Depending on the degree of approximation in the equation solution, three possible approaches are available:

1. *Direct Numerical Simulation (DNS*): it is based on a direct resolution of the Navier-Stokes equations. However, the computational effort is extremely expensive in terms of both time and memory. Indeed, to achieve a correct solution, the computational grid must be so fine to capture all temporal and spatial turbulent scales, up to the smallest one (Kolmogorov scale).

2. *Reynolds Averaged Navier-Stokes (RANS) equations:* the turbulent field is decomposed into its time-averaged and fluctuating quantities. The RANS equations derive from the time-average of the original flow equations. Thus, they express the time-averaged behaviour, or in the case of quasi-periodic flows, the phase-averaged flow development, such as in internal combustion engines. The time-averaging introduces new terms, named "Reynolds stresses", whose solution requires the development of proper turbulence sub-models to close the problem.

3. *Large Eddy Simulation (LES):* the larger eddies, strongly affected by the domain geometry, are directly solved. With the aim to reduce the computation efforts, only the smaller scales are computed by dedicated sub-models.

Nowadays, as already mentioned, the employment of both 0D-1D and 3D simulations to drive the engine development phase is a common practice. Although 3D models allow achieving accurate analyses of the engine fluid-dynamic behaviour, the high computational costs limit its application to few engine geometrical configurations or operating conditions. Instead, considering 0D/1D models, they can explore the whole engine system with a reduced computational effort and adequate accuracy.

In the following the approach followed in this research activity is reported, where 0D/1D/3D models are employed. Four main steps have been performed for the characterization of a conventional SI engine:

- *1*: Based on the engine geometric characteristic, a 0D/1D model was developed. Preliminary 1D simulations under motored operations were performed at various engine speeds.
- *2:* 3D in-cylinder motored analyses to describe the in-cylinder flow motion were performed, imposing as the boundary condition the 1D computed time-varying pressure and temperature. The mean and turbulent flow fields were extracted over the entire engine cycle.
- *3:* The outcomes from the previous two steps were used to calibrate the 0D turbulence model, needed for the closure of the phenomenological combustion model, described in the next section.
- *4:* Once completed the turbulence model tuning, the 1D engine model was performed under fired conditions. The combustion model tuning was performed comparing the outcomes with experimental data to fit in-cylinder pressure cycles.

The design of a new engine concept can require the development of new models, or the strengthening of previously available ones, with the aim to correctly describe the in-cylinder phenomena. This was the case of the pre-chamber SI engine examined in this work. Here, 3D simulations allowed, not only to tune the turbulence model but also to clarify the physical phenomena occurring in this novel architecture.

3.4. Combustion modelling for SI Engine

The very first version of the fractal combustion model has been proposed some years ago [15]. This approach poses its theoretical basis on the combustion characteristics to be expected in the most common combustion regime occurring in a conventional SI engine, i.e. the wrinkled-corrugated flamelet zone, as recalled in *Figure 2-12*. In this condition, as already highlighted, the flame front

exhibits an increased surface, A_T, compared to the laminar area, A_L, because of its interaction with the turbulence, *u'*. The flame locally still propagates at a laminar speed, S_L, but the burn rate is enhanced because of the turbulence effect. This process is schematically represented in *Figure 3-2* The flame surface area geometrical increment is included in the model through the theories of the fractal geometry. Several experiments demonstrated that a wrinkled flame front shows a fractal behaviour, resulting in the auto-similarity of its basic structure [12], [16], [17], [18]. This allows correlating the turbulent flame front extent to the laminar one, on the basis of turbulence characteristic speed, time, and length scales [15], [19].

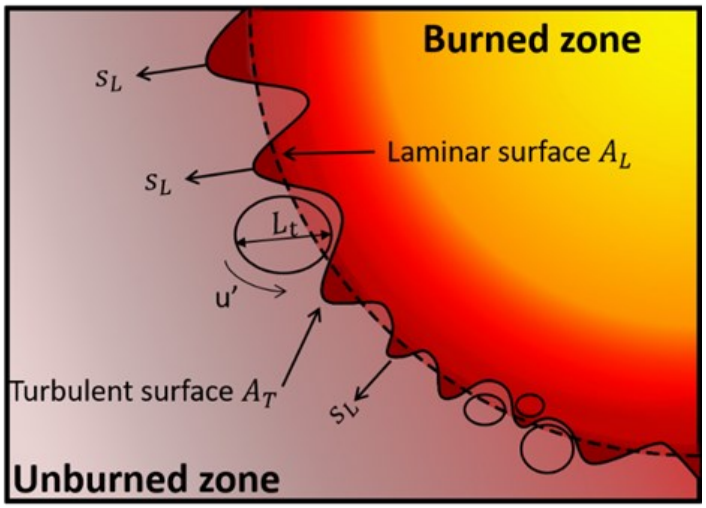

Figure 3-2 Schematic of the fractal combustion model.

Considering the above-mentioned hypothesis, the burn rate can be expressed as a function of the wrinkling factor, Σ, in turn, defined as the ratio between the turbulent and the laminar flame area A_T/A_L:

$$\left(\frac{dm_b}{dt}\right)_{fractal} = \rho_u A_T S_L = \rho_u A_L S_L \left(\frac{A_T}{A_L}\right) = \rho_u A_L S_L \Sigma \tag{3.11}$$

$$\Sigma = \left(\frac{L_{max}}{L_{min}}\right)^{D_3-2} \tag{3.12}$$

The wrinkling factor can be estimated, according to the expression stated in [8], depending on the fractal dimension, D_3, and the maximum and minimum flame wrinkling scales L_{max}, and L_{min}. D_3 is a function of turbulence intensity, u' ,and laminar flame speed S_L, according to the correlation [18] as express in the following eq. (3.13):

$$D_3 = \frac{2.35u' + 2.00S_L}{u' + S_L} \tag{3.13}$$

Considering the wrinkling scales, L_{max} is associated with a macroscopic characteristic dimension of the flame front, here considered proportional to the flame radius r_f, by the tuning constant c_{wrk} (wrinkling multiplier).

$$L_{max} = c_{wrk} r_f \tag{3.14}$$

while L_{min} is assumed equal to the size of the smallest turbulent eddies [15], expressed by the Kolmogorov length scale, L_k:

$$L_{mim} = L_k \tag{3.15}$$

The model above described in *Figure 3-2* applies for a fully developed and freely expanding turbulent flame. Regarding the early flame development and the combustion completion, proper modifications of the model are required.

Since the combustion beginning, as already underlined, is featured by a laminar propagation rather than a turbulent one, the flame front does not result effectively corrugated. Then, the transition from laminar to turbulent combustion can be modelled by a progressive increase of the fractal dimension D_3, according to eqs. (3.16) and (3.17).

$$D_3 = \frac{D_{3,max} u' + D_{3,min} S_L}{u' + S_L} \tag{3.16}$$

$$D_{3,min} = 2.00\ ;\ D_{3,min} = 2.00(1 - \ w_{trans}) + 2.35 w_{trans} \tag{3.17}$$

The wrinkling evolution depends on the variable w_{trans}, stated in eq. (3.18), as a function of a characteristic time scale, t_{trans}, and a model tuning constant, c_{trans} (transition multiplier), considering that the characteristic time scale is calculated using the turbulence kinetic energy, k, and its dissipation rate, ε:

$$w_{trans} = \int \frac{dt}{c_{trans} t_{trans}};\ t_{trans} = \frac{k}{\varepsilon} \tag{3.18}$$

During the combustion process evolution, when the flame front interacts with the combustion chamber walls, a further modification of the burning rate is introduced. Even if a detailed description of flame-wall interaction is concretely not achievable by employing a quasi-dimensional model, it

can be stated that flame front wrinkling no more occurs near the walls, leading to a burning rate slow down.

Hence, the overall burning rate can be expressed as a weighted average of the fractal burning rate and a laminar wall combustion, according to eqs. (3.19) and (3.20).

$$\left(\frac{dm_b}{dt}\right) = (1 - w_{wall})\left(\frac{dm_b}{dt}\right)_{fractal} + w_{wall}\left(\frac{dm_b}{dt}\right)_{wall} \tag{3.19}$$

$$\left(\frac{dm_b}{dt}\right)_{wall} = \rho_u A_L S_L \tag{3.20}$$

Here, the variable w_{wall} describes the transition from turbulent to wall combustion, according to (3.21), being the ratio between the area wetted by the flame front on piston, head, and cylinder, A_w, and the total flame front area, A_{tot}. This ratio is multiplied by the mass fraction of burned gas, x_b, raised to an exponent amplified by the tuning constant x_{wc} (wall combustion multiplier).

$$w_{wall} = \frac{A_w}{A_{tot}} x_b^{10x_{wc}} \tag{3.21}$$

The laminar flame area, A_L, is evaluated through a tabulated approach to shorten the computational time. The flame area table is read at runtime having as input data the current piston position and the burned gas volume. The table is calculated by an off-line automatic procedure which determines the intersections between an "ideal" spherically smoothed flame front, centred on the spark plug, and the piston / head / cylinder surfaces.

3.4.1. Laminar Flame Speed Correlations

The laminar flame speed is here evaluated by a numerical correlation. Since the LFS plays a critical role in the burning rate prediction, it has been largely investigated, as highlighted by the available literature. Concerning the laminar flame speed formulations for gasoline, these can be divided into two main categories: experimental-based, such as [20],[21],[22],[23] and reaction kinetic calculations based as [26],[27]. Considering the first category, the main drawback is related to the experimental tests' conditions featured by a limited range of equivalence ratios and by low pressure and temperature (usually below 15 bar and 600 K, respectively), due to technical [24],[25] and ignitability [20] limitations. Therefore, these correlations may lead to inaccuracies in predicting the LFS if employed outside the measurement range, such as in the case of typical SI engine operations featured

by high pressures and temperatures. Instead, considering the second category, the kinetic-based approach allows overcoming these issues, extending the validation ranges of the correlation and leading to a more reliable LFS prediction for engine-like operating conditions. However, the accuracy and the computational burden of such models strongly depend on the number of species and reactions of the adopted kinetic scheme [28],[29],[30], and surrogate fuel formulation.

A novel LFS correlation based on 1D chemical kinetics computations have been developed during this research activity [31] and assessed with the experimentally derived Metghalchi and Keck correlation [20].

Both correlations express the LFS (S_L) according to the power-law form of eq. (3.22), where S_{L0} is the flame speed at reference conditions $T=T_0$ and $p=p_0$ for given fuel type and equivalence ratio, while EGR_{factor} is a LFS reduction term that accounts for the inert gases contained in the unburned mixture.

$$S_L = S_{L,0}\left(\frac{T}{T_0}\right)^{\alpha}\left(\frac{p}{p_0}\right)^{\beta} EGR_{factor} \tag{3.22}$$

For Metghalchi and Keck correlation here labelled as "Cor A", exponents α and β depend only on equivalence ratio ϕ, and EGR_{factor} is a function of the residual gas molar fraction, $\tilde{x}_r$, raised to a constant exponent, δ. The equations for "Cor A" are:

$$S_{L0} = B_m + B_\Phi(\Phi - \Phi_m)^2 \tag{3.23}$$

$$\alpha(\Phi) = \alpha_0 + \alpha_1\Phi^{\alpha_2};\quad \beta(\Phi) = \beta_0 + \beta_1\Phi^{\beta_2};\quad EGR_{factor} = (1 - \gamma\tilde{x}_r^{\delta}) \tag{3.24}$$

The values of the constants, listed in *Table 3.2.*, are the default ones used in software GT-Power™. The original values proposed by Rhodes and Keck [21] for fuel RMFD-303 have been slightly modified to reflect the results reported in [22].

Table 3.2 Coefficients and reference conditions for correlation "Cor A".

Coefficients			
$B_m\ [m/s]$	0.35	β_0	-0.357
$B_\phi\ [m/s]$	-0.549	β_1	0.14
ϕ_m	1.1	β_2	2.77
α_0	2.4	γ	2.06
α_1	-0.27	δ	0.77
α_2	3.51		
Reference conditions			
$T_0\ [K]$	298	$p_0\ [bar]$	1.013

This correlation was based on experimental tests, where the operating parameters could span the following ranges:

- Pressure, p: 0.4 – 50.7 atm
- Temperature, T: 300 – 700 K
- Equivalence ratio, ϕ : 0.8 – 1.4
- EGR molar fraction, $\tilde{x}_r$: 0 – 0.2

The second correlation, labelled as "Cor B", [31], has been obtained by fitting the results of a chemical kinetics solver (CANTERA) applied to 1D planar laminar flames. The actual gasoline is modelled by a Toluene Reference Fuel (TRF), composed of iso-octane, n-epthane, and toluene. The volume fractions of the three components of the surrogate fuel are selected to match the RON and MON of typical commercial gasoline, according to the methodology reported in [32]. Various oxidation mechanisms for gasoline surrogates exist in the literature, and they are classified as simplified [28], semi-detailed [29], and detailed kinetics[30]. Because of a large number of flame speed data (more than 6000 evaluations) needed to achieve a quite general correlation, a compromise between accuracy and computational effort is required. For this reason, it was decided to use the semi-detailed mechanism developed by Andrae et al.[33], well describing both low and high temperature kinetics. This mechanism includes 5 elements, 137 species, and 633 reactions.

The LFS calculations are performed for several values of pressure, p, temperature, T, equivalence ratio, ϕ, RON, MON, and exhaust gas mass fraction, x_r, in the following ranges:

- Pressure, p: 1 – 20 bar
- Temperature, T: 323 – 923 K
- Equivalence ratio, ϕ : 0.5 – 1.5
- RON: 90 – 98
- MON: 80 – 94
- EGR mass fraction, x_r: 0 – 0.2

The composition of the residual gas is established in each condition (TRF blend, ϕ, T, p) as the equilibrium composition of the combustion products. Then, the LFS results are fitted depending on ϕ, T, p, x_r, and TRF composition. An important finding is that, in the considered ranges of RON and MON, the LFS mainly depends on the fuel sensitivity, S = RON – MON, rather than on the specific TRF blend. This entails a strong simplification of the data fitting, leading to a correlation that can still be expressed in power-law form, eq. (3.22). But in this case, the expressions for the coefficients are more complex if compared to "Cor A", and EGR_{factor} depends also on T, p and ϕ, according to the following equation:

$$EGR_{factor} = [1 - \gamma_{EGR}(\Phi, T)x_r]^{\delta_{EGR}(\Phi,p)} \tag{3.25}$$

The coefficients of "Cor B" are stated as polynomials in ϕ according to eqs. (3.27)-(3.30). The polynomial coefficients are generally in function of *T*, *p,* and *S*, resulting in a cross-dependency of the correlation terms on all the considered independent variables. The values of the correlation constants that provide the best fitting of the LFS data are listed in *Table 3.3.* The average fitting error is 1.75% and the maximum error reaches 6.0%, only for some extreme values of the variables.

$$S_{L0}(\Phi,S)=\sum_{j=1}^{6}\mathrm{A}_j\Phi^{(j-1)} \qquad \mathrm{A}_j=\mathrm{A}_{j1}+\mathrm{A}_{j2}S \tag{3.26}$$

$$\alpha(\Phi,T,p)=\sum_{j=1}^{4}\alpha_j\Phi^{(j-1)} \qquad \alpha_j=\alpha_{j1}+\alpha_{j2}\left(\frac{T}{T_0}\right)+\alpha_{j3}\left(\frac{p_0}{p}\right) \tag{3.27}$$

$$\beta(\Phi,S)=\sum_{j=1}^{5}\beta_j\Phi^{(j-1)} \qquad \beta_j=\beta_{11}+\beta_{12}\left(\frac{1}{S}\right) \tag{3.28}$$

$$\gamma_{EGR}(\Phi,T)=\sum_{j=1}^{3}\gamma_{EGR_j}\Phi^{(j-1)} \qquad \gamma_{EGR_j}=\gamma_{EGR_{j1}}+\gamma_{EGR_{j2}}\left(\frac{T}{T_0}\right) \tag{3.29}$$

$$\delta_{EGR}(\Phi,p)=\sum_{j=1}^{4}\delta_{EGR_j}\Phi^{(j-1)} \qquad \delta_{EGR_j}=\delta_{EGR_{j1}}+\delta_{EGR_{j2}}\left(\frac{p_0}{p}\right) \tag{3.30}$$

Table 3.3 Coefficients and reference conditions for correlation "Cor B".

S_{L0} $[m/s]$ Coefficients			
A_{11}	-2.3832	A_{41}	51.659
A_{12}	0.1877	A_{42}	-3.3700
A_{21}	15.636	A_{51}	-30.793
A_{22}	-1.1768	A_{52}	1.9040
A_{31}	-40.547	A_{61}	6.8282
A_{32}	2.8624	A_{62}	-0.4117
α Coefficients			
α_{11}	6.2174	α_{31}	11.646
α_{12}	0.1307	α_{32}	-1.5433
α_{13}	-0.8983	α_{33}	-5.0751
α_{21}	-13.125	α_{41}	-3.1843
α_{22}	1.0024	α_{42}	0.6125
α_{23}	3.8909	α_{43}	1.8919
β *Coefficients*			
β_{11}	0.8055	β_3	9.0203
β_{12}	0.1295	β_4	-6.5708
β_2	-5.2798	β_5	1.7142
EGR Coefficients			
$\gamma_{EGR,11}$	6.0973	$\delta_{EGR,12}$	-0.2562
$\gamma_{EGR,12}$	-2.1178	$\delta_{EGR,21}$	18.398
$\gamma_{EGR,21}$	-10.696	$\delta_{EGR,22}$	2.8590
$\gamma_{EGR,22}$	4.3429	$\delta_{EGR,31}$	-21.094

$\gamma_{EGR,31}$	6.8101	$\delta_{EGR,32}$	-4.9623
$\gamma_{EGR,32}$	-2.6495	$\delta_{EGR,41}$	7.4949
$\delta_{EGR,11}$	-2.4850	$\delta_{EGR,42}$	2.0624
Reference conditions			
$T_0\ [K]$	323	$p_0\ [bar]$	1.000

As a final remark, an interesting feature of the "Cor B" is that it does not require the specification of the surrogate fuel composition, but only the RON and MON of the actual gasoline. This simplifies the setup of the 1D engine simulation while properly accounting for the effects of the fuel composition.

It is worth to underline that during this work, concerning the pre-chamber engine architecture, the LFS correlation applied has been provided from IFPEN and presented in [34]. The main reason is that this correlation applies for ultra-lean mixtures (from λ= 0.58 up to 2.00), covering most of the operating conditions considered in this work. It is derived from 1D simulations of flame propagation in a gasoline / air mixture. Further, this correlation allows simulating a fuel with hydrogen addition. As known, this element can support the flame propagation and extends the dilution limits with improved combustion stability. It has been obtained by fitting the results of a chemical kinetics solver (PREMIX and AURORA libraries of CHEMKIN-PRO package version 15131.) applied to 1D planar laminar flames. The actual gasoline is modelled by a surrogate defined as Toluene Reference Fuel Ethanol (TRFE), composed of 30.8% of toluene, 42.4% of iso-octane, 17.6% of n-epthane, and 9.2% of ethanol in liquid volume. The oxidation mechanism applied includes 2118 reactions and 276 species. Its validation is established within ranges of common pressure, temperature, and equivalence ratios, considering the experimental limitations of dedicated apparatus.

The LFS calculations are performed for several values of pressure, p, temperature, T, equivalence ratio, ϕ, percentage of H_2 at the intake, and exhaust gas mass fraction, x_r, in the following ranges:

- Pressure, p: 1 – 120 bar
- Temperature, T: 500 – 850 K
- Equivalence ratio, ϕ : 0.58 – 2.0
- EGR mass fraction, x_r: 0 – 0.1
- H_2 % at intake air: 0 - 6

The power low formula was then modified to include all the dependencies. Once obtained the new formulation, reported in eqs. (3.31)-(3.34), a MATLAB algorithm including a nonlinear optimization function was used to obtain the equation coefficients shown in *Table 3.4*.

$$S_L = S_{L,0}\left(\frac{T}{T_0}\right)^{\alpha}\left(\frac{p}{p_0}\right)^{\beta} EGR_{factor}H_{2_{factor}}EGR\ H_{2_{factor}} \tag{3.31}$$

$$S_{L0} = (1 + a x_{H_2})^b c\ \Phi \exp\left(e|\Phi - f|^2\right) \tag{3.32}$$

$$\alpha(\Phi) = \alpha_0 + \alpha_1(\Phi - 1)^2 + \alpha_2(\Phi - 1); \qquad \beta(\Phi) = \beta_0 + \beta_1(\Phi - 1)^2 + \beta_2(\Phi - 1) \tag{3.33}$$

$$\begin{cases} EGR_{factor} = (1 + \gamma_0 x_r^2 + \gamma_1 x_r) \\ H_{2_{factor}} = \left(1 + \gamma_2 x_{H_2}(\Phi - 1)\right) \\ EGR\ H_{2_{factor}} = (1 - \gamma_3 x_r x_{H_2}) \end{cases} \tag{3.34}$$

Table 3.4 Coefficients and reference conditions for IFPEN correlation.

Coefficients			
a	0.04703	α_2	– 0.58956
b	1.0653	β_0	–0.33945
c	36,476.8183	β_1	– 0.021676
d	5.7836	β_2	0.13269
e	–1.2436	γ_0	–0.03584
f	1.2857	γ_1	0.00016
α_0	2.3139	γ_2	–0.032399
α_1	2.7353	γ_3	–0.00058
Reference conditions			
$T_0\ [K]$	298	$p_0\ [bar]$	1.013

Finally concerning the large-bore engines analysed during this work, since these are fuelled with methane, a further correlation has been implemented in the combustion model. The formulation has been taken from [35], where a modified power-law formula has been considered:

$$S_L = \left(B_m \Phi^{\eta} e^{-\xi(\Phi - \Phi_m)^2}\right) \left(\frac{T}{T_0}\right)^{\alpha} \left(\frac{p}{p_0}\right)^{\beta} EGR_{factor} \tag{3.35}$$

where η represents the equivalence ratio exponent, and ξ is the laminar speed exponent. Concerning α, β, and EGR_{factor} they are respectively evaluated as:

$$\alpha(\Phi) = \alpha_0 \Phi^2 + \alpha_1 \Phi + \alpha_2; \quad \beta(\Phi) = \beta_0 \Phi^2 + \beta_1 \Phi + \beta_2\ ; \quad EGR_{factor} = (1 - \gamma \tilde{x}_r^{\delta}\ ) \tag{3.36}$$

In *Table 3.5* coefficients for eq. (3.35) and eq. (3.36) are reported:

Table 3.5 Coefficients and reference conditions for methane correlation from GT-Power 2020.

Coefficients			
$B_m\ [m/s]$	0.3885	α_2	6.9258
η	-0.2	β_0	-1.3712
ξ	6.45	β_1	2.6808
ϕ_m	1.08	β_2	1.7492

α_0	4.9199	γ	0.75
α_1	-10.287	δ	7
Reference conditions			
$T_0\ [K]$	298	$p_0\ [bar]$	1.013

3.4.2. Flame Stretch Model

As stated above, the considered LFS correlations provide the velocity of one-dimensional planar flames related to the unburned mixture. But it is well known that in SI engines, especially at the combustion beginning, the flame geometry and dynamics are much more complex because of the flame stretch. This phenomenon consists in local modifications of the flame speed produced by two effects: the *preferential diffusion,* which results in local variations of flame temperature and burning rate (depending on the effective Lewis number), and the *flow divergence*, which induces an increase in the flame speed at the upstream boundary of the preheat zone with respect to the speed of the reaction zone [36],[37].

For a stretched flame, its speed can be related to that of a planar flame introducing a flame-thickness-dependent coefficient that accounts for the effects of diffusion and chemical reactions in the flame zone. This coefficient is known as the Markstein length, *L*, and depends on fuel type and reactivity, and mixture composition [38].

Concerning a conventional SI engine, the flame front shows a very different shape from a planar one, and thus it propagates relative to the unburned gas having a displacement speed, S_d, that differs from the planar flame speed, S_L, according to the following equation:

$$S_d = S_L - L\mathbb{K} \tag{3.37}$$

where $\mathbb{K}$ is the flame stretch rate, originally defined by Karlovitz [39] as the Lagrangian time derivative of the logarithm of the flame surface area, *A*:

$$\mathbb{K} = \frac{d}{dt} \cdot (lnA) = \frac{1}{A} \cdot \frac{dA}{dt} \tag{3.38}$$

The flame stretch rate accounts for the effects of the curved flame motion and the velocity gradients inside the flame [40], as shown by the equation:

$$\mathbb{K} = \kappa S_L + K_s \tag{3.39}$$

where κ is the flame curvature and K_S is the hydrodynamic strain. Considering an outwardly propagating quasi-spherical flame, such as the one occurring in a SI engine, the flame curvature and strain can be respectively expressed as:

$$\kappa = \frac{2}{r_f}; \qquad K_s = 2(\sigma - 1) \cdot \frac{S_L}{r_f} \tag{3.40}$$

where r_f is the flame radius while $\sigma = \rho_u/\rho_b = T_b/T_u$ is the thermal expansion parameter. Replacing the terms of eq. (3.40) in eq. (3.39) the following form for the total stretch rate is achieved:

$$\mathbb{K} = \frac{2\sigma S_L}{r_f} \tag{3.41}$$

Then, based on the description provided in [41], a real flame of finite thickness δ_{th} can be subdivided in a number of layers characterized by different temperatures. Each of them propagates with a different speed, evaluable through eq. (3.38) once the appropriate Markstein length, varying through the flame front, is selected. With the aim to synthesize in a 0D phenomenological framework this detailed flame description, the flame layer characterized by a complete fuel oxidation has been chosen as representative of the modelled zero-thickness flame front. This layer, whose Markstein length is labelled as L_b, is located on the burned side of the real flame front, propagating with a speed expressed as:

$$S_{L,stretched} = S_L - L_b\mathbb{K} \tag{3.42}$$

The linear relation expressed in eq. (3.42) is properly applicable to low turbulence intensities, namely in the corrugated flamelet regime. As the turbulence intensity increases, the relation between flame speed and stretch becomes increasingly non-linear [42], but at the moment this aspect is not included in the here presented model. The asymptotic theory of Matalon et al. [40] allows expressing the L_b as:

$$L_b = \left(\alpha - \int_1^{\sigma} \frac{\lambda(x)}{x} dx\right) \cdot \delta_{th} \tag{3.43}$$

where $\delta_{th} = \lambda_u/\left(c_{pu}\rho_u S_L\right)$ is the flame thermal thickness and λ is the thermal conductivity of the mixture scaled with respect to its value in the unburned gas. The term α in eq. (3.43) can be express as [41]:

$$\alpha = \frac{\sigma}{\sigma - 1} \cdot \int_1^{\sigma} \frac{\lambda(x)}{x} dx + \frac{Ze(Le_{eff} - 1)}{2(\sigma - 1)} \cdot \int_1^{\sigma} \ln\left(\frac{(\sigma - 1)}{x - 1}\right) \frac{\lambda(x)}{x} dx \tag{3.44}$$

where $Ze = E_a(T_b - T_u)/RT_b^2$ is the Zel'dovich number, which depends on the apparent activation energy E_a, and Le_{eff} is the effective Lewis number. The apparent activation energy is defined through the formulation:

$$\frac{E_a}{2R} = \frac{\partial \ln(\rho_u S_L)}{\partial(1/T_b)} \tag{3.45}$$

where R is the universal gas constant. E_a is expressed as a function of p, ϕ, x_r, and S through a specially developed correlation based on 1D flame computations by CANTERA. For any given set of pressure, equivalence ratio, EGR mass fraction, and fuel sensitivity, the temperature of the unburned mixture is perturbed (it is assumed that E_a does not depend on T_u) and the derivative on the right-hand side of eq. (3.45) is estimated. Finally, the values of E_a so achieved are fitted by the following four variables polynomial:

$$\begin{gathered} E_a(\Phi, p, x_r, S) = \left(\sum_{j=1}^{5} A_{E,j}(p)\Phi^{(j-1)}\right) \cdot \left(1 + \gamma_{E,EGR} x_r\right) \cdot \left(1 + \gamma_{E,S} S\right) \\ A_{E,j}(p) = A_{E,j1} + A_{E,j1}\left(\frac{p}{p_0}\right) \end{gathered} \tag{3.46}$$

The values of the constants minimizing the interpolation error are reported in *Table 3.6*.

Table 3.6 Coefficients of the correlation for the apparent activation energy.

$A_{E,j1}$ $[MJ/kmol]$		$A_{E,j2}$ $[MJ/kmol]$	
$A_{E,11}$	1919.9	$A_{E,12}$	-20.666
$A_{E,21}$	-8705.1	$A_{E,22}$	128.99
$A_{E,31}$	15554	$A_{E,32}$	-269.09
$A_{E,41}$	-11343	$A_{E,42}$	222.81
$A_{E,51}$	2911.2	$A_{E,52}$	-63.394
EGR coefficient		*Sensitivity coefficient*	
$\gamma_{E,EGR}$	0.4615	$\gamma_{E,S}$	0.0087

Concerning the other parameters in eq. (3.44), Le_{eff} is calculated as a function of equivalence ratio [40] and temperatures T_u and T_b, while the thermal conductivity is assumed to have a linear

dependence on the temperature. The L_b values, provided by eq. (3.43), have been compared to outcomes of the experimental correlation proposed by Galmiche et al. [42] to check the consistency of the here proposed formulation. The comparison showed a reasonable agreement between the two approaches.

Considering the flame stretch effect on the LFS calculation, it is expected to induce a reduction in the combustion speed when the flame radius is small and consequently the stretch rate is higher. To clarify this aspect, *Figure 3-3* shows the comparison between the stretched (magenta) and unstretched (blue) laminar flame speeds at varying crank angle for different Brake Mean Effective Pressures (BMEPs). Hence, the influence of the stretch is strongest at the combustion start, becoming small once the combustion proceeds. In addition, *Figure 3-3* highlights that the stretch effect is higher at very low loads, where it is expected to improve substantially the numerical estimation of the combustion duration.

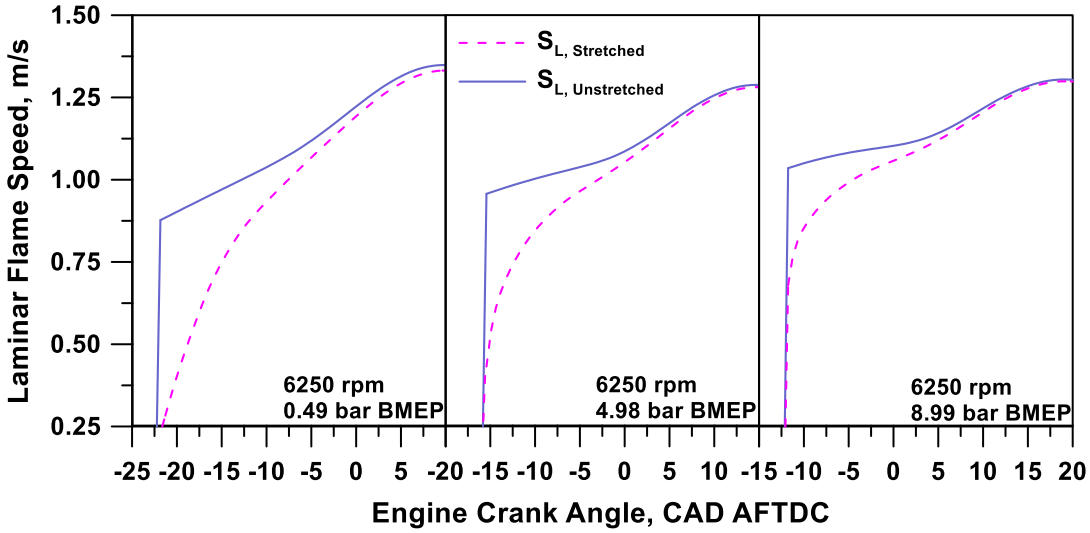

Figure 3-3 Effect of the flame stretch on the laminar flame speed for three BMEP levels and constant engine speed (6250 rpm).

3.4.3. Turbulence model

Aiming at the combustion model closure, several turbulence and flow parameters in the combustion chamber have to be estimated, such as u', L_k, L_t, and ε. Hence, a phenomenological procedure, derived from the 3D RNG $k-\varepsilon$ turbulence formulation presented in [43], has been synthesized in a 0D framework, leading to the following equation system:

$$\begin{cases} \dfrac{dmk}{dt} = (\dot{m}k)_{inc} - (\dot{m}k)_{out} + \dfrac{2}{3}\dfrac{\dot{\rho}}{\rho}\left(-mv_t\dfrac{\dot{\rho}}{\rho} + mk\right) + P - m\varepsilon & (I) \\ \dfrac{dmK}{dt} = (\dot{m}K)_{inc} - (\dot{m}K)_{out} - f_d\dfrac{mK}{\tau_T} + mK\dfrac{\dot{\rho}}{\rho} - P & (II) \\ \dfrac{dmT}{dt} = (\dot{m}T)_{inc} - (\dot{m}T)_{out} - f_d\dfrac{mT}{\tau_T} & (III) \end{cases} \quad (3.47)$$

The system expressed in (3.47) includes the balance equations of turbulent kinetic energy, k, mean flow kinetic energy, K, and tumble angular momentum, T, defined as follows:

$$k = \frac{3}{2}u';\ K = \frac{1}{2}U_{fK}^2;\ T = U_r r_T \tag{3.48}$$

where *u'* is the turbulence intensity, U_{fK} is the mean flow velocity, U_T is the tumble velocity, r_T is the radius of the tumble vortex; v_t is the turbulent viscosity:

$$v_t = c_\mu \frac{k^2}{\varepsilon} \tag{3.49}$$

The first and the second terms on the right side of all the three equations describe the incoming and outcoming convective flows through the valves. The third term, in eq. (3.47) (II) and (III), describes the decay due to the shear stresses due to the flow interaction with the combustion chamber walls. This effect is modelled through a decay function, f_d, and a characteristic time scale, t_T, as:

$$f_d = c_{fd0} + c_{fdm}\left[max\left(\frac{B}{H}, 1\right), -1\right] \tag{3.50}$$

$$t_T = \frac{r_T}{u'} \tag{3.51}$$

The decay function depends on the instantaneous geometrical dimensions of the combustion chamber eq. (3.50). It is conceived with the aim to be maximum at the TDC, where the tumble vortex collapse is expected to occur. Further, the tuning constant c_{fd0} operates as an offset for the tumble and kinetic energy dissipations due to internal viscous forces. Because of this offset, the tumble prediction around the BDC can be improved. Finally, c_{fdm} is a multiplier utilized to change the intensity of the tumble collapse.

According to the k formulation, the K equation includes an additive compressibility term, $mK\,\dot{\rho}/\rho$, and a subtractive turbulent production term, P, that represents the energy cascade mechanism. This last quantity is related to the difference between the overall mean flow kinetic energy, K, and the one associated with the tumble motion, $K_T = U_T^2/2$, according to:

$$P = c_{pKk} m \frac{K - K_T}{t_T} \tag{3.52}$$

c_{PKk} is a model constant, that modulates the energy transfer from the mean flow to the turbulent one. Regarding the convective terms in system (3.47) the following relations eqs. (3.53), (3.54), (3.55) are employed, according to cylinder incoming and outcoming contributions, for both forward and reverse flow (*f* and *b* subscripts, respectively). Particularly, in the eqs. (3.54), (3.55), the mean flow and tumble velocities (v_K and v_T) take into account the flow losses through the valves, depending on tumble and discharge coefficient, respectively. Those coefficients are specified as a function of the valve lift.

Incoming flow contributions can be tuned by two global multipliers c_{Tin0} and c_{Kin0}, acting respectively on *K* and *T* balances. The turbulence integral length scale is not directly modelled, but its evolution during the engine cycle is defined by a sequence of S-shaped functions. It is assumed fixed with the engine operating conditions.

$$\left(\dot{m}k\right)_{inc} = 0; \quad \left(\dot{m}k\right)_{out} = k(\dot{m}_{inb} + \dot{m}_{exf}); \tag{3.53}$$

$$\begin{gathered}\left(\dot{m}K\right)_{inc} = \frac{1}{2}\left[\dot{m}_{inf}\left(c_{Kin0}v_{Kinf}\right)^2 + \dot{m}_{exf}v_{Kexf}^2 + \dot{m}_{exb}v_{Kexb}^2\right]; \\ \left(\dot{m}K\right)_{out} = K(\dot{m}_{inf} + \dot{m}_{exf});\end{gathered} \tag{3.54}$$

$$\begin{gathered}\left(\dot{m}T\right)_{inc} = r_t(\dot{m}_{inf}c_{Tin0}v_{Tinf} - \dot{m}_{exf}v_{Texf} - \dot{m}_{exb}v_{Texb}); \\ \left(\dot{m}T\right)_{out} = 2T(\dot{m}_{inf} + \dot{m}_{exf});\end{gathered} \tag{3.55}$$

The dissipation rate, ε, needed to integrate the k equation, is calculated as:

$$\varepsilon = c_\mu^{3/4}\frac{k^{3/2}}{L_t} \tag{3.56}$$

The tumble radius is assumed as a geometrical parameter, independent from the operating conditions. It is expressed by eq. (3.57) having two adjustable constants, c_{rT0} and c_{rTm}.

$$r_t = c_{rT0+}c_{rTm}\frac{1}{4}\sqrt{B^2 + H^2} \tag{3.57}$$

3.5. Combustion modelling for Pre-chamber SI Engine

Several experimental investigations are available in the current literature concerning a pre-chamber SI engine [44]-[50], but the development and application of numerical tools are fundamental to understand the physics beyond this novel architecture. This is especially due to the strong limitation in performing experimental tests because of technological and economic issues. As an example, experimental activities on mixture preparation and combustion development within a pre-chamber volume can be challenging, due to its small dimension, also considering the possibility of an optical access. In addition, considerable time and cost are needed to check the impact of variations in design features of the PC, such as injector location, spark plug position, holes number, length, and diameter. A 3D-CFD model can provide detailed information regarding the pre-chamber mixing and combustion processes, supporting the optimization of the jet ignition process. Therefore, numerous studies were realized, mostly focused on design optimization, or on analysing different operating conditions. Shah [51] examined the impact of the pre-chamber volume and holes diameter on the jet propagation in the main chamber, concluding that the optimal design requires a balance between contrasting effects as described below. In a smaller pre-chamber, the pressure increase causes a short burst of pre-chamber ejection instead of long-lasting jets, which promotes turbulent mixing in the main chamber. Instead, a larger pre-chamber, even when pressure growth inside it is sufficient, may not expel completely the fuel before the main chamber ignites, hence contributing to overall combustion efficiency losses [39]. Moreover, for a fixed PC volume, a smaller nozzle diameter produces a higher flow restriction across the holes, resulting in high combustion enhancement in the main chamber, but leading to the possibility of quenching phenomena when the flame crosses the PC holes. Instead, a larger nozzle diameter results in a short-lived burst of pre-chamber ejection, not ensuring a sufficient turbulence level to sustain the lean combustion. In [52] the effects of the hole orientations and the pre-chamber volume variations on the turbulence flow field were examined. The outcomes reveal a higher TKE-level at the spark plug for the biggest pre-chamber, because of the establishment of tumble motion, not visible in the smallest one. Further, they highlight that the high turbulence level required near the spark plug can be obtained having a hole orientation creating a swirl motion. An extensive study has been realized in [53], performing both 3D-CFD simulation and experimental activity with the aim to investigate the influence of both relevant design and engine parameters on the fluid-dynamics and thermodynamic proprieties of active and passive pre-chambers.

The above-discussed studies and many other available in the literature highlight that the optimal PC layout arises from the right combination of different parameters. Consequently, a highly specific knowledge of the engine under study is mandatory to achieve the potential advantages of this technology.

Since the phenomena above described are very complex, the preferable approach for a pre-chamber engine is a 3D simulation, being able to well-describe the interaction between combustion, chemical kinetics, and turbulence. Nevertheless, due to the high computational effort, the engine operating plane cannot be entirely explored. A numerical engine calibration, employing 0D/1D approaches, allows overcoming this issue, even if with a loss of accuracy compared to 3D models.

The current literature presents several 0D phenomenological models and approaches to physically describe the different phenomena occurring in a pre-chamber engine. Turbulence (K-k-ε) and heat transfer models have been proposed for a passive pre-chamber in [54]. These models can accurately reproduce 3D reference results in terms of pressure traces and turbulence variables. However, in this study, only analyses during compression stroke have been performed, not covering the combustion process simulation. Instead, in [55], the heat transfer was calculated through a PC-engine-adapted correlation. While Wiebe functions were imposed in both main and pre-chamber to describe the combustion, resulting in a non-predictive model.

Further approaches phenomenologically define the combustion process in an active PC as in [56]. A common hypothesis in phenomenological PC combustion models states that the conical hot jets from the holes of the pre-chamber control the initial phase of the main-chamber combustion. For instance, a model dependency was introduced in [57] based on the second Karlovitz number, estimated at the PC holes outlet. Thus, until the Karlovitz number is higher than one, the combustion is assumed to be regulated by the hot turbulent jets ejected by the PC. Then, the flame propagation in the main chamber is considered self-sustained thanks to the turbulence enhancement, comparably to a conventional engine. In [58], the combustion process was modelled including an additional entrainment effect, to consider that the fresh charge is entrained in the burning jets. Further, in [59], an increment of the flame front area was also hypothesized, because of jets penetration. A transition from a drop-shaped flame to a hemisphere was assumed, depending on a characteristic jet length.

Considering all the approaches above described, although including a reasonably detailed description of the pre-chamber engine characteristic phenomena, their validation range is often limited to few operating conditions, particularly concerning the air / fuel ratio. Therefore, it is reasonable to assert that these studies are not reliable enough to perform simulations able to investigate the whole engine plane in different load, speed, or air / fuel proportion.

3.5.1. Model Extension

One of the main aims of this thesis is to develop a quasi-dimensional model for a pre-chamber SI engine capable of physically sensing different engine control variables and of preserving an adequate reliability in the entire engine operating domain without the need for a case-dependent tuning. This

model is an enhanced version of the fractal approach, developed and utilized at the University of Naples Federico II. Below, the procedure to model the basic phenomena occurring in an engine equipped by PC, such as mixture preparation, turbulence evolution, flame area enhancement, burn rate development, etc., will be briefly described.

In *Figure 3-4* the 0D schematization of the Pre-Chamber Spark Plug engine is depicted: the main chamber is considered as a variable 0D volume, connected to the constant volume of the pre-chamber through an orifice. In both volumes, mass and energy balance equations are solved and a filling / emptying method is applied to evaluate the mass exchange between them, as a function of pressure difference, overall cross-sectional area, and discharge coefficient of the orifice.

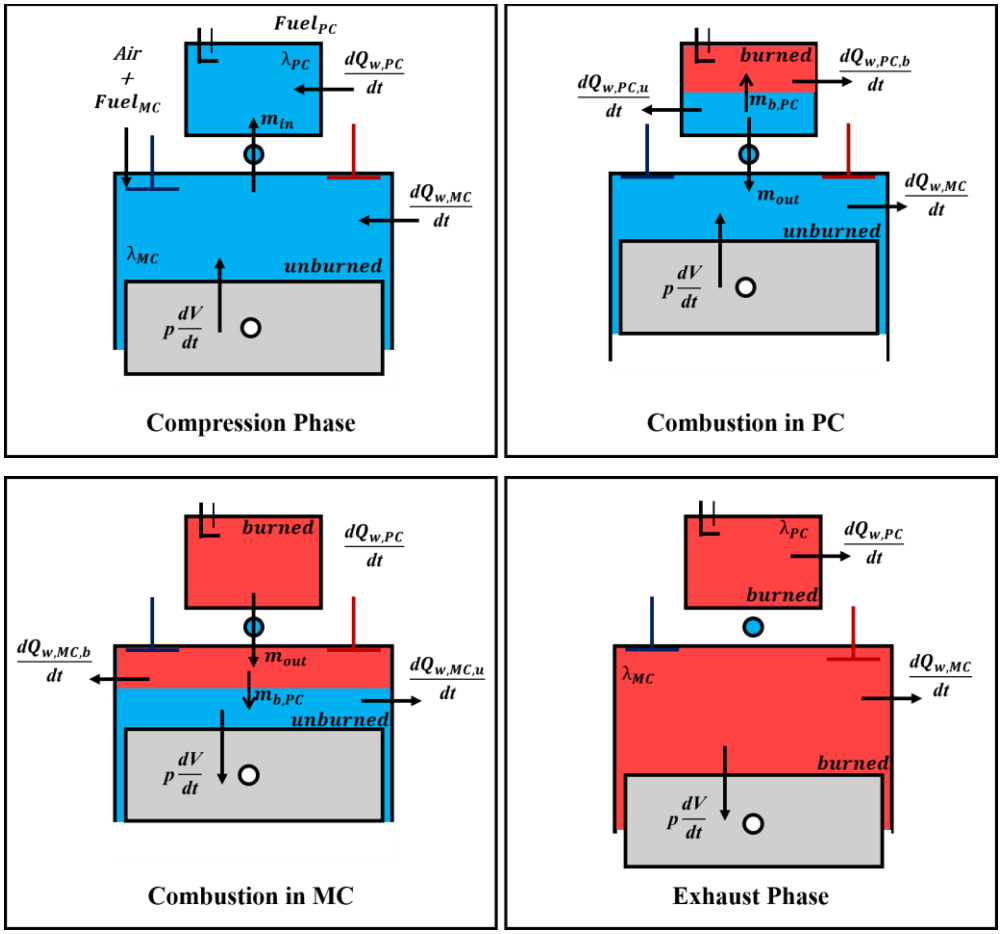

Figure 3-4 0D schematization of the pre-chamber spark plug engine model.

During the valve opening and the compression stroke, the two volumes are featured by a time-varying composition, depending on the mass exchange between the two chambers. Further, during the compression, after the direct fuel injection into the PC, a rich air-fuel mixture is established inside it, then progressively leaned due to high-lambda air-fuel mixture coming from the MC. In this phase, some air-fuel stratification into the pre-chamber is expected to occur in the real engine. A unique feature of this model is the possibility to take into account the above mixture stratification. To better explain this characteristic, in *Figure 3-5* the instantaneous predicted lambda levels in both pre- and

main chamber are depicted. It can be observed that at the end of the fuel injection into the pre-chamber, a very rich mixture establishes ($\lambda_{PC} \approx 0.2 \div 0.3$). Subsequently, all along the compression stroke, lean air / fuel mixture from the MC ($\lambda_{MC} \approx 1.8 \div 2.0$) is pushed inside the PC through its holes, causing on average a rapid increase of λ_{PC}. Further, since an incomplete mixing occurs inside the PC, as confirmed by 3D CFD analyses, a richer mixture close to the spark plug results, while leaner level, similar to one in the MC, occurs at the holes [60]. Hence, to reproduce this behaviour, a simple correlation has been applied, modifying the λ value at the flame borderline, λ_F, used to calculate the laminar flame speed inside the PC. The resulting λ_F profile, reported in cyan in *Figure 3-5*, demonstrates a variation, from a value richer than the average to a value leaner than the average, during the combustion evolution in the pre-chamber.

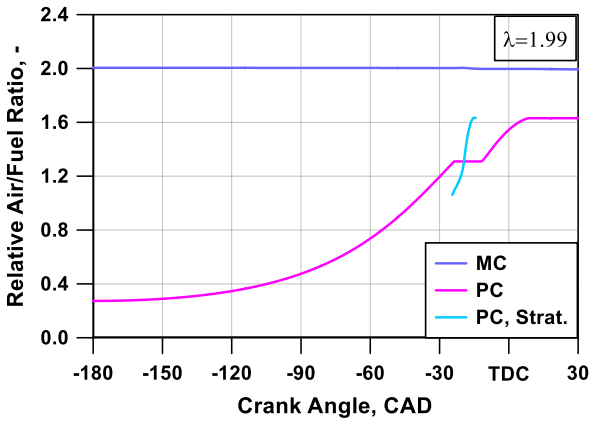

Figure 3-5 λ_{MC} (blue), λ_{PC} (pink), and λ_F (cyan) into the pre-chamber.

Once the combustion begins, the PC is treated by a two-zone approach (*Figure 3-4* top-right). When the PC combustion is ending, the combustion in the main chamber starts, and also in this case a two-zone approach is adopted (*Figure 3-4* bottom-left). At the combustion end, a single zone approach is restored (*Figure 3-4* bottom-right).

Following this approach, the mass evolution in both main and pre-chambers is computed in a representative case and shown in *Figure 3-6(a)* together with their unburned and burned contributions. In the pre-chamber, the total mass increases during the compression stroke, whereas it slightly decreases in the main chamber. The overall in-cylinder content is depicted solid black line, to verify its conservation during the closed valve phase (no crevices and blow-by flows).

Another model feature is the possibility to control the composition of the mass flow leaving the pre-chamber as soon as the pressure increases due to the combustion. Initially, unburned gases are assumed to be ejected from the PC (blue line in (blue line in *Figure 3-6(b)*) together with some limited residual gases (orange line). Subsequently, hot burned gases are assumed to be ejected during the pre-chamber combustion, once the flame approaches the orifices, simulating a scavenging process in

between a perfect displacement and a perfect mixing. The description of both PC mixture stratification and scavenging help to correctly reproduce the burn rate and the pressure evolution in the pre-chamber, as shown by the results presented in the chapter 5.2.1and 5.2.2 of this thesis.

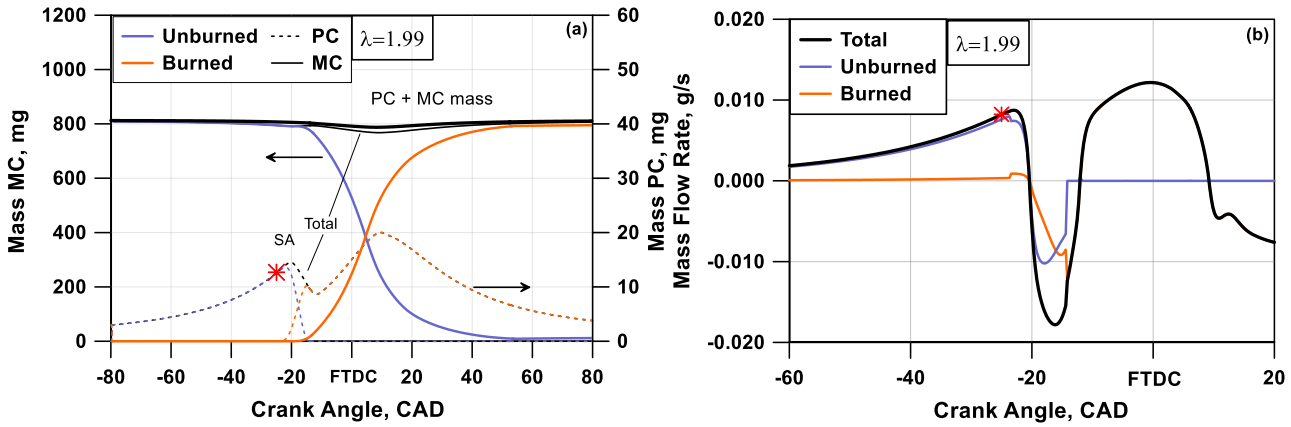

Figure 3-6 (a) Mass evolution of the unburned and burned gases in the PC and MC, (b) instantaneous mass flow rate through the PC orifices.

The burning rate estimation in both pre- and main chambers is a challenging task because of the highly complex phenomena occurring in this novel architecture. Further, intense turbulence levels and organized flow motions developed into the PC due to the incoming flux during the compression stroke have to be considered. Observing experimental and 3D outcomes [53], [44], they exhibit a flame propagation inside the pre-chamber, also occurring in the corrugated flame regime. Hence, based on this hypothesis, the burn rate into the PC has been modelled using the fractal approach too and considering a smooth spherically shaped surface, centred on the spark plug. Minor corrections are required to properly deal with the turbulence production and evolution inside the PC. Similar modifications are needed to describe the turbulence formation into the MC, generated by the hot incoming jet gases from the PC.

In *Figure 3-7* are reported 3D preliminary outcomes, given by IFPEN, showing different phases of the typical combustion development in a PC engine. These images allow understanding the physical events of the combustion process in a main chamber. A further insight is given by the burn rates in the MC and PC in *Figure 3-8(b)*, obtained through a two-zone / two-volume inverse analysis of the experimental pressure cycles, *Figure 3-8(a)*. The PC burn rate profile shows the typical bell-shaped featuring a conventional SI engine, thus reinforcing the assumption of a quasi-spherical propagation in a corrugated flame regime. Instead, the MC burn rate suffers a more complex evolution. Indeed, its profile shows an initial knee, due to the turbulence enhancement caused by the jet released from the PC. During this phase, the jets directly entrain the fresh charge (air and fuel), so that the entrained mass progressively burns releasing heat. Here, the combustion is mainly controlled

by jets velocity and mixture entrainment. Then, once the turbulent jets have almost dissipated their initial kinetic energy, a quasi-spherical propagation begins from multiple ignition sites (*Figure 3-7*). In this phase, the occurring burn rate enhancement is mainly related to the increment of the overall flame surface, however having a lower extent if compared to the first phase one. Once the flame spheres, of different ignition sites, interact each other and with the cylinder walls, the flame propagation direction modifies into a quasi-conical propagation. Finally, a sudden collapse of the flame area occurs, and the combustion rapidly ends.

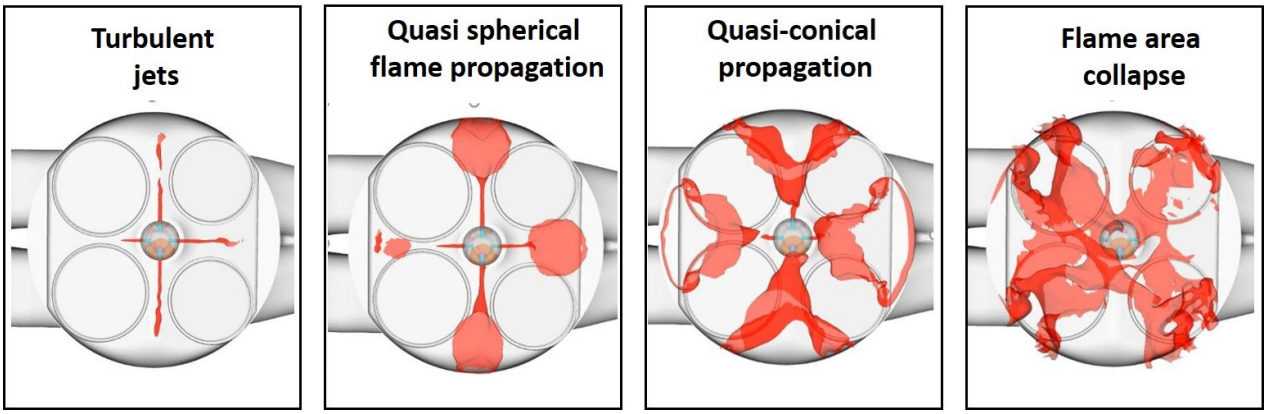

Figure 3-7 3D flame propagation within the MC for at 3000@13 bar IMEP, λ=1.8.

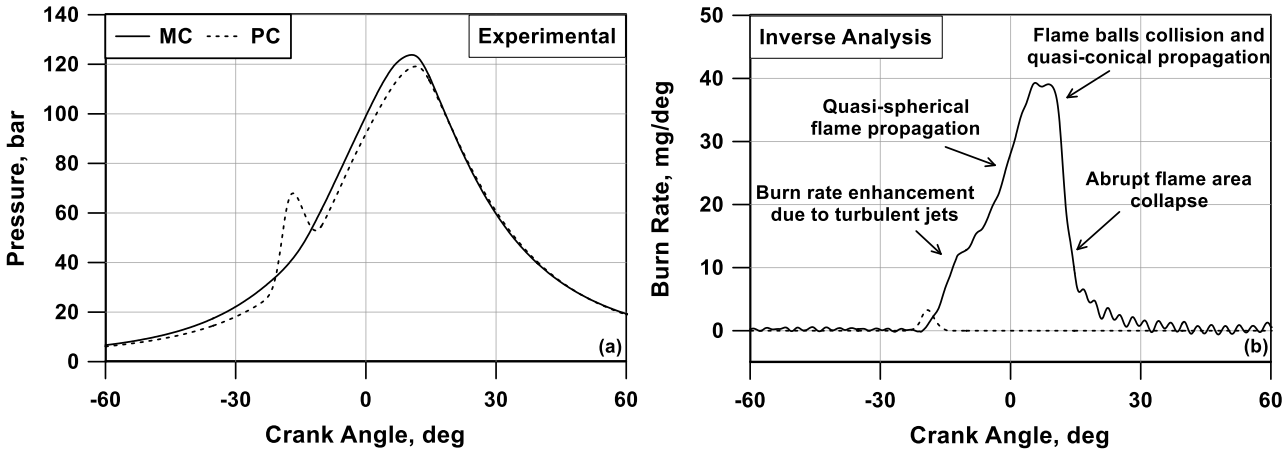

Figure 3-8 (a) Experimental pressure in PC and MC, (b) burn rate in the PC and MC, carried out through an inverse analysis.

Then, based on the above qualitative considerations, the burn rate in the main chamber depends on the superimposition of two phenomena: the flame propagation from multiple ignition sites and the initial flame enhancement exerted by the turbulent jets.

Hence, the overall burn rate can be expressed as the sum of "*classical flame propagation*" characterized by multiple corrugated flame fronts, and a "*turbulent jet combustion*", resulting in the following expression:

$$\left(\frac{dm_b}{dt}\right)_{overall} = \left(\frac{dm_b}{dt}\right)_{fractal} + \left(\frac{dm_b}{dt}\right)_{jet} \tag{3.58}$$

The first term on the right side can be applied to both PC and MC, defining the burning rate by the fractal approach, depending on the laminar flame speed, S_L, and on the turbulent surface of the unique (PC) or multiple (MC) flame fronts A_T. The second term is considered only for the MC, representing the burning rate contribution due to the turbulent jets. Hence, the jets entrain fresh charge (air and fuel) and the entrained mass progressively burns and releases heat. This release rate is assumed to be proportional to the difference between the current entrained mass (m_{entr}) and its burned portion ($m_{b,entr}$), and it is inversely proportional to a characteristic time scale τ, as expressed by eq. (3.59). The time scale is evaluated as the ratio between the Taylor length scale, Λ_T, and the laminar flame speed, S_L. The current total entrained mass, m_{entr}, is computed by integrating its time derivative, in eq. (3.60), in turn calculated by the semiempirical correlation proposed in [57]. The above-mentioned term depends on the mass flow rate coming out of the PC, $\dot{m}_{jet}$, on a tuning constant, c_{jet}, and on the density ratio between PC and MC. Comparably, the burned entrained mass, $m_{b,entr}$, is computed by the integration of eq. (3.59).

$$\left(\frac{dm_b}{dt}\right)_{jet} = \frac{dm_{b,entr}}{dt} = \frac{m_{entr} - m_{b,entr}}{\tau};\ \tau = \frac{\Lambda_T}{S_L} \tag{3.59}$$

$$\frac{dm_{entr}}{dt} = c_{jet}\dot{m}_{jet}\sqrt{\frac{\rho_{PC}}{\rho_{MC}}} \tag{3.60}$$

The combustion starts in the PC is defined by the spark timing, given as a simulation input. Instead, the combustion onset in the MC is predicted according to the current flame radius in the PC. Once it overcomes a critical value, named r_{crit}, the MC combustion is activated. This parameter, normalized by the PC height, is an additional tuning constant, adjusting the combustion begin in the MC. In the model is not included a direct estimation of the flame quenching through the PC holes. Hence, this phenomenology will be roughly considered through a proper selection of the tuning constants.

The laminar flame area A_L in eq. (3.11) is calculated at each simulation step depending on the burned gas volume and, in the MC case, also of the piston position. For the pre-chamber, as already said, a smooth spherically shaped propagation is considered having a centre moving at a speed proportional to the jet velocity. For the main chamber, it is assumed that the flame mainly develops when the turbulent jets have almost dissipated their initial kinetic energy [61]. Presumed ignition sites

are located along each turbulent jet, from which the flame propagates spherically. The sphere centres position, unlike the PC, is imposed as fixed during the combustion development and provided as an additional input parameter. Testing a moving centre in the MC, it turns out that using this approach does not significantly improve the simulation accuracy, but considerably increases the computational time. *Figure 3-9*. representative flame fronts are depicted to clarify the hypothesis about the flame front description above illustrated.

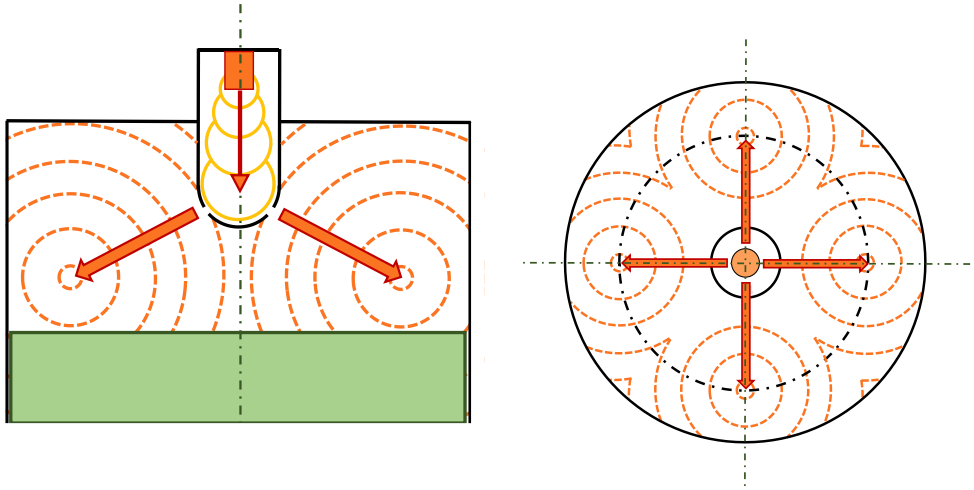

Figure 3-9 Flame front schematizations pre-chamber and main chamber (a) front view, (b) top view.

3.5.1. Turbulence model extension

The turbulence model, as already said, is needed for the combustion model closure. Further, the combustion model, presented in the above section, has been indeed extended including the turbulence production generated by the incoming / outcoming flow through the orifices. In *Figure 3-10*, 3D reference profiles are depicted for both MC (solid line) and PC (dashed one), reporting turbulent intensity, integral length scale, tumble velocity, and swirl velocity during the engine cycle.

As can be seen, if compared to a conventional engine profile, additional turbulence peaks occur. Concerning the pre-chamber, during the first stage of the intake phase, a first peak is visible because of the injection inside it. Subsequently, the turbulence attains a minimum level, and, during the compression, progressively rises due to the flux from the MC. Once the combustion begins in the PC, *u'* suddenly decreases (*Figure 3-10(a)*) and a slight increment in the main-chamber profile is evident depending on the hot jets ejected from the PC. Then, at the end of the compression, the turbulent intensity in the PC presents a peak, because of the incoming flux from the MC through the orifices. This is related to the pressure increase in the MC, due to the progressing combustion.

Further, into the PC, tumble and swirl motions are considered. Concerning the first one, although tumble vortices arise during the compression, they rapidly collapse during the combustion as shown

in *Figure 3-10(c)*. With a similar behaviour, the swirl motion initially increases, but, during the combustion and expansion, progressively decay. The decay process is less intense than the one occurring for tumble, thanks to the PC cylindrical shape (*Figure 3-10(d)*).

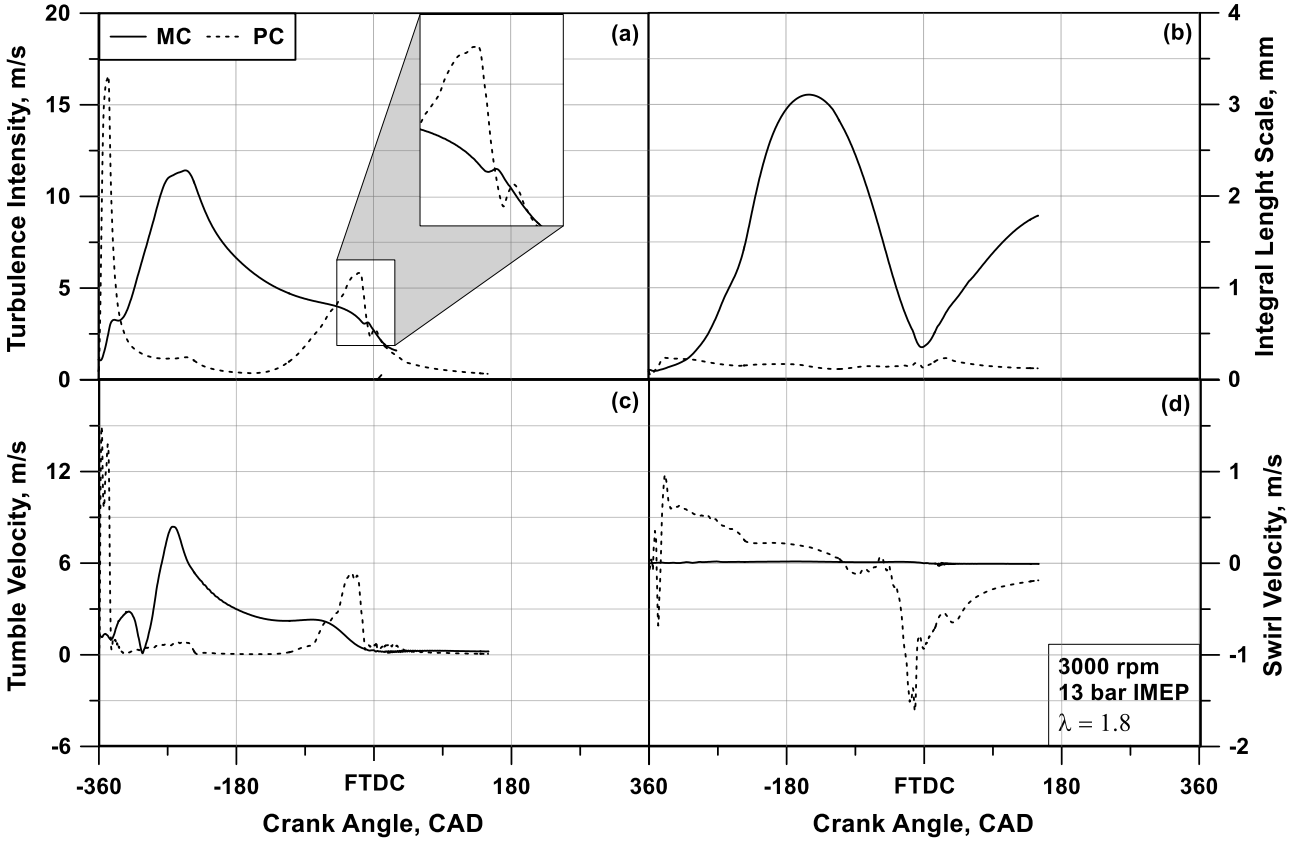

Figure 3-10 3D results of turbulence intensity(a) and integral length scale (b) in PC and MC under fired condition.

The above-described phenomena can be modelled by the following equations, which are an extension of equations presented in section 3.4.3, for a conventional SI engine:

$$\begin{cases} \dfrac{dmk}{dt} = \left(\dot{m}k\right)_{inc} - \left(\dot{m}k\right)_{out} + \dfrac{2}{3}\dfrac{\dot{\rho}}{\rho}\left(-mv_t\dfrac{\dot{\rho}}{\rho} + mk\right) + p - m\varepsilon & (I) \\ \dfrac{dmK}{dt} = \left(\dot{m}K\right)_{inc} - \left(\dot{m}K\right)_{out} - f_d\dfrac{mK}{\tau_T} + mK\dfrac{\dot{\rho}}{\rho} - P + \dot{K}_{inj} + \dot{K}_p & (II) \\ \dfrac{dmT}{dt} = \left(\dot{m}T\right)_{inc} - \left(\dot{m}T\right)_{out} - f_d\dfrac{mT}{\tau_T} + \dot{T}_{inj} + \dot{T}_p & (III) \\ \dfrac{dmS}{dt} = \left(\dot{m}S\right)_{inc} - \left(\dot{m}S\right)_{out} - f_d\dfrac{mS}{\tau_S} + \dot{S}_{inj} + \dot{S}_p & (IV) \end{cases} \tag{3.61}$$

Note that the swirl equation is considered for the PC volume, where the swirl represents the most relevant ordered motion. In the MC, the swirl equation is not solved, being all the considered engines designed to promote tumble. Compared to eqs. (3.47), the extended model presents some additional

terms. The *K* production due to the fuel injection (hence available only for an active pre-chamber) is introduced with the term $\dot{K}_{inj}$, included in the K equation.

$$\dot{K}_{inj} = \frac{1}{2}\dot{m}_{inj}\left(c_{inj}v_{inj}\right)^2 \tag{3.62}$$

The *K* production due to mass exchange between main and pre-chamber, $\dot{K}_p$ (only considered in the mass-receiving volume, either MC or PC) is estimated as:

$$\dot{K}_p = \frac{1}{2}\dot{m}_p\left(c_p v_p\right)^2 \tag{3.63}$$

where v_p is an equivalent velocity, c_p is a tuning constant, and $\dot{m}_p$ is the mass flow rate passing through the PC holes.

v_p is estimated by the following equation:

$$v_p = \frac{\dot{m}_p}{A_p \rho_p} \tag{3.64}$$

where A_p is the overall geometrical flow area of the pre-chamber holes ($A_p = n_{holes}\,\pi\, D_{hole}^2/4$) and ρ_p is the density related to the volume from which the flow comes out (either MC or PC). The flow through the valves, represented by the incoming term, is nullified in each equation of the system (3.61) if considering the pre-chamber.

The *T* and *S* productions due to the fuel injection are respectively introduced with the terms $\dot{T}_{inj}$ and $\dot{S}_{inj}$ included in the T and S equations, following the eq. (3.65) and (3.66).

$$\dot{T}_{inj} = \dot{m}_{inj}\left(r_T v_{inj}\right) \tag{3.65}$$

$$\dot{S}_{inj} = \dot{m}_{inj}\left(r_S v_{inj}\right) \tag{3.66}$$

The *T* and *S* productions due to the mass exchange between main and pre-chamber, $\dot{T}_p$ and $\dot{S}_p$ are estimated as:

$$\dot{T}_p = \dot{m}_p\left(r_T v_p\right) \tag{3.67}$$

$$\dot{S}_p = \dot{m}_p(r_S v_p) \tag{3.68}$$

The PC swirl radius is assumed equal to the geometrical radius of the pre-chamber. The PC tumble radius is assumed constant and derived from 3D outcomes. Tumble radius in MC is computed in a manner similar to the one already introduced for a conventional engine.

As already said, the integral length scale, L_t, is defined on the basis of 3D calculation (*Figure 3-10)*. Concerning the MC, L_t, is specified by a sequence of S-shaped curves, while, for the PC, it is reasonably assumed as a constant.

3.6. Knock and Heat Transfer modelling

Another main aspect to consider during the engine calibration at the test bench is the identification of the knock limited spark advance (KLSA), with the aim to avoid the occurrence of abnormal combustions. Hence, in the same way, to perform a numerical calibration, a knock model has to be coupled to the combustion one.

In 0D framework, the knock phenomenon is commonly modelled by the evaluation of the auto-ignition (AI) process within the unburned gas. A suitable description of the complex AI processes needs to manage the solution of detailed chemical kinetic schemes, involving hundreds of species and thousands of reactions [62]. The main drawback is related to the excessive CPU time. Hence, a simpler model, according to empirical formulations of auto-ignition delay [63], can be applied. The major weakness of this approach arises if boundary conditions (initial pressure and temperature) and mixture compositions (air / inert / fuel proportions) the proportions are outside the ranges considered for the correlation development. Another drawback is related to the limited ability in predicting the chemical effects generated by advanced knock suppression strategies, such as EGR or water injection. A tabulated approach [64] to evaluate the AI, based on the off-line solution of chemical reactions in a Constant-Pressure (CP) or Constant Volume (CV) reactor, proved to be a good trade-off between accuracy and complexity. This approach has been chosen and applied to perform the simulation shown in the present thesis. Particularly, the AI time, τ_{AI}, is collected in the table depending on discrete values of pressure, temperature, equivalence ratio, and residual content. Then, in the engine model, the knock event occurs when the AI integral, expressed by eq. (3.69) overcomes the unit.

$$\int \frac{dt}{\tau_{AI}} \tag{3.69}$$

Indeed, aiming at introducing a slight safety margin, a tuneable threshold level, less than unit, is introduced. As above-mentioned, the AI table can be achieved through off-line solutions of a kinetic

scheme performed by changing pressure, temperature, and air / fuel ratio of the unburned reactants in a constant pressure rector. During this work, two different kinetic schemes have been applied since, depending on the engine, different fuels have been considered. Concerning the conventional gasoline SI engines, the kinetic scheme utilized is the one developed by Andrae et al.[30] including 5 elements,138 species, and 633 reactions. Whereas the AI table for the pre-chamber engine was provided by the IFPEN Partner of the EAGLE project. This table derives from AI calculations by the scheme in [65], including 5 elements, 201 species, and 1548 reactions.

A Woschni-like correlation is here employed for the heat transfer in the pre- and main-chambers [66]. According to the standard formulation, the wall heat losses are assumed to be controlled by the pressure and temperature within the volume. An additional dependence on the mean flow velocity, derived by the above turbulence model, is introduced, which replaces the traditional dependence on the mean piston speed [66]. This allows to properly handle the heat transfer estimation within the PC, where the traditional Woschni correlation cannot be straightforwardly applied. In the case of conventional engines, the standard Woschini correlation is employed.

3.7. Combustion model tuning

The fractal model presented in this thesis, describing the combustion in a conventional SI engine, as stated above shows three tuning constants (c_{trans}, $c_{wrk,}$ and x_{wc}) required to match the experimental data with the modelled ones. Downstream of a sensitivity analysis, a proper strategy for model tuning can be drawn. The procedure aims to minimize the global speed-averaged error between the computed and experimental characteristics combustion angles. They apply when full load experimental data are available at various speeds, that is the more common case in practical experiences. Referring to the fractal model, the method is composed of three steps, listed below:

1. MFB_{10-50} error is minimized through c_{wrk} adjustments.
2. MFB_{0-10} error is controlled by c_{trans} tuning.
3. MFB_{50-90} error is minimized by a proper x_{wc} selection.

Steps 2 and 3 do not require any iteration, since c_{trans} and x_{wc} constants selectively control a unique combustion phase.

After the model extension to simulate pre-chamber engines, it is worth underlining that the tuning constants are 8 in number: indeed, the combustion model includes 3 tuning constants for each chamber. As said, they respectively act on the flame wrinkling, c_{wrk}, on the transition between an

initially-laminar and a fully-turbulent combustion, c_{trans} as well as on the combustion tail, x_{wc}. These constants have to be independently set for both PC and MC volumes, having two additional constants, namely r_{crit} and c_{jet} to control the combustion transition between the two chambers. The first, r_{crit}, triggers the MC combustion start, while the second, c_{jet}, acts on the burn rate enhancement due to the penetration of the jets into the MC. A sequential methodology is followed for their identification:

1. The 3 tuning parameters are identified for the PC, following the procedure above described for a conventional SI engine. I.e. a sequential identification of c_{trans}, $c_{wrk,}$ and x_{wc}, looking for the better agreement between numerical and experimental combustion durations of early, main and completion phases, respectively.
2. c_{trans} for the MC is imposed equal to 0, under the hypothesis that the combustion begins in a fully turbulent stage. Concerning the values of r_{crit} and c_{jet}, they are selected aiming to reproduce the combustion onset and burning speed in the main chamber at the beginning of the process.
3. c_{wrk} and x_{wc} for the MC are selected to adjust the core of the combustion process and its completion according to the procedure adopted for a conventional SI engine.

Relying on a trial-and-error procedure, a single set of tuning constants is finally found, determining the lowest average experiment / simulation error for all the investigated operating conditions, especially regarding the pressure cycles in both PC and MC.

3.8. Emission modelling

As a matter of fact, the increasing stringency of pollutant emission regulations for engines is pushing the research and development process toward advanced and complex solutions, once unpractical or too expensive. Nowadays there is still place for efficiency enhancement and emissions abatement. Facing this challenge of improvement—as the only option to ensure the future survival of the ICE—the development process of modern internal combustion engines must be as effective as possible. With the aim to achieve these improvements several technical solutions can be tested and then embedded. Considering all the available methods described in the above section, this clearly reveals that the ICE of the future is becoming very complex and it must fulfil more and more stringent emission regulations.

Hence, also concerning the reduction of pollutant emissions, the available simulation tools can offer reliable results to guide the improvement of this aspect. Indeed, once again, their application allows a cost-effective development process and a considerable reduction of the time duration of the

whole procedure, to test new technology or engine modification aimed at decreasing the emissions values.

As said, the most critical pollutants for SI engine applications are carbon monoxide, nitrogen oxides, and unburnt hydrocarbons. If the first two are mainly associated with the thermochemical states of unburnt and burnt mixtures, HC has several origins, some of them depending on geometrical features, whose contributions change substantially depending on the engine design. The model presented in the following allows estimating the above-mentioned three regulated emissions. The estimated instantaneous concentrations in the cylinder of the pollutant emissions are imposed as boundary conditions at the exhaust pipe inlet. In this way, the species are transported along the exhaust line, and pollutants are detected at the same location where the probes for pollutant measurements are placed. Further, the pollutant emissions are provided as output under the form of both concentrations and Indicated Specific (IS) or Brake Specific (BS) indices.

3.8.1. Carbon Monoxide and Nitrogen Oxides model

For the evaluation of CO and NO, a multi-zone approach is applied to mimic the burned gas temperature stratification. In this framework, each burned parcel is compressed / expanded adiabatically according to the in-cylinder pressure. The local zone temperatures are used in the well-known extended Zel'dovich mechanism for the evaluation of the NO kinetics [67], whereas the CO is computed with a two-step reaction scheme [68]. The experimental findings show that in ultra-lean engines, the nitric emissions are mainly composed of NO_2. For this reason, in the adopted approach, the NO production derived by the Zel'dovich mechanism is assumed to completely oxidize into NO_2 when the burned gases evolve along the exhaust pipes.

Concerning the NOx emissions, as said, they are mostly represented by NO and NO_2 species, result from out-of-equilibrium chemical processes controlled by the kinetics of relevant reactions. For a conventional stoichiometric SI engine, NO_2 emission is usually smaller than NO one (this last, on average, estimated as 98% of the total). Hence, for these ICEs, the only NO formation will be detailed since its concentration is enough to obtain reliable estimations of global NOx emissions. It is well known that four paths leading to NO formation are commonly considered, namely thermal NO, prompt NO, nitrous NO, and fuel NO paths. As known, the thermal NO path is the most important source for ICE, depending on the high temperature oxidation of atmosphere-N_2. This process is described by the extended Zel'dovich chemical mechanism [67], describing NO formation around stoichiometry. This mechanism is based on a set of three reversible equations:

$$\begin{cases} N_2 + O \rightarrow NO + N & (I) \\ N + O_2 \rightarrow NO + O & (II) \\ N + OH \rightarrow NO + H & (III) \end{cases} \tag{3.70}$$

This system is solved using the kinetic constants k_i of the different equations i, with indexes + for the forward direction and – for the backward one.

The overall evolution of NO concentration is then estimated as:

$$\frac{d[NO]}{dt} = k_1^+[O][N_2] + k_2^+[N][O_2] + k_3^+[N][OH] - k_1^-[NO][N] - k_2^-[NO][O] - k_3^-[NO][H] \tag{3.71}$$

where [ ] denotes species concentrations in moles per cubic centimetre, and k_i values are reported in *Table 3.7*. The forward rate constant for reaction (I) in eq. (3.71) and the reverse rate constants for reactions (II) and (III) have large activation energies, which result in a strong temperature dependence of NO formation rates.

Table 3.7 Rate constants for the extended Zel'dovich NO formation mechanism.

Coefficients	*Value [cm^3/mol/s]*	*Temperature range [K]*
k_1^+	$7.6 \cdot 10^{13} exp(-38000/T)$	$2000 - 5000$
k_2^+	$1.6 \cdot 10^{13}$	$300 - 5000$
k_3^+	$6.4 \cdot 10^{9} T_b exp(-3150/T)$	$300 - 3000$
k_1^-	$1.5 \cdot 10^{9} T_b exp(-19500/T)$	$1000 - 3000$
k_2^-	$4.1 \cdot 10^{13}$	$300 - 2500$
k_3^-	$2.0 \cdot 10^{14} T_b exp(-23650/T)$	$2200 - 4500$

The experimental findings showed that in ultra-lean engines, the nitric emissions are mainly composed of NO_2. For this reason, in the adopted approach, the NO production derived by the Zel'dovich mechanism is assumed to completely oxidize into NO_2 when the burned gases evolve along the exhaust pipes. Hence, emission indices ($ISNO_x$ and $BSNO_x$) in the case of ultra-lean operations are computed based on the above assumption.

Concerning the carbon monoxide emission modeling, the process is kinetically controlled, as well as NO formation. In a premixed hydrocarbon-air flame, the CO concentration in the flame zone rapidly rises to a maximum value, larger than the equilibrium value for adiabatic combustion of the fuel-air mixture. The principal CO oxidation reactions in hydrocarbon-air flames are:

$$\begin{cases} CO + OH \leftrightarrow CO_2 + H & (I) \\ CO_2 + O \leftrightarrow CO + O_2 & (II) \end{cases} \tag{3.72}$$

As said, CO concentration increases rapidly in the flame front zone, mainly produced by thermal decomposition of partially oxidized HC compounds. The partial CO is then oxidized to CO_2 through a kinetic controlled mechanism. The rate of CO formation is then given by:

$$\frac{d[CO]}{dt} = k_1^-[CO_2][H] - k_1^+[CO][OH] + k_2^+[CO_2][O] - k_2^-[CO][O_2] \tag{3.73}$$

Once again, [ ] are the species concentration in moles per cubic centimetre, k_i rate constants, and + is forward, - is backward. Parameters in brackets refer to combustion products concentration. If O, O_2, OH, H and CO_2 are in equilibrium state, the CO formation rate can be expressed as:

$$\frac{d[CO]}{dt} = (R_1 + R_2)\left(1 - \frac{[CO]}{[CO]_{eq}}\right) \tag{3.74}$$

$[\,]_{eq}$ represents equilibrium concentration, and the variables R_1 and R_2 are defined as:

$$\begin{cases} R_1 = k_1^+[CO]_{eq}[OH]_{eq} = k_1^-[CO_2]_{eq}[H]_{eq} \\ R_2 = k_1^+[CO_2]_{eq}[O]_{eq} = k_2^-[CO]_{eq}[O_2]_{eq} \end{cases} \tag{3.75}$$

Only two values of k_i are needed among the four constants in eq. (3.75) for R_1 and R_2 determination, and here are taken from a detailed chemical kinetic mechanism developed by Lawrence Livermore National Laboratory [69] The constants here selected are k_1^+ and k_2^- whose values are shown *Table 3.8*.

Table 3.8 Rate constants for the CO formation mechanism.

Coefficients	*Value [cm³/mol/s]*
k_1^+	$2.23 \cdot 10^5 T_b exp(582.723/T)$
k_2^-	$1.05 \cdot 10^{12} exp(-21406.96/T)$

Summarizing, this CO model here adopted is a simple empirical model based on equilibrium concentrations. The equilibrium concentration is good enough to define the value of species only when the temperature is high (during the combustion process). However, at a lower temperature, during the late expansion stroke, the equilibrium is not an accurate solution anymore, and the full kinetic model is needed for a better model accuracy.

As introduced at the beginning of this section, a multi-zone approach is employed for both NO_x and CO emissions estimation. The multi-zone approach is below briefly summarized. At each crank angle, the combustion chamber volume is subdivided in *i* number of zones, $\forall\, i$ = 1, n-zones. The zones progressively form during the combustion evolution. At an intermediate time during the combustion development, assume the *n-zone* as the zone just formed in the last time step. At this stage, the enthalpy is imposed equal to the unburned gas (before the combustion). This assumption allows to estimate the *n-zone* temperature, named $T_{b0,n}$, at the equilibrium imposing a pressure equal to the cylinder one, $p_{0,n}$. The numerical algorithm, at each crank angle, saves as initialization values, $T_{b0,n,}$ and $p_{0,n}$ for the *n-zone*. The same occurred for the other zones (i = 1, (n-zones)-1) in the previous time steps. The temperature of all the other zones is updated on the hypothesis of the adiabatic and isentropic transformation.

$$T_{b,i} = T_{b0,i}\left(\frac{p}{p_{0,i}}\right)^{\frac{k-1}{k}} \tag{3.76}$$

These updated temperatures are passed to NOx and CO models to evaluate the pollutant concentration variations in each zone This is repeated until the exhaust valve opens.

3.8.2. Unburned Hydrocarbon model

As know, the mechanisms of uHC production in SI, dual fuel, or pre-chamber engines are similar, being the result of the partial escape of some fuel from the regular flame propagation. Among those mechanisms, the most relevant ones are the filling / emptying of the crevice volumes, the flame quenching and the wall quenching, the adsorption / desorption from oil layer and from deposits, and the exhaust valve leakage.

Regardless of the source, the uHC released behind the flame front or at the end of the combustion process, are subjected to post-oxidation. This drastically decreases the uHC concentration at the exhaust phase, impacting to an additional production of heat. The post-oxidation may continue along the exhaust valves and along the exhaust ducts, but usually those effects are less intense. Further, this phenomenon highly depends on the available residual oxygen and on the temperature level and typically allows to abate the uHC concentration from 40% up to 70%.

In the current literature, several works describe the uHC mechanisms formation from both experimental and numerical perspectives. Concerning piston top land crevices, in [70] a physical model to describe the mass fluxes between the ring pack and the cylinder is presented. While in [71], [72], [73], [75] the influence of the ring pack geometry on the uHC production is experimentally examined. The flame wall quenching phenomenon has been deepened in specific studies [76],

proposing empirical or theoretical correlations to estimate the quenching distance. Hence, simplified approaches illustrating the fuel adsorption / desorption from the oil layer were proposed in [77], [78]. Further, a recent study analyses the uHC formation using 3D simulations, as for instance [79].

The superimposition of the several mechanisms contributing to the uHC emission makes a very challenging task the development of a phenomenological 0D model to predict engine-out emissions. Some phenomenological models were proposed in literature, exclusively describing one or two of the mechanisms above listed. As an example, in [80], the crevices and oil adsorption / desorption are studied. A more extensive approach was proposed in [81], adding to the above mechanisms the flame quenching. However, since only stoichiometric operations were tested, the consistency of the flame quenching model was not directly investigated, indeed none of the available phenomenological models have been validated and tested under lean or ultra-lean combustion, being conditions where both uHC from crevices and from flame quenching have a comparable weight.

As said, the uHC formation depends on various sources, but in the proposed model, the ones explicitly considered are piston-ring pack crevices, wall quenching, and oil absorption / desorption from oil film layers. It is worth underlining that this last contribution, considering engines fuelled with natural gas, provides a negligible contribution due to its solubility.

The entire uHC formation process can be schematized in some main steps: firstly, the creation of unburned hydrocarbon from the above sources; then, the oxidation, inside the cylinder, of a fraction of uHC, after their mixing with the hot bulk gases; finally, the flowing out, from the cylinder to the exhaust, of the residual uHC and the mixing of contributions from the different cylinders. In the following, the three different formation model will be described together with simulation of the post oxidation and of transport along exhaust pipes ones.

Crevices

It is well known that the largest source of uHC emissions is the crevices volume located between liner, piston, and top piston ring. Further, some gas flows out of these regions, through the ring gaps and into the crankcase (blowby).

During the compression stroke, in-cylinder pressure increases, cylinder volume decreases, while the unburned mixture is forced into each crevice region. These volumes, because of their thinness, present a large surface / volume ratio. The fuel-air mixture flowing into the crevices reduces its temperature due to the wall heat losses. During combustion, while the pressure continues to rise, the unburned mixture still flows into the crevice volume. Once the cylinder pressure starts to fall down, gas flows back from each crevice into the cylinder. This qualitative description applies for a conventional homogeneous charge engine, ignited by a conventional spark plug, but is also suitable for a dual fuel engine for which pure unburned gas is assumed to fill the crevices during the

compression phase. While considering a pre-chamber engine, a different behaviour might be expected, namely that the turbulent hot jets ejected from the pre-chamber push burned gas into the crevice volumes, instead of pure unburned gas. This is simulated imposing that a mixture of unburned / burned mixture enters the ring pack volume, whose composition follows the instantaneous in-cylinder fuel burned fraction. Further, two of the large-bore engine subjects of study in the following, are characterized by the presence of the anti-polishing ring (APR) (see *Figure 3-11*) that subtracts volume around the TDC to the top land crevice, affecting its filling / emptying process.

In the developed model, the storage of gas mixture and the corresponding mass flow into and out of the piston top land crevice is evaluated applying the equation of state for ideal gases as:

$$p_{tl} \cdot V_{tl} = m_{tl} \cdot R \cdot T_{tl} \tag{3.77}$$

where p_{tl} is imposed equal to the cylinder pressure, R is the specific gas constant, T_{tl} is the temperature in top land crevices, assumed equal to the piston one, and V_{tl} is the top land crevices volume. One of the main features of the here proposed model is related to the V_{tl} specification. Indeed, differently from other simplified models, top land crevices volume is not constant during the engine cycle, but computed in real-time, according to the dynamics of the ring pack and to the volume eventually subtracted by the APR. Likewise, the instantaneous volumes of second and third lands are estimated, depending on the positions of first, second, and oil rings. For this purpose, a detailed schematization of the ring pack geometry is needed together with the estimation of the pressures in all lands and grooves of the ring pack, and with the computation of ring dynamics. It is worth to underline that, if the detailed ring pack geometry is not available, the crevices volume can be imposed in the developed model as a percentage of the total combustion chamber volume, using values from literature [68] of around 1-3%.

Starting the description from the geometrical model, all the details depicted in *Figure 3-11(a)* are considered. More precisely, axial and radial dimensions of all the lands and grooves are needed as an input in the geometrical schematization. Further, the flow model discussed below is solved by subdividing the ring pack volumes according to the representation in *Figure 3-11(a),* where the lands are identified by a purple filling (top land, second land, and third land), while the grooves (top, second and third lands) in pink. Further, the model considers the ring main characteristics, namely width, radial wall thickness, and gap (*Figure 3-12*). The piston geometrical schematization also includes the inclined face at its top and, as above-mentioned, the volume subtraction to the top land because of the APR presence.

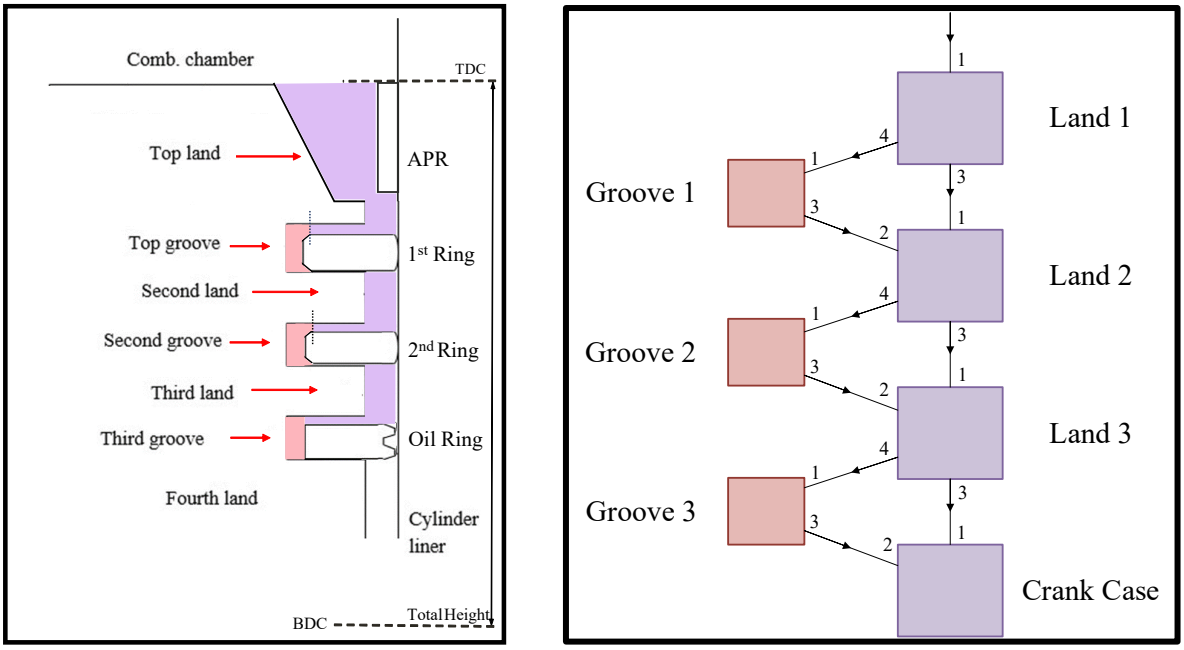

Figure 3-11 (a) Schematic of piston, cylinder liner, ring pack, and anti-polishing ring; (b) ring pack flow model schematic.

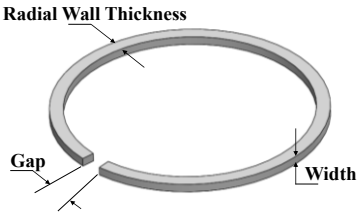

Figure 3-12 Ring dimensions.

As already mentioned, the pressure in the top land is assumed equal to the one in the cylinder, while the ones in the second and third land, and in the grooves, are evaluated through dedicated mass balances, coupled to the assumption of gas temperature equal to the piston one. The flow model is shown in *Figure 3-11(b)*, where the boxes represent the lands and grooves of the ring pack. Note that the same convention of the filling colour as *Figure 3-12* is borrowed in *Figure 3-11(b)*. The arrows in *Figure 3-11(b)* represent a mass flux exchanged between two volumes. The vertical arrows are fluxes passing through the ring gap, while the diagonal ones are fluxes through the clearances besides the rings. The first vertical arrow on the top of the scheme is the connection between the combustion chamber and the top land, while the links on the bottom, connect the third land and groove to the crank case. The pressure in the crank case is assumed constant and equal to the ambient one.

It is worth noting that, although the ring gap is functional to the mounting operation and to ensure a radial force toward the cylinder liner, it becomes the main escape route for the gas. Further, to account for thermal expansion and groove distortion, the ring axial width is smaller than the respective groove height. This leads to the presence of a clearance responsible for an additional escape route for the gas when the rings are in motion. As already mentioned, both are considered in this

model, estimating the flow through the ring gap and through the clearance through the nozzle flow equation, based on the compressible flow hypothesis. The discharge coefficient is calculated according to the correlation in [82]:

$$c_d = 0.85 - 0.25\left(\frac{p_d}{p_u}\right)^2 \tag{3.78}$$

where p_d is the pressure downstream the gap / clearance, while p_u is the one upstream. The passage areas, as well as the related clearances volumes, are estimated in real-time since their values depend on the current ring position.

As already said, the geometrical schematization above described is coupled with a simplified ring dynamics model. Even if into the groove each ring has three degrees of freedom, axial, radial, and toroidal (torsion around its central axis) motions, the here proposed simplified model assumes the ring as a rigid body (no component deformation) and considers only the ring dynamics along the cylinder axial direction. This is described by the equilibrium force equation (Newton second law) [83]:

$$m_{ring}\frac{d^2x}{dt^2} = F_p - F_i - F_f \tag{3.79}$$

where m_{ring} is the ring mass, x is the ring position (relative to the piston), F_p is the gas pressure force in axial direction, F_i is the inertia force and F_f is the oil friction force. The force equilibrium is expressed in a non-inertial reference frame, jointed to the piston. F_p is computed according to the pressure difference between top and bottom faces of the ring.

Flame wall quenching

Concerning the wall quenching, this mechanism is responsible for uHC formation due to the flame extinction occurring at the walls of the combustion chamber. Due to the lower wall temperature, once the flame reaches the farthest regions from the combustion chamber core, it extinguishes. When the flame quenches, it leaves a thin layer or volume of unburned mixture ahead of the flame. In the following, a simplified model is presented to physically describe the above-mentioned phenomena. Firstly, the combustion chamber is geometrically schematized as a cylinder with a centred spark plug to estimate the quenched volume. Then, the combustion chamber walls are subdivided into three zones (*Figure 3-13*): cylinder head, cylinder liner, and piston crown. Each zone is characterized by its own temperature. The wall areas entering in contact with the flame front are evaluated in real-time, starting from the burned gas volume and assuming a spherical flame propagation and a cylindrical combustion chamber [84].

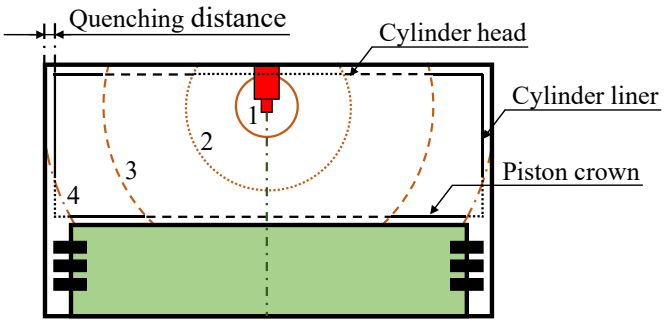

Figure 3-13 Combustion chamber areas schematization.

Considering three different instants during the flame propagation, representative flame configurations are depicted in *Figure 3-13*. In the first stage, the flame has no contact with the cylinder walls (1); then, expanding, part of the front licks the cylinder head extinguishing near the wall (2). Thereafter, it grows getting in contact with the piston crown (3) and the cylinder liner (4). The combustion chamber wall areas i, namely head, liner, and piston ones, licked by the flame front in a time step, multiplied by quenching distances, $\delta_{q,i}$, return the quenched volume variation.

$$dv_{q,i} = dA_{q,i} \cdot \delta_{q,i} \tag{3.80}$$

The estimation of the quenching distance arises from the Peclet number (Pe_q) definition:

$$Pe_q = \frac{\delta_q}{\delta_{fl}} \tag{3.81}$$

where it is related to the diffusive flame thickness δ_{fl}:

$$\delta_{fl} = \frac{\bar{\lambda}}{\rho_u \bar{c}_p S_L} \tag{3.82}$$

where ρ_u is the unburned gas density, S_L is the laminar flame speed. This last is computed by the empirical correlation described in section 3.4.1 The thermal conductivity $\bar{\lambda}$ and the specific heat capacity $\bar{c}_p$ are estimated at a representative temperature between the adiabatic flame temperature and the wall temperature:

$$\bar{T}_{wq} = \frac{T_w + T_f}{2} \tag{3.83}$$

The wall temperature T_w is adjusted according to the region touched by the flame front, among head, liner, or piston. To quantify and assess the flame–wall interactions, the wall heat flux in the

moment of quenching $\dot{Q}_{W,q}$ can be normalized by the heat release rate of an undisturbed flame $\dot{Q}_{\Sigma}$, to achieve the normalized wall heat flux φ_q:

$$\varphi_q = \frac{\dot{Q}_{W,q}}{\dot{Q}_{\Sigma}} = \frac{\dot{Q}_{W,q}}{\rho_u \bar{c}_p S_L (T_b - T_u)} \tag{3.84}$$

The Peclet number Pe_q and the normalized wall heat flux φ_q are inversely related. Boust et al. [76], [85], [86] proposed the following expression:

$$Pe_q = \frac{(T_b - T_W)}{(T_b - T_u)} \cdot \left(\frac{c_q}{\varphi_q} - 1 \right) \tag{3.85}$$

In this model, the normalized wall heat flux φ_q is assumed is assumed equal to 0.3, which was advised for a laminar head-on quenching at ambient conditions [79]. The tuning constant, c_q, is introduced in the original formulation, allowing to correct the inaccuracies of the correlation. Quenching distances $\delta_{q,i}$, and wetted area, $dA_{q,i}$, are combined with the gas density to derive the infinitesimal quenched mass in a time step:

$$dm_q = \sum dV_{q,i} \cdot \rho_{q,i} \tag{3.86}$$

where, once again, the density is calculated at the cylinder pressure and at a representative temperature expressed by eq. (3.76). Thus, the quenched mass, dm_q, is determined and integrated during the engine cycle to derive the contribution from quenching to uHC production.

Oil layer

The modelling of uHCs formation mechanism from oil layer assumes the equilibrium absorption / desorption of the vaporized fuel into this layer, considering mass diffusion resistance in the liquid (oil film) and in the gas phases. The concentration variation of dissolved fuel in the oil film can be evaluated by Fick's second law [68]. In the absorption / desorption process the mass transfer is determined by Henry's law, describing the interface condition between the gas and liquid phases as:

$$k_H \cdot X_{fuel,oil} = p \cdot X_{fuel,oil} \tag{3.87}$$

where X is the fuel concentrations and p is the in-cylinder pressure.

In the model, the concentration of fuel varies in the different phases, passing from the bulk gas state (G) to the oil film (F). The mass flux $\dot{m}''_{fuel,oil}$ at the interface between the above phases can be computed as:

$$\dot{m}"_{fuel,oil} = \frac{g^*_{gas} \cdot g^*_{fluid}}{N_H \cdot g^*_{gas} + g^*_{fluid}} \cdot \left(m_{f_G} - m_{f_F} \cdot N_H\right) \tag{3.88}$$

where N_H is the Henry number, g^*_{gas} is the gas phase mass transfer conductance, while g^*_{fluid} is the liquid phase one. m_{fG} is mass concentrations of vapor fuel diluted in the bulk gas state (G) and m_{fF} is mass concentrations of dissolved fuel in the bulk of the oil film (F). This equation is positive during the absorption of fuel vapor into the oil film, changing its sign when desorption starts. The fuel mass flow rate is obtained by multiplying $\dot{m}"_{fuel,oil}$ by the value of the surface area of the oil layer in contact with the gas mixture. This area is estimated in real-time considering the piston movement.

Boundary layer model

The introduction of the boundary layer arises from the need for suitable representative conditions of temperature and concentrations for the post-oxidation rate estimation. The presented approach should impose more consistent conditions at which the oxidation process occurs if compared to the conventional methods [87],[88],[89], where an average between wall and cylinder gas temperature is fixed, and the concentrations of the species are referred to the entire cylinder volume.

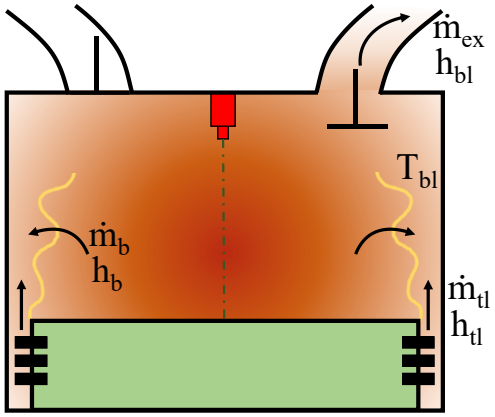

Figure 3-14 Boundary layer areas schematization.

The boundary layer (BL) states are determined separately for the post-oxidation of uHC from crevices, from wall quenching, and from oil layer, but adopting the same mathematical approach. Concerning the uHC source from crevices, the boundary layer can be identified as a volume close to the cylinder wall storing the mass arriving from crevices during the expansion phase, where the released mass combines with a portion of burned hot gas, from the bulk region of the cylinder. A scavenged mass is also considered during the exhaust phase. The schematization of the boundary layer contributions is reported in *Figure 3-14*.

The temperature and volume of the boundary layer are computed, crack angle based, solving dedicated mass and energy balances. The mass balance is expressed as:

$$\frac{dm_{bl}}{dt} = \dot{m}_{tl} + \dot{m}_b - m_{bl} \cdot \frac{\dot{m}_{ex}}{m_{cyl}} \tag{3.89}$$

$$\dot{m}_b = k_{oxid} \cdot \dot{m}_{tl} \tag{3.90}$$

where m_{bl} is the boundary layer mass, $\dot{m}_{tl}$ the mass flow arising from the top land crevice, $\dot{m}_b$ is the burned gas mass, $\dot{m}_{ex}$ the one that flows through the exhaust valve, and m_{cyl} the total mass inside the cylinder. The second term in eq. (3.89), expressed in eq. (3.90), describes the flow of burned gas coming from the bulk region of the cylinder, weighted by the tuning constant k_{oxid} and assumed proportional to the mass flow coming from crevices. The energy balance is written as:

$$\frac{d(m_{bl} \cdot e_{bl})}{dt} = \dot{m}_{tl} \cdot h_{tl} + \dot{m}_b \cdot h_b - m_{bl} \cdot \frac{\dot{m}_{ex}}{m_{cyl}} \cdot h_{bl} - \frac{p \cdot dV_{bl}}{dt} \tag{3.91}$$

where e_{bl} is the boundary layer internal energy, V_{bl} is its volume, p the pressure in the cylinder, and h_{tl}, h_b, and h_{bl} are the enthalpies of top land crevices, burned gas, and boundary layer, respectively.

As said, the boundary layer state computation for the uHCs produced by flame quenching and absorption / desorption from oil are realized in a manner similar to the ones from crevices. Considering the flame quenching, the only difference consists of the production terms in equations (3.89) and (3.91) due to the top land flow, which is substituted by the mass variation expressed by eq. (3.86). The choice to differentiate the boundary layer computation between the above contributions arises from the will to distinguish the conditions at which the post-oxidations occurs, since uHC from quenching are expected to be released in an early stage, when the in-cylinder pressure and temperature are increasing, while the uHC contribution from crevices mainly arises in a subsequent stage, when the piston moves down, and in-cylinder pressure and temperatures are decreasing. Instead, the oxidation of uHC released from oil layer can be assumed negligible, since the release occurs usually during the second half of the exhaust stroke, when temperatures are very reduced for oxidation progression.

Post-Oxidation modeling

During and after the end of the combustion, the uHCs contributions are subjected to an oxidation process with residual oxygen. As known, in addition to the oxygen and fuel amounts, the temperature has a relevant impact on the oxidation rate. This process is described through a detailed reaction kinetics only in few works [90],[91]. For sake of simplicity and to limit the computational burden, a simplified method is here employed. It deals with a one-step kinetics approach, adapting an Arrhenius-like equation [92]:

$$\frac{d[HC]}{dt} = -A \cdot T^{\beta} \cdot e^{\left(-\frac{Ea}{RT}\right)}[HC]^{a}[O_2]^{b} \tag{3.92}$$

where R is the gas constant, T is the post-oxidation temperature, and [HC] and [O_2] are the concentrations of fuel and residual oxygen, A is a pre-exponential factor and E_a is the activation energy of the reaction. In particular, the parameters A, E_a, a, and b and β are fitted depending on the fuel. Depending on the fuel, the values of A, E_a, a, and b and β are selected: in the case of gasoline, the values of the constants are derived from [93], which refer to the iso-octane, while in the case of natural gas the values proposed in [94] are adopted, which refers to pure methane (see *Table 3.9*).

Table 3.9 Reaction rate parameters for iso-octane / air and methane / air mixtures.

	A (cm^3/mol)	$\mathbf{E_a}$ (kcal/mol)	**a** (-)	**b** (-)	**β** (-)
Isoctane	$4.6 \cdot 10^{12}$	63.8	0.02	1.2	0.3
Methane	$1.3 \cdot 10^{13}$	48.4	0.7	0.8	0

Transport of pollutant along exhaust line

Once assessed the formation of pollutant emission, both NOx, CO and uHC, within the cylinder, the model further allows to transport those species along the exhaust pipes. The pollutant concentrations in the cylinder are imposed as a boundary condition of the 1D flow model of the exhaust pipes. Thus, the effects of flow interactions and concentration inhomogeneity among the cylinders are considered, especially once they are not perfectly in balance each other. Moreover, the possibility of fuel short-circuiting is also considered in the case of exhaust / intake valve overlap, which contributes to increasing uHC engine-out emission.

References

[1] De Nola, F., Giardiello, G., Gimelli, A., Molteni, A. and Muccillo, M., "Definition of a Methodology Promoting the Use of 1D Thermo-Fluid Dynamic Analysis for the Reduction of the Experimental Effort in Engine Base Calibration," SAE Technical Paper, 2019-24-0013, 2019, doi:10.4271/2019-24-0013.

[2] Boretti, A. Scalzo, J., "Exploring the Advantages of Variable Compression Ratio in Internal Combustion Engines by Using Engine Performance Simulations," SAE Technical Paper 2011-01-0364, 2011, doi:10.4271/2011-01-0364.

[3] Woschni, G. "A universally applicable equation for the instantaneous heat transfer coefficient in the internal combustion engine," SAE Technical Paper, 670931, 1967, doi:10.4271/670931.

[4] Hohenberg, G., "Advanced Approaches for Heat Transfer Calculations," SAE Technical Paper 790825, 1979, doi: 10.4271/790825.

[5] Thermodynamics and Fluid Mechanics Group, & Annand, W., "Heat transfer in the cylinders of reciprocating internal combustion engines," Proceedings of the Institution of Mechanical Engineers, 177(1), 973-996,1963, doi: 10.1243/PIME_PROC_1963_177_069_02.

[6] Demesoukas, S., Caillol, C., Higelin, P., Boiarciuc, "Zero-Dimensional Spark Ignition Combustion Modeling-A Comparison of Different Approaches", SAE Technical Paper, 2013-24-0022, 2013, doi:10.4271/2013-24-0022.

[7] Richard, S., Bougrine, S., Font, G., Lafossas, F.A., Le Berr, F., "On the Reduction of a 3D CFD Combustion Model to Build a Physical 0D Model for Simulating Heat Release, Knock and Pollutants in SI Engines", Oil & Gas Science and Technology 64(3):223-242, 2009, doi:10.2516/ogst/2008055.

[8] Matthews, R., D., Chin, Y., W., "A Fractal-Based SI Engine Model: Comparisons of Predictions with Experimental Data", SAE Paper 910075, 1991, doi:10.4271/910079.

[9] Perlman, C., Frojd, K., Seidel, L., Tuner, M. et al., "A Fast Tool for Predictive IC Engine In-Cylinder Modelling with Detailed Chemistry", SAE Technical Paper 2012-01-1074, 2012, doi:10.4271/2012-01-1074.

[10] Rakopoulos, C., D., Michos, C., N., Giakoumis, E., G., "Thermodynamic analysis of SI engine operation on variable composition biogas-hydrogen blends using a quasi-dimensional, multi-zone combustion model", SAE Int. J. Engines 2(1):880-910, 2009, doi:10.4271/2009-01-0931.

[11] Verhelst, S., Sheppard, C., G., W., "Multi-zone thermodynamic modelling of spark-ignition engine combustion–an overview", Energy Conversion and management 50(5): 1326-1335, 2009, doi: 10.1016/j.enconman.2009.01.002.

[12] Franke, C., Wirth, A., Peters, N., "New Aspects of the Fractal Behaviour of Turbulent Flames," 23 Symp. (Int.) on Combustion, Orleans, 1990.

[13] De Bellis, V., Severi, E., Fontanesi, S., Bozza, F., "Hierarchical 1D/3D approach for the development of a turbulent combustion model applied to a VVA turbocharged engine. Part II: Combustion model." Energy Procedia 45: 1027-1036, 2014, doi: 10.1016/j.egypro.2014.01.108.

[14] De Bellis, V., Bozza, F. and Tufano, D., "A Comparison Between Two Phenomenological Combustion Models Applied to Different SI Engines," SAE Technical Paper, 2017-01-2184, 2017, doi:10.4271/2017-01-2184.

[15] Gouldin, F., "An application of Fractals to Modeling Premixed Turbulent Flames", Combustion and Flame 68(3):249-266, 1987, doi:10.1016/0010-2180(87)90003-4.

[16] Gatowsky, J., A., Heywood, J., B., "Flame Photographs in a Spark-Ignition Engine", Combustion and Flame 56:71-81, 1984.

[17] Bates, C., S., "Flame Imaging Studies of Combustion Completion in a SI Four-Stroke Engine", TvU Thoughtventions Unlimited LLC, http://www.tvu.com/.

[18] North, G., L., Santavicca, D., A., "The fractal nature of premixed turbulent flames", Combustion Science and Technology 72(4-6): 215-232, 1990, doi: 10.1080/00102209008951648.

[19] Peters, N., "Laminar flamelet concepts in turbulent combustion", Symposium (International) on Combustion 21(1): 1231-1250, 1988, doi: 10.1016/S0082-0784(88)80355-2.

[20] Metghalchi, M., Keck, J., C., "Burning velocities of mixtures of air with methanol, isooctane, and indolene at high pressure and temperature", *Combustion and flame*, 48:191-210, 1982, doi: 10.1016/0010-2180(82)90127-4.

[21] Rhodes, D. B., Keck, J. C. "Laminar burning speed measurements of indolene-air-diluent mixtures at high pressures and temperatures," SAE Technical Paper, 850047, 1985.

[22] Hara, T., Tanoue, K. "Laminar flame speed of ethanol, n-heptane, iso-octane air mixtures, "JSAE paper, 20068518, 2006.

[23] Liao, S., Y., Jiang, D., M., Cheng, Q., "Determination of laminar burning velocities for natural gas", *Fuel*, 83(9): 1247-1250, 2004, doi: 10.1016/j.fuel.2003.12.001.

[24] D. Bradley, R.A. Hicks, R.A. Lawes, C. Sheppard, R. Wolley, "The Measurement of Laminar Burning Velocities and Markstein Numbers for Iso-octane–Air and Iso-octane–nHeptane–Air Mixtures at Elevated Temperatures and Pressures in an Explosion Bomb", *Combust. Flame,* 115, 126–144, 1998, doi: 10.1016/S0010-2180(97)00349-0.

[25] Gülder, Ö. L. "Correlations of laminar combustion data for alternative SI engine fuels," SAE Technical Paper, 841000, 1984, doi: 10.4271/841000.

[26] Bougrine, S., Richard, S., Nicolle, A., Veynante, D. "Numerical study of laminar flame properties of diluted methane-hydrogen-air flames at high pressure and temperature using detailed chemistry," *International journal of hydrogen energy* 36(18), 12035-12047, 2011, doi: 10.1016/j.ijhydene.2011.06.053.

[27] Hann, S., Grill, M., & Bargende, M. "Reaction Kinetics Calculations and Modeling of the Laminar Flame Speeds of Gasoline Fuels," SAE Technical Paper, 2018-01-0857, 2018, doi:10.4271/2018-01-0857.

[28] Tanaka, S., Ayala, F., Keck, J.C., "A reduced chemical kinetic model for HCCI combustion of primary reference fuels in a rapid compression machine", *Combustion and Flame* 133(4): 467-481, 2003, doi: 10.1016/S0010-2180(03)00057-9.

[29] Liu, Y., Jia, M., Xie, M., Pang, B., "Development of a New Skeletal Chemical Kinetic Model of Toluene Reference Fuel with Application to Gasoline Surrogate Fuels for Computational Fluid Dynamics Engine Simulation", *Energy Fuels* 27(8):4899–4909, 2013, doi: 10.1021/ef4009955.

[30] Andrae, J., "Comprehensive chemical kinetic modeling of toluene reference fuels oxidation", Fuel 2013; 107:740-748, doi: 10.1016/j.fuel.2013.01.070.

[31] De Bellis, V., Malfi, E., Teodosio, L., Giannattasio, P., Di Lenarda, F., "Novel Laminar Flame Speed Correlation for the Refinement of the Flame Front Description in a Phenomenological Combustion Model for Spark-Ignition Engines", *SAE International Journal of Engines*, 12(3): 251-270, 2019, doi: 10.4271/03-12-03-0018.

[32] Morgan, N., Smallbone, A., Bhave, A., Kraft, M., Cracknell, R., Kalghatgi, G., "Mapping surrogate gasoline compositions into RON/MON space", *Combustion and Flame* 157(6): 1122–1131, 2010, doi: 10.1016/j.combustflame.2010.02.003.

[33] Andrae, J., C., G., Brinck, T., Kalghatgi, G., T., "HCCI experiments with toluene reference fuels modeled by a semidetailed chemical kinetic model", *Combust. Flame* 155(4):696–712, 2008, doi: 10.1016/j.combustflame.2008.05.010.

[34] Iafrate, N., Matrat, M., Zaccardi, J-M, "Numerical investigations on hydrogen-enhanced combustion in ultra-lean gasoline spark-ignition engines," *International Journal of Engine Research*. August 2019. doi:10.1177/1468087419870688.

[35] Manual, GT-Power User'S. "GT-Suite version 2020" Gamma Technologies Inc (2020).

[36] Wu, C., K., Law, C., K., "On the determination of laminar flame speed from stretched flames", *Twentieth Symposium (International) on Combustion*, 20(1): 1941-1949, 1985, doi: 10.1016/S0082-0784(85)80693-7.

[37] de Goey, L., P., H., ten Thije Boonkkamp, J., H., M., "A flamelet description of premixed laminar flames and the relation with flame stretch", *Combustion and Flame* 119(3): 253-271, 1999, doi: 10.1016/S0010-2180(99)00052-8.

[38] Markstein G., Nonsteady Flame Propagation, (McMillan Publication, New York, 1964).

[39] Karlovitz, B., Denniston Jr., D. W., Knapschaefer, D. H., Wells, F. E., in Fourth Symposium (International) on Combustion, The Combustion Institute, Pittsburgh, 1953, pp. 613–620.

[40] M. Matalon, C. Cui, J. K. Bechtold, "Hydrodynamic theory of premixed flames: effects of stoichiometry, variable transport coefficients and arbitrary reaction orders", *J. Fluid Mech*. 487: 179–210, 2003, doi: 10.1017/S0022112003004683.

[41] Giannakopoulos, G.K., Gatzoulis, A., Frouzakis, C.E., Matalon, M., Tomboulides, A.G., "Consistent definitions of "Flame Displacement Speed" and "Markstein Length" for premixed flame propagation", *Combustion and Flame* 162(4): 1249-1264, 2015, doi: 10.1016/j.combustflame.2014.10.015.

[42] Chen, J.H., Im, H.G., "Correlation of flame speed with stretch in turbulent premixed methane/air flames", *Symposium (International) on Combustion* 27(1):819-826, 1998, doi: 10.1016/S0082-0784(98)80477-3.

[43] Bozza, F., De Bellis, V., Berni, F., D'Adamo, A. Maresca, L., "Refinement of a 0D turbulence model to predict tumble and turbulent intensity in SI engines. Part I: 3D analyses," 2018-01-0850. SAE Technical Paper, 2018-01-0850, 2018 doi: org/10.4271/2018-01-0850.

[44] Mueller, C., Morcinkowski, B., Habermann, K., Uhlmann, T., Schernus, C. "Development of a pre-chamber for spark ignition engines in vehicle applications," 4th International Conference on Ignition Systems for Gasoline Engines, Dec. 2018.

[45] Pape, J., Getzlaff, J., Gruenig, C., Kuhnert, D. and Latsch, R., "Investigations on Pre-Chamber Spark Plug with Pilot Injection," SAE Technical Paper 2007-01-0479, 2007, doi:10.4271/2007-01-0479.

[46] Attard, W.P., Fraser, N., Parsons, P. and Toulson, E., "A Turbulent Jet Ignition Pre-Chamber Combustion System for High Fuel Economy Improvements in a Modern Vehicle Powertrain," SAE Technical Paper 2010-01-1457, 2010, doi:10.4271/2010-01-1457.

[47] Roethlisberger, R., Favrat, D., "Comparison between direct and indirect (prechamber) spark ignition in the case of a cogeneration natural gas engine, part I: engine geometrical parameters," Applied Thermal Engineering, 22(11), 1217-1229, 2002, doi: 10.1016/S1359-4311(02)00040-6.

[48] Xu, G., Wright, Y., Schiliro, M., Boulouchos, K., "Characterization of combustion in a gas engine ignited using a small un-scavenged pre-chamber," International Journal of Engine Research, 2018, doi: 10.1177/1468087418798918.

[49] Jamrozik, A., "Lean combustion by a pre-chamber charge stratification in a stationary spark ignited engine," Journal of Mechanical Science and Technology, 29(5):2269-2278, 2015, doi:10.1007/s12206-015-0145-7.

[50] Toulson, E., Schock, H., Attard, W., "A Review of Pre-Chamber Initiated Jet Ignition Combustion Systems," SAE Technical Paper 2010-01-2263, 2010, doi:10.4271/2010-01-2263.

[51] Shah, A., Tunestål, P., Johansson, B., "CFD Simulations of Pre-Chamber Jets' Mixing Characteristics in a Heavy Duty Natural Gas Engine," SAE Technical Paper 2015-01-1890, 2015, doi: 10.4271/2015-01-1890.

[52] Serrano, D., Zaccardi, J.M., Müller, C., Libert, C. Habermann, K., "Ultra-Lean Pre-Chamber Gasoline Engine for Future Hybrid Powertrains" SAE Technical Paper, 2019-24-0104, 2019, doi: 10.4271/2019-24-0104.

[53] Sens, M., Binder, E., Benz, A., Kramer, L., at all. "Pre-chamber ignition as a Key Technology for Highly Efficient SI Engines-New Approaches and Operating Strategies," 39th International Vienna Motor Symposium, Apr. 2018

[54] Bardis, K., Xu, G., Kyrtatos, P., Wright, Y. et al., "A Zero Dimensional Turbulence and Heat Transfer Phenomenological Model for Pre-Chamber Gas Engines," SAE Technical Paper 2018-01-1453, 2018, doi:10.4271/2018-01-1453.

[55] Cruz, I., Alvarez, C., Teixeira, A., Valle, R., "Zero-dimensional mathematical model of the torch ignited engine," *Applied Thermal Engineering*, 103, 1237-1250, 2016, doi: 10.1016/j.applthermaleng.2016.05.017.

[56] Kouremenos, D., A, Rakopoulos C., D., Hountalas, D., D. "Thermodynamic Analysis of Indirect Injection Diesel Engines by Two-Zone Modeling of Combustion", *ASME. J. Eng. Gas Turbines Power,* 112(1):138-149, 1990. doi:10.1115/1.2906468.

[57] Hiraoka, K., Nomura, K., Yuuki, A., Oda, Y. et al., "Phenomenological 0-Dimensional Combustion Model for Spark-Ignition Natural Gas Engine Equipped with Pre-Chamber," SAE Technical Paper 2016-01-0556, 2016, doi: 10.4271/2016-01-0556.

[58] Shojaeefard, M. H., Keshavarz, M. "Flame propagation model for a rotary Atkinson cycle SI engine", *International Journal of Automotive Technology,* 19(1), 9-25, 2018, doi:10.1007/s12239-018-0002-7.

[59] Auer, M., Wachtmeister, G. "Phenomenological models for pre-calculation of the combustion in gas engines". MTZ worldwide, 70(6), 52-59, 2019, doi:10.1007/BF03226962

[60] Müller, C., "Investigation of a Pre-chamber Ignition System for the Application in an Ultra-Lean-Gasoline Hybrid Powertrain Engine", Ph.D. thesis, Institute for Combustion Engines (VKA), RWTH, Aachen, 2020.

[61] Mastorakos, E., Allison, P., Giusti, A., De Oliveira, P., Benekos, S., Wright, Y., Boulouchos, K., "Fundamental Aspects of Jet Ignition for Natural Gas Engines," *SAE International Journal of Engines*, doi:10.4271/2017-24-0097.

[62] Lu, T., Law C., "Toward accommodating realistic fuel chemistry in large scale computations," *Progress in Energy and Combustion Science* 35(2):195-215, 2009, doi: 10.1016/j.pecs.2008.10.002.

[63] Livengood, J., C., Wu, P., C., "Correlation of Autoignition Phenomena in Internal Combustion Engines and Rapid Compression Machines," *Symposium (International) on Combustion* 5(1):347-356, 1955, doi: 10.1016/S0082-0784(55)80047-1.

[64] Bozza, F., De Bellis, V. Teodosio, L., "A Tabulated-Chemistry Approach Applied to a Quasi-Dimensional Combustion Model for a Fast and Accurate Knock Prediction in Spark-Ignition Engines" SAE Technical Paper, 2019-01-0471, 2019, doi: 10.4271/2019-01-0471.

[65] Bounaceur, R., Herbinet, O., Fournet, R., Glaude, P. et al., "Modeling the Laminar Flame Speed of Natural Gas and Gasoline Surrogates," SAE Technical Paper 2010-01-0546, 2010, doi: 10.4271/2010-01-0546.

[66] Woschni, G., "Universally Applicable Equation for the Instantaneous Heat Transfer Coefficient in the Internal Combustion Engine," SAE Paper 670931, 1967, doi:10.4271/670931.

[67] Lavoie, G., Heywood, J., Keck, J., "Experimental and theoretical study of nitric oxide formation in internal combustion engines" Combustion science and technology, 1(4): 313–326, 1970, doi:10.1080/00102206908952211.

[68] Heywood, J., B., "Internal combustion engine fundamentals (2nd edit.)," New York: McGraw-Hill Education, 2018, ISBN: 978-1-26-011611-3.

[69] Lawrence Livermore National Laboratory (LLNL), California, USA, http://wwwcmls.llnl.gov/?url science_and_technology-chemistry-combustion-prf/, 2006.

[70] Namazian M, Heywood JB. Flow in the piston-cylinder-ring crevices of a spark-ignition engine: Effect on hydrocarbon emissions, efficiency and power. SAE Technical Paper 820088, 1982.

[71] Königsson F, Kuyper J, Stalhammar P, Angstrom HE. The influence of crevices on hydrocarbon emissions from a diesel-methane dual fuel engine. SAE International Journal of Engines, 2013-01-0848, 2013.

[72] Smith P, Cheng W, Heywood JB. Crevice volume effect on spark ignition engine efficiency. SAE Technical Paper 2014-01-2602, 2014.

[73] Bignion E, Spicher U. Investigation of the Influence of Top Land Crevice Geometry on Hydrocarbon Emissions from SI Engines. SAE Technical Paper 982560, 1998.

[74] Hochgreb S. Combustion-Related Emissions in SI Engines. In: Sher E. Handbook of Air Pollution From Internal Combustion Engines: Pollutant Formation and Control. 1st ed. San Diego: Academic Press, 1998.

[75] Christensen M, Bengt J, Anders H. The effect of piston topland geometry on emissions of unburned hydrocarbons from a homogeneous charge compression ignition (HCCI) engine. SAE Technical Paper 2001-01-1893, 2001.

[76] Boust B, Sotton J, Labuda SA, Bellenoue M. A thermal formulation for single-wall quenching of transient laminar flames. Combust. Flame 2007, 149(3): 286-294.

[77] Dent JC, Lakshminarayanan, PA. A Model for Adsorption and Desorption of Fuel Vapour by Cylinder Lubricating Oil Films and Its Contribution to Hydrocarbon Emissions. AE Technical Paper 830652, 1983.

[78] Min K, Cheng WK. Oil layer as source of hydrocarbon emissions in SI engines. J. Eng. Gas Turbines Power 1998; 120(3): 669-677.

[79] Suckart D, Linse D, Schutting E, Eichlseder E. Experimental and simulative investigation of flame–wall interactions and quenching in spark-ignition engines. Automot. Engine Technol. 2017, 2: 25–38.

[80] Sodré J, Yates D. An Improved Model for Spark Ignition Engine Exhaust Hydrocarbons. SAE Technical Paper 971011, 1997.

[81] Dorsch M, Neumann J, Hasse C. Application of a phenomenological model for the engine-out emissions of unburned hydrocarbons in driving cycles. J. Energy Resour. Technol. 2016, 138(2): 022201-1-022201-10.

[82] Wannatong K, Chanchaona S, Sanitjai S. Simulation algorithm for piston ring dynamics. Simulation modelling practice and theory 2008, 16(1): 127–146.

[83] Delprete C, Selmani E, Bisha A. Gas escape to crankcase: impact of system parameters on sealing behaviour of a piston cylinder ring pack. Int J Energy Environ Eng 2019, 10: 207-220.

[84] Grill M, Billinger T, Bargende M. Quasi-Dimensional Modeling of Spark Ignition Engine Combustion With Variable Valve Train. SAE Technical Paper 2006-01-1107, 2006.

[85] Boust B, Bernard L, Sotton J, Labuda SA, Bellenoue M. A model of flame quenching in non-isothermal initial conditions. In: Proceedings of the European Combustion Meeting, Vienne, Austria, April 2009.

[86] Boust B, Sotton J, Labuda SA, Bellenoue M. Simultaneous measurements of laminar head-on quenching distance and wall heat flux for methane-air mixtures. In: Proceedings of the European Combustion Meeting, Louvain-la-Neuve, Belgium, 2005.

[87] Ahmad Q, Qazi JI. Thermophilic fermentations of lignocellulosic substrates and economics of biofuels: prospects in Pakistan. Int J Energy Environ Eng 2014, 5:94.

[88] Jensen TK, Schramm J. The role of post flame oxidation on the UHC emission for combustion of natural gas and hydrogen containing fuels. SAE Technical Paper 2003-01-1775, 2003.

[89] Kuppa K, Nguyen HD, Goldmann A, Korb B, Wachtmeister G, Dinkelacker F. Numerical modelling of unburned hydrocarbon emissions in gas engines with varied fuels. Fuel 2019, 254: 115532.

[90] Curran HJ, Gaffuri P, Pitz WJ, Westbrook CKA. Comprehensive Modeling Study of Iso-Octane Oxidation. Combust. Flame 2002, 129(3): 253-280.

[91] Wu KC, Hochgreb S, Norris MG. Chemical Kinetic Modeling of Exhaust Hydrocarbon Oxidation. Combust. Flame 1995; 100(1): 193-201.

[92] Lavoie GA. Correlations of Combustion Data for S.I. Engine Calculations—Laminar Flame Speed, Quench Distance and Global Reaction Rates. SAE Technical Paper 780229, 1978.

[93] Kwon, H., and K. Min. “Modified one-step reaction equation for modeling the oxidation of unburned hydrocarbons in engine conditions.” International Journal of Automotive Technology 11.5 (2010): 637-650.

[94] Westbrook CK, Dryer FL. Simplified Reaction Mechanisms for the Oxidation of Hydrocarbon Fuels in Flames. Combustion Science and Technology 1981, 27(1-2): 31-43.

4. Simulation of Vehicle

In recent years, numerical analysis has become essential also concerning the description of vehicle behaviour and powertrain management and control. Indeed, the new-generation vehicles have been equipped with additional components, such as the electric units, arising the need to properly combine them through an Energy Management Strategy, exponentially increasing the complexity of the development process. Hence, the development of a hybrid powertrain, including a thermal engine and one or more electric motors, can be effectively supported by numerical analyses. These last can be used to determine the optimal sizing and management of such power units. This represents a challenging task since more degrees of freedom are available compared to a conventional pure-thermal engine powertrain. Then, once developed, the EMS can be eventually embedded in the control unit of the vehicle if the computational time is reasonably low, otherwise, these EMSs are generally used to define the benchmark.

Instead, during this Ph.D. work, vehicle simulations have been performed with the aim to assess the CO_2 and pollutant emission along several standardized cycles, such as the WLTC or the Artemis ones, and along Real Driving Emission cycles for one of the examined engines, namely the gasoline multi-cylinder ultra-lean engine.

To this aim, three different powertrain architectures have been analysed: a conventional vehicle, a HEV, and a PHEV. The vehicle powertrains were modelled according to the state of art [1][2][3], while three EMSs for hybrid architectures have been considered. The first is based on the well-assessed theoretical method known as Pontryagin's Minimum Principle [4], while the second is related to the actual implementation of the previous one in a real vehicle, known as Equivalent Consumption Minimization Strategy [5]. The last is a novel approach developed in the framework of this research activity, labelled as Efficient Thermal Electric Skipping Strategy.

In this chapter, vehicle architectures will be examined. Then, the methodology used to model the vehicle components will be briefly described. Finally, the three EMSs will be explained in detail.

4.1. Powertrain classification

The modern vehicles can be typically classified, as reported in *Figure 4-1*, based on the sizes of the thermal engine and electric machine, resulting in six different architectures:

1. *Conventional ICE vehicles:* The only power source is the ICE; hence, all the torque propelling the vehicles are produced by the thermal engine.
2. *Micro hybrids (start / stop):* The system equipping these vehicles allows the shut down and restart of the ICE to reduce the fuel consumption at idle conditions. This solution is very

helpful for urban vehicles, due to a large amount of time usually spent being stuck in traffic or waiting at traffic light. This application can be optionally available in a conventional vehicle (micro-hybrid), while it is always present in a hybrid vehicle.

3. *Mild hybrids (start / stop + kinetic energy recovery + engine assist*): This configuration is characterized by a thermal engine coupled to an electric machine. The thermal unit can be turned off once the car is coasting, braking or stopping. These vehicles can be featured by regenerative braking and some level of power assist, but the electric unit is not able to move alone the vehicle.
4. *Full hybrids (mild hybrid capabilities + electric launch):* The vehicles can be moved alternatively by thermal engine, electric machine, or by combining them. Hence, a high-capacity battery pack is needed to ensure the electric drive. Differently from the mild hybrid, here a vehicle energy management strategy is mandatory to fully exploit the benefit of the hybridization.
5. *Plug-in hybrids (full hybrid capabilities + electric range):* These vehicles are equipped with batteries rechargeable through the connection to an external electric power source, such as the grid. The electric autonomy is higher than a full hybrid vehicle.
6. *Electric Vehicles (battery or fuel cell):* In this configuration, the vehicle propulsion is only realized by the electric units, powered by a battery or by a hydrogen fuel cell.

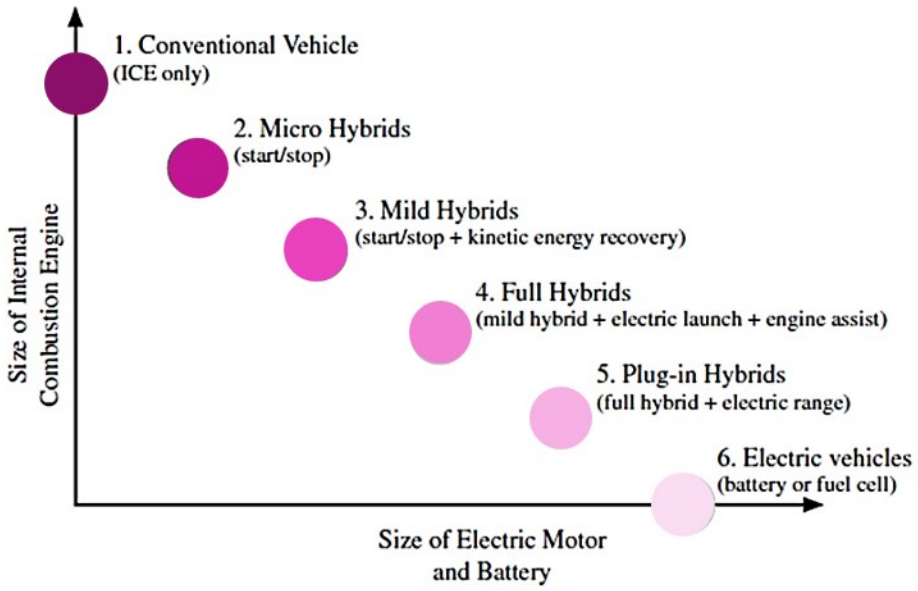

Figure 4-1 Vehicle classification as a function of the ICE and electric motor / battery size [6].

Concerning the HEV architecture, a further classification applies, depending on thermal and electric units layout, as shown in Figure 4-2:

1. *Series:* The electric unit drives alone the vehicle. The electricity required by the electric motor can be supplied by both a battery and an engine-driven generator.
2. *Parallel:* The power required to drive the vehicle is the sum of two sources: the engine and the electric machines. The torque produced by driving units is summed up by a gear set, a chain, or a belt, and transmitted to the wheels.
3. *Power split:* In this configuration, one thermal unit and two electric machines are connected to a power split device (generally a planetary gear set). The power produced by engine and electric machines can be merged through both mechanical and electrical paths, combining series and parallel modes.
4. *Series / parallel:* The vehicle is equipped with clutches, allowing to modify the powertrain configuration from series to parallel and vice versa. The flexibility of this architecture allows selecting the most suitable configuration for the current operating condition.

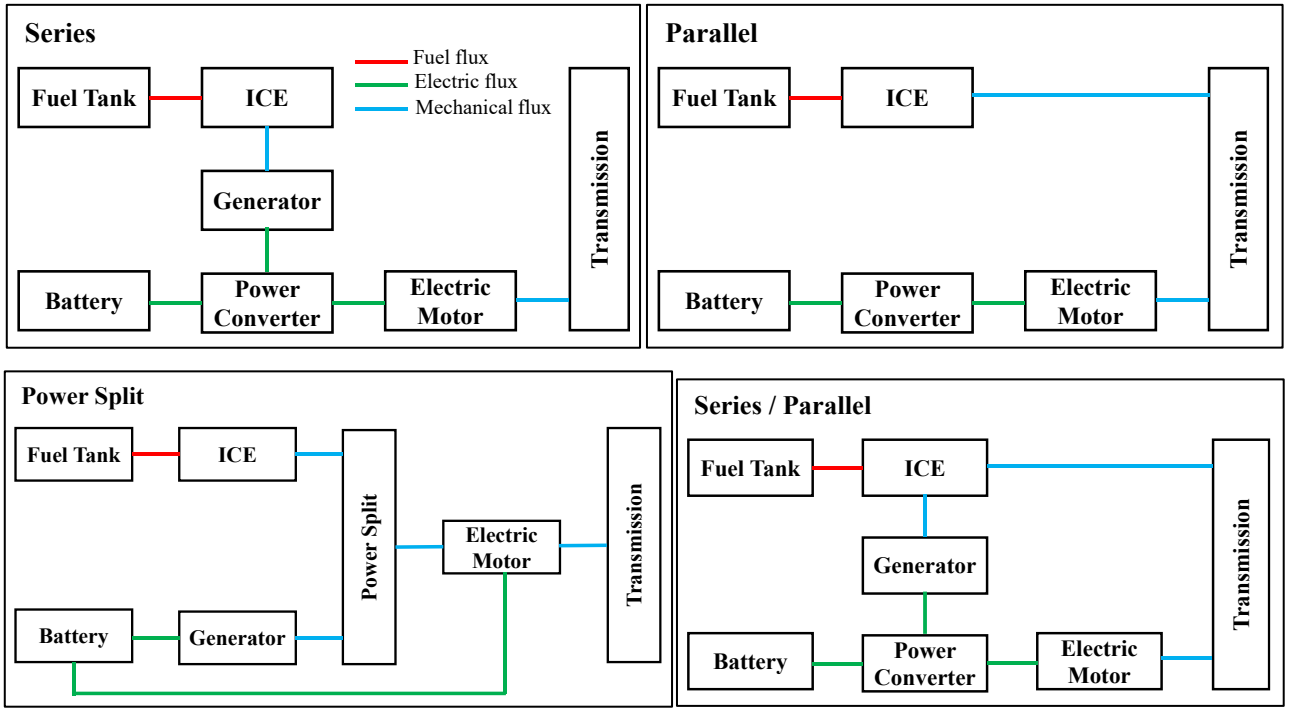

Figure 4-2 Classification of the HEV architectures

Regardless of the considered configuration, a vehicle simulation aims to reproduce the energy flows within the powertrain and the driveline, obtaining an accurate estimation of all the relevant parameters, such as fuel consumption, pollutant emissions, or battery state of charge. A vehicle-level energy analysis is the most widely used approach for the estimation of the above parameters, and it is the one considered for this work. In this method, the vehicle is considered as a point mass and its interactions with the external environment are studied. In this framework, the vehicle longitudinal dynamics and the energy flows inside the powertrain are analysed.

4.2. Vehicle longitudinal dynamics

To describe the longitudinal dynamics of the vehicle, a simplification is imposed considering the vehicle itself as a point mass. Under this hypothesis, the forces acting on the vehicle along the longitudinal axis are shown in *Figure 4-3*.

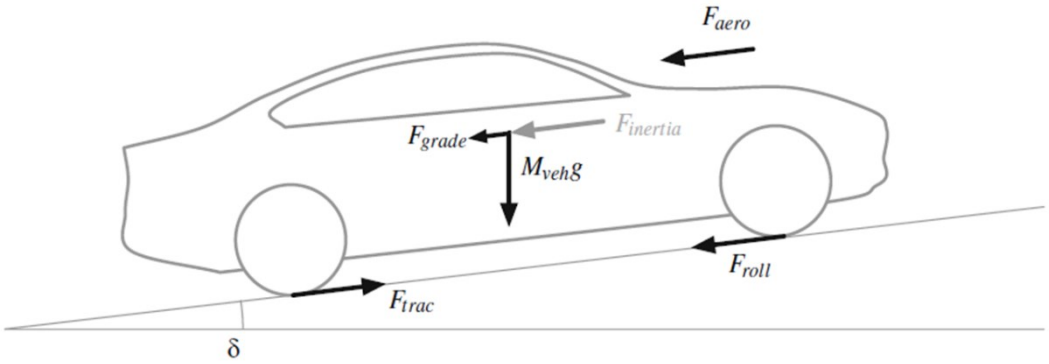

Figure 4-3 Longitudinal forces acting on the vehicle.

The vehicle dynamic equation can be express through the equilibrium of forces, as follows:

$$m_{veh}\frac{dv_{veh}}{dt} = F_{inertia} = F_{trac} - F_{roll} - F_{aero} - F_{grade} \tag{4.1}$$

where m_{veh} and v_{veh} are the effective mass and the longitudinal velocity. $F_{inertia}$ represents the inertial force, being positive if the vehicle is accelerating, while negative if decelerating. On the right hand of eq. (4.1), the first term, F_{trac}, represents the tractive force generated by the powertrain, i.e. F_{pwt} (or during braking phases at the wheels, i.e. F_{brake}). F_{roll} is the rolling resistance factor and it takes into account the friction due to the tire deformation and losses. This last force is generally express as reported in eq. (4.2) depending on a rolling resistance coefficient, c_{roll}, the gravitational acceleration, g, the vehicle mass and the road slope δ:

$$F_{roll} = c_{roll}(v_{veh}, p_{tire}, \dots)m_{veh} \cdot g \cdot cos\delta \tag{4.2}$$

In eq. (4.2), the term ($m_{veh} \cdot g \cdot cos\delta$) stands for the vertical component of the weight. c_{roll} can be assumed constant or depending on the vehicle speed, tire pressure p_{tire}, and temperature, etc. The order of magnitude for c_{roll} is about 0.01-0.03. This force is always dissipative since it opposes the vehicle motion.

Considering F_{aero}, it is the aerodynamic resistance, function of the air density, ρ, (1.25 kg/m^3 in standard ambient conditions), A_f the vehicle frontal area, C_d the aerodynamic drag coefficient. This force, along with F_{roll}, is always dissipative.

$$F_{areo} = \frac{1}{2} \cdot \rho \cdot C_d \cdot A_f \cdot v_{veh}^2 \tag{4.3}$$

Finally, F_{grade} takes into account the force due to road slop, being positive once the vehicle is driven uphill and negative if it is going downhill:

$$F_{grade} = m_{veh} \cdot g \cdot sin\delta \tag{4.4}$$

These equations represent the basis for vehicle modeling, being sufficiently accurate if the utilized parameters are correctly specified. Typical values for these parameters are stated in *Table 4.1.*

Table 4.1 Typical values of vehicle-dependent parameters to describe longitudinal vehicle dynamics models.

Parameter	*Compact Car*	*Full-size*	*SUV*
m_{veh}	$1200 - 1500$ kg	$1700 - 2000$ kg	$1900 - 2200$ kg
C_d	$0.3 - 0.35$	$0.28 - 0.33$	$0.32 - 0.38$
A_f	$1.3 - 1.7\ m^2$	$1.8 - 2.2\ m^2$	$2 - 2.5\ m^2$
C_{roll}	$0.01 - 0.03$	$0.01 - 0.03$	$0.01 - 0.03$

Aiming at making explicit the tractive force required to the powertrain, the eq. (4.1) can be rewritten as:

$$F_{trac} = F_{pwt} - F_{brake} = F_{inertia} + F_{grade} + F_{roll} + F_{aero} \tag{4.5}$$

The different ways to express the equilibrium of forces in eq. (4.1) and (4.5) respectively correspond to the forward and backward modelling approaches.

Concerning the forward approach, the vehicle acceleration (dv_{veh}/dt) is calculated through a balance between the tractive force generated by the powertrain and the passive resistance acting on it. Hence, vehicle speed is obtained by integrating the acceleration.

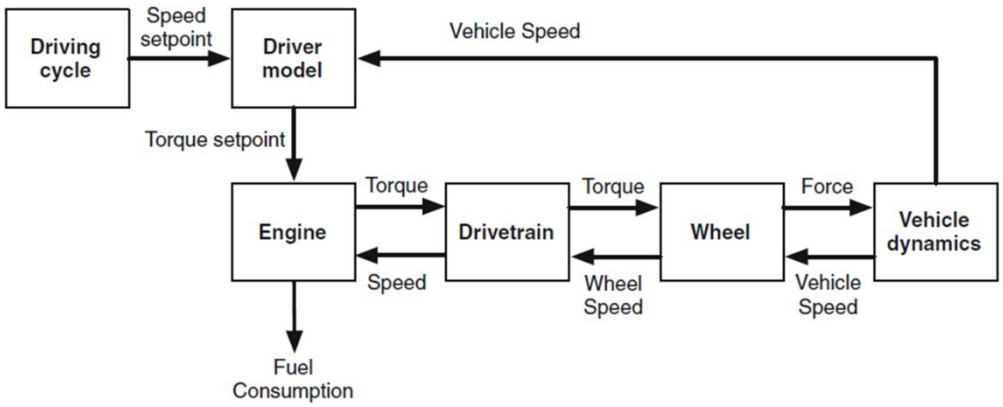

Figure 4-4 Information flow of a forward approach [1].

This approach well reproduces the physical causality of the system, which is why it is the option typically chosen in most simulation. It is synthesized by the information flow depicted in *Figure 4-4*. The model input is the required speed profile, and it is compared with the actual vehicle speed. Using a driver model, generally schematized through a PID controller, a braking or throttle control is produced to follow the prescribed vehicle speed. The driver command is sent to the supervisory block, responsible for issuing the actuators setpoints (engine, electric machines, and braking torques) to the powertrain components, which ultimately produce a tractive (or breaking) force. Finally, the estimated force is applied to the vehicle dynamics model, determining the acceleration (or deceleration) by using eq. (4.1).

Differently, in the backward approach, the velocity is imposed, calculating the tractive force from the inertia and dissipative forces. It is assumed that the vehicle will always follow the prescribed velocity and acceleration profiles. Then, F_{trac} represents the force that must be supplied by the powertrain. No driver model is needed, since the required speed is a direct input, whereas the outputs are the engine torque and the fuel consumption. In *Figure 4-5* the information flow for a backward approach is shown. In this case, the simulator directly determines the net tractive force to be applied depending on the velocity and all the vehicle characteristics. On the basis of this information, the torque required to move or brake the vehicle is estimated, with the related fuel consumption.

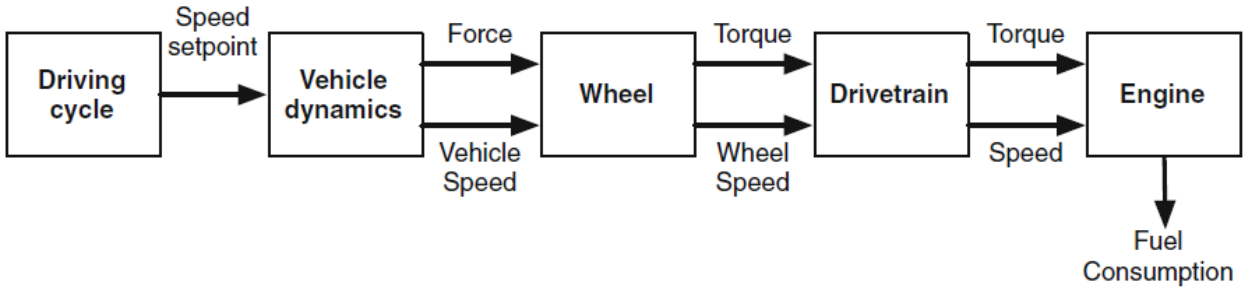

Figure 4-5 Information flow of a backward approach [1].

In a vehicle simulation, in addition to the force balance equilibrium, power and energy balances can be calculated. Multiplying all terms of eq. (4.5) by the vehicle speed (v_{veh}), the power balance can be expressed as:

$$P_{trac} = P_{inertia} + P_{grade} + P_{roll} + P_{aero} \tag{4.6}$$

If P_{trac} is greater than zero, the powertrain produces power to drive the vehicle. If $P_{trac}$is negative, for conventional vehicles, this power is lost in the brakes and in the engine pumping losses, while for a hybrid vehicle, this is partially recovered by the electric unit, recharging the battery.

By integrating eq. (4.6) over the duration of a prescribed route, the energy balance can be obtained as:

$$E_{trac} = \int_{t_o}^{t_f} P_{trac}(t)dt = E_{kin} + E_{pot} + E_{roll} + E_{aero} \tag{4.7}$$

where the integral of the inertial power is the variation of the kinetic energy (E_{kin}), and the one of the grade powers is the variation of the potential energy (E_{pot}).

By solving equations (4.1), (4.6), and (4.7), the energetic and dynamic analysis over a driving mission is performed. In particular, considering a conventional vehicle, the E_{trac}^{+} is entirely supplied by the thermal engine while E_{trac}^{-} is dissipated in friction losses at the brakes or in pumping losses in the ICE. While, considering a hybrid architecture, E_{trac}^{+} can be provided by both thermal unit and/or electric units depending on the architecture and the energy strategy chosen. Instead, E_{trac}^{-} is recovered by the electric units. The energy flux from thermal engine or from the battery to the wheels requires a proper description for all the powertrain components. To this aim, in the following section, the models employed to characterize the internal combustion engine, the electric units and the battery will be briefly recalled.

4.3. Modelling of Internal Combustion Engine, Electric unit, and battery

Two main approaches are commonly used for vehicle simulation to model the thermal engine, namely static map or static map combined with lumped-parameter dynamic mode. The first considers the engine as a perfect actuator, responding immediately to the demands. All the variables, such as the fuel consumption, are computed from the map (or table) as a function of engine speed and torque, both assumed to be known. This first approach can be modified into the second, once including dynamic limitation in the torque output, hence leading to a lumped-parameter dynamic model. This approach considers a delay between the demanded torque and the actual torque generated. To this

aim, a transfer function must be coupled to the map, representing the air / fuel dynamics during transients and, if possible, the crankshaft inertia.

Concerning the electric machine, its efficiency can be assumed constant or modelled, once again, by a map-based approach. The map can be expressed depending on the speed and torque or on speed and electric power. The relationship between mechanical torque and electric power is as follows:

$$P_{mec} = \omega_{EM} \cdot T_{EM} = \begin{cases} \eta_{EM}(\omega_{EM}, P_{El}) \cdot P_{el} & if\ P_{el} \geq 0\ (\ motoring\ mode) \\ \dfrac{1}{\eta_{EM}(\omega_{EM}, P_{El})} \cdot P_{el} & if\ P_{el} < 0\ (\ generating\ mode) \end{cases} \tag{4.8}$$

where η_{EM} represents the efficiency of the electric unit, ω_{EM} is its rotational speed and T_{EM} is the mechanical torque. Several models have been proposed for the battery system [7] in the available literature, characterized by different degrees of accuracy. Realizing a consistent prediction of the battery dynamic in a HEV is a challenge because of the mutual correlation between all the main variables characterizing the battery behaviour e.g. State of Charge (SoC), voltage, and temperature. The SoC is defined as the amount of electrical charge stored in the battery ($Q(t)$) normalized by its total capacity (Q_{nom}).

$$SoC(t) = \frac{Q(t)}{Q_{nom}} = \begin{cases} -\dfrac{1}{\eta_{coul}} \dfrac{I(t)}{Q_{nom}} & if\ I(t) > 0 \\ -\eta_{coul} \dfrac{I(t)}{Q_{nom}} & if\ I(t) < 0 \end{cases} \tag{4.9}$$

where $I(t)$ is the battery current, positive / negative during its discharge / charge, η_{coul} is the Coulombic efficiency, depending on the current intensity and temperature. Even if the battery capacity and the Coulombic efficiency are function of some parameters, the evaluation of the SoC from eq. (4.9) is usually realized assuming those quantities as constants. A simplified circuit linear model is here chosen to describe the battery behaviour. Following this approach, the battery current and voltage are related to the power exchanged with the powertrain by:

$$IV_{oc} - I^2 R_{int} - \eta_{coul} P_{batt} = 0 \tag{4.10}$$

An explicit expression of the current can be identified by solving eq. (4.10), where V_{oc} is the open circuit voltage and R_{int} is the internal resistance of the battery. These two last values can be determined through proper maps, as a function of temperature and SoC.

$$I = \frac{-V_{oc} + \sqrt{V_{oc}^2 - 4R_{int}P_{batt}\eta_{coul}}}{2R_{int}} \tag{4.11}$$

During battery charging, eq. (4.11) returns always real roots since the value of P_{batt} is negative. While in battery discharge condition, imaginary roots can be obtained from the above quadratic equation. This occurs when the power requested by the motor exceeds the one available from the battery. For this reason, a further equation is included in the model, to determine the maximum current suppliable by the battery.

$$I_{max} = \frac{V_{oc}}{2R_{int}}; V = V_{oc} - \mathrm{I_{max}}\, R_{int}; \quad P_{batt} = \mathrm{I_{max}}\ V \tag{4.12}$$

It is worth highlighting that even if the integration of the current to calculate the SoC is a widely adopted mode, it is characterized by some limitations. Firstly, considering a real application, this approach is not stable and accurate enough. For this reason, different algorithms are employed to estimate the SoC from the available measurement of terminal voltage and current. Furthermore, this method does not consider the aging of the battery. Indeed, this phenomenon causes a loss of the capacity, increasing the internal resistance and leading to the reduction of vehicle performance. However, the dependence on aging does not affect the battery performance in the short term, for this reason, this aspect has not been considered in this study.

4.4. Mechanical component and auxiliary loads

Together with the components providing the energy requested to the powertrain, the devices responsible for its transmission or conversion have to be modelled, as, for instance, the gearbox or the wheels.

The gearing is responsible for changing the speed and the torque between two shafts, ideally with no alterations of the power flow. Nevertheless, the output power is always reduced if compared to the input one, because of the friction losses. Hence, these power losses are taken into account by introducing a lossy gear model. This model considers the speed ratio fixed for a selected gear (γ_{GB}) and the output power as a function of the transmission efficiency (η_{GB}).

$$T_{out} = \begin{cases} \dfrac{\eta_{GB}}{\gamma_{GB}} T_{in} & if\ P_{in} = T_{in}\omega_{in} \geq 0 \\ \dfrac{1}{\eta_{GB}\gamma_{GB}} T_{in} & if\ P_{in} = T_{in}\omega_{in} < 0 \end{cases} \tag{4.13}$$

In eq. (4.13) the efficiency η_{GB} can be assumed as constant or variable depending on gear ratio, speed, and input torque through a map or an analytic expression. More complex models are applied for drivability studies. Concerning the wheels and brakes, a simplified approach is typically employed for longitudinal vehicle simulation, namely a quasi-static model, expressing the tractive force as follows:

$$F_{trac} = \frac{1}{R_{wh}}\left(T_{pwt} - T_{brake}\right);\ \ \omega_{wh} = \frac{v_{veh}}{R_{wh}} \tag{4.14}$$

where T_{pwt} is the torque generated by the powertrain at the wheel shaft, while T_{brake} is the braking torque and R_{wh}represents the wheel radius. The wheel angular speed ω_{wh} , as reported in eq. (4.14) can be calculated from the longitudinal vehicle speed.

Concerning the engine passive power related to the auxiliaries, it is commonly described by a simplified model because of the lack of detailed data collectable during a driving cycle. Specifically, this energy is considered as an additional battery load depending on its current operating point.

4.5. The Energy Management Problem for Hybrid Electric Vehicles

The hybrid electric vehicles, from both a numerical and real perspective, requires a proper control, which is carried out by an energy management strategy. The EMS purpose is to determine the amount of power delivered at each instant by the energy sources available in the powertrain, simultaneously complying with several constraints. Most of the EMSs for HEVs are addressed to minimize a cost function, especially accounting for the fuel consumption, while controlling the SoC of the battery. Generally, two main categories can be identified in the energy management problem, e.g. rule-based and model-based optimization problems [2],[8],[9].

The approaches belonging to the first category can be executed in real-time, since not entailing explicit minimization or optimization. Commonly, rule-based strategies are based on a set of rules to determine the value of the control variable to be applied at each time. Instead, the approaches of the second category are featured by a power split optimization, minimizing a cost function over an imposed driving cycle, leading to a global optimal solution. In this case, even if these optimizations cannot be implemented on a real vehicle, because of the missing knowledge of future information and due to their huge computational time, they represent a useful tool to support the design phase. Indeed, these approaches can be employed to design a series of rules for an on-line application or can represent a benchmark solution to compare different control strategies. Further, these model-based optimization problems can be numerically or analytically solved. In the first case, the entire driving cycle is considered, numerically finding the global optimum. Among the different available methods,

Dynamic Programming (DP) [5] is the most widely used in the vehicle application field. In the case of analytical solution, the optimization method solves an analytical problem formulation achieving the solution in closed / analytical form or, at least, providing an analytical formulation making the numerical solution faster if compared to the purely numerical methods. Among these methods, Pontryagin's minimum principle [4] is the one most commonly used.

4.6. The Optimal Control Problem in HEVs

The aim of any control strategy for vehicle powertrain is the minimization of predetermined quantities such as the consumed fuel or the pollutant emissions along a driving mission, fufofilling some constraints, e.g. complying with maximum or minimum engine torque or rotational speed, etc. A simplified procedure, largely applied, requires minimizing a combination of the above-mentioned parameters, resulting in the following mathematical expression of the problem:

$$\begin{gathered} \arg\min_{u(t)} J[x(t),t] \\ u(t)\ \epsilon\ U \\ x(t)\ \epsilon\ X \end{gathered} \tag{4.15}$$

where J represents the performance index to minimize, x is the generic state variable and u is the generic control variable, while X and U are the related range of variation. The performance index depends on the integral of a cost function L from t_0 to t plus the difference between the current and the initial state variable, through the penalization factor β.

$$J[x(t),t] = \int_{t_o}^{t} L[x(t),u(t),t]dt + \beta\,(x(t_0) - x(t)) \tag{4.16}$$

According to the common hypothesis of minimizing the consumed fuel along the driving cycle, the only state variable is the battery SoC, while the power-split between thermal engine and electric units ($u = P_{el}/P_{trac}$) represents the control variable. Under those assumptions, the cost function can be reformulated as:

$$J[x(t),t] = \int_{t_o}^{t} \dot{m}_f[u(t),t]dt + \beta\,(SoC(t_0) - SoC(t)) \tag{4.17}$$

On the right of eq. (4.17), the second term represents a global constraint for the considered state variable. Indeed, the optimization problems are usually subject to several constraints. Some of them

are integral in nature, such as the above-mentioned second term on the right of eq. (4.17), required to ensure the energy-storage balance. Other constraints are local in nature, such as instantaneous power limits or state of charge boundaries. The local constraints related to the SoC are needed to ensure that the battery works with a high efficiency and to preserve its cycle-life. Concerning the local constraints on the control variable, they are imposed to guarantee physical operation limits. Generally, the local constraints can be expressed as follows:

$$\begin{cases} SoC_{min} \leq SoC(t) \leq SoC_{max} \\ P_{batt,min} \leq P_{batt}(t) \leq P_{batt,max} \\ T_{x,min} \leq T_x(t) \leq T_{x,max} \\ \omega_{x,min} \leq \omega_x(t) \leq \omega_{x,max} \end{cases} x = eng, mot, gen \tag{4.18}$$

The last two inequalities of eq. (4.18) represent the limits imposed on the instantaneous torque and speed, respectively. $(\cdot)_{min}$, $(\cdot)_{max}$ stand for the minimum and maximum values of SoC / power / torque / speed at each instant. Furthermore, other constraints are embedded in the model, for instance, a limit on the frequency of switching between operating modes or gear number to ensure an acceptable vehicle drivability.

4.7. Pontryagin Minimum Principle

As said, the Pontryagin Minimum Principle [4] is the widely analytical optimization methods used to solve the problem of HEV energy management. It is based on the instantaneous minimization of the Hamiltonian function, once determined the optimal trajectory of the costate, both mathematically defined in the following. This approach requires the *a-priori* knowledge of driving mission to achieve the condition of energy balance for the battery between the start and end of the driving mission.

For the PMP strategy, the optimal solution is found at each time through the minimization of the Hamiltonian function, defined in (4.19) for HEV application:

$$H[u(t), SoC(t), t, \lambda(t)] = \dot{m}_f[u(t), t] + \lambda(t)\dot{SoC}[u(t), SoC(t), t] \tag{4.19}$$

The first term of Hamiltonian function in eq. (4.19) is the instantaneous cost, while $\lambda(t)$ is a vector of the optimization variable, also known as *adjoint states* or *costate* of the system and its dynamic equation is given by:

$$\dot{\lambda}(t) = -\frac{H[u(t), SoC(t), t, \lambda(t)]}{\partial SoC} = -\lambda(t)\frac{\partial \dot{SoC}[u(t), SoC(t), t]}{\partial SoC} \tag{4.20}$$

According to the main assumption, for which the SoC time derivative is not dependent on its current level [10], the costate is constant over time, whereas the optimal costate, identified as λ^*, demands only to fulfil the energy balance for the battery between the beginning and the end of the driving cycle:

$$SoC(t_0) = SoC(t_f) \tag{4.21}$$

λ^* can be evaluated only by defining "a-priori" the vehicle driving mission, based on the future information knowledge. If the Hamiltonian cannot be given as an explicit function of the control variable, to solve the problem, it is mandatory to realize a discretization of the control variable domain at each simulation step. By changing the grid sizing, the problem solution may show variations, resulting in a quite different cost function minimum and control variable trajectory. Finer grids lead to better outcomes, but the computational time could become an issue to be reckoned with.

Further, when including state constraints in the problem definition, some difficulties in the PMP application arise. Hence, a possible solution is combining the PMP with a penalty function approach [11]. The aim is to increase the Hamiltonian value, whenever the optimal trajectory violates its constraints. An effective penalty approach through an implicit Hamiltonian minimization is used in [12] having several states and inputs under mixed input-state constraints.

The application of real-time local optimal solution leads to long optimization time and computational complexity [13]. Hence, aiming at improving the efficiency of the optimization process, different solutions have been proposed in literature, such as the application of an approximate PMP algorithm [14]. By introducing a simple convex approximation to the local Hamiltonian, this strategy only requires the calculation and comparison of five candidate Hamiltonians, before deciding on the optimal control for the powertrain. Another crucial matter of these approaches is related to the discretization of the operating domain of the powertrain components, which relies on the conflicting requirements of computational effort and fine control.

4.8. Equivalent Consumption Minimization Strategy

To overcome the problem concerning lack of information on future events, the off-line strategies can be modified into an on-line version. One of the most common methodologies is the Equivalent Consumption Minimization Strategy [15], considered as an extension of the PMP [10].

This approach aims to the on-line minimization of an equivalent fuel consumption, also considering a contribution associated to the battery power consumption through an equivalence factor, s_0. The adequacy for on-line applications is realized by an adaptive s_0, modified by a fuzzy PI controller [16], or by a correction term related to the battery State of Charge [17]. Another option for the correction is the utilization of a 2-dimensional look-up table, derived from an equivalence factor optimization, and then applied for real-time adjustments [18]. Once tuned, these approaches showed sub-optimal performance, but quite similar to off-line approaches [19],[20],[21]. Once more, if a dense discretization for the exploration of the performance maps of powertrain sub-components is required, the computational time represents a remarkable issue.

As said, the ECMS requires to minimize an equivalent fuel rate at each time, that is the sum of the actual fuel rate and of a contribution arising from the battery electrical power through an equivalence factor, according to:

$$\dot{m}_{eq}[u(t),t] = \dot{m}_f[u(t),t] + s_0 \cdot \frac{P_{batt}[u(t),t]}{LHV} \tag{4.22}$$

LHV is the lower heating value of the fuel, P_{batt} represents the power released or absorbed by the battery, and s_0 the equivalence factor. A piecewise linear type description of s_0 (different for battery charge and discharge phases) proves realizing very close to the optimal powertrain management, but requiring an adjustment depending on the vehicle characteristics and driving mission [20]. Several methodologies have been developed to achieve an adaptative adjustment of the equivalence factor [16],[17],[20],[21]. Some of them are developed according to the outputs deriving from off-line optimization strategies [17],[18]. The impact on performance by using a constant value for s_0 is evaluated in [20], finding results very close to the optimality.

Among the available alternatives, a very robust approach presents an equivalence factor correction depending on the difference between the current SoC level and a target value [16]. The correction is computed by a PID controller, expressed as:

$$s_{corr}(t) - s_0 = K_p \cdot \Delta SoC + K_i \cdot \int_0^t \Delta SoC \cdot d\tau + K_d \cdot \frac{d}{dt}\Delta SoC \tag{4.23}$$

$$\Delta SoC = SoC(t) - SoC_{target} \tag{4.24}$$

where SoC_{target} is a reference SoC level and ΔSoC is the error between the current SoC and the above reference. The first term on the right hand of eq. (4.23) represents a proportional correction term, while the second and the third ones are respectively an integral and a derivative correction.

4.9. Efficient Thermal Electric Skipping Strategy

In the light of the above-mentioned criticisms of PMP and ECMS, one of the main purposes of this thesis work has been the development of a simplified control strategy, available in off-line and on-line versions, featured by performance similar to PMP / ECMS one, but extremely efficient from a computational point of view. As highlighted by analysing the current literature [12],[13],[14], the computational effort still remains an open point in the development of optimal control strategies, especially if those strategies are addressed to a real-time implementation. Hence, the computational efficiency is one of the most relevant aspects addressed in the development of the proposed strategy.

The power-split principle is not applied and is replaced by an alternate utilization of thermal and electric units, leading to the here called Efficient Thermal Electric Skipping Strategy. At each time, the choice between the traction modalities is based on the evaluation of an equivalent fuel rate in a pure electric driving, to be compared to the actual fuel rate in a pure ICE driving.

With the aim to prove the ETESS consistency, it is implemented in an "in-house developed" simulation platform and tested on different HEV architectures along different driving cycles. Further, to validate both the off-line / on-line ETESS variant, the outcomes of this proposed control strategy have been processed and compared to PMP and ECMS methodologies, respectively.

In opposition to the power-split concept, the basic idea of ETESS is to alternatively utilize the electric units and thermal engine to fulfil the power demand at the vehicle wheels, P_{dem}. At each time, the choice between the power units is made comparing the actual fuel consumption of the thermal engine, operating to fully satisfy the power demand, $\dot{m}_{f,th}$, and an equivalent fuel consumption, $\dot{m}_{f,el}$, related to a pure electric driving of the vehicle. While the first fuel rate, $\dot{m}_{f,th}$ is simply quantifiable, the description of the second one is the most critical issue for strategy implementation. The value of $\dot{m}_{f,th}$, for each available gear ratio, n_{GB_1}, only depends on the power demand, P_{dem}, and on the losses in the Gear-Box$_1$ (GB$_1$) and in the differential (see power flux *Figure 4-6*), and can be express as follows:

$$\dot{m}_{f,th}\left(n_{GB_1}\right) = \frac{P_{dem} \cdot BSFC\left(n_{GB_1}\right)}{\eta_{GB_1}(n_{GB1}) \cdot \eta_{diff}} \tag{4.25}$$

where η_{GB_1} is the efficiency of GB_1 and BSFC is the actual fuel consumption of the engine operating with the load and speed imposed by the vehicle velocity and by P_{dem}.

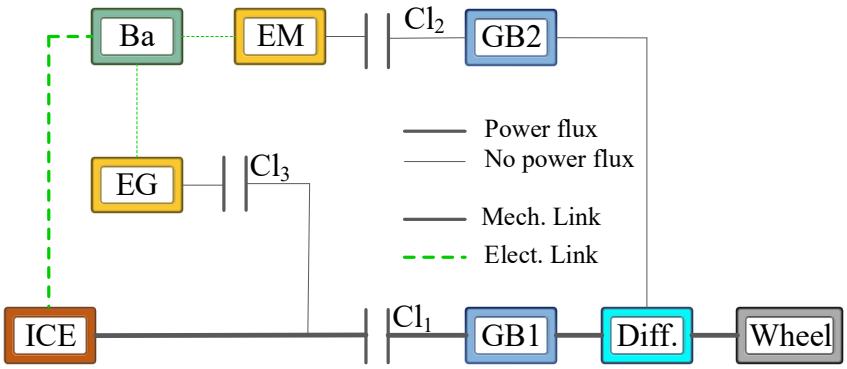

Figure 4-6 Power flux in pure thermal driving.

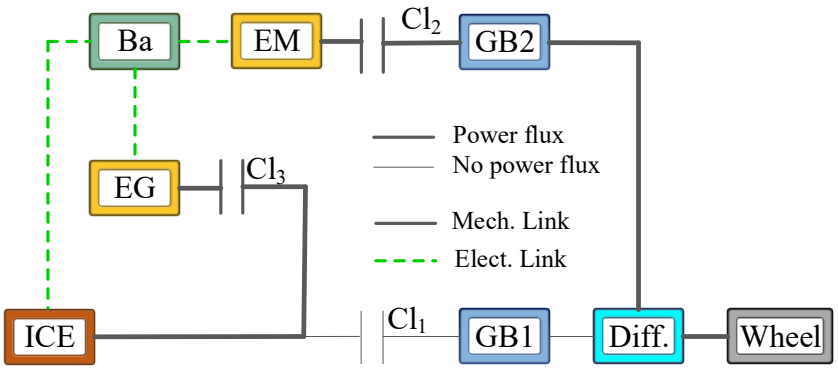

Figure 4-7 Power flux in pure electric driving.

The concept behind the estimation of the fuel rate $\dot{m}_{f,el}$ is that in a pure series-electric driving, the power delivered by the EM (Electric Motor) was supplied by the thermal engine in an undefined time, working in its optimal operating point, characterized by a $BSFC_{min}$. The power flux from the thermal engine to the wheel, in a pure series driving, involves some losses in the EG (Electric Generator), in the EM, in the battery, in the GB_2, and in the differential, quantifiable by the efficiencies of each component (see power flux in *Figure 4-7*). Hence, the equivalent fuel consumption in a pure electric mode is expressed as the product of P_{dem} and an "adapted" $BSFC_{min}$, corrected by the above-mentioned efficiencies to consider the losses from the ICE to the wheels.

$$\dot{m}_{f,el} = c_0 \cdot \frac{P_{dem} \cdot BSFC_{min}}{\eta_{GB_2} \cdot \eta_{EG_{charge}} \cdot n_{EM} \cdot \eta_{diff}} \tag{4.26}$$

where η_{GB_2}, $\eta_{EG_{charge}}$, n_{EM} and η_{diff} are the efficiencies of GB_2, EG, EM, and differential, respectively, and c_0 is a tuning constant. Note that $\eta_{EG_{charge}}$ is the EG efficiency calculated in the torque-speed couple where the battery charge occurs, in turn depending on the engine operating point of minimum BSFC. The tuning constant c_0 is introduced to achieve the energy balance for the battery, as expressed by eq. (4.21). The choice between either pure thermal or electric driving is realized on the basis of the inequality reported below:

$$\begin{cases} \dot{m}_{f,el} < \dot{m}_{f,th} \rightarrow pure\ electric\ mode \\ \dot{m}_{f,el} > \dot{m}_{f,th} \rightarrow pure\ thermal\ mode \end{cases} \tag{4.27}$$

In this assessment, the gear ratio involving the lowest fuel consumption is chosen for the definition of $\dot{m}_{f,th}$. If the maximum power delivered by the thermal engine for a certain gear ratio, $P_{ICE_{MAX}}(n_{GB_1})$, is lower than the power demand, the fuel rate is corrected as:

$$\dot{m}_{f,th}(n_{GB_1}) = P_{ICE_{MAX}}(n_{GB_1}) \cdot BSFC(n_{GB_1}) + \Delta\dot{m}_{f,el}(n_{GB_1}) \tag{4.28}$$

$$\Delta\dot{m}_{f,el} = c_0 \cdot \frac{\left(P_{dem} - P_{ICE_{MAX}}(n_{GB_1}) \cdot \eta_{GB_1}(n_{GB_1}) \cdot \eta_{diff}\right) \cdot BSFC_{min}}{\eta_{GB_2} \cdot \eta_{EG_{charge}} \cdot n_{EM} \cdot \eta_{diff}} \tag{4.29}$$

where on the right hand of eq. (4.28), the first term represents the fuel rate achieved when the engine operates at its maximum power and the second term, $\Delta\dot{m}_{f,el}$, is an equivalent fuel consumption needed to fulfil the power demand with the support of the electric motor, as expressed by eq. (4.29). Moreover, when the wheel power demand becomes negative, a regenerative braking is realized by the EM.

A simplified description of the ETESS principle can be related to a specialization of the ECMS, where the only acceptable values for the power-split are either 0 or 1. Even if introducing this simplification means to achieve a certain penalization of the fuel economy, a drastic reduction of the computational effort is expected.

The flowchart shown in *Figure 4-8* summarizes the ETESS logics. This highlights the choice between a pure electric or thermal driving, based on the fuel rates $\dot{m}_{f,th}$and $\dot{m}_{f,el}$, and the activation of a parallel mode only when the ICE or the EM is not able to fulfil alone the power demand. Based on this approach, the battery charge is activated especially when the vehicle brakes rather than in a phase with a positive power demand. Hence, it is feasible to reduce as much as possible the energy

flux from the ICE to the battery (throughout the electric units) with the aim to minimize the related unavoidable mechanical and electrical losses.

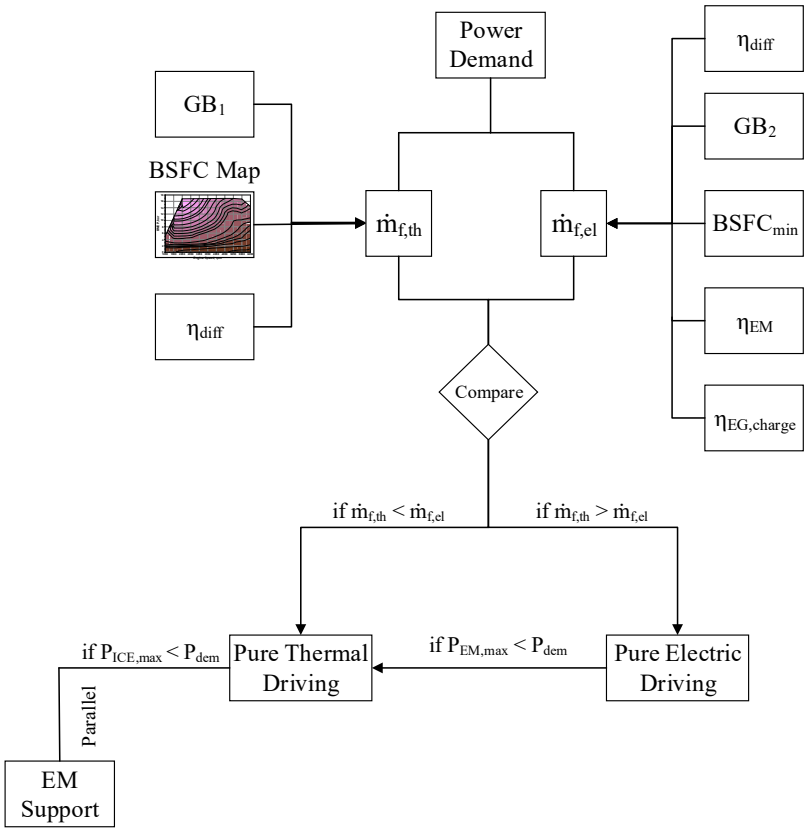

Figure 4-8 Flowchart schematizing the logics of the ETESS.

Along a driving cycle, if the torque limits, for each unit (thermal and electric), are not overcome, the only energy available for a pure electric driving is the one recuperated from the regenerative braking, and the thermal engine, when switched on, will supply the power strictly needed for the vehicle driving.

According to the inequalities of eq. (4.27) the choice between pure electric or thermal driving is straightforward, without requiring a discrete map exploration. To evaluate $\dot{m}_{f,th}$, the engine operating point is univocally identified by the tractive power demand, by the vehicle speed, by the losses along the driveline from the wheels to the engine. Likewise, also the fuel rate $\dot{m}_{f,el}$ for a pure electric driving is univocally identified by the traction power demand, by the vehicle speed, and by the losses along the driveline, and in addition by the dissipations in the electric units.

It is worth highlighting that this control strategy is versatile and suitable for any hybrid powertrain fitted with a gearbox.

4.10. Setting of the map gridding

In this thesis, for the PMP and ECMS implementations, a grid has been identified to explore the EM and EG efficiency maps, composed of 29 and 19 torque levels for each rotational speed, respectively. This choice represents a reasonable compromise between computational effort and degree of accuracy of the solution. No gridding is needed for access to the engine BSFC map since the engine load level is univocally determined by the power demand at the vehicle wheels and by the torque levels of the electric units, which in turn are iteratively explored by the above grids. Indeed, for the ETESS implementation, the power request for both EM, EG, and ICE is univocally determined (once assigned the gear number), and for this reason, no gridding is required. This characteristic is expected to drastically improve its simulation time if compared to PMP or ECMS. However, the ETESS undergoes a drawback similar to the PMP one, i.e. the requirement of a-priori knowledge of the speed-profile needed to identify the value of c_0. Anyway, it can be easily extended to a real-time implementation introducing an adaptive correction for c_0, similarly to the ECMS method.

References

[1] Miller, J., "Propulsion systems for hybrid vehicles," Vol. 45. Iet, 2004.

[2] Guzzella, L., Sciarretta, A., "Vehicle Propulsion Systems, Introduction to Modeling and Optimization," 2005, ISBN 978-3-642-35913-2.

[3] Guzzella, L. Sciarretta, A., "Electric and hybrid-electric propulsion systems. In Vehicle Propulsion Systems" Springer, Berlin, Heidelberg, (pp. 67-162), 2013, doi:10.1007/978-3-642-35913-2_4.

[4] Kim, N., Cha, S. Peng, H., "Optimal control of hybrid electric vehicles based on Pontryagin's minimum principle," *IEEE Transactions on control systems technology*, 19(5), pp.1279-1287,2010, doi: 10.1109/TCST.2010.2061232.

[5] Paganelli G, Delprat S, Guerra TM, Rimaux J, Santin, JJ, Equivalent consumption minimization strategy for parallel hybrid powertrains. Vehicular Technology Conference IEEE 55th Vehicular Technology Conference VTC Spring 2002; 4:2076-2081. doi: 10.1109/VTC.2002.1002989.

[6] Onori, S., Serrao, L. Rizzoni, G., "Hybrid electric vehicles: energy management strategies" Berlin Heidelberg, Springer, doi:10.1007/978-1-4471-6781-5.

[7] Drouilhet, S., Johnson, B., Drouilhet, S. Johnson, B., "A battery life prediction method for hybrid power applications," in 35th Aerospace Sciences Meeting and Exhibit (p. 948), 1997, doi: org/10.2514/6.1997-948.

[8] Salmasi F. R. "Control Strategies for Hybrid Electric Vehicles: Evolution, Classification, Comparison, and Future Trends," *IEEE Transactions on Vehicular Technology*, 56(5), 2393–240, 207, doi: 10.1109/TVT.2007.899933.

[9] Salman M., Chang, M., Chen. J., "Predictive energy management strategies for hybrid vehicle, "Proceedings of the 2005 IEEE Vehicle Power and Propulsion Conference,2005.

[10] Sciarretta, A., Guzzella, L., "Control of hybrid electric vehicles," IEEE Control Systems Magazine 27(2):60-70, 2007, doi: 10.1109/MCS.2007.338280.

[11] Kareem Ulla T, Delprat S, Czelecz L. State constrained hybrid vehicle optimal energy management: an interior penalty approach. IFAC-PapersOnLine 2017, 50(1): 10040-10045. doi: 10.1016/j.ifacol.2017.08.1774.

[12] Sánchez M, Delprat S, Hofman T. Energy management of hybrid vehicles with state constraints: A penalty and implicit Hamiltonian minimization approach. Appl Energy 2020, 260: 114149. doi: 10.1016/j.apenergy.2019.114149.

[13] Yeqin W, Zhen W, Yuyan W, Aoyun X, Chang G, Zhongyi T. Research on energy optimization control strategy of the hybrid electric vehicle based on Pontryagin's minimum principle.

Computers & Electrical Engineering 2018, 72:203-213. doi: 10.1016/j.compeleceng.2018.09.018.

[14] Chong H, Minggao O, Liangfei X, Hewu W. Approximate Pontryagin's minimum principle applied to the energy management of plug-in hybrid electric vehicles. Appl Energy 2014; 115: 174-198. doi: 10.1016/j.apenergy.2013.11.002.

[15] Paganelli G, Delprat S, Guerra TM, Rimaux J, Santin, JJ, Equivalent consumption minimization strategy for parallel hybrid powertrains. Vehicular Technology Conference IEEE 55th Vehicular Technology Conference VTC Spring 2002; 4:2076-2081. doi: 10.1109/VTC.2002.1002989.

[16] Zhang F, Xi JQ, Langari R. An adaptive equivalent consumption minimization strategy for parallel hybrid electric vehicle based on Fuzzy PI. Proceeding of 2016 IEEE Intelligent Vehicles Symposium (IV) 460-465, 2016. doi: 10.1109/IVS.2016.7535426.

[17] Pei D, Leamy MJ. Dynamic Programming-Informed Equivalent Cost Minimization Control Strategies for Hybrid-Electric Vehicles. J. Dyn. Sys., Meas., Control 2013; 135(5):051013. doi: 10.1115/1.4024788.

[18] Chao, Siyu D, Liang L, Sixong Y, Yiyong Y, Yue Z. Adaptive real-time optimal energy management strategy based on equivalent factors optimization for plug-in hybrid electric vehicle. Appl Energy 2017, 203: 883-869. doi: 10.1016/j.apenergy.2017.06.106.

[19] Serrao L, Onori S, Rizzoni G. A comparative analysis of energy management strategies for hybrid electric vehicles. J. Dyn. Sys., Meas., Control 2011; 133(3):031012. doi: 10.1115/1.4003267.

[20] Musardo C, Rizzoni G, Guezennec Y, Staccia B. A-ECMS: An Adaptive Algorithm for Hybrid Electric Vehicle Energy Management. European Journal of Control 2013; 11(4-5): 509-524. doi: 10.3166/ejc.11.509-524.

[21] Chao S, Fengchun S, Hongwen H. Investigating adaptive-ECMS with velocity forecast ability for hybrid electric vehicles. Appl Energy 2017, 185: 1644-1653. doi: 10.1016/j.apenergy.2016.02.026.

5. Engine Model Validation

During this Ph.D. work, several engine architectures have been studied and analysed, very different from each other. In the first stage, a conventional SI engine has been examined, with the aim to assess the sub-models described in section 3.4 in the standard combustion system. The engine performances have been evaluated and compared to the available experimental data over the whole engine operating plane. Subsequently, ultra-lean engines have been examined. In this framework, the model reliability for different geometrical configurations (pre-chamber design, bore, stroke, and intake port geometry) and fuels (methane and gasoline) for a single cylinder engine (SCE), equipped by a pre-chamber device, has been studied. At this stage, the sub-models for SI engine have been adapted to describe this unconventional engine architecture. The models have been validated for the SCE in terms of turbulence, combustion, and pollutant predictions. Finally, two large-bore gas engines have been analysed, featured by different ignition modalities i.e. a SCE with a dual fuel mode and a multi-cylinder engine (MCE) equipped by a PC device, with special regard to unburned hydrocarbon emission modelling.

5.1. Conventional Engine

5.1.1. Naturally Aspirated Small SI Engine

5.1.1.1 Engine Description

The engine under study is a naturally aspirated small size VVT 3-cylinder SI engine, having its main features listed in *Table 5.1*.

Table 5.1. Conventional SI engine main features

Parameters	*Values*
Compression ratio	12:1
Displaced volume, cm^3	996.36
Bore, mm	70
Stroke, mm	86.3
Connecting rod length, mm	149.3
Maximum brake power, kW	46.031@6000 rpm
Maximum brake torque, Nm	90.31@3500 rpm
Valve number	4 valve/cylinder

The considered engine is a naturally aspirated PFI SI engine, with the typical pent-roof architecture of the combustion chamber. Each cylinder is equipped with a centred spark plug, a standard ignition

system, and two intake / exhaust valves. The valves are controlled by a phased VVT system acting on both intake and exhaust sides.

An external cooled EGR (eEGR) circuit allows recirculating the exhaust gas to the intake manifold. The recirculated gas temperature is lowered by a water-cooled heat exchanger and the amount of eEGR is adjusted by an automatically controlled throttle valve.

An extensive experimental campaign was carried out, investigating the whole operating plane of the engine. Operations with (about 355 operating points) and without EGR (about 364 operating points) actuation were considered. For all the analysed operating conditions the fuel is metered to realize a stoichiometric Air-to-Fuel (A/F) ratio. The spark advance is generally set to ensure engine operation at maximum brake torque. Only at low speeds and high loads, it is delayed avoiding knocking combustion. Additionally, 33 operating points have been investigated, where the pollutant emissions were measured. These points are composed of six EGR-sweeps at various loads and engine speeds.

No particular constraint is applied to limit the maximum in-cylinder pressure and exhaust gas temperature. The VVT device is controlled to maximize the torque at full load, whereas the valve timing is delayed with decreasing load to promote the internal EGR, thus reducing the need for intake throttling. This latter strategy is adopted when the external EGR device cannot ensure an adequate recirculation level, namely for very low BMEPs. The considered engine speeds range from 1000 to 6500 rpm, with a maximum BMEP of about 12 bar at 3500 rpm.

The instrumentation of the test bench enabled measuring both the overall engine performance (fuel flow rate, A/F ratio, torque, fuel consumption) and the in-cylinder pressure cycles. The latter were post-processed using an inverse analysis to obtain the burning rate profiles and the characteristic combustion angles, namely MFB_{10}, MFB_{50}, and MFB_{90}.

Concerning the pollutant emission, a reduced set of operating points, 33 in number, is available at different fixed loads and speeds by varying the EGR percentage.

5.1.1.2 Model description

The tested engine has been schematized and simulated in the GT-Power environment. The simulation is based on a 1D model of the unsteady flow inside the intake and exhaust pipes and a 0D model of the in-cylinder processes. The engine schematic includes cylinders, intake and exhaust pipe systems, airbox, throttle valve, and EGR circuit (composed of a valve and an EGR cooler). The cylinder description, based on a 0D approach, is hence coupled with quasi-dimensional phenomenological models to predict the in-cylinder process.

The experimental A/F ratio and valve timing are used as input data to the simulations. According to the experiments, the throttle valve is fully opened for the full load analysis, while it is adjusted by a PID controller to match the measured BMEP for the part load calculations. The EGR valve is controlled to reproduce the measured external EGR rate. The spark advance is automatically modified by another controller targeting the experimental angle of 50% Mass Fraction Burned (MFB_{50}).

The combustion and the turbulence are simulated according to the models of section 3.4 of this thesis, namely the fractal approach and *K-k-T* turbulence model, suitable for a conventional SI engine. As discussed, the auto-ignition table for the knock modelling is based on the kinetic scheme developed by Andrae [1].

The knock model is validated at full load, where the selected engine always operates at the knock limit. In these analyses, the spark advance was iteratively modified to realize a numerical knock index below a predefined threshold level [2], [3],[4]. This methodology allowed to correctly agree with the experimental knock limited spark advance, with a maximum error of 1-2 CADs, also referring to different engines.

A refined model of the heat transfer inside the cylinder and exhaust pipes is introduced, applying a wall temperature solver based on a finite element approach. Concerning the in-cylinder heat transfer, a Woschni-like correlation is used, while convective, radiative, and conductive heat transfer modes are considered for the exhaust pipes.

5.1.1.3 Model tuning and validation

The first stage of the model tuning is the identification of the constants of the turbulence sub-model, according to a hierarchical 1D/3D methodology [5],[6]. The constants are adjusted by fitting the results of 3D CFD simulations for various engine operating conditions. Previously, a number of 3D simulations were carried out using the commercial software STAR-CD v4.28, as described in detail in [7]. The computational domain includes the combustion chamber and the in-head intake and exhaust ports. Base and minimum cell sizes are 0.6 mm and 0.1 mm, respectively. The total number of fluid cells at the TDC is nearly 350k, and the addition of mesh layers at increasing cylinder volume leads to a maximum of about 700k cells at the BDC. The simulations are based on a RANS approach coupled with a k-ε RNG turbulence model [8] adapted for compressible flows. The time-varying boundary conditions at the intake and exhaust ports are derived from 1D simulations under motored conditions. The tuning of the 0D turbulence model and the investigated operating conditions for the considered engine are detailed in [6], where a satisfying agreement between the 0D and mass-averaged 3D turbulence parameters is found.

Concerning the combustion model, it was tuned at full load for both laminar flame speed correlations "Cor A" and "Cor B", discussed in section 2.2.1, to reproduce the experimental burning rates and in-cylinder pressure cycles. In the full-load calculations, the effect of the flame stretch on the LFS is not considered, since preliminary simulations showed that it had a negligible influence on the results. The optimal values of the three tuning constants discussed in section 3.7 have been selected as the ones that produce the best fitting of experimental data of combustion core duration, $MFB_{10\text{-}50}$ (c_{wrk}), initial combustion stage duration, $MFB_{0\text{-}10}$ (c_{trans}), and combustion tail duration, $MFB_{50\text{-}90}$ (x_{wc}). Single values of c_{wrk}, $c_{trans,}$ and x_{wc} were identified at full load as the best compromise over the entire range of engine speeds.

The tuning of the combustion parameters was performed separately for each of the considered LFS correlations, and the optimal values of the constants are reported in *Table 5.2* for both "Cor A" and "Cor B". It is observed that x_{wc} takes the same value for both correlations, whereas c_{trans} and c_{wrk} exhibit slightly different values, just to compensate the difference in the LFS predictions.

Table 5.2. Values of the tuning constants of the combustion model

	Cor. A	*Cor. B*
c_{trans}	1.2	1.1
c_{wrk}	0.58	0.7
x_{wc}	0.5	0.5

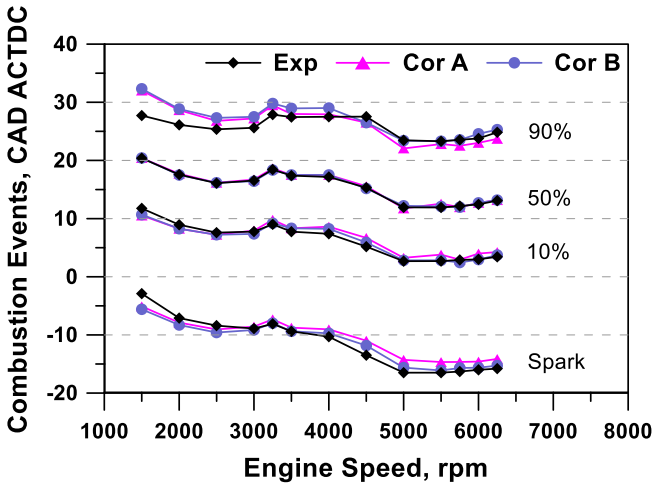

Figure 5-1 Experimental / numerical comparison of the characteristic combustion angles at full load.

Figure 5-1 shows the comparison between experimental and predicted values of the characteristic combustion angles at full load and various engine speeds. The numerical values, computed using either "Cor A" or "Cor B", are observed to be in good agreement with the experimental data for both correlations. This means that they respond in a similar way to the variations in pressure, temperature, residual gas content, and equivalence ratio that typically occur at full load operations. However, some

differences are detected at high engine speeds. In fact, the predictions of spark, MFB_{10}, and MFB_{90} over 4500 rpm resulting from the use of "Cor B" turn out to be more accurate than those obtained via "Cor A".

Since the two correlations behave in a very similar way at full load, the validation of the engine model reported below refers only to the use of "Cor B". The model ability to simulate the engine breathing results from the experimental / numerical comparison of the volumetric efficiency shown in *Figure 5-2(a)*. Moreover, the good agreement between predicted and measured BMEPs (*Figure 5-2(b)*) and in-cylinder pressure peaks (*Figure 5-2(c)*) shows that the model is capable of reproducing properly the combustion process and the wall heat transfer.

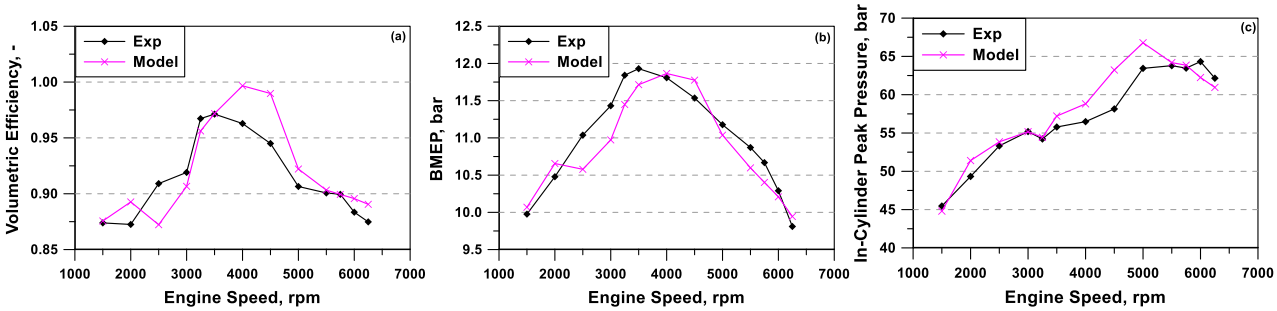

Figure 5-2 Experimental/numerical comparison of volumetric efficiency (a), BMEP (b), and in-cylinder peak pressure (c) at full load.

A further insight into the model reliability is provided by the numerical / experimental comparisons of the in-cylinder pressure cycles and burning rates at three different engine speeds reported in *Figure 5-3*. A satisfactory agreement is found for all the considered speeds, despite the significant variations in BMEP, in-cylinder pressure, temperature, EGR rate, and turbulence intensity.

Only at 1500 rpm, the model predictions are somewhat inaccurate, probably due to a slight overestimation of heat transfer or turbulence intensity. Summarizing, all these results prove that the proposed approach is capable of reproducing the engine operations at full load, without the need of any case-dependent tuning and regardless of the adopted LFS correlation.

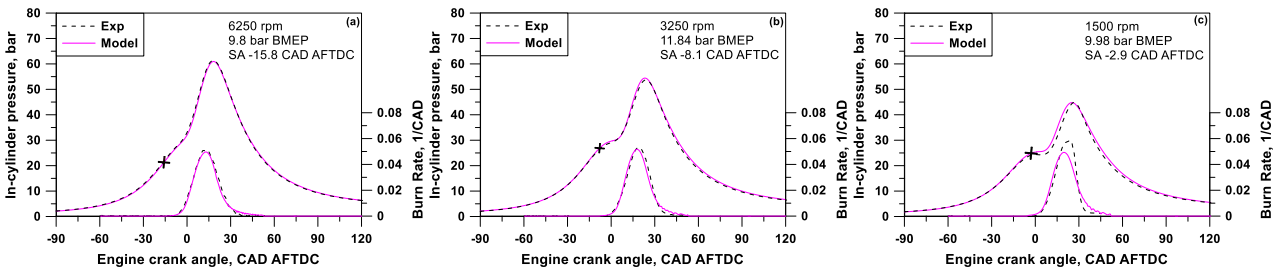

Figure 5-3 Experimental / numerical comparison of in-cylinder pressure cycle and burn rate at 6250x9.8 (a),3250x11.84 (b), and1500x9.98 (c).

The engine model has been validated also for the second data set (33 operating points), using the same constants presented above for the turbulence and combustion sub-models. *Figure 5-4(a)* depicts

the engine loads, in terms of BMEP, and the rotational speeds against the case number. In *Figure 5-4(b)* the examined EGR percentages are reported. As can be seen, six different EGR sweeps have been investigated, at four load and speed conditions. While in *Figure 5-4(c)* the experimental / numerical BSFC comparisons are reported, showing a quite good agreement, with a maximum error of less than 2.5 % at the lowest load.

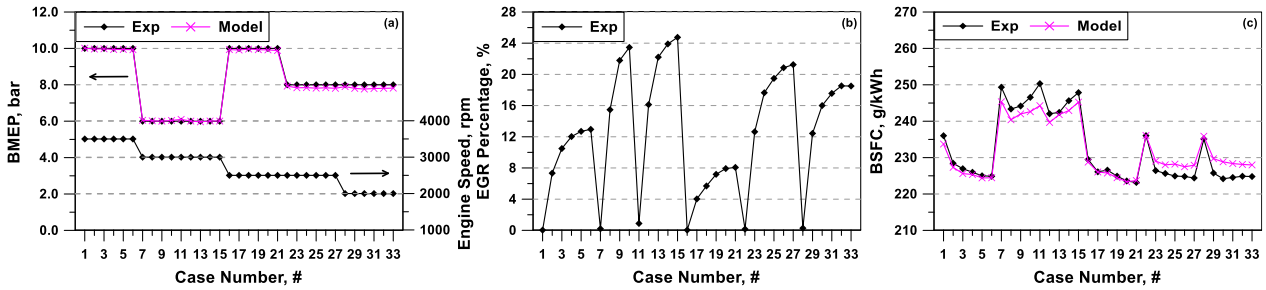

Figure 5-4 Experimental / numerical comparison of BMEP and engine speed (a), EGR percentage (b), and experimental/numerical comparison of BSFC (c) against the case number, for the set of 33 operating points.

The emission sub-models presented in section 3.8 have been here employed to predict the NO_x, CO, and uHCs. *Figure 5-5(a)* underlines a good model accuracy in the estimation of NO_X emissions. As expected, while increasing the EGR percentage, the NO_x production rate is less intense thanks to the lower temperatures of the burned gas. In *Figure 5-5(b)*, both computed and measured uHC_1 emission present an increasing trend when the EGR percentage increases. This can be justified by a less effective post-oxidation process of the uHC released from the crevice volumes, due to lower in-cylinder temperatures. The model in some cases overpredicts the intensity of this effect, for instance, the second and third EGR-sweep. *Figure 5-5(c)* reports the experimental / numerical results for CO. This figure, coupled to *Figure 5-4(b),* shows an inverse relation between CO and EGR rate. This is quite well captured by the model, once again, excepting for the second and third EGR-sweep. Despite the above-mentioned inaccuracies, the pollutant sub-models provide satisfactory results, being capable to correctly sense the superimposed variations of in-cylinder thermodynamic conditions (pressure, temperature) and composition (EGR percentage).

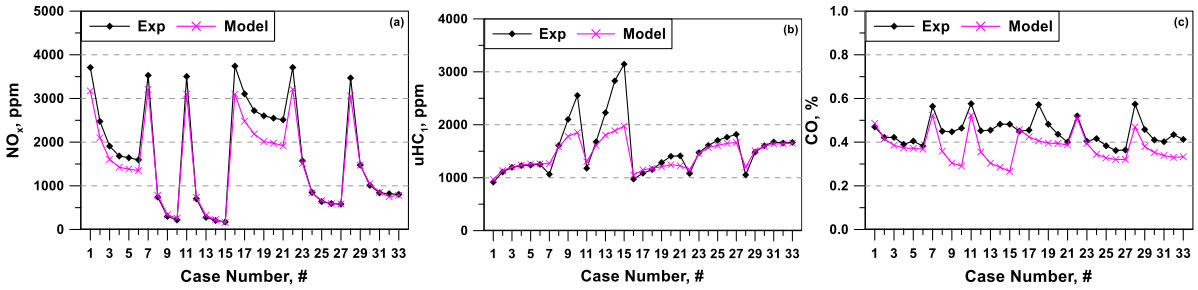

Figure 5-5 Experimental / numerical NO_x, [ppm] (a), uHC, [ppm] (b), and CO, [%] (c) comparison against the case number, for the set of 33 operating points.

5.1.1.4 Model assessment at part load

After ascertaining the prediction capabilities of the model at full load, it is used to compute the engine performance and combustion parameters over its whole operating range. The two LFS correlations are compared once again to assess their relative impact on the combustion simulation under part load conditions. Coherently with the full load calculations, the effect of the flame stretch on the LFS is not taken into account at this stage. The present assessment includes operations with and without the application of an external EGR. Note that all the following results are obtained without modifying the values of the model tuning constants identified at full load operations. *Figure 5-6(a)* shows the contour plot in the engine operating plane of the percent difference between experimental and numerical BSFCs, computed according to the definition below:

$$\Delta BSFC\% = \frac{BSFC_{exp} - BSFC_{model}}{BSFC_{exp}} \cdot 100 \tag{5.1}$$

The contour plot of the measured BSFC is shown in *Figure 5-6(b)* for completeness. Both pictures refer to EGR-free operating conditions and to simulations performed using only "Cor B", as the Metghalchi correlation provides very similar BSFC levels. The error map in *Figure 5-6(a)* shows a satisfactory global accuracy of the BSFC predictions, which mainly depends on the good reproduction of engine breathing, combustion evolution, and wall heat transfer also under part load operations. The largest errors are observed at medium loads and low speeds, where the BSFC is overestimated by up to 5%, and at high speeds, where the BSFC is underestimated by up to 6%. These disagreements are probably due to an overestimation of the heat transfer at low engine speeds and an underestimation of the pumping work at high speeds.

A similar comparison is reported in *Figure 5-7* for the case of activated eEGR circuit. The experimental mass percentages of recirculated gas are shown in *Figure 5-7(c)*. Looking at the latter, it can be noted that the highest eEGR rates are applied at low speeds and medium-high loads, resulting in a maximum BSFC reduction of 10 g/kWh, i.e. about 4% (compare *Figure 5-6(b)* with *Figure 5-7(b)*). At increasing engine speed, the EGR rate is reduced because of the unfavourable pressure gradient between the intake and exhaust pipes. After testing the overall accuracy of the model also at part load, the relative impact of two LFS correlations is assessed with reference to the prediction of the characteristic combustion durations $MFB_{10\text{-}50}$ and $MFB_{0\text{-}10}$. The maps in *Figure 5-8(a)* and *Figure 5-8(b)* show the angular differences between experimental and predicted $MFB_{10\text{-}50}$ for "Cor A" and "Cor B", respectively, and for EGR-free operations. Similar data are plotted in *Figure 5-9(a)* and *Figure 5-9(b)* for the case with eEGR. For completeness, *Figure 5-8(c)* and *Figure 5-9(c)* display the values of $MFB_{10\text{-}50}$ resulting from the measurements. As a first consideration, the comparison of the

experimental combustion durations with and without eEGR (*Figure 5-8(c)* and *Figure 5-9(c)*) shows that the exhaust gas recirculation causes, as expected, some increase in the combustion duration. This effect is more pronounced for the highest eEGR percentages, namely at low speeds and low-to-medium loads (*Figure 5-7(c)*).

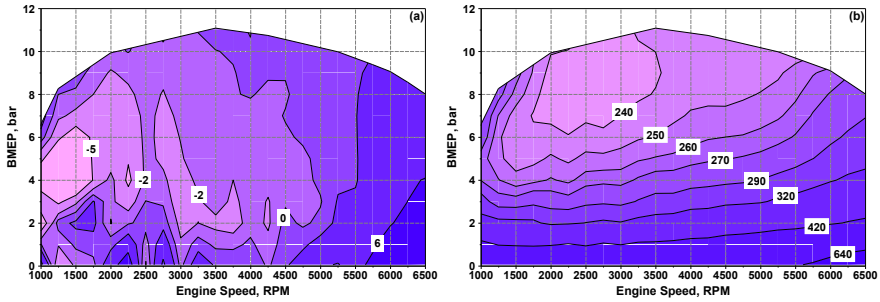

Figure 5-6 Maps of (a) BSFC percent error without eEGR, and (b) experimental BSFC without eEGR [g/kWh].

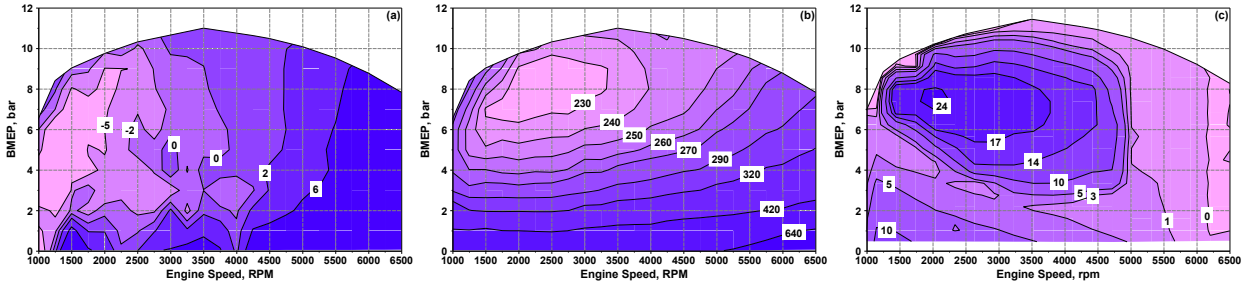

Figure 5-7 Maps of (a) BSFC percent error with eEGR, (b) experimental BSFC with eEGR [g/kWh], and (c) measured EGR mass fractions.

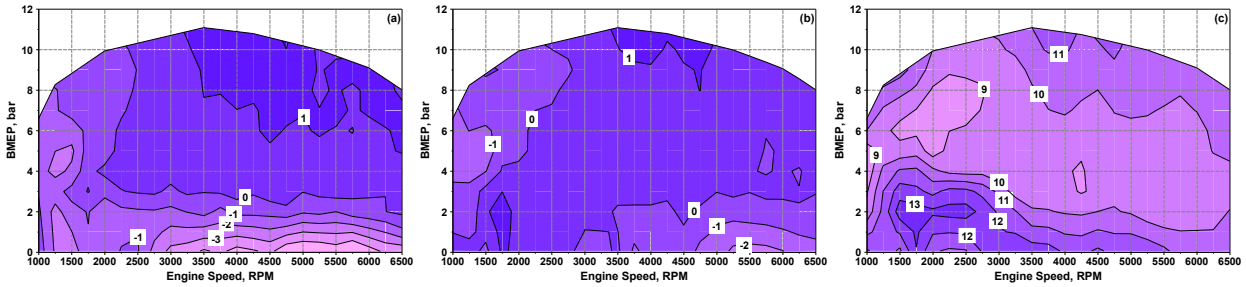

Figure 5-8 Maps of $MFB_{10\text{-}50}$ [CAD] without eEGR: (a) $MFB_{10\text{-}50,exp}$ - $MFB_{10\text{-}50,model}$ for "Cor A", (b) $MFB_{10\text{-}50,exp}$ - $MFB_{10\text{-}50,model}$ for "Cor B", (c) experimental data.

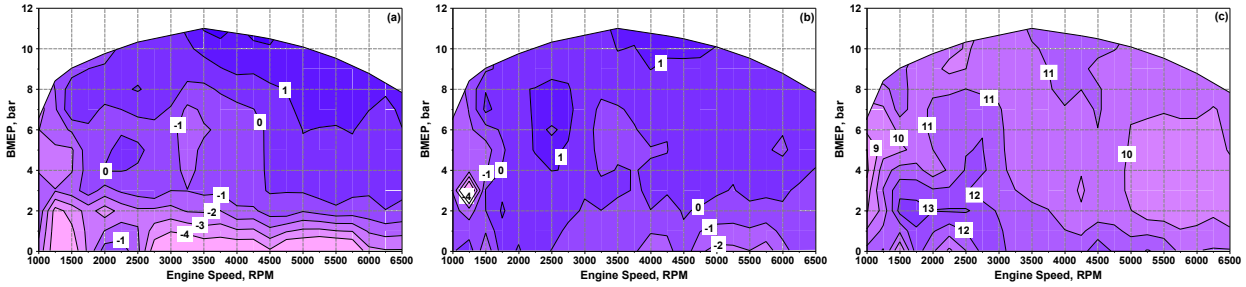

Figure 5-9 Maps of $MFB_{10\text{-}50}$ [CAD] with eEGR: (a) $MFB_{10\text{-}50,exp}$ - $MFB_{10\text{-}50,model}$ for "Cor A", (b) $MFB_{10\text{-}50,exp}$ - $MFB_{10\text{-}50,model}$ for "Cor B", (c) experimental data.

Looking at the results for "Cor A" in *Figure 5-8(a)* and *Figure 5-9(a)*, the combustion duration is correctly predicted in most of the engine operating plane. However, at decreasing BMEP, the model overestimates the $MFB_{10\text{-}50}$ duration, especially for eEGR operations, where a maximum error of 4 CADs is obtained at medium / high speeds and low load. When using "Cor B" *Figure 5-8(b)* and *Figure 5-9(b)*), the prediction errors decrease, being mostly in the range ± 1 CAD. In summary, both LFS correlations prove to be sufficiently accurate over the whole engine operating plane, although "Cor B" leads to better predictions in the most critical conditions (high eEGR rates and very low engine loads). Moving to the analysis of the combustion process first stage, the simulated durations from the spark event to the MFB_{10} angle are compared with the experimental data in *Figure 5-10 and Figure 5-11*, for operations without and with eEGR, respectively. As expected, the measurements show that the combustion duration significantly lengthens at decreasing BMEP (*Figure 5-10(c)*), especially in the presence of exhaust gas recirculation (*Figure 5-11(c)*). The differences between experimental and numerical data in *Figure 5-10(a)* and *Figure 5-10(b)*, which refer to eEGR-free operations, show that the model provides accurate predictions only for load levels over 6 bar BMEP, whereas it underestimates the combustion duration for lower engine loads. For very low BMEPs, errors as high as 22 CADs are obtained. In presence of eEGR (*Figure 5-11(a)* and *Figure 5-11(b)*), the model exhibits a similar behaviour, but a significant underestimation of $MFB_{0\text{-}10}$ is also observed in the map region with the highest EGR rates, namely, at medium-high loads and low speeds.

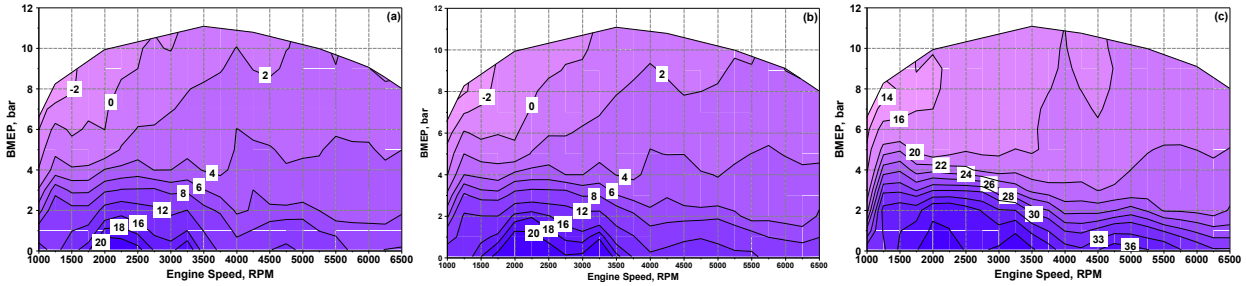

Figure 5-10 Maps of $MFB_{0\text{-}10}$ [CAD] without eEGR: (a) $MFB_{0\text{-}10,exp}$ - $MFB_{0\text{-}10,model}$ for "Cor A", (b) $MFB_{0\text{-}10,exp}$ - $MFB_{0\text{-}10,model}$ for "Cor B", (c) experimental data.

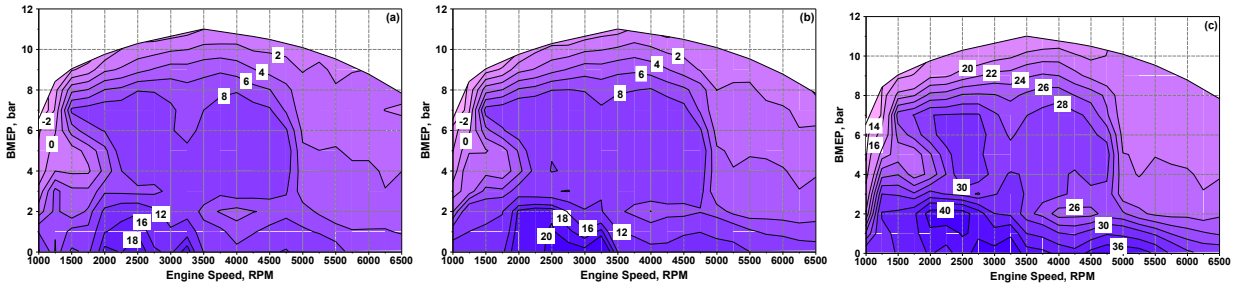

Figure 5-11 Maps of $MFB_{0\text{-}10}$ [CAD] with eEGR: (a) $MFB_{0\text{-}10,exp}$ - $MFB_{0\text{-}10,model}$ for "Cor A", (b) $MFB_{0\text{-}10,exp}$ - $MFB_{0\text{-}10,model}$ for "Cor B", (c) experimental data.

The analysis of the characteristic combustion durations leads to two main outcomes:

- The model predicts the combustion core ($MFB_{10\text{-}50}$) with good accuracy for both LFS correlations. Better results are provided by "Cor B".
- The model underpredicts the duration of the initial combustion stage ($MFB_{0\text{-}10}$), with higher errors at decreasing engine load and increasing eEGR rate. The LFS correlations behave similarly to each other.

Based on the above observations, a model refinement is required to improve the $MFB_{0\text{-}10}$ prediction at low loads. This issue is addressed by introducing the stretch effect in the LFS calculation, as discussed in the following, where only "Cor B" is considered since this correlation showed to provide a more accurate description of the combustion core.

To assess a possible improvement of the model formulation, the calculations over the whole engine operating plane are repeated considering the flame stretch effect. The resulting maps of $MFB_{0\text{-}10}$ are shown in *Figure 5-12(a)* for EGR-free operations and in *Figure 5-12(b)* for the case with eEGR.

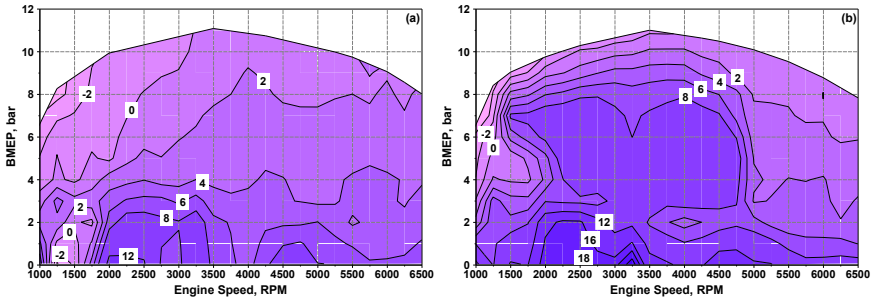

Figure 5-12 Maps of difference $MFB_{0\text{-}10,exp}$ - $MFB_{0\text{-}10,model}$ [CAD] when using "Cor B" and flame stretch model: (a) without eEGR and (b) with eEGR

Comparing these results with those obtained ignoring the flame stretch (*Figure 5-10(b)* and *Figure 5-11(b)*, respectively), it is observed that significant improvements arise for loads lower than 4 bar BMEP. Except for very low engine speeds, the model continues to underestimate the $MFB_{0\text{-}10}$ duration, with errors smaller than 6-8 CADs in most cases (see *Figure 5-12(a)* and *Figure 5-12(b)*). However, these results are considerably better than the ones obtained ignoring the stretch effect, which exhibits errors of 12 to 20 CADs at low engine loads (see *Figure 5-10(b)* and *Figure 5-11(b)*). The predicted maps of $MFB_{10\text{-}50}$ (*Figure 5-8(b)* and *Figure 5-9(b)*) and $MFB_{0\text{-}10}$ (*Figure 5-12(a)* and *Figure 5-12(b)*) show that the present model is able to reproduce quite accurately the variations in in-cylinder pressure and temperature, equivalence ratio, turbulence intensity and residual gas content over most of the engine operating plane. However, some inaccuracies emerge in the prediction of the eEGR influence on the early stage of the combustion process, as highlighted by the comparison of *Figure 5-12(a)* and *Figure 5-12(b)*. In fact, the latter shows errors of 6-8 CADs in the map region of

higher eEGR (medium / high loads), whereas in the same operating conditions without eEGR (*Figure 5-12(a)*), the error drops to 0-2 CADs. This is probably due to a poor description of the ignition process, which is not directly modeled. This problem could be overcome by introducing a dedicated model, such as the ones proposed in [9],[10]. However, these models require additional information concerning, for instance, the spark discharge duration and power, which are not directly available in most practical applications. Despite these difficulties, an ignition model will be investigated in future developments of the present work.

As a final check on the applicability of the present flame speed and stretch models, the combustion regimes in all the operating conditions experienced by the engine (both with and without eEGR) are reported in the Borghi diagrams shown in *Figure 5-13*. The plots depict the ratios of characteristic velocities (turbulence intensity, u', over laminar flame speed, S_L) and lengths (turbulence integral length scale, L_t, over flame thickness, δ_f) halfway through the combustion process (MFB_{50} events). It can be observed that most points lie within the corrugated flamelet regime, where the assumptions of the present models are valid. A few points fall close or just within the thin reaction regime, and they correspond to high engine speeds (large values of u') and/or large residual gas fractions (small values of S_L). Under such borderline operating conditions, where the combustion regime is expected to change, the predicted combustion durations, especially $MFB_{10\text{-}50}$, continue to agree well with the experimental data.

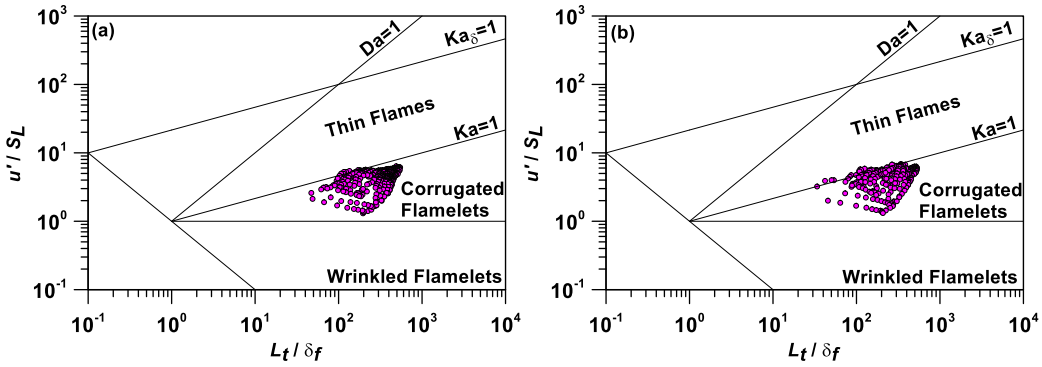

Figure 5-13 Borghi diagrams of the combustion regimes over the whole operating plane of the considered engine for operations (a) without and (b) with eEGR at MFB_{50} ($\delta_f = \nu / S_L$ is the flame thickness).

5.2. Ultra-lean Engines

Analysing the above conventional stoichiometric SI engine, minimum BSFC levels of about 230 g/kWh and 240 g/kWh emerged with and without the adoption of external EGR, respectively. Those levels drastically increase at reducing load. Those fuel consumptions result in CO_2 emissions of a B segment vehicle which are almost in line with the EU target of 95 g/km. At the current stage, pollutant

emissions (CO, NOx, uHC) of the considered engine architecture do not represent an issue for vehicle homologation, thanks to the abatement exerted by the EATS.

The CO_2 production remains a limit of stoichiometric SI engines for the fulfilment of CO_2 limits to come. A very promising solution is the ultra-lean combustion concept, which is expected to simultaneously improve the thermal efficiency and reduce CO_2 emissions. For this reason, two categories of ultra-lean engines will be investigated in the following, namely SI engines equipped by a pre-chamber device. Moreover, an insight into the issue of uHC emission will be discussed with reference to two large-bore engines fuelled with methane.

5.2.1. Single Cylinder Pre-chamber Engine fuelled with methane

The single cylinder engine here presented has been experimentally investigated at the Institute for Combustion Engines (VKA) of the RWTH Aachen University. Concerning this SCE, equipped with a direct fuel injection into the main chamber, its main specifications are listed in *Table 5.3*.

Table 5.3 Main features of pre-chamber methane SCE.

Parameters	*Values*
Bore	75 mm
Stroke	90.5 mm
Stroke / Bore Ratio	1.207
Displacement	399 cm^3
Peak pressure capability	170 bar
Geometrical compression ratio	13
Injection system	Lateral solenoid, 350 bar
Fuel in main chamber	DI injector, gasoline RON 98
Fuel in pre-chamber	DI injector (CNG or H_2)
Pre-chamber volume	1080 mm^3
$V_{pre\text{-}chamber}$ / V_{TDC}	3.6 %
Pre-chamber holes	4 - two pairs of different hole size
$A_{jet\ holes}$ / $V_{pre\text{-}chamber}$	0.033 cm^{-1}
Intake valve opening	3 CAD BTDC (@1mm lift)
Exhaust valve closure	3 CAD ATDC (@1mm lift)
Start of injection MC	295 CAD BTDC
Start of injection PC	180-215 CAD BTDC

Due to the long stroke (90.5 mm) combination with the arrangement of the valves with the intake port and the combustion chamber shape, the charge motion level obtained is comparable to state-of-the-art series production turbocharged engines. Additional details of the layout process are reported in [11], while the SCE design is shown here in *Figure 5-14*.

The pre-chamber device is equipped with CFD-optimized 4 holes (*Figure 5-14*(*d)*), and a 350 bar DI fuel injection system. An ignition module is incorporated in the cylinder head. The combustion chamber designed has been realized on the basis of the size of a generally used M12 spark plug. Thus, the outer diameter of the pre-chamber shaft is set equal to 12 mm to perfectly fit into the defined combustion chamber geometry. In the sectional view of *Figure 5-14*(*a-b),* the PC is arranged in a central combustion chamber position. As usual with spark plug shafts, cooling water flows around it.

This prototype of SCE has been investigated considering three different configurations: Conventional Spark Plug, active or passive pre-chamber. The CSP operations have been performed equipping the engine head with an adapter, instead of the pre-chamber, to realize a conventional engine design with an undivided combustion chamber. Hence, this design reproduces a conventional SI engine architecture with a spark plug. This modular design allows an easy replacement with different pre-chambers geometries. For both pre-chamber and conventional SI operation, a single electrode M10 spark plug with a heat value of 8 has been used.

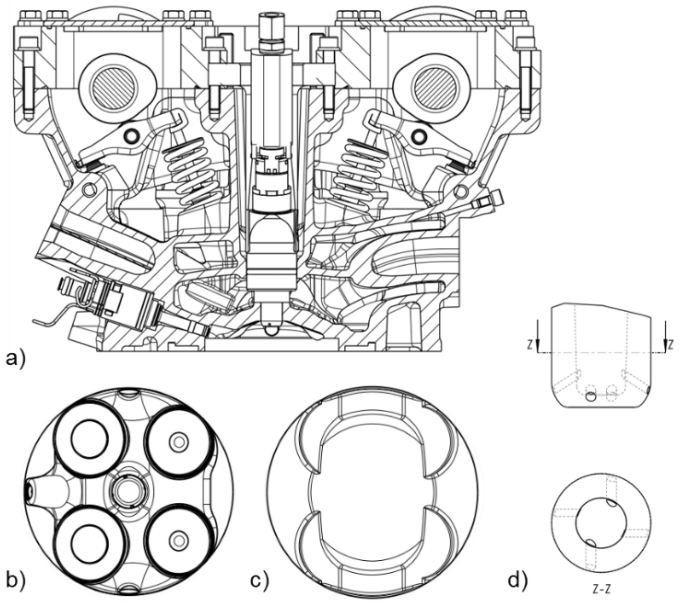

Figure 5-14 PC engine layout: a) sectional view of cylinder head b) combustion chamber dome c) piston crown for CR=13, d) pre-chamber.

Concerning the active pre-chamber, it can be fed by Compressed Natural Gas (CNG) or hydrogen from pressure bottles. In the case of CNG, the injection pressure is between 4.5 and 8 bar, depending on the desired mass flow rate. While, in the case of hydrogen, a higher pressure of about 20 bar is set

and a piezo actuated outward opening injector is applied. In passive conditions, the pre-chamber injection is simply switched off. Hence, the same pre-chamber geometry is used in either active or passive mode.

The intake air is conditioned to 30 °C in the intake runner. The pressure upstream of the throttle flap and into the exhaust manifold is fixed at 1.01 bar during throttle operation. Instead, considering boosted conditions, the pressure into the exhaust is fixed equal to the one into the manifold. The exhaust gas relative air-fuel ratio is obtained by the formula of Spindt [12]. The share of the employed fuels (CNG, H_2, and gasoline) is considered to establish the correct air / fuel ratio.

Concerning the experimental set-up, at each tested point the Spark Advance is selected to realize an optimal combustion phasing, namely an angular position of the 50% of the Mass Fraction Burned at 7-8 CAD AFTDC. But if knocking combustions are detected, the SA is properly retarded. Pressure measurements are carried out with the equipment listed below:

- two Kistler A6045 B pressure transducers are flush mounted in the combustion chamber side roof;
- one Kistler 6054 BR pressure transducer is flush mounted in the pre-chamber;
- signal sampling is performed via Kistler charge amplifiers and a FEV combustion analysis system at a resolution of 0.1 CAD;
- for the dynamic intake and exhaust gas pressures, Kistler 4045 A5 pressure transducers are chosen and data are sampled with a resolution of 1 CAD.

For the measurement of the static pressures and temperatures, conventional pressure transducers and thermocouples are adopted (measurement averaging interval: 30 s). Oil and water conditioning systems enable steady-state operations.

Aiming at developing and validating the model, 39 different operating points, listed in *Table 5.4*, are investigated. Different λ sweeps at constant load have been performed at various engine speeds. For each operating point, 500 consecutive cycles are recorded, deriving an ensemble average of these cycles for the model comparison. All the operating points have shown a satisfactory stability with a IMEP CoV. This has been assessed in each operating condition, resulting in rather low values (1-2%), with higher levels at leaner λ values. The engine operating point selection allows yielding a database to validate the model predictive potential by varying mixture composition (from stoichiometric to very lean) and turbulence levels.

Table 5.4 List of investigated points of the pre-chamber engine

Case	*Operating condition rpm @ IMEP*	*Engine*	λ	*SA CAD AFTDC*	MFB_{50} *CAD AFTDC*
1	2000 rpm @ 15 bar	CSP	1.0	2.1	23.3
2		CSP	1.2	0.8	25.5
3		CSP	1.4	-4.5	22.1
4		CSP	1.6	-8.8	21.2
5	2000 rpm @ 15 bar	PASSIVE	1.0	11.7	29.1
6		PASSIVE	1.4	2.7	24.1
7	4000 rpm @ 15 bar	PASSIVE	1.0	3.6	20.1
8		PASSIVE	1.4	-3.4	17.6
9	2000 rpm @ 3 bar	CNG	1.6	-15.8	8.6
10	2000 rpm @ 4 bar	CNG	1.0	-11.3	8.1
11		CNG	1.4	-10.8	7.5
12		CNG	1.8	-17.6	7.9
13	2000 rpm @ 10 bar	CNG	1.0	2.3	17.1
14		CNG	1.5	-7.6	7.7
15		CNG	2.0	-16.4	7.1
16	2000 rpm @ 15 bar	CNG	1.0	14.9	33.2
17		CNG	1.4	6.8	25.6
18		CNG	1.8	-3.4	16.7
19		CNG	2.0	-7.5	14.2
20		CNG	2.4	-17.2	9.8
21	2500 rpm@ 12 bar	CNG	1.0	4.0	21.7
22		CNG	1.4	-2.6	15.8
23		CNG	1.8	-13.2	7.78
24		CNG	2.0	-16.4	7.7
25		CNG	2.2	-23.0	7.9
26	2500 rpm @ 6 bar	CNG	2.0	-21.3	7.50
27	3000 rpm @ 13 bar	CNG	1.0	5.8	23.6
28		CNG	1.4	0.3	20.3
29		CNG	1.8	-12.2	9.1
30		CNG	2.0	-16.9	7.8
31		CNG	2.2	-21.0	7.8
32	3000 rpm @ 7 bar	CNG	2.0	-22.7	7.4
33	4000 rpm @ 16 bar	CNG	1.0	11.4	33.7
34		CNG	1.4	5.7	32.2
35		CNG	1.6	2.3	35.2
36	2000 rpm @ 15 bar	H_2	1.4	11.9	29.7
37		H_2	1.8	1.9	20.2
38		H_2	2.0	-4.1	13.8
39		H_2	2.4	-15.7	7.9

Consistently with the experimental setup, a detailed 0D/1D scheme is developed for all the investigated engine architectures (conventional engine and PC ones, both active and passive) in a

commercial modelling framework. The description of the flow inside the intake and the exhaust pipes is based on a 1D simulation approach, whereas the previously described phenomenological 0D sub-models are used to reproduce in-cylinder phenomena inside the pre-chamber engine.

The combustion evolution is handled by the re-assessed quasi-dimensional fractal model, presented in section 3.5 to consider the propagation of the turbulent jet. Since this SCE during the experimental campaign has been fed by three different fuels, different laminar flame speed correlations are embedded into the model. Concerning the MC, a simulation-derived correlation for a TRF gasoline blend is employed in all the tested operating points [13]. The same formulation is also applied for the passive PC. Whereas for the active pre-chamber, the correlations proposed in [14] and [15] are employed for the combustion of CNG and H_2, respectively. However, due to the mass exchanges, some fuel blending may occur in an active pre-chamber. Hence, the utilization of pure-fuel correlations for the actual operation of this engine represents a simplification.

For the model closure, the phenomenological K-k-T turbulence extended model, described in 3.5, is applied to both chambers, including the turbulence production due to incoming flow through the orifices. As said, a Woschni-like correlation is employed for the heat transfer in the pre- and main-chamber, neglecting the heat losses in the PC holes.

Firstly, some preliminary comparisons have been performed between 3D CFD results provided by IFPEN, for a similar pre-chamber engine. A single operating point was available at 3000rpm@13bar IMEP, with an average relative air / fuel ratio of 1.8. In this calculation, the pre-chamber is directly fed with a commercial gasoline, whereas a homogenous premixed charge is supplied through the inlet port in the MC. More details on the 3D analysis can be found in [16].

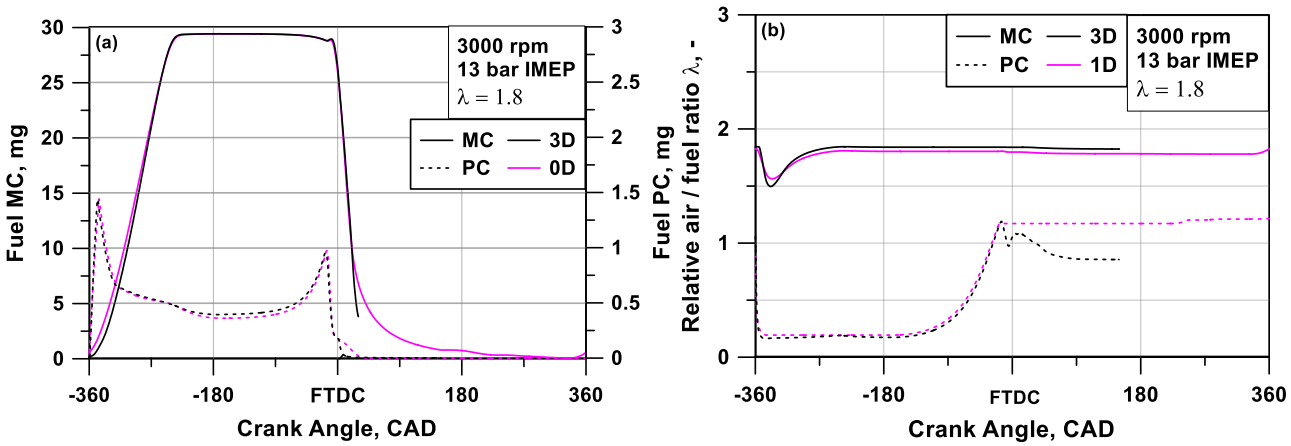

Figure 5-15 0D/3D comparison of fuel mass (a) and λ (b) in PC and MC at 3000rpm@13bar, λ=1.8

The capacity of the 1D model to reproduce the mass exchange is primarily analysed. In *Figure 5-15*, the fuel in both chambers (*a*) and the related air / fuel ratio (*b*) are shown crank angle based.

The comparison is well-assessed, demonstrating the model potential to properly sense the mass flux through the orifice, and the related variations in composition. In *Figure 5-15(a)*, the abrupt increment of the fuel mass, due to the injection into the PC during the intake phase, is well captured by the model, so as the following decrement due to outflow in the MC. Around the TDC, another fuel mass increment the PC arises, because of the fresh charge pushed within the PC depending on the pressure gradient between the two chambers. As expected, the MC is less sensitive to the mass exchange, even if, as can be seen in *Figure 5-15(b),* a λ decrement occurs around -340 CAD because of the injection into the PC. Since the agreement in terms of both fuel mass and relative air / fuel ratio is well captured, also the trapped air in the cylinder is correctly estimated.

Subsequently, following the hierarchical 1D-3D approach, the k-K-T model was tuned, according to the 3D results, whose analyses were carried out in motored conditions on the SCE engine. The model tuning allows to follow the 3D profiles of the turbulence intensity and integral length scale along the entire engine cycle and in both the chambers with satisfactory accuracy, as shown in *Figure 5-16*.

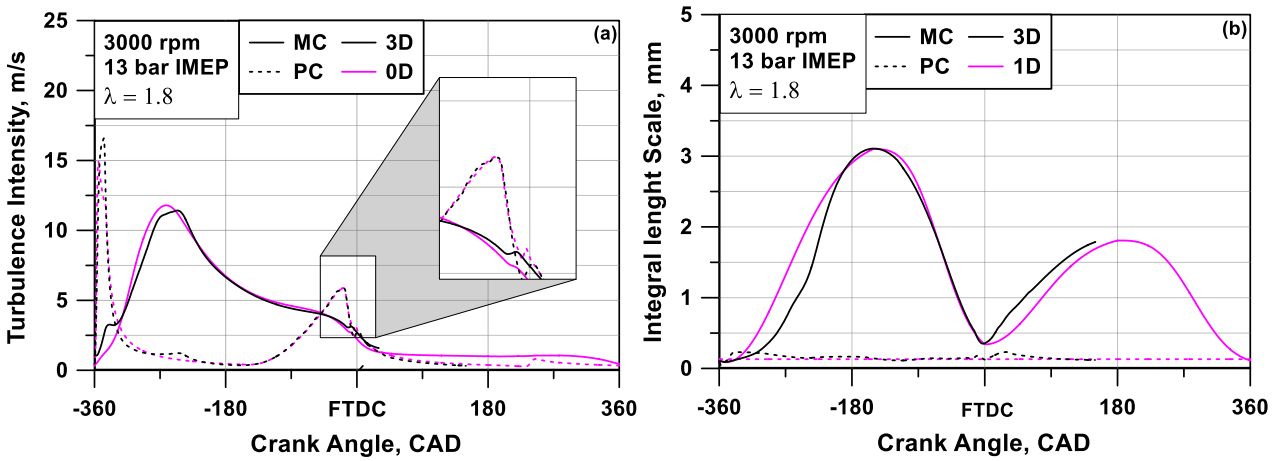

Figure 5-16 0D/3D comparison of turbulence intensity (a) and integral length scale(b) in PC and MC at 3000rpm@13bar, λ=1.8.

Then, the identified turbulence tuning constants are embedded in the 1D model of the tested engine, with the aim to tune and validate the combustion model. Hence, the model was validated through experimental / numerical comparison for all the operating points listed in *Table 5.4*. To get the maximum experimental / numerical congruence, the same boundary conditions as in the experiments have been assigned in the simulations, i.e. the spark timing, intake and exhaust pressures and temperatures, and the injected fuel masses.

Through a trial-and-error procedure, a single set of tuning constants was identified to determine the lowest average experiment / simulation error for all the investigated configurations, with special regard to the pressure cycles in both PC and MC.

Concerning the model validation, in the first stage, the global performances by experimental / numerical comparisons, including the Root Mean Squared Error (RMSE) as a global indicator of the model accuracy are analysed, then comparisons in terms of pressure cycles and related burn rate are presented.

Starting from the air flow rate, depicted in Figure 5-17, it is observed a satisfactory prediction, since all the investigated points are within an error band ± 5%. The related RMSE of 1.92 kg/h demonstrates an accurate schematization of the intake and exhaust pipe geometry and a proper specification of the valve flow coefficients. The IMEP values, in Figure 5-17, remains in most cases in the allowable error band of ± 5%, showing a good agreement with the experimental data.

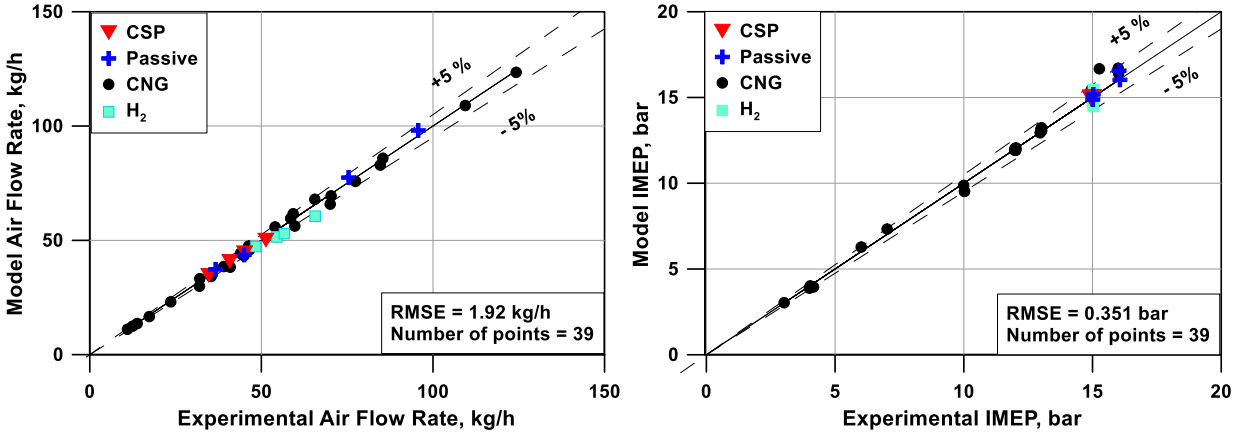

Figure 5-17 Experimental vs. numerical air flow rate (a), IMEP (b) comparisons.

Indeed, the exhaust temperature depicted in Figure *5-18*, is affected by a certain systematic overestimation, with a RMSE of around 56.4 K. A potential reason could be the underestimation of the heat exchange in the cylinders or in the exhaust pipes.

The MFB_{50} can be used to measure the overall combustion model reliability since in these simulations the spark timing is imposed. A satisfactory model accuracy is shown in Figure *5-18* having an error within a ± 5 CAD band in most cases, and an average of 2.42 CAD.

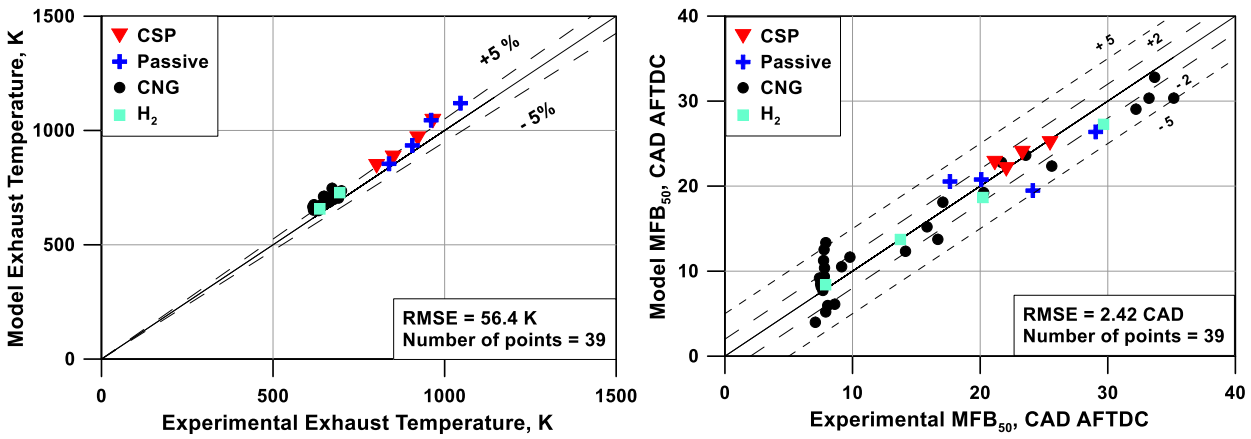

Figure 5-18 Experimental vs numerical exhaust temperature (a), MFB_{50} (b) comparisons.

The good prediction in terms of combustion phasing and speed in both PC and MC is confirmed by *Figure 5-19*, reporting the comparison of the peak pressure crank angle locations (*a*) and levels (*b*), The peak location is better predicted in the PC (RMSE equal to 2.09 CAD) than in the MC (RMSE equal to 2.83 CAD). In the latter, the combustion prediction is more complex since it depends on the superimposition of various effects (combustion processes in both PC and MC). Concerning the PC, the results are more directly related to the spark timing, which is an imposed datum. Moreover, the air / fuel ratio in the PC is almost stoichiometric for all the considered operating conditions, while it widely changes in the MC among the different tested cases.

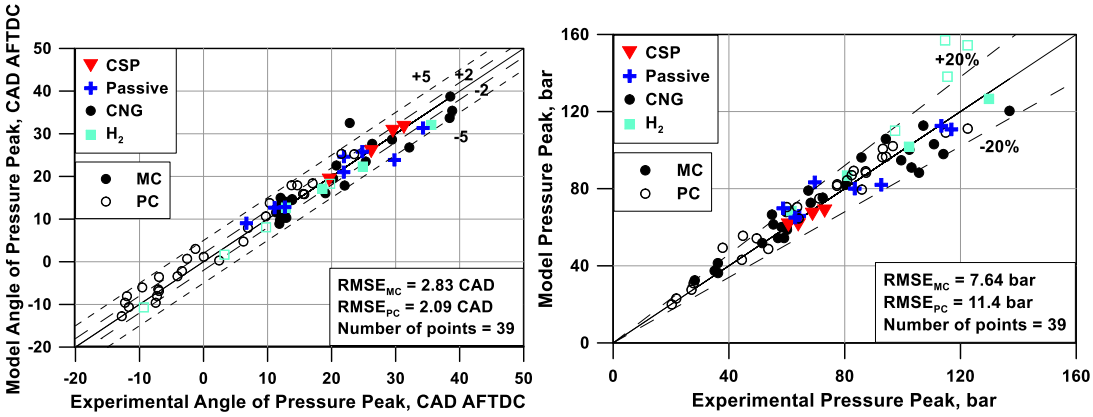

Figure 5-19 Experimental vs numerical angle of pressure peak (a) and pressure peak (b) for both MC and PC.

Further, to check the consistency of the combustion model, in *Figure* 5-20 the angular positions of representative combustion stages (spark event and 10%, 50% as well as 90% of MFB) are depicted, versus the air / fuel ratio. The trends concern all the investigated engine architectures for a representative low speed / high load operating point (2000 rpm @ 15 bar IMEP). Globally, the model has demonstrated to realize very accurate predictions of all the considered combustion angles for the conventional architecture. However, for the pre-chamber device (both active and passive modes), a certain underestimation of the combustion duration for the cases at reduced λ arises. The combustion slow-down for leaner mixtures (more evident for the conventional engine) is captured by the model mainly thanks to the decrease of the laminar flame speed. This behaviour is compensated for the pre-chamber configurations, especially for the active version, by the effect of the turbulent jets emerging from the PC. This is quite well captured by the model, as shown in *Figure 5-20(a)*. An overestimation of the combustion duration only occurs at the leanest air / fuel mixtures for the CNG case.

The final check for the simulation reliability is reported in *Figure 5-20(b)*, by the experimental / numerical comparisons of the Indicated Thermal Efficiency (ITE) for all the tested variants at 2000 rpm@15 bar IMEP. Because of confidentiality, all the data are normalized by the efficiency of the conventional engine under stoichiometric operation. Once again, the model demonstrates to well capture the efficiency improvement, achievable with leaner air / fuel rates, for all the considered

ignition devices. However, it is evident that, for the analysed engine, CSP and passive variants are not able to operate with λ values above 1.5-1.6, due to excessively high IMEP CoV and misfires. This limit is indeed extended up to 2.4 by the active pre-chamber, fuelled with either CNG or H_2. Another interesting outcome is that a conventional ignition device is preferable in terms of efficiency if the engine works with a stoichiometric or slightly lean air / fuel mixture. With λ values greater than 1.1, a pre-chamber system becomes indeed better from the ITE viewpoint, and the advantages constantly rise with increasing air / fuel ratio. The model, as stated above, demonstrates to capture this behaviour with adequate accuracy.

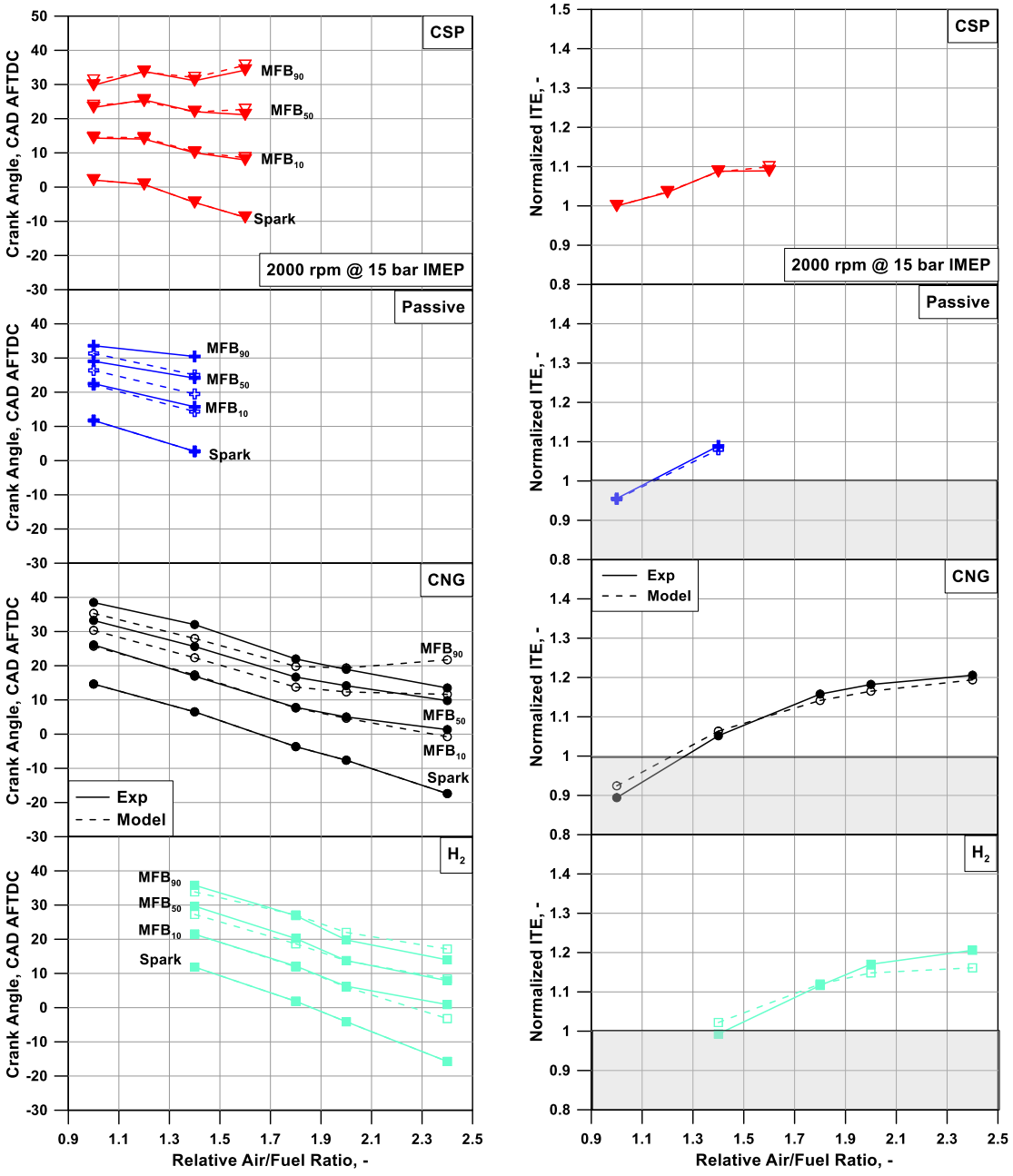

Figure 5-20 Experimental vs numerical angles of significant combustion stages (Spark, MFB_{10}, MFB_{50}, MFB_{90}) (a) and numerical normalized ITE(b) vs. the relative air / fuel ratio for different engine architectures at 2000 rpm @ 15 bar IMEP.

As said, a deeper insight into the combustion model reliability is given by the experimental / numerical comparisons of the pressure traces and of the related filtered burn rates, shown in *Figure 5-21, Figure 5-22*, for nine representative cases. In the reported figures, the experimental (numerical) data are represented with black (magenta) curves, continuous or dashed for the MC or PC, respectively.

For the conventional engine configuration, a λ sweep at 2000rpm@15 bar is reported in *Figure 5-21*, showing a quite satisfactory agreement for both pressure traces and burning rate. The experimental / numerical accuracy slightly worsens at increasing λ, probably due to a reduced sensitivity of the adopted laminar flame speed correlation to the air / fuel ratio.

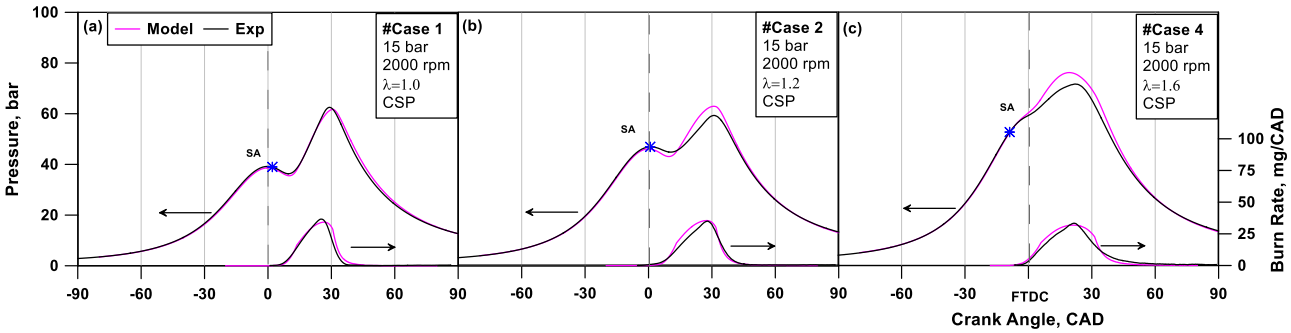

Figure 5-21 Experimental / numerical comparison of cylinder pressure traces and burn rates at 2000 rpm@15 bar IMEP for a CSP engine configuration, (a) λ=1.0, (b) λ=1.2, (c) λ=1.6.

In *Figure 5-22,* three different operating variants with the PC configuration (CNG and H_2 injection as well as no injection) are compared at 2000rpm@15 bar in each case for the minimum / maximum leaning of the air / fuel ratio. Comparing the three profiles on right with the correspondent ones on the left of *Figure 5-22*, it appears a boost pressure increment a unique possible way to gain the prescribed load with lean mixtures. It emerges that during the compression, the model well reproduces the gap between PC and MC pressure traces, thanks to a proper selection of the PC hole discharge coefficient. Concerning the combustion development, the model is able to properly sense the different fuels injected in the PC, detecting the maximum (minimum) burning speeds in the PC for H_2 (passive) mode. An intermediate behaviour emerges for CNG PC fuelling. The pressure peaks in both main- and pre-chamber are rather well predicted in most cases. In H_2 operation, the model generally overestimates the PC burning speed probably because of the absence of fuel blending coming from the main chamber. In some cases (#20 and #39), the numerical burning rate in the MC has lower peaks than the experimental datum, compensated by a faster burning rate at the combustion beginning.

Concerning the other operating points of *Table 5.4*, the experimental / numerical agreement is quite satisfactory in terms of global shape, phasing, and location of the peaks in both MC and PC.

All the results reported in this section in terms of global performance parameters and combustion events demonstrate the consistency and reliability of the proposed numerical approach, considering the relevant range of operating conditions (speed, load, and air / fuel ratio).

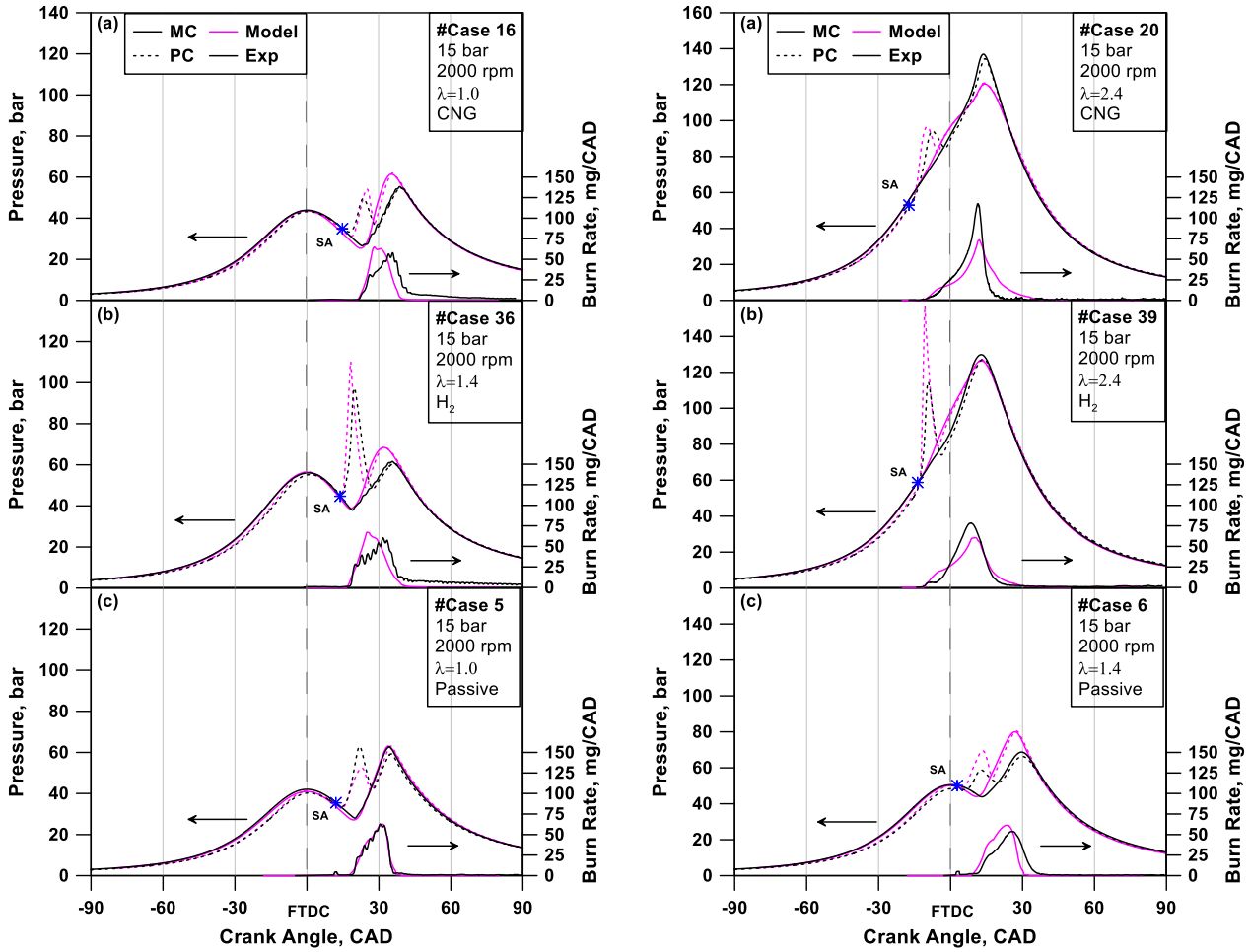

Figure 5-22 Experimental / numerical comparison of cylinder pressure traces and burn rates at 2000 rpm@15 bar IMEP, (a) λ=1.0 CNG (b) λ=2.4 CNG, (c) λ=1.4 H_2 (d) λ=2.4 H_2 , (e) λ=1 passive (f) λ=1.4 passive.

5.2.2. Single Cylinder Pre-chamber Engine fuelled with gasoline

The second pre-chamber engine here analysed presents a similar architecture (SCE, comparable displacement), but some differences, especially regarding the compression ratio, the valve timing, and the PC design. The engine design and experimental testing were conducted at IFPEN facilities. In this new configuration, the SCE is equipped with an active pre-chamber, fitted with a spark plug and a gasoline direct injector. The PC has 4 holes with two pairs of different hole sizes of around 1 mm diameter to exchange gases with the main combustion chamber. The details of the design process for this SCE are reported in [16]. The engine is featured by a compression ratio of around 15:1 together with an early intake valve closing strategy (intake valve lift duration of 123 CAD). The intake and exhaust camshafts are phased to obtain maximum positive valve overlap. The fuel used for these tests is a standard E10 gasoline. The engine is operated with a gasoline port fuel injection at

200 bar. The same injection pressure is used for the gasoline direct injection inside the pre-chamber. The main engine specifications are listed in *Table 5.5*.

Table 5.5 Main features of pre-chamber gasoline SCE.

Parameters		*Values*
Bore		76 mm
Stroke		90 mm
Displacement		408 cm^3
Peak pressure capability		180 bar
Geometrical compression ratio		~15
Fuel injection		gasoline port fuel injection, 200 bar
Intake valve lift duration		123 CAD (@1mm lift)
Active PC	Volume	~1 cm^3
	Hole	4 - two pairs of different hole size
	Fuel inj.	gasoline direct injection, 200 bar
Intake valve opening		+3 CAD BTDC (@1mm lift)
Exhaust valve closure		+14 CAD ATDC (@1mm lift)
Start of injection MC		140 CAD BTDC
Start of injection PC		300 CAD BTDC

Pressurized intake air is provided by an external compressor through a sonic flowmeter in order to simulate boosted conditions at the test bench. The intake dry air is conditioned at 40 °C for all tests. An exhaust flap is used to simulate the backpressure of a real turbocharging system. For the tests reported here, the exhaust flap position is adjusted in order to set the exhaust pressure equal to the intake pressure in order to reproduce the actual behaviour of a turbocharged engine, where boost pressure and backpressure are comparable. Oil and coolant are supplied by external electrically driven pumps and temperatures are kept constant at 90°C ± 2°C.

Ignition and injection timings are controlled with an in-house IFPEN control module. The global gasoline consumption is measured with a Low Pressure (LP) Coriolis Micromotion Elite CFM10 mass flowmeter located upstream of the gasoline high pressure pump. A gasoline fuel rail distributes the fuel for the pre-chamber and for the main chamber (port fuel injection). The gasoline mass flow rate injected in the PC is measured by a High Pressure (HP) Coriolis flowmeter. Therefore, the gasoline mass flow rate for port fuel injection can be obtained by subtracting the measure from the HP flowmeter to that from the LP flowmeter. Extremely low injection durations and fuel flow rates (<0.5mg/st) are used in the PC. This means that a shot-to-shot deviation can be expected for the intrinsic pre-chamber injector performance. In addition, even small rail pressure oscillations can

further alter the shot-to-shot repeatability at such low fuel flow rates for which usual injection systems are not designed. Consequently, it means that the measure of the fuel mass flow rate injected in the PC might be inaccurate when extremely low. In the end, the consistency of each fuel mass flow rate is validated by the measure of the LP Coriolis flowmeter.

Measurements of static pressures and temperatures are performed with conventional pressure transducers and thermocouples during an averaging interval of 30 seconds. The combustion process is monitored by different pressure transducers as follows:

- For the main combustion chamber, a Kistler 6043A pressure transducer is flush mounted in the combustion chamber side roof;
- For the pre-chamber, a Kistler 6054 BR pressure transducer is flush mounted in the PC volume;
- For the dynamic intake pressure, a Kulite XT123B190-100A pressure transducer is chosen and the signal is sampled by an Endevco charge amplifier;
- For the dynamic exhaust pressure, an AVL QC43D pressure sensor is implemented at the cylinder head outlet.

These pressure signals are recorded each 0.1 CAD for 300 consecutive engine cycles. Excepting the intake pressure sensor, all the other sensor signals have their sampling performed via Kistler 5064C22 charge amplifiers. The average pressure traces of both PC and MC pressure sensors are used for performing the heat release rate analyses, as detailed below. The pressure transducers in MC and PC are relative and both pressure signals are fitted by equalizing them with the average value of the high frequency exhaust pressure at the end of the exhaust stroke, close to Top Dead Centre when pressures at the exhaust and inside the cylinder are well balanced.

The main measurements performed on the single cylinder engine are summarized in *Figure 5-23*. Real-time engine-out emissions (uHC, CH4, CO, CO2, O2, NO, and NO2) are measured with Horiba MEXA-7100DEGR analyser thanks to the exhaust gas sampling at the end of the exhaust line. The relative air / fuel ratio λ is determined based upon the exhaust gas composition. The principle is based on the balance of carbon, hydrogen, oxygen, and nitrogen atoms between on the one side the exhaust gas molecules, and on the other side the air / fuel mixture at the intake. In these conditions, the reference λ is global, and it is not possible to determine the relative air / fuel ratios into the MC and PC separately. The experimental assessment of the relative air / fuel ratio into the pre-chamber is essential but would require the use of advanced techniques (such as fast FID) with, however, significant implementation constraints due to the very limited access into the PC. This issue will be addressed with the help of the numerical analyses reported below.

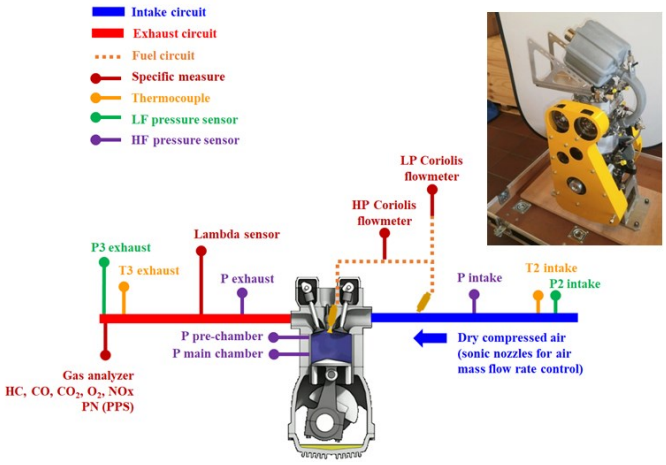

Figure 5-23 Measurement schematic of the single cylinder engine at the test bed [16].

The tests have been conducted in steady-state conditions at 3000 rpm engine speed and 13 bar IMEP. This operating point is selected following previous investigations as it is expected to be close to the point with a maximum indicated efficiency. The varied parameter is λ value. The fuel mass flow rate in the pre-chamber is optimized at $\lambda = 1.67$ and is kept constant at this value for the whole test. The SA is set for optimal combustion phasing (maximum torque), considering no knocking limitation (in case of knock, delayed spark advances are used until the knock limit is achieved). The start of injection for main-chamber and pre-chamber are also optimized and set constant for the λ variation (see *Table 5.5*). The investigated points are shown in *Table 5.6.*

Table 5.6 List of the investigated points of pre-chamber SCE at IFPEN at 3000 rpm @ 13 bar.

Case	#1	#2	#3	#4	#5	#6	#7	#8	#9	#10	#11	#12	#13
λ	1.00	1.11	1.25	1.42	1.53	1.59	1.64	1.73	1.79	1.97	2.06	2.11	2.15

The 1D model has been properly re-assessed to take into account the geometrical modifications and the different fuelling. Concerning the combustion model, the one described in section 3.5 has been applied, also considering mixture stratification and scavenging in the PC. The turbulence and combustion models have been tuned by following the procedure described in section 3.7. For this engine, the pollutant emission models, reported in section 3.8, have been applied too. To get the maximum experimental / numerical congruence, the same boundary conditions as in the experiments have been assigned in the simulations.

The model has been validated by comparing the simulation prediction with the experimental findings for all the available operating points. Firstly, global performance comparisons including the Root Mean Square Error are reported, followed by the comparison of cylinder pressure and related

burn rate. The air flow rate, depicted in *Figure 5-24(a)*, is satisfactorily predicted, with an error within the band ± 1%. The related RMSE of 0.39 kg/h denotes an accurate schematization of the intake and exhaust pipe geometry and a proper specification of the valve flow coefficients. The IMEP values, illustrated in *Figure 5-24(b),* are satisfactorily computed, with a model error of ± 1% in most of the operating points, and a RMSE of 0.062 bar *Figure 5-24(b)* also depicts the measured Coefficient of Variation (CoV) of IMEP. This highlights an allowable level (below 1.3%) for λ lower than 2, while substantially increases for the leanest cases. These additional data will help the interpretation of the emissions results.

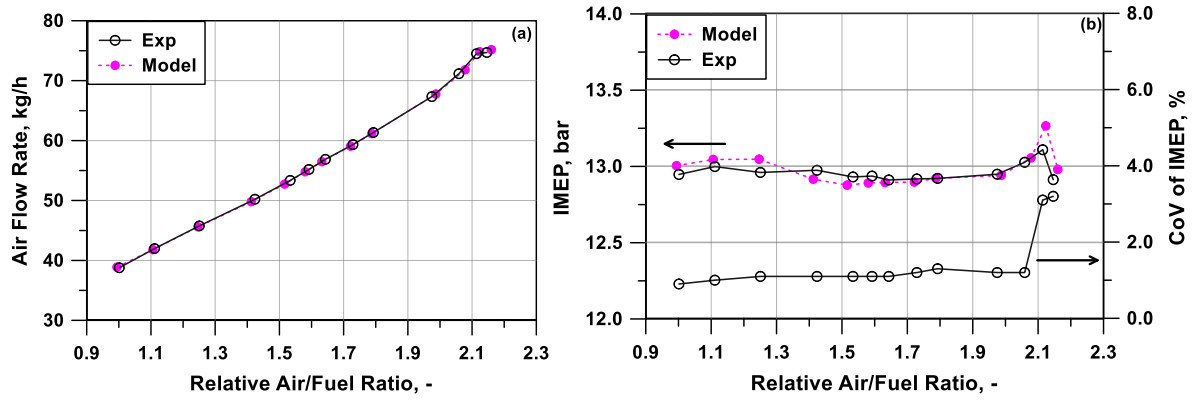

Figure 5-24 Experimental / numerical air flow rate (a) and IMEP (b) comparisons, with experimental CoV of IMEP (b) against the relative air / fuel ratio.

The combination of IMEP and air flow rate results in a good prediction of the indicated efficiency, as shown in *Figure 5-25(a)*. The model finds a maximum efficiency of about 47% at λ = 2, in accordance with the experimental findings, with an improvement greater than 5 points compared to the stoichiometric case. Moving from the stoichiometric case, leaning the mixture determines less intense heat losses and more favourable thermo-chemical properties of the in-cylinder mixture (lower ratio of specific heats), reflecting on the efficiency improvement. The more pronounced efficiency gaining for λ lower than 1.5 is promoted by the possibility of progressively anticipating the combustion phasing, thanks to a higher knock resistance of the air / fuel mixture. Moving towards λ greater than 2, the efficiency reduction is caused by the combustion slowdown, which also determines a greater presence of uHC, which subtracts a fraction of heat to the combustion process.

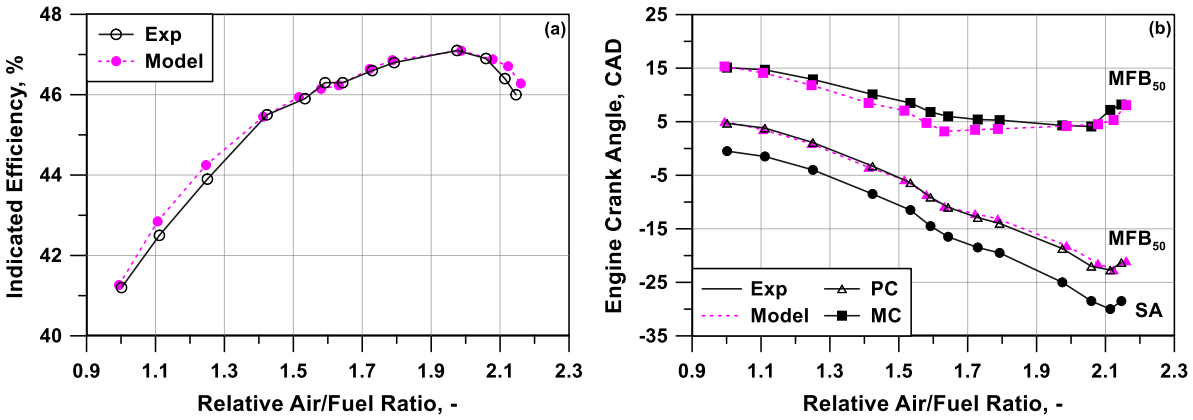

Figure 5-25 Experimental / numerical indicated efficiency (a), MFB_{50} in PC, and MC (b) comparisons against the relative air / fuel ratio.

Since the spark timing is imposed in simulations, the MFB_{50} angular position in PC and MC can be considered as a measure of the overall combustion model reliability. Note that the MFB_{50} angular position extracted from the 1D simulation is computed as the ratio of the burned mass and the current total mass, accounting for the PC / MC mass exchange, congruently with the approach used in the indicated analysis. *Figure 5-25(b)* shows a good model accuracy for both pre-chamber and main chamber, with an RMSE of 1.44 CAD and 0.44 CAD, respectively. The figure confirms that leaning the mixture the spark event can be progressively advanced thanks to the higher knock resistance of the in-cylinder mixture. The plot also underlines that an experiment-advised optimal MFB_{50} at about 5 CAD aTDC is reached when λ is greater than 1.5, while, for lower λ, a delayed non-optimal combustion phasing is mandatory. *Figure 5-25(b)* also highlights that the combustion speed in the PC is slightly sensitive to the overall air / fuel, being the MFB_{50} angular position primarily controlled by the SA phasing. This is due to the flexibility of an active pre-chamber device, where the PC local air / fuel ratio can remain close to the stoichiometric level whatever is the λ in the main chamber. *Figure 5-25(b)* also points out that the combustion speed in the MC slows down by leaning the reactive mixture. This is well captured by the model, thanks to the reduction of the laminar flame speed.

A satisfactory prediction of the combustion phasing and speed in both PC and MC is confirmed by the comparisons of the peak pressure crank angle locations and levels, depicted in *Figure 5-26(a)* and *Figure 5-26(b),* respectively. Concerning the MC, the predicted peak pressure angular position appears slightly advanced in the comparison with the experimental counterpart. This is due to some inaccuracies in the description of the combustion tail, as better clarified in the following. The results in terms of global performance parameters and combustion events demonstrate the consistency and reliability of the proposed numerical approach, considering the relevant variation range of the air / fuel ratio and the absence of a case-dependent model tuning.

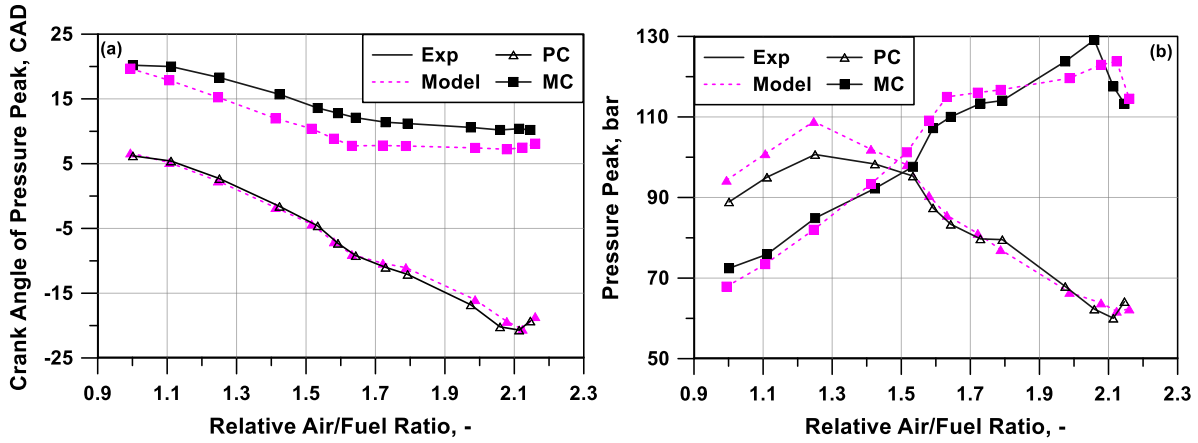

Figure 5-26 Experimental / numerical angular position (a) and level (b) of peak pressure comparison in PC and MC against the relative air / fuel ratio.

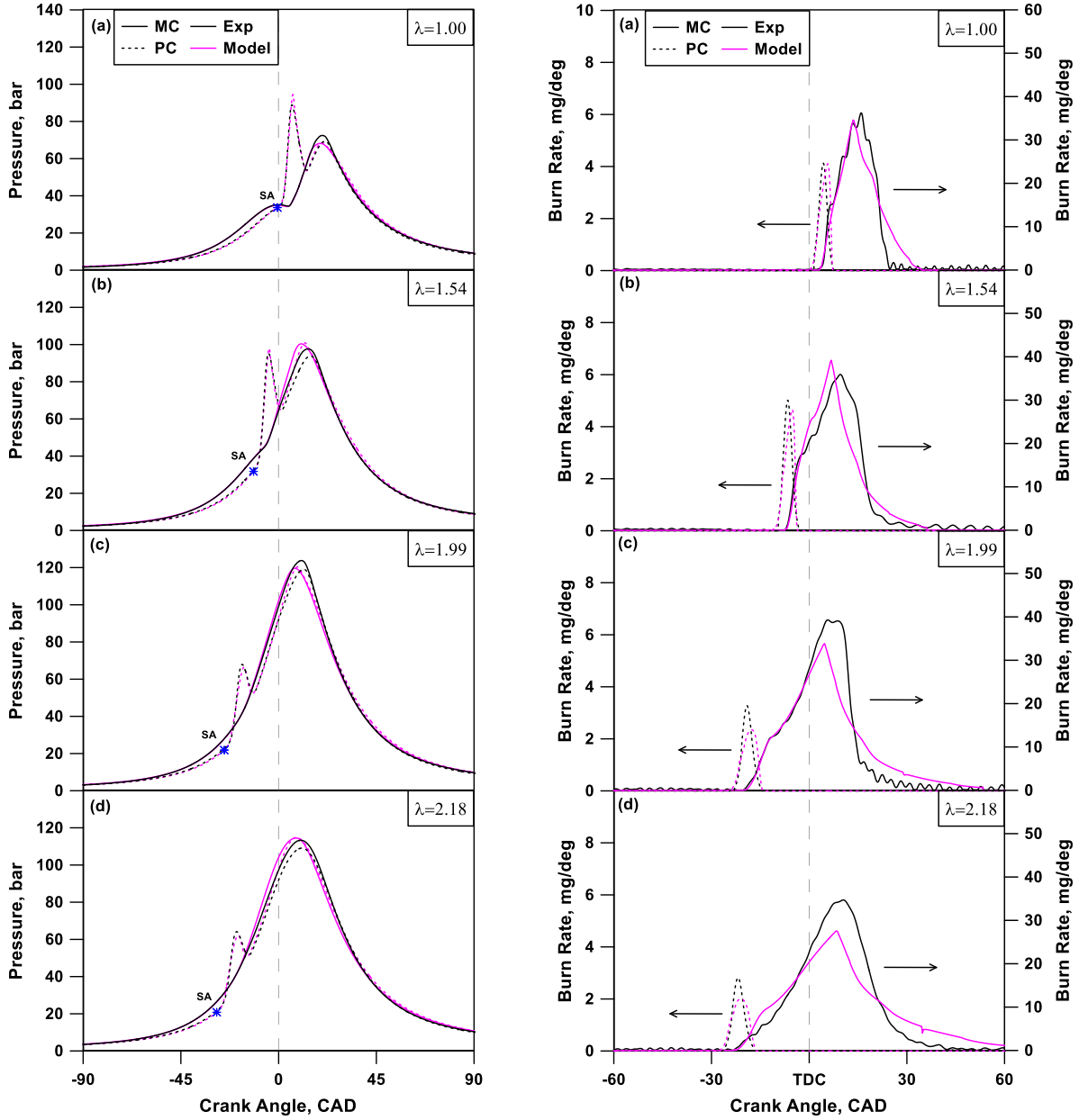

Figure 5-27 Experimental / numerical comparison of MC and PC pressure traces and related burn rates at (a) λ=1.00, (b) λ=1.54, (c) λ=1.99, (d) λ=2.18.

A deeper insight into the combustion model reliability is given by the experimental / numerical comparisons of the pressure traces (*Figure 5-27(left)*) for 4 representative cases, and of the related burn rates (*Figure 5-27(right)*). In those figures, the experimental (numerical) data are represented with black (red) curves, continuous or dashed for the MC or PC, respectively. As a first consideration, the pressure difference between PC and MC during the compression phase is well captured by the simulation, thanks to a proper selection of the flow coefficient of the orifice linking PC and MC. The pressure rises in the PC due to the combustion is well reproduced in all case. Minor inaccuracies appear in the pressure decreasing phase, especially for the leaner cases. Concerning the MC, the model accuracy in the first part of the combustion process is very good. More specifically, the simulation demonstrates to adequately predict the burn rate knee, which is due to the combustion enhancement caused by the hot turbulent jets ejected by the PC.

The model follows quite well the λ variation, overestimating its effect only for the leanest case (*Figure 5-27(left(d)*). Moving on during the combustion, the burn rate presents a slope reduction, which can be related to the onset of a regular self-sustained flame propagation. This rate reduction is more evident in the cases with leaner air / fuel mixtures, and this is captured by the model by the reduction of the laminar flame speed. After this phase, the burn rate presents its maximum, followed by a gradual decrease, caused by the contact of the flame front with the combustion chamber walls and by the cross-interaction of the multiple flame fronts. The systematic disagreement between numerical and experimental trends towards the combustion end is probably due to the absence in the flame front geometrical schematization of its conical propagation. This possibly sustains the flame front surface extension during the last portion of the process, but, at the combustion completion, this also determines its sudden decrease.

As an additional result of the proposed methodology, in *Figure 5-28*, the experimental / numerical comparisons between the indicated specific NO_2, uHC, and CO emissions are reported.

Figure 5-28(a) underlines a good model accuracy in the prediction of NO_2 emissions. As expected, while leaning the air / fuel mixture, thanks to the lower temperatures of the burned gas, the NO_2 production rate is less intense. As a peculiar feature of the proposed approach, the model allows to distinguish the NO_2 productions from PC and MC, as reported in *Figure 5-28(a)*. This last depicts the percentage of NO_2 arising from the PC, normalized by the total production. *Figure 5-28(a)* points out that the main source of NO_2 is the main chamber for λ below 1.7 while leaning the mixture the PC production assumes an increasing importance and becomes the unique contribution for λ above 2.1. In *Figure 5-28(b)*, both computed and measured uHC emission present an increasing trend when the mixture becomes leaner. This can be justified by a less effective post-oxidation process of the uHC released from the crevice volumes, due to lower in-cylinder temperatures. The model is able to

describe the above phenomenology, denoting a sensitivity to λ variations similar to the experimental data. On the other hand, excepting for the less lean cases, it underestimates the ISuHC level. For the leanest cases (λ>2), the measured ISuHC presents a higher sensitivity to λ, whose trend brings up. This is probably due to the combined effect of combustion cyclic instabilities (see *Figure 5-24(a)*), which determines the combustion incompleteness of some individual cycles in experiments, and to the increase of the relative weight of the uHC related to wall quenching. While the first effect cannot be straightforwardly taken into account in the proposed methodology, which does not consider the cyclic variability, the second effect is modeled. The relevance of such an aspect is highlighted in *Figure 5-28(b)*, where an additional line is introduced, depicting the numerical results without uHC related to wall quenching. As already mentioned, the progressive increase of the uHC emission is one of the reasons for the indicated efficiency trend flattening and reduction by leaning the mixture. This is satisfactorily captured by the model, as highlighted in *Figure 5-25(a)*. *Figure 5-28(c)* reports the experimental / numerical results for ISCO. The figure shows a reduced sensitivity of experimental ISCO to the λ variation, excepting for extreme cases.

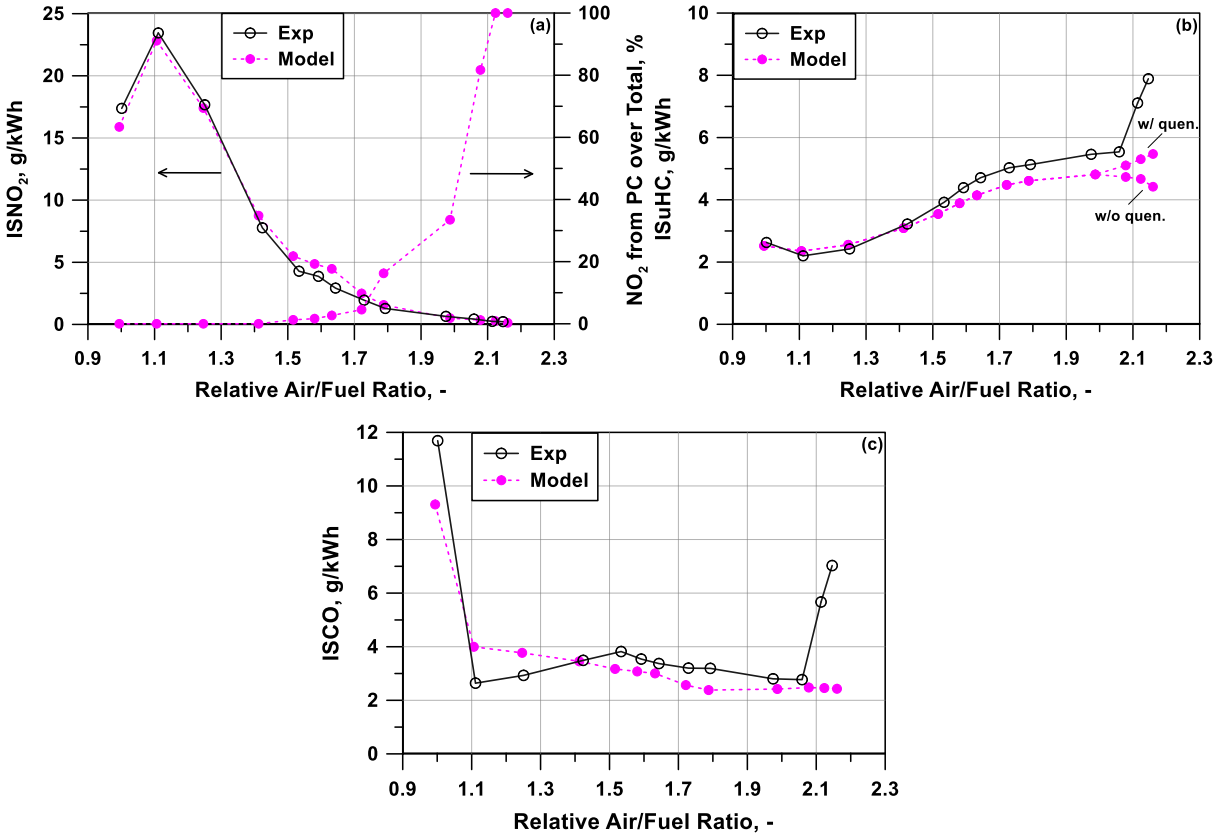

Figure 5-28 Experimental / numerical $ISNO_2$ (a), ISuHC (b), and ISCO (c) comparison against the relative air / fuel ratio.

For the stoichiometric operating point, the ISCO over-production could be caused by some individual rich cycles in the experimental train, where the CO formation is much more favoured.

Similarly, for the leanest cases (λ>2), incomplete combustions may occur in some individual cycles, induced by higher cyclic variability. As already mentioned, this phenomenology is not handled by the adopted model. Anyway, the predicted CO emission presents an almost flat trend with the air / fuel mixture, similarly to the experimental counterpart. The model underestimation when λ is greater than 1.5 is consistent with the uHC results, considering that the CO production is assumed proportional to the amount of post-oxidized uHC. Despite the above-mentioned inaccuracies, the pollutant production sub-model furnishes satisfactory results, being capable to correctly sense the superimposed variations of in-cylinder thermodynamic conditions (pressure, temperature) and composition (air / fuel mixture).

5.2.3. Single cylinder marine dual fuel engine

The tested engine described in this section applies in the marine sector, presenting a large-bore design, and being fuelled with natural gas. This engine is representative of the so-called W31 platform (whose name refers to the bore of 31 cm), and the variant here considered is a research Single Cylinder Engine. This engine is a multi-fuel multipurpose research SCE that makes flexibility its strongest characteristic. In *Table 5.7* the engine specifications during the test campaign are summarized together with the SCE main sub-systems. The SCE layout is according W31 engine platform in its Dual Fuel (DF) variant [17].

Commercial W31 DF is a two-stage turbocharged engine using the lean-burn principle when operating in natural gas mode. The main charge of the air-gas mixture is ignited with a small amount of pilot fuel injected directly in the combustion chamber as in a conventional diesel process. The liquid fuel is injected by high pressure common rail fuel injection system, featuring a twin needle injector valve [18], while the main gas fuel is introduced upstream the intake valves through a low pressure solenoid valve, *Figure 5-29*.

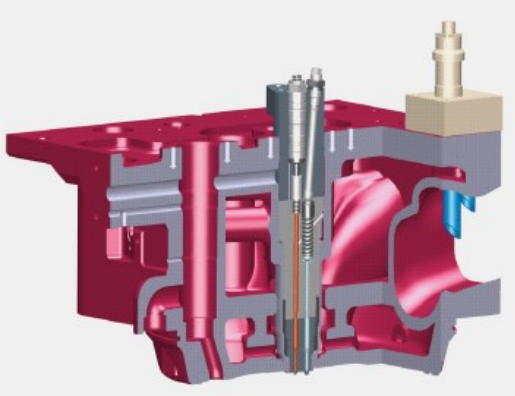

Figure 5-29 Gas admission valve.

Table 5.7 W31 SCE, engine, and system specifications.

Parameters	*Values*
Bore	310 mm
Stroke	430 mm
Nominal Speed	720 rpm
Air System	External air compressor w/ air temperature and pressure control (up to 10barg)
Fuel System	Common rail 2 with twin needle
Intake Valve Train System	Variable valve closure (VIC)
Exhaust Valve Train System	On / off variable valve closure (VEC)
Emission System	Horiba Mexa-One (NO_X, CO, THC, CO_2, O_2) AVL415S (FSN-Soot)

The tests campaign was carried out with liquified natural gas as the main fuel and with light fuel oil as pilot fuel. The focus of this test campaign was to evaluate the impact of the only top land crevices on uHC. For this reason, while the top land crevice volume was changed by means of different top land heights, the following actions were taken to minimize the impact of other sources of uHC:

- Compression ratio was kept constant.
- Combustion characteristics, such as combustion start, phasing, and duration were kept as comparable as possible between the different tested configurations. In this way, the contribution to uHC due to the flame quenching phenomenon was expected to be similar between the considered configurations.
- The gas injection phase was selected in a way to minimize the fuel short circuit during valve overlap.

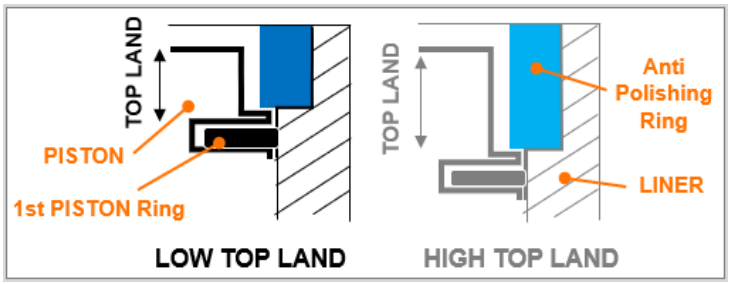

Figure 5-30Top land scheme, comparison between “low” and “top” configurations.

For this purpose, two different piston top designs were prepared (*Figure 5-30*) with two different top land heights, labelled as “low top land” and “high top land” in the following. The volume

difference between the two geometries is 36%. The following steady state performances were recorded for each test points:

- exhaust gas emissions: NOx, CO, CO_2, O_2, uHC;
- Engine fuel consumption, main and pilot side;
- Component temperature: piston top, liner, valves, cylinder head.

Along with the steady state performance records, crank angle resolved pressure traces were measured in the cylinder and in the head ducts, upstream, and downstream the combustion chamber.

Furthermore, the clearance between piston top and Anti Polishing Ring, and between piston top and liner wall were measured in hot conditions at the highest load for a more accurate crevices volume estimation. The APR is a peculiar feature of the tested engines, allowing to increase the clearance between the piston top and the liner wall when the piston is far from the TDC, and to considerably reduce the contact between carbon deposits and the liner wall due to piston tilting.

For each top land geometry, the test matrix included a load sweep of five points at a constant rotational speed of 720 rpm (*Table 5.8*). The load was adjusted modifying the pressures at the intake and exhaust pipe ends, in order to mimic a load sweep of the W31 multi-cylinder engine. The injection of natural gas is controlled to realize a λ of about 2.1, and a higher value of about 2.6 only for the lowest considered engine load. The light oil mass is about 3-4% of the total fuel amount.

Table 5.8 W31 test matrix.

Engine speed, rpm	*720*				
Ring pack geometry	Low Top Land / High Top Land				
Nominal load	100	85	77	50	25
λ, -	2.1				2.6

The tested engine has been schematized and simulated in the GT-Power environment. The simulations are based on a 1D model of the unsteady flow inside the intake and exhaust pipes coupled with a 0D model of the in-cylinder processes. The main components of the engine schematic are cylinders, intake and exhaust pipe systems, supply system of the natural gas, etc.

In the W31 SCE 1D model, the measured rotational speed of 720 rpm is imposed for all considered operating points. The pressures in the intake and exhaust environments are assigned according to the experimental data. All conditions of the test matrix in *Table 5.8* are computed, specifying for each load sweep the different geometry of the piston ring pack. The experimental mass of natural gas and

light oil are imposed as input boundary conditions in the simulations. For the W31 engine, the 1D model also includes the direct injector to describe the light oil supply.

The heat transfer inside the cylinder is computed based on a Woschni-like correlation and on the measured wall temperatures (for both liner, piston, and cylinder head). It is worth noting that, for the considered engines, the cylinder head presents wall temperatures higher than the piston and the cylinder liner of about 303/313 K. This aspect, as better highlighted below, is relevant for the rate of instantaneous uHC production from wall quenching. The combustion process is described by a two-zone (burned / unburned) approach. It is not predicted but computed assigning the experimentally derived burn rates. These last are extracted by inverse analyses of the experimental pressure cycles. A lower-than-unity final fuel burned fraction is recognized in the inverse simulations considering the heat occulted to the combustion related to uHC emissions. When applied in the direct simulations, the above burn rate profiles are normalized so to impose a final value of the burned mass fraction equal to one. The direct simulations properly handle the imposed normalized burn rate profiles. Indeed, the burn rate curve is automatically reduced during the simulation accounting for the heat hidden away by the total in-cylinder uHCs mass.

The model result discussion and validation are realized normalizing all the data by the experimental values of the operating point featured by a nominal load of 100% and referred to the low top land configuration. This normalization is due to confidentiality reasons. For sake of brevity, the validation of the 1D model under the viewpoint of the global performance concerns the only high top land configuration, since very similar results are obtained for the other piston geometry. As a global indicator of the model accuracy, the Root Mean Squared Error (RMSE) between experimental / numerical data will be reported, estimated over all the tested operating points.

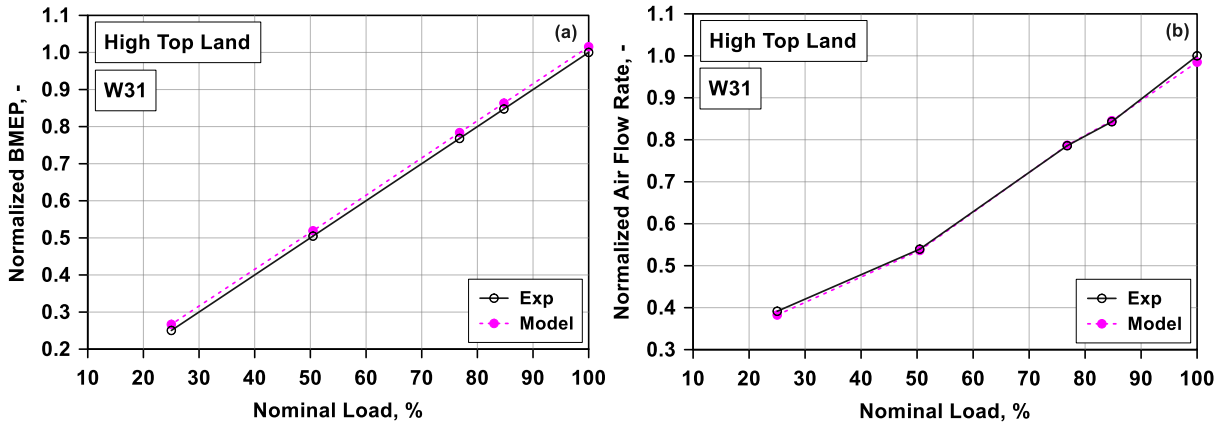

Figure 5-31 Experimental vs. numerical normalized BMEP (a) and air flow rate (b) comparison for W31, for the high top land configuration.

In *Figure 5-31(a)*, the experimental / numerical normalized BMEP values of the W31 engine are depicted against the nominal engine load. They are satisfactorily predicted, remaining in most cases in an error band of ± 3% with a RMSE of around 0.012. The systematic model overestimation could be related to the reduced in-cylinder wall heat losses. The air flow rate, illustrated in *Figure 5-31(b)*, is accurately predicted, being the error for all the investigated points, within the band ± 2%. The related RMSE of 0.007 denotes an accurate schematization of the intake and exhaust pipe geometry, and a proper specification of the valve flow coefficients.

Concerning the emission model, described in section 3.8, the values for the tuning constants for the engine W31 are found by a trial-and-error procedure, as a compromise between all considered operating conditions and the two top land geometries. A unique set of tuning constants is hence identified and kept fixed in all cases.

As described in the theoretical section, the uHCs model is able to assess the evolution of uHCs release from crevices, the formation from wall quenching, and their reduction because of post-oxidation on a crank angle base. Hence, as an example, for this engine in its low top land configuration, the uHC trends of two different operating points are reported in *Figure 5-32(a)* and *Figure 5-32(b)*. The first one refers to the highest nominal load (100%), while the second one to the lowest one (25%). The pink (blue) line represents the quenching (crevices) contribution evolution. Continuous lines depict released uHCs, while dashed lines correspond to post-oxidized levels. The pressure cycle, reported in black, allows to temporally locate the phenomena occurrence with respect to the combustion process.

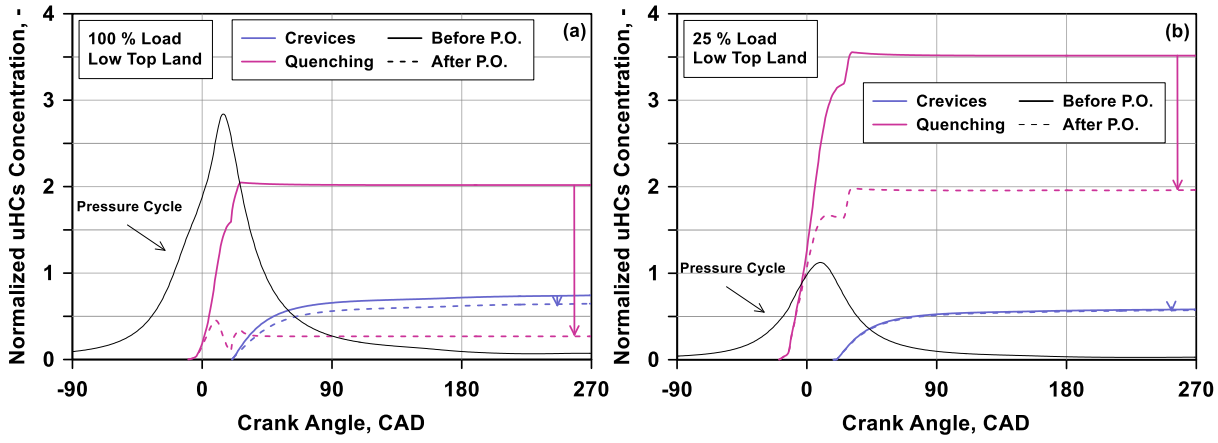

Figure 5-32 Crank angle based uHCs evolution before and after post-oxidation process at high load (a) and low load (b) for low top land configuration.

As can be seen in *Figure 5-32(a)*, looking at the trends before post-oxidation, the highest uHC production is due to the wall quenching phenomenon, if compared to crevices uHC release. But, considering the post-oxidation effect, the opposite situation occurs. The explanation of such

behaviour relies on the different timing of formation and post-oxidation of the uHCs contributions. Indeed, the post-oxidation of the uHCs from wall quenching takes place during all the combustion process, since its beginning, resulting in a more effective uHC abatement, which in turn is due to a longer time for the uHCs at higher pressure and temperature. Concerning the uHCs from crevices, during the most part of the combustion, they are trapped in the related volume. Only when the piston is far away from the TDC, uHCS are released from the crevices and their post-oxidation begins. This means that the hydrocarbons encounter decreasing pressure and temperature, reflecting in a less effective post-oxidation if compared to the one experienced by the uHCs from wall quenching. The observation of *Figure 5-32(a)* also highlights a knee towards the combustion end in the uHC contribution from wall quenching. This numerical outcome is justified by the fact that the flame front begins to touch the cylinder liner, which is the coolest surface within the combustion chamber. Consequently, the mass included in the wall quenching layer suddenly increases, leading to a rising of the uHC production.

Comparing *Figure 5-32(a)* and *Figure 5-32(b)*, the main difference is related to the uHCs released from quenching. The model is able to perceive this significant variation because of the lower laminar flame speed typical of low load operations, which reflects on an increased thickness of the flame front and hence in the quenching distance. In terms of global behaviours, comparing the two cases at different loads, a qualitatively similar trend can be observed, although with different final levels. Focusing on the post-oxidation of the quenching contribution, for the low load point, it can be observed that it is less intense. mainly due to a lower in-cylinder temperature, which affects the post-oxidation effectiveness. HC released from crevices are higher at the maximum load, due to the higher pressure in the cylinder and in the crevices volume, but after post-oxidation, the uHC levels at high and low load align. This is explainable by the same mechanisms discussed for the post-oxidation of the quenching contribution, even if in this case, the post-oxidation intensity results lower since the uHC formation is later during the expansion phase.

Another outcome of the comparison of *Figure 5-32(a)* and *Figure 5-32(b)* is that the release of uHCs from crevices happens at the same crank angle (about 20 CADs after the TDC) in both operating points. The above-mentioned phenomenon also occurs for the other operating conditions with the low top land piston geometry. This verifies even if the in-cylinder peak pressure occurs at a different crank angle, as a consequence of a different combustion phasing. The reason is explainable by the detailed geometrical description of the piston ring pack, especially of its top land. This influences the time evolution of the top land crevices volume, as shown on top of *Figure 5-33*[1]. The figure highlights

[1]The volumes are normalized by the maximum in-cylinder volume, while ring position relative to the piston is normalized by the height of the top groove.

that the volume trend is generally constant, but, around the TDC, it exhibits a reduction, which is due to the APR. Indeed, once the piston approaches the TDC, the APR slides inside the top land causing a reduction of the crevices volume, while the opposite occurs during the descending stroke of the piston. The above-described mechanism interferes with the uHCs release, since, in the first stage, the top land crevices proceed in filling even when the pressure decreases, due to its volume increase Only when the APR emerges at all from the piston top land, a delayed release of uHC begins. This underlines the relevance of a detailed description of the top land geometry.

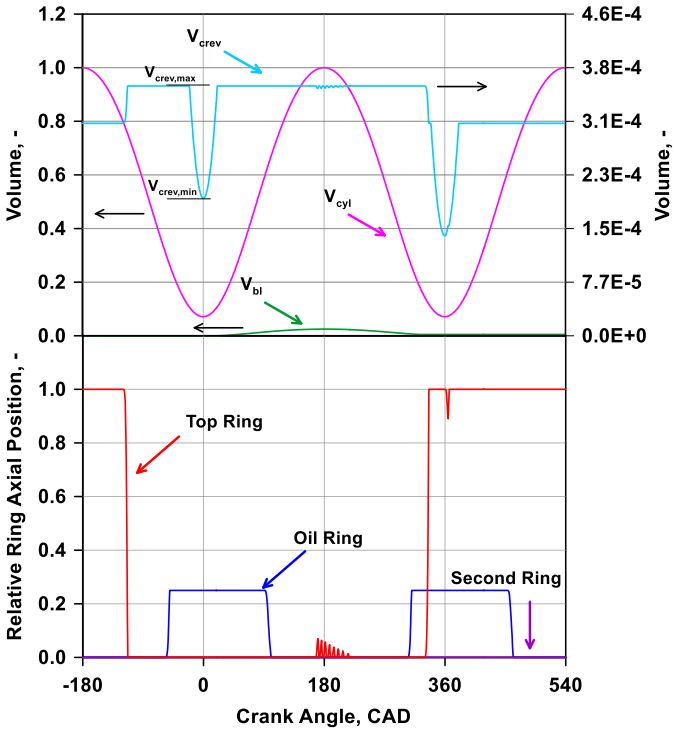

Figure 5-33 (top) Crank angle based volume evolution for the cylinder, crevices, and crevices boundary layer; (bottom); relative ring pack axial motion inside the grooves.

To further highlight the relevance of APR influence on uHC release, two additional simulations are performed, deactivating the ring pack model, and imposing fixed values for the crevices volume. In particular, for this volume, the minimum and maximum values ($V_{crev,min}$ and $V_{crev,max}$, respectively), reported at the top of *Figure 5-33,* are imposed. The results, shown in *Figure 5-34*, highlights that the release from crevices, in both cases, happens in correspondence of the in-cylinder pressure peak, as expected, and in advance if compared to the result arising from the application of the ring pack model. The final uHC level obtained by the detailed ring pack model is between the two extreme cases. This reveals the possibility to derive similar results with a conventional fixed-volume crevices model, but, in this case, the appropriate crevices dimensions would be unknown.

Once proved the influence of a detailed geometrical description of the top land geometry, some considerations can be drawn observing the outcomes of the ring dynamics model, shown in *Figure*

5-33 for the low top land design and the maximum load. This figure depicts the axial position of the rings during the engine cycle relative to the piston. It can be observed that, during all the phases of uHCs release from crevices, the top ring and the second one are placed at the bottom of the corresponding groove. For this reason, the ring motion does not affect the above-mentioned formation mechanism. A similar behaviour applies for all the other tested operating conditions, for the high top land piston design and for the other considered engine. Anyway, to confirm the generality of the insensitivity of uHC release from crevice to the ring dynamics, further analyses will be performed in the next development of this activity for different engines, ring pack characteristics, and operating conditions.

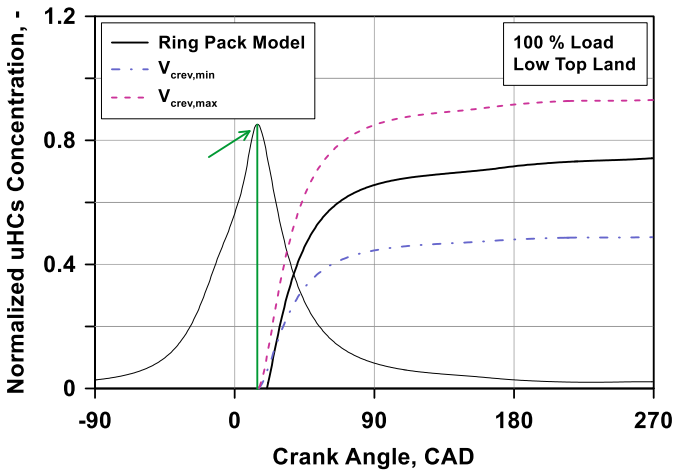

Figure 5-34 Comparison between uHCs from crevices obtained with ring pack geometry model and the ones obtained imposing a fixed crevice volume.

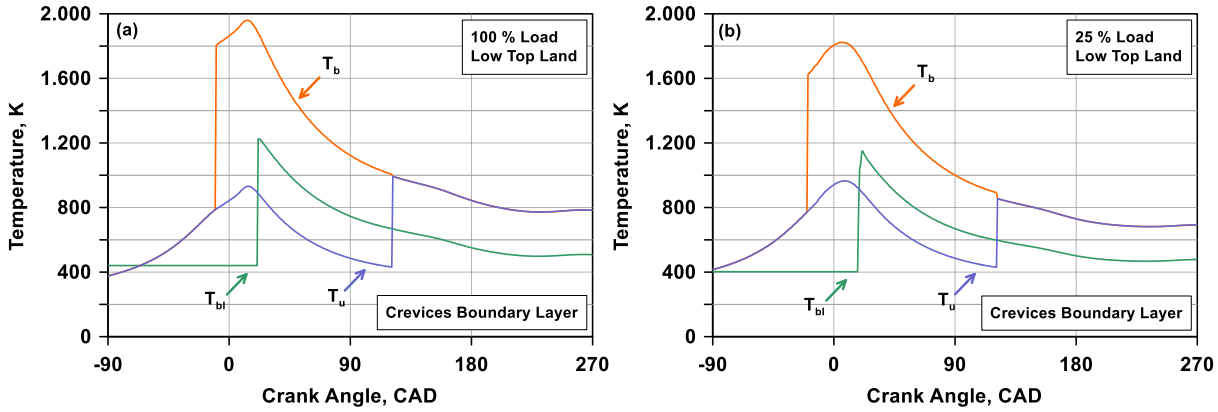

Figure 5-35 Crank angle based temperature evolution for the burned and unburned zone and for the crevices boundary layer at high load (a and low load (b) for low top land configuration.

To further explore the variation of the post-oxidation effect on the uHCs from crevices as observed in *Figure 5-32(a)* and *Figure 5-32(b),* the trends of the temperature inside the boundary layer can be analysed. They are plotted in *Figure 5-35(a)* and *Figure 5-35(b)*, together with the unburned and burned gas temperatures. Comparing the BL temperature peaks for the two loads, it can be observed

that the lowest load reflects in a reduced temperature, affecting the post-oxidation effectiveness. Another quantity influencing the post-oxidation process is the boundary layer volume. The BL volume related to uHC from crevices is shown as an example in green at the top of *Figure 5-33* for a representative case. It can be noted that the volume originates and gets bigger according to the uHC release (compare *Figure 5-32(a)* and *Figure 5-33*), then decreases during the exhaust phase, reaching a maximum value of about 2.5% of the maximum cylinder volume.

The model results in terms of global uHCs prediction are shown in *Figure 5-36*. This comparison between experimental and numerical data is performed considering the concentrations along the exhaust line, at the same location as the measuring probe. The bar chart highlights quite good agreement among the data with a percent error of less than ±10%, with an averaged percentage error of 7%. The most interesting outcome is the model capability to reproduce uHCs variations depending on the load and varying the top land geometry. The unburned hydrocarbons values increase at decreasing load and are higher for the greater top land volume. It can be noted that the model sensitivity to the top land volume is not fully adequate, observing a general underestimation for the high top land geometry, while the opposite occurs for the other piston design.

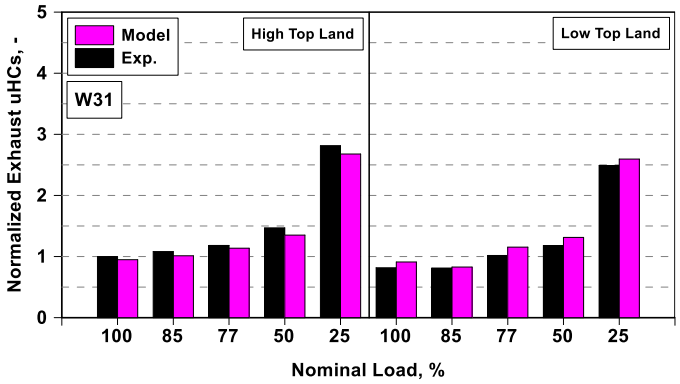

Figure 5-36 Experimental vs numerical total uHCs comparison at load sweep for W31.

For this engine, a study on uHCs sharing, depending on the source and on their post-oxidation, is reported in *Figure 5-37*, with reference to the high (left) and low (right) top land geometries. The blue bars represent the overall released uHCs, divided in crevices and quenching contributions (slashed and solid bars, respectively), while the pink ones are the post-oxidized corresponding levels. Both Figures highlight that similar crevices and quenching contributions occur at medium and high load for the released HC, while, once the post-oxidation takes place, the major uHC source comes from crevices. Nevertheless, the quenching phenomenon strongly impacts the overall uHC at very low load., if compared to crevices contribution, but considering the post-oxidation effect, the opposite occurs.

This is still more evident looking at *Figure 5-38*, where the previous results are presented in percentage values. Looking at the pink bars, at the nominal load, the crevices / quenching sharing of the total uHCs is 90% to 10%, while at the lowest load it moves to 30% to 70%.

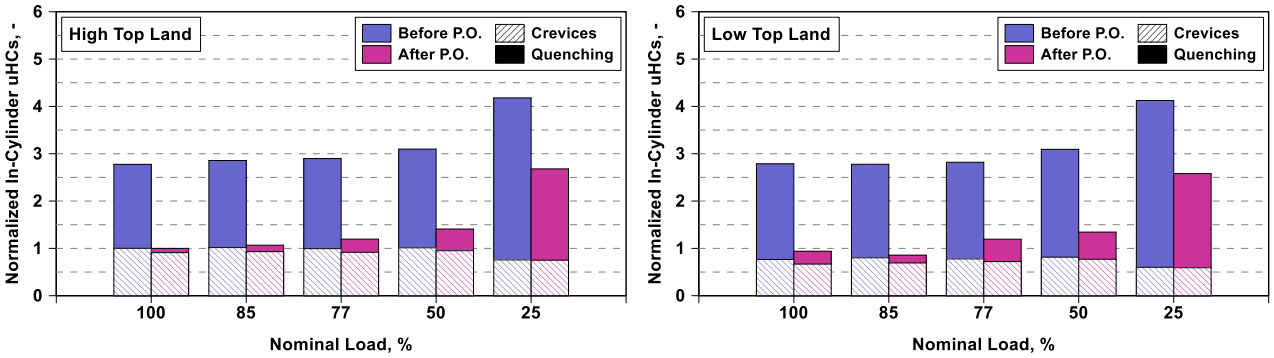

Figure 5-37 Comparison of uHCs sources, namely crevices (slashed) and quenching (solid), before (blue) and after (pink) post-oxidation process for high (left) and low (right) top land configurations.

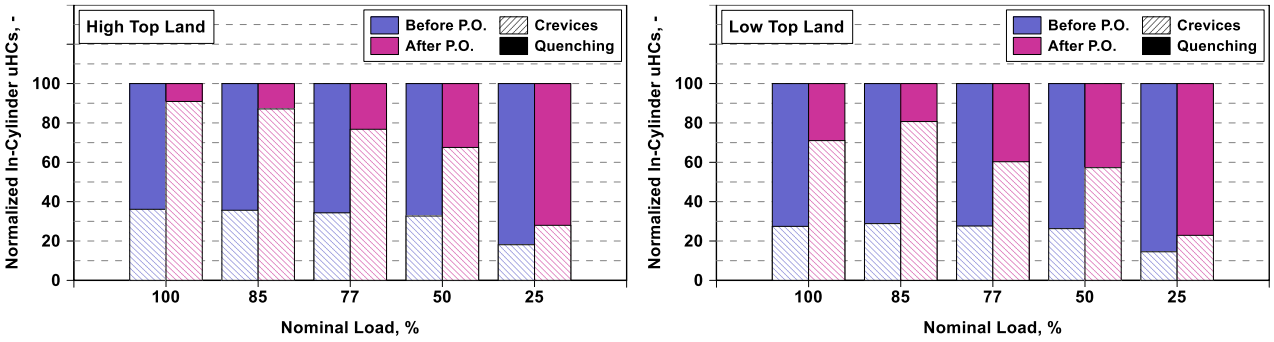

Figure 5-38 Percentage splitting of uHCs sources before (blue) and after (pink) post-oxidation for high (left) and low (right) top land configurations.

5.2.4. Multi-cylinder marine engine equipped with Pre-Chamber

In this section, the tested engine, as the SCE presented in the above section, applies in the marine sector, presenting a large-bore design, and being fuelled with natural gas. This engine belongs to the W46 platform (whose name recalls the bore of 46 cm) and is a commercial variant composed of six cylinders and a two-stage turbocharger system. This engine is a commercial six-cylinder engine, whose main specifications are reported in *Table 5.9*. The engine is according W46 engine platform in its spark gas variant. Alon with the W31 SCE, the W46 is fuelled with natural gas. In this case, for the ignition system, a spark plug is in a pre-chamber with auxiliary fuelling to create a proper lambda around the spark plug, while lean mixture similar to the W31 concept characterizes the main chamber. A cross-section, showing the principles of this pre-combustion chamber system, is depicted in *Figure 5-39*.

Once again, the main gas fuel is introduced upstream the intake valves through a low-pressure solenoid valve, *Figure 5-29*. The experimental setup allows for the measurement of pollutant emissions and of pressure traces in the intake and exhaust ports and in the cylinder.

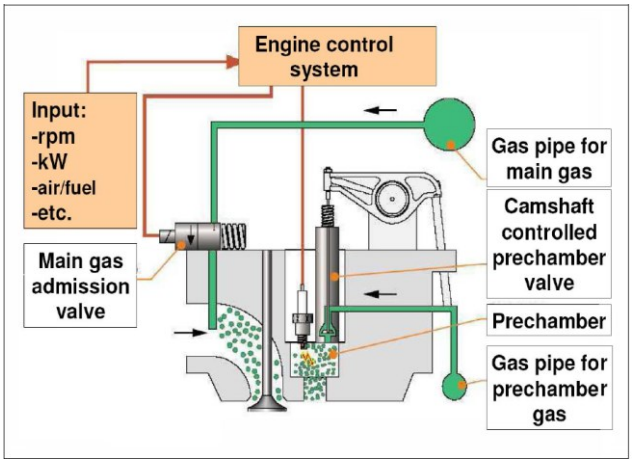

Figure 5-39 Pre-combustion chamber ignition system schematization.

The test matrix of this engine is reported in *Table 5.10*. It included a load sweep of six operating conditions at a rotational speed of 600. Also for this engine, two variants of the top land geometry were compared, characterized by different heights and volumes. Once again, the main combustion characteristics, the compression ratio, and the injection phases were kept similar between homologous operating conditions.

Table 5.9 W46 MCE, engine, and system specifications.

Parameters	*Values*
Bore, mm	460
Stroke, mm	580
Number of cylinders, -	6
Nominal Speed, rpm	600
Air System	Two-stage Turbocharger system
Intake Valve Train System	Variable valve closure (VIC)
Exhaust Valve Train System	On / off variable valve closure (VEC)
Emission System	Horiba Mexa-One (NO_X, CO, THC, CO_2, O_2)

Table 5.10 W46 test matrix.

Engine speed, rpm	600					
Ring pack geometry	Low Top Land / High Top Land					
Nominal load	100	85	75	50	25	11
λ, -	2.1					

The tested engine, as the similar previous one, has been schematized and simulated in the GT-Power environment. In the W46 1D model, the 1D schematic includes the six cylinders, the two-stage turbocharger system, and the related waste-gate valve. The turbochargers are controlled in the simulation to realize the same boosting pressure as in the experiments. The amount of natural gas is metered by a PID controller to match the measured BMEP level. All the operating points of *Table 5.10* are simulated, implementing the two geometrical variants of the ring pack. In all cases, the rotational speed is set at 600 rpm.

For this multi-cylinder large-bore engine, the heat transfer and the combustion are modelled in the same way presented for the previous SCE large-bore engine.

Once again, the model result discussion and validation are realized normalizing all the data by the experimental values of the operating point featured by a nominal load of 100% and referred to the low top land configuration. Here too, the model validation concerns the only high top land configuration.

For the W46 engine, the air flow rate, reported in *Figure 5-40(a)*, is also well reproduced. The RMSE is about 0.001, with an error of about 5-7% only at the lower loads, while from medium to high loads, it is less than ±1%. In *Figure 5-40(b)*, the comparisons of average speeds for the high-pressure and low-pressure turbochargers (TC) are shown. A satisfactory model accuracy, with an error less than ±1% in most cases and a RMSE of 0.010, is obtained for the HP TC. Considering the LP TC speed results, the error grows at decreasing load, passing from a value less than 1% at higher loads to about 20% at lower loads, with a global RMSE of 0.046. The inaccuracy at a low load is mainly due to the poor description of the TC behaviour in these conditions since the LP compressor and turbine operating points move outside the available experimental maps and an unreliable map extrapolation may affect the simulation reliability.

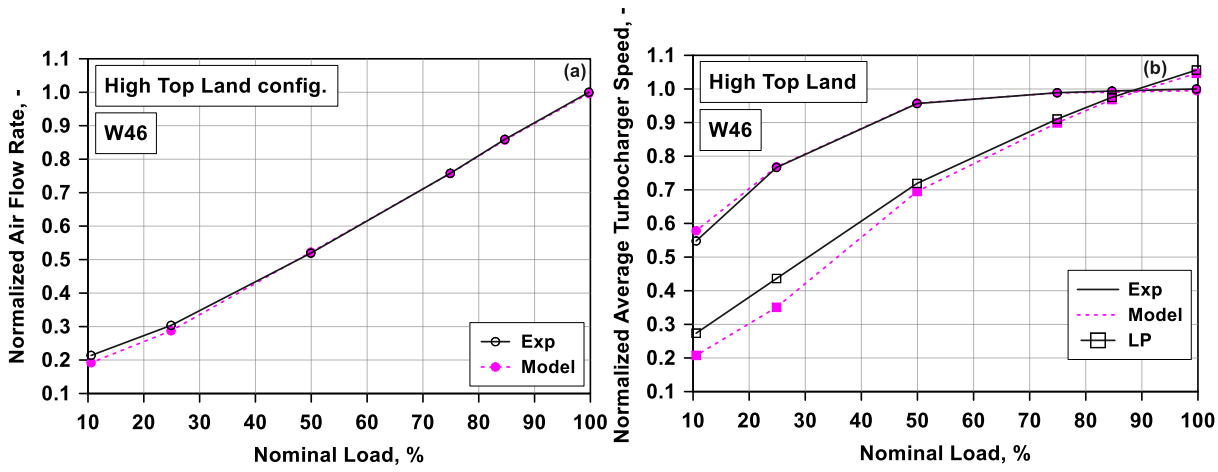

Figure 5-40 Experimental vs numerical normalized air flow rate (a) and average turbocharger speed(b) comparison for 46TS, for the high top land configuration.

Concerning the emission model, since the two engines are quite similar, and to further prove the model reliability and consistency, the same set of tuning constants as the ones of W31 have been applied to the W46 engine.

For this engine the instantaneous outcomes, in terms of uHC production and post-oxidation, are not reported since the trends and the behaviours observed are equal to the W31 ones.

Concerning the experimental / numerical uHC emission comparison, they are shown in *Figure 5-41*.

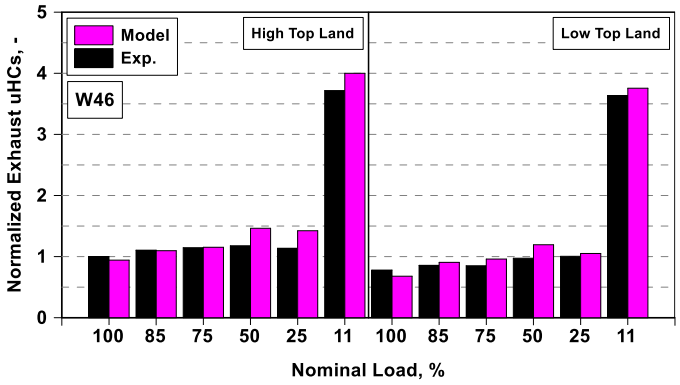

Figure 5-41 Experimental vs numerical total uHCs comparison at load sweep for 46TS.

Differently from the W31 engine, for the W46 engine, the uHC results, in addition to the in-cylinder formation and post-oxidation, also depend on the way the flow pulses from the six cylinders combine along the exhaust line, due to an imbalance between the cylinders. Following the normalization criterion applied to the W31, all data are divided by the one related to the maximum load with the low top land design. Also considering the multi-cylinder engine, the model demonstrates to properly sense the load variations and the crevice dimensions, with an averaged percentage error of 10%. The outcomes appear even more remarkable since the uHC model constants are the same as the ones determined for the other tested engine (W31), which is different in terms of cylinder number, bore, combustion chamber shape, and ignition system.

Concerning the uHCs sharing depending on the source and on their post-oxidation, it is shown in *Figure 5-42*, with reference to the high top land geometry. The blue bars are the overall released uHCs, divided into crevices and quenching contributions (slashed and solid bars, respectively), while the pink ones are the post-oxidized corresponding levels. The Figures show that similar crevices and quenching contributions occur at medium and high load for the released HC, while, once the post-oxidation takes place, the major uHC source comes from crevices. Once again, it can be more evidently observed in *Figure 5-43*, where the previous results are presented in percentage values. Looking at the pink bars, at the nominal load, the crevices / quenching sharing of the total uHCs is 90% to 10%, while at the lowest load it moves to 30% to 70%.

Hence, the proposed uHC model demonstrated to be an accurate tool to predict the total amount of unburned hydrocarbons under various operating conditions, being capable to perceive some geometrical variation such as cylinder dimension and top land design.

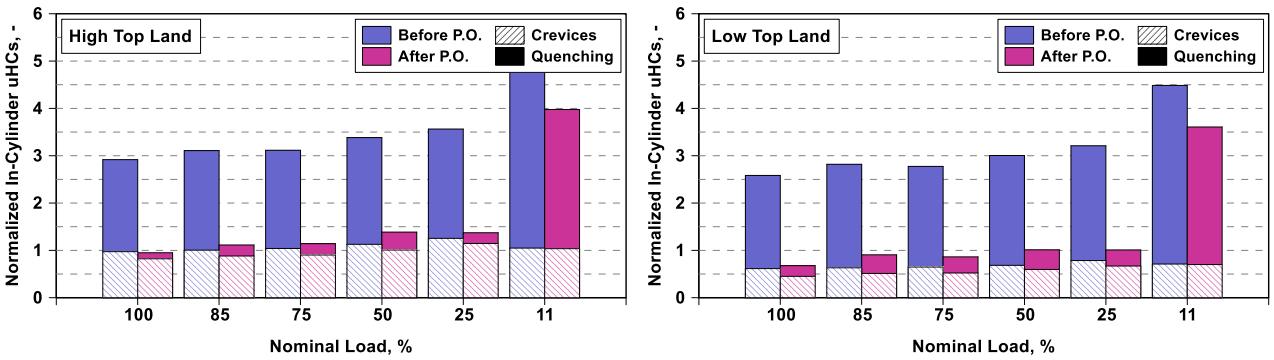

Figure 5-42 Comparison of uHCs sources, namely crevices (slashed) and quenching (solid), before (blue) and after (pink) post-oxidation process for high (left) and low (right) top land configurations.

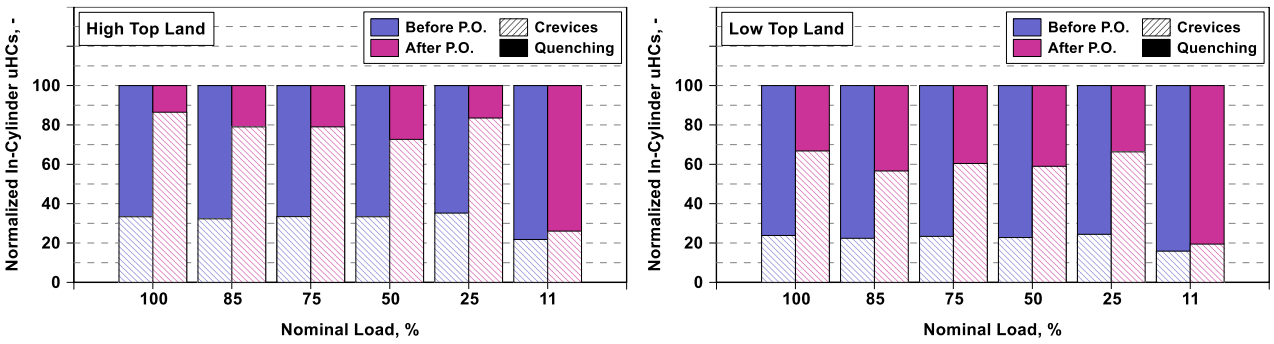

Figure 5-43 Percentage splitting of uHCs sources before (blue) and after (pink) post-oxidation for high (left) and low (right) top land configurations.

References

[1] Andrae, J., "Comprehensive chemical kinetic modeling of toluene reference fuels oxidation", Fuel 2013; 107:740-748, doi: 10.1016/j.fuel.2013.01.070.

[2] Bozza, F., De Bellis, V., Minarelli, F. and Cacciatore, D., "Knock and Cycle by Cycle Analysis of a High Performance V12 Spark Ignition Engine. Part 2: 1D Combustion and Knock Modeling," *SAE International Journal of Engines*, 8(5), pp.2002-2011, 2015 doi: www.jstor.org/stable/26278098.

[3] De Bellis, V., Teodosio, L., Siano, D., Minarelli, F. et al., "Knock and Cycle by Cycle Analysis of a High Performance V12 Spark Ignition Engine. Part 1: Experimental Data and Correlations Assessment" SAE Int. J. Engines 8(5):1993-2001, 2015, doi:10.4271/2015-24-2392.

[4] Corti, E., Moro, D., "Knock Indexes Thresholds Setting Methodology", SAE Technical Paper 2007-01-1508, 2007, doi:10.4271/2007-01-1508.

[5] De Bellis, V., Bozza, F., Fontanesi, S., Severi, E. et al., "Development of a Phenomenological Turbulence Model through a Hierarchical 1D/3D Approach Applied to a VVA Turbocharged Engine", SAE Int. J. Engines 9(1): 506-519, 2016, doi:10.4271/2016-01-0545.

[6] Bozza, F., Teodosio, L., De Bellis, V., Fontanesi, S. et al., "Refinement of a 0D Turbulence Model to Predict Tumble and Turbulent Intensity in SI Engines. Part II: Model Concept, Validation and Discussion", SAE Technical Paper 2018-01-0856, 2018, doi: 10.4271/2018-01-0856.

[7] Bozza, F., De Bellis, V., Berni, F., D'Adamo, A., Maresca, L., "Refinement of a 0D Turbulence Model to Predict Tumble and Turbulent Intensity in SI Engines. Part I: 3D Analyses", SAE Technical Paper 2018-01-0850, 2018, doi: 10.4271/2018-01-0850.

[8] Yakhot, V., Orszag, S., A., "Renormalization group analysis of turbulence. I. Basic theory", *J. Sci. Computing* 1:3–51, 1986, doi: 10.1007/BF01061452.

[9] Herweg, R., Maly, R.R., "A fundamental model for flame kernel formation in S. I. engines", SAE Technical Paper 922243, 1992, doi: 10.4271/922243.

[10] Song, J., Sunwoo, M., "Flame kernel formation and propagation modelling in spark ignition engines", *Proceedings of the Institution of Mechanical Engineers, Part D: Journal of Automobile Engineering* 215(1): 105-114, 2001, doi: 10.1243/0954407011525494

[11] Mueller, C., Morcinkowski, B., Schernus, C., Habermann, K., Uhlmann, T., "Development of a pre-chamber for spark ignition engines in vehicle applications," 4th International Conference on Ignition Systems for Gasoline Engines, Dec. 2018, doi: 10.5445/IR/1000088588.

[12] Spindt, R., "Air-Fuel Ratios from Exhaust Gas Analysis," SAE Technical Paper 650507, 1965, doi: 10.4271/650507.

[13] Bounaceur, R., Herbinet, O., Fournet, R., Glaude, P. et al., "Modeling the Laminar Flame Speed of Natural Gas and Gasoline Surrogates," SAE Technical Paper 2010-01-0546, 2010, doi:10.4271/2010-01-0546.

[14] Amirante, R., Distaso, E., Tamburrano, P., Reitz, R. D., "Laminar flame speed correlations for methane, ethane, propane and their mixtures, and natural gas and gasoline for spark-ignition engine simulations," *International Journal of Engine Research*, 18(9), 951-970, 2017, doi:10.1177/1468087417720018.

[15] Verhelst, S., Sierens, R., "A quasi-dimensional model for the power cycle of a hydrogen-fuelled ICE," *International Journal of Hydrogen Energy*, 32(15), 3545-3554, 2007, doi: 10.1016/j.ijhydene.2007.02.011

[16] Serrano, D., Zaccardi, J., Müller, C., Libert, C. et al., "Ultra-Lean Pre-Chamber Gasoline Engine for Future Hybrid Powertrains," *SAE Int. J. Adv. & Curr. Prac. in Mobility* 2(2):607-622, 2020, doi:10.4271/2019-24-0104.

[17] Åstrand U, Aatola H, Myllykoski JM, Wärtsilä 31 – World's most efficient four stroke engine. In: *28th CIMAC World Congress*, Helsinki, Finland, 06-10 June 2016, paper no 225.

[18] Jay D. CR development in the last decade in Wärtsilä. In: *28th CIMAC World Congress*, Helsinki, Finland, 06-10 June 2016, paper no 232.

6. Potential of ultra-lean Pre-Chamber SI engine

Among the various pathways to improve the thermal efficiency of ICEs, various measures were attempted, as already discussed, such as VCR, cooled EGR, and WI. The benefits of fuel consumption highly depend on the considered operating condition. Hence, nowadays an increasing research work is devoted to ultra-lean combustion systems. These techniques have the potential to simultaneously reduce the fuel consumption and the cylinder-out NOx emissions in the whole engine operating domain. Considering the various concepts proposed in the literature to sustain a lean combustion, such as fuel stratification, HCCI, and SACI, the utilization of a Pre-Chamber ignition system is nowadays considered the most promising solution since the high turbulence intensity of the jets ejected from the PC allows to ignite the mixture and to ensure a stable flame propagation even under extremely lean conditions [1],[2].

Among the engines considered in this Ph.D. thesis, the innovative ultra-lean pre-chamber SI engine was selected to explore its potential in complying with current pollutant and CO_2 limitations when installed in a hybrid powertrain.

To this aim, this engine has been numerically calibrated and then virtually embedded into an HEV through vehicle simulations using the energy management strategy ETESS described in section 4.9.

The propulsion system under investigation has been developed within the framework of the EAGLE H2020 project (https://h2020-eagle.eu/). The hybrid architecture and the components' sizing have been completely defined by two of the project partners, IFPEN and Renault SA (RSA), and includes two Electric Motor / Generator units, a battery, and two gearboxes. The system has been designed with the aim to provide the maximum flexibility and versatile series / parallel operations. The choice of a hybrid series-parallel architecture has the aim to combine the advantages of series powertrain in urban driving (including smooth take-off) and of the parallel mode over rural / highway routes. Close-to-optimal operations for the ICE are guaranteed by a four-speed gearbox placed between the ICE and differential. A gearbox is preferred to a CVT power-split device to get a higher mechanical efficiency. The switch between series and parallel modes is handled by three clutches, which also help to decrease the mechanical losses when one of the motors is not used.

As said, the thermal unit is equipped with an active pre-chamber ignition system and a flexible intake and exhaust VVT device. The very high air flow demand of the ultra-lean architecture needs the adoption of a two-stage boosting system, composed of a turbocharger composed of a vaneless compressor and a variable geometry turbine, coupled in series to an E-compressor (E-Comp). Due to the presence of an electrically driven compressor, the energy input to the engine is not just the chemical energy given by the fuel. The energy input in the E-Comp also plays a role in the effective engine efficiency. The overall boost level can be then shared between the turbocharger compressor

and the E-Comp, depending on the electrical energy input given to the second one. This last is provided by the same battery pack of the hybrid propulsion system.

Therefore, the possibility to modify the overall boost level sharing between the LP compressor and the E-comp paves the way to two calibration variants. On one hand, an intensive use of the E-Comp leading to a reduced backpressure and an improved BTE but resulting in an expected more frequent battery discharge / recharge along a driving mission. On the other, the opposite situation occurs if the boost level is mainly provided by the standard turbocharger. Hence, in the following subsection, some insights will be supplied on the best engine calibration which provides the minimum CO_2 and pollutant emission along representative vehicle missions.

6.1. Multi-cylinder engine description

The Spark Ignition engine under study, whose schematic is depicted in *Figure 6-1*, is a prototype power unit constituted by four-cylinders and equipped with active pre-chambers. The main features of the investigated engine are summarized in *Table 6.1*. The PC features four orifices of 1 mm [3], and each cylinder has two intake and exhaust valves. The engine presents a cam phaser for both the intake and the exhaust camshaft. Moreover, two different cams profiles can be selected on the intake camshaft, allowing for an early valve closure (Standard Miller Lift - SML), or an extremely advanced valve closure (Extreme Miller Lift - EML) [3],[4],[5]. The latter is particularly suitable to limit the knock occurrence at high load.

The engine is fed with liquid gasoline through four port fuel injectors, located just upstream the intake valves (Inj_{MC}), and four direct injectors located into each PC (Inj_{PC}). A two-stage boosting system provides the needed boosting level to match the prescribed load target. It is composed of a variable geometry turbocharger (LPC and LPT) and a High-Pressure (HP) compressor (E-Comp), driven by an Electric Motor. An Electric Generator, mounted on the engine shaft, provides the electrical energy to recharge the battery and to power the EM. The electric fluxes are shown as a dashed line in *Figure 6-1*.

As experimentally and numerically demonstrated [2],[6],[7], the introduction of a pre-chamber allows to strongly extend the lean burn limit of a conventional SI engine. This engine is designed to operate with very lean air / fuel mixtures to improve the engine efficiency and reduce the NO_X emission, in the as wide as possible zone of the operating domain.

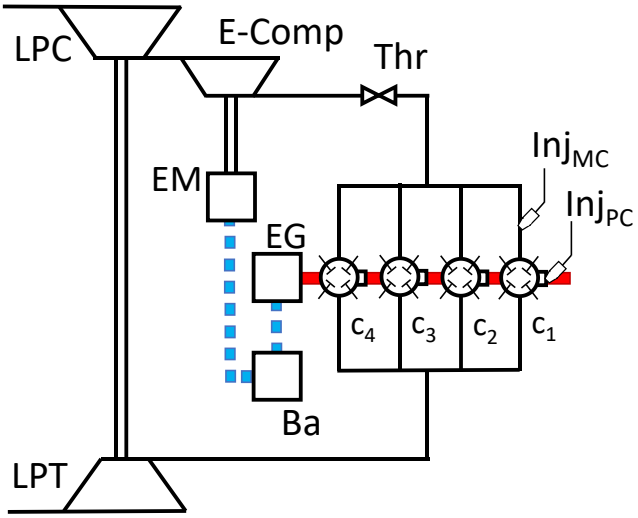

Figure 6-1 Schematic engine layout.

Table 6.1 Multi-cylinder pre-chamber engine main features.

Parameters	*Values*
Bore	76mm
Stroke	90mm
Displacement	1633 cm^3
Compression ratio	15.8
Fuel in main chamber	PFI, RON 95
Fuel in pre-chamber	DI RON 95
Pre-chamber volume	~ 1000 mm^3
Minimum PC injection duration	300 μs
$V_{pre\text{-}chamber}$ / V_{TDC}	~ 3 %
PC hole number	4
PC hole diameter	1 mm
$A_{jet\ holes}$ / $V_{pre\text{-}chamber}$,	~ 0.03 cm^{-1}
Intake Valve Opening	344-370 CAD (@0.7 mm lift)
Exhaust Valve Closure	350-380 CAD (@0.7 mm lift)
Start of PFI	140 CAD BTDC
Start of in-PC injection	300 CAD BTDC

As said, the engine above described have been used to virtually drive a HEV, belonging to the C segment, whose main characteristics will be deeply described in the last section of this chapter.

6.2. Multi-cylinder engine model and optimizer calibration

Consistently with the engine geometry, reported in *Table 6.1*, a detailed 0D/1D scheme is developed in a commercial modelling framework. The description of the flow inside the intake and exhaust pipes is based on a 1D approach, whereas "in-house" 0D sub-models are used to reproduce the in-cylinder phenomena typical of this novel architecture, such as air / fuel mixture preparation, combustion, turbulence, and heat transfer. Its reliability has been validated in the prototype IFPEN single-cylinder research unit presented in section 5.2.2. Then, here the same model, with few enhancements, has been applied to foresee the behaviour of the multi-cylinder engine, as well.

Regarding PFI and DI injections, it is assumed that the 30% of the injected fuel instantaneously evaporates, without considering spray evolution and liquid wall film formation. An empirical correlation is used to estimate the mechanical friction losses, depending on engine speed, combustion phasing, and in-cylinder pressure-peak. The steady-state flow coefficients for both the intake and the exhaust valves have been also measured on the SCE and are here assigned to predict the flow permeability through the cylinder head [3],[6],[7]. A standard map-based approach is employed to reproduce the boosting system.

The presence of a high number of degrees of freedom makes the calibration of such a complex engine very challenging. In particular, the engine has nine control parameters, namely the relative air / fuel ratio (λ) in the chambers (labelled as λ_{PC} and λ_{MC}), the LPT rack position, the power input to the E-Comp, the intake and exhaust cam phases, the spark timing (or equivalently the 50% combustion phasing), the throttle valve position, and the SML / EML cam profile.

Hence, with the aim of calibrating the engine, a value for each of the 9 control parameters above listed must be specified in each operating condition. The purpose of this task is the multi-objective optimization of the engine performance over the entire operating domain.

The calibration procedure here followed targets the maximum possible efficiency, fulfilling several constraints – i.e. maximum pressure inside MC and PC, knock intensity, turbo speed, boost level, E-Comp power, internal EGR amount, etc., – prescribed to confine thermal and mechanical stresses and operating reliability for the engine and for its components.

To find the optimal set of the control parameters, at variable speeds and loads, an automatic optimization is performed, realized by using an external multi-purpose optimizer. The optimization is performed considering two different control strategies, with differentiated fuel and electric consumptions. Particularly, the first control strategy (strategy #1) aims to maximize the conventional BTE, namely:

$$BTE = \frac{P_{ICE}}{\dot{m}_f LHV} \tag{6.1}$$

where P_{ICE} is the brake power at the engine shaft, and $\dot{m}_f$ is the total injected fuel flow rate and LHV is the lower heating value.

The second one (strategy #2) is oriented to the optimization of the *Overall* BTE:

$$OBTE = \frac{P_{ICE} - P_{HPC}/\eta_{HPC}}{\dot{m}_f LHV} \tag{6.2}$$

where P_{HPC} is the mechanical power at the E-Comp shaft and η_{HPC} is the overall electric conversion efficiency of the E-Comp imposed equal to 0.81 whatever is the operating condition. This value roughly considers the processes of battery charging via the energy delivered by the engine through the electric generator and the inverter, and the process of E-Comp electric consumption through the inverter and electric motor. Each of those four processes are assumed to occur with an efficiency of 0.95. Based on its definition, the Overall Brake Thermal Efficiency (OBTE), also considers the electric energy required by the E-Comp and drained from the battery.

For both examined control strategies, the optimization is realized along a BMEP sweep at two different engine speeds, namely 2000 and 3000 rpm. Low / medium engine rotational speeds are selected because of their relevance regarding the vehicle homologation cycles. The load sweep is automatically realized by alternatively maximizing or minimizing the BMEP, together with the BTE/OBTE, hence performing 4 different multi-objective problems, for each engine speed. Each optimization problem hence identifies a single branch of the BTE / BMEP or OBTE / BMEP Pareto frontiers. In *Figure 6-2* the logical scheme of the considered optimizations process is reported.

The selected optimization tool is the genetic MOGA-II algorithm, which represents the best choice for the case of a multi-variable / multi-objective problem. The 9 control parameters previously listed, apart from the relative air-fuel ratio in the main-chamber which is always metered to fix a value of 2, represent the independent variables of the optimization problem. Each variable is changed within a prefixed allowable range, listed in *Table 6.2*. The selection of the intake valve lift profile is indeed handled by introducing a fictitious discrete variable, associating values of 0 / 1 to the Standard / Extreme Miller valve lifts, respectively.

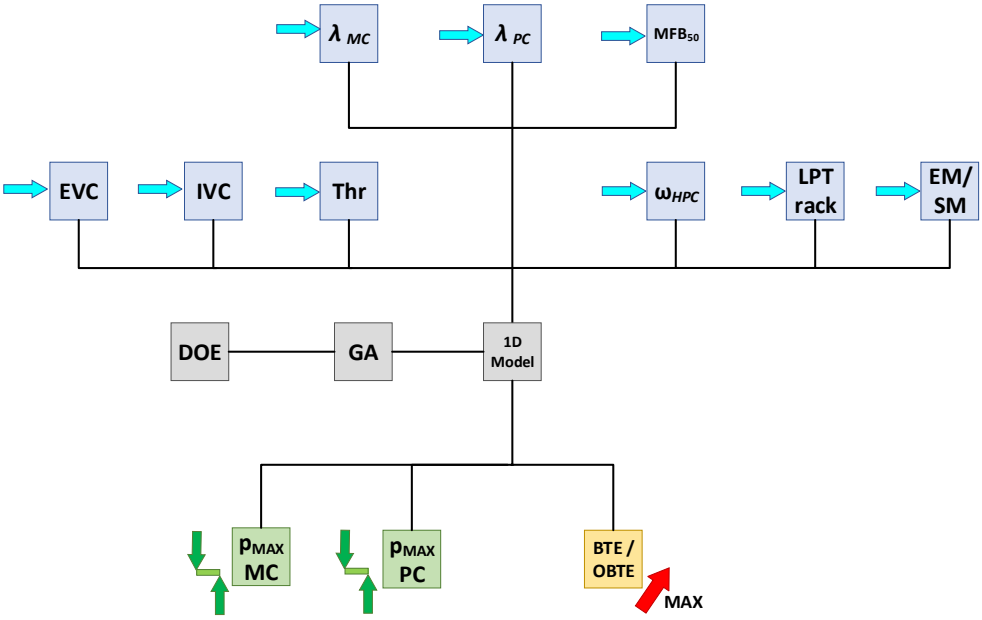

Figure 6-2 Workflow of the optimization process.

For model simplicity the normalized rack position of the LPT and the non-dimensional velocity of E-Comp (ω_{HPC}) are considered. In the case of the LPT, the highest value refers to the maximum opening of the turbine rack, which corresponds to the lowest possible turbine expansion ratio. The second parameter is the E-Comp compressor rotational speed, normalized according to the following expression:

$$\omega_{HPC} = \frac{\eta_{HPC} - \eta_{HPC,min}}{\eta_{HPC,min} - \eta_{HPC,max}} \tag{6.3}$$

where η_{HPC} is the actual rotational speed of the E-Comp, with the related maximum and minimum levels.

Table 6.2 Control parameters of the optimization process.

Parameters	*Value*
$Thr.$	$50 - 90$ degrees
MFB_{50}	$2 - 9$ CAD AFTDC
IVC	$505 - 540$ CAD AFTDC
EVC	$385 - 415$ CAD AFTDC
$Lift\ Profile - SM/EM$	$0/1$
$Normalized\ LPT\ rack\ opening$	$0.5 - 1.0$
ω_{HPC}	$0 - 1$
λ_{MC}	2
λ_{PC}	$0.8 - 1.3$

The optimizer algorithm, at each step, with an iterative process, selects the 8 engine control variables, passing them to the 1D engine model to evaluate the variables of interest. At the end of each simulation, the estimated values of the objective function are returned to the optimizer to start the next iteration. This process pursues as long as the optimal levels, being part of the Pareto frontier, are achieved.

As said, the optimizer evaluations are post-processed and filtered to check that some monitored variables do not exceed prescribed threshold levels. As an example, the maximum in-cylinder pressure is limited to 180 bar, the maximum plenum pressure to 4.3 bar, the maximum E-Comp power to 10kW, the maximum AI integral to 0.8, etc.

6.3. Numerical calibration strategies assessment and validation

The previously described optimization procedure is too much time consuming to be directly employed to compute the complete engine performance map. Hence, to speed-up the numerical calibration, a set of heuristic rules is defined to reproduce as best as possible the behaviour of the mathematical optimization (rule-based calibration). The RB is applied by including a network of logical switches, PID controllers, and "math functions" in the 0D/1D environment [8].

The RB calibration strategy proposed for the multi-cylinder engine is based on the maximization of the engine efficiency in each operating point, while complying with the classical constraints of a SI engine, such as knock intensity, and the additional ones related to the introduction of a pre-chamber, such as the maximum in-PC pressure. The maximum allowable levels imposed for the constrained parameters with additional limitations are reported in *Table 6.3*:

Table 6.3 Control parameters of the optimization process.

Parameters	*Value*
$Maximum\ in-PC\ and\ in-MC\ pressures$	180 bar
MFB_{50}	4.5 CAD AFTDC
$Maximum\ AI\ time\ integral$	0.8
$Injection\ duration\ in\ PC$	$300-900$ µs
$IVC\ range$	$505-540$ CAD AFTDC
$Maximum\ spark\ advance$	-80 CAD AFTDC
$Maximum\ speed\ LP\ group$	205000
$Maximum\ speed\ E-Comp$	140000

Differently from the conventional SI engine where the optimal MFB_{50} was imposed as about 9 CAD AFTDC, a slightly advanced value is now selected, as suggested in [3]. The prefixed MFB_{50} target of 4.5 CAD is effectively selected only under knock free operation. Otherwise, the combustion

phasing is delayed until the specified threshold level for the knock index is reached. The fuel injected in the PC is metered to get a stoichiometric level, as long as the in-PC pressure peak is lower than 180 bar, otherwise a richer mixture is selected. The limit of the injection duration of 300 μs is due to the dynamic response of the injector, which does not guarantee a repeatable and reliable operation below such interval. The fuel injection in the main chamber is controlled to realize $\lambda_{MC} = 2$ over the widest possible operating domain. This setting is modified only at high speed / high load as discussed below.

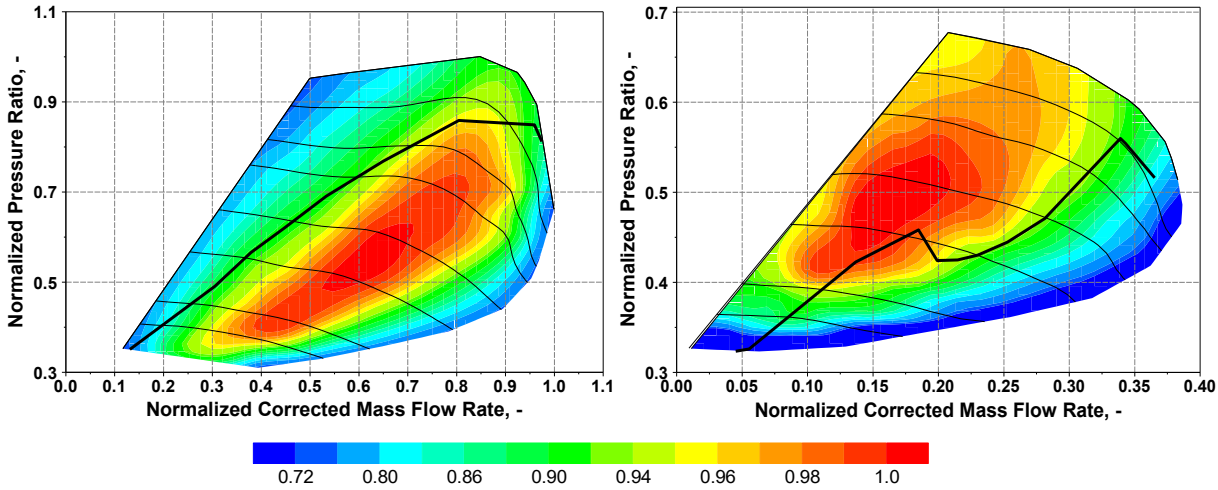

Figure 6-3. LP (a) and HP (b) compressor maps, including the running lines at full load. Due to confidentiality reasons, the pressure ratio, the mass flow rate, and the iso-efficiency lines are reported in a normalized form (min-max range converted to 0-1) [9].

Preliminary, a prefixed running line is chosen on the LPC map, reported over a normalized LPC map in *Figure 6-3(a)*, as a trade-off between an appropriate surge margin and a suitably high-pressure ratio, so to avoid an excessive E-Comp shaft power absorption (below 10 kW). Under these operating conditions, the E-Comp running line is directly identified (*Figure 6-3(b)*) to reach the HP boost level necessary to fulfil a prescribed full load (FL) target, depicted in red in *Figure 6-4*. By changing the LPC running line, a different sharing of the overall boost level between the LPC and the E-Comp would have been accordingly identified. However, whatever is the choice for the LPC running line, at very high engine speeds (usually over 4500 rpm) for the selected boosting devices, the constraints on the maximum E-Comp power and/or maximum boost level cannot be fulfilled. For this reason, the only way to achieve the FL target is to inject more fuel into the main chamber, resulting in a $\lambda_{MC} < 2$. The L2 line in *Figure 6-4* identifies the BMEP region below which a $\lambda_{MC} = 2$ operation can be sustained (light red domain), while the area above the L2 line defines the operating domain with $\lambda_{MC} < 2$ (highlighted in cyan).

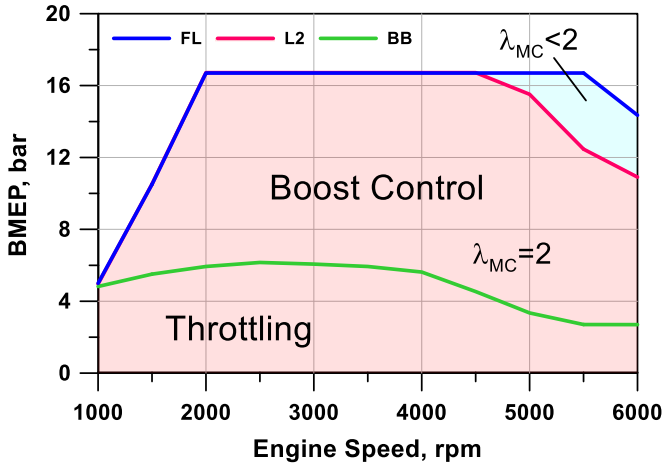

Figure 6-4 BMEP – rpm map containing the BMEP target (FL), and the L2 and BB lines.

In the low-load region, an additional line is defined, corresponding to the BMEP levels reached with the LPT fully opened and no-power given to the E-Comp, named Base Boost Line (BB in green in *Figure 6-4*). In these conditions, the E-Comp is by-passed acting on dedicated control valves. Above the BB line, the engine load is regulated by a progressive closing of the LPT and a proportional increase of the E-Comp power. Below the BB line, the LP and HP compressor settings continue to be fixed, while the load is only regulated by the progressive closure of the throttle valve.

Concerning the VVT position of intake and exhaust camshafts, simple rules are defined to select an advanced IVC at low load to have a pumping loss reduction. The intake valve advancing is however limited at very low load to avoid an internal EGR rate above 20%. In this way, a stable combustion process can be guaranteed in the real engine, at the expense of a certain pumping losses increase.

In the mid-load range, the intake VVT is moved towards a later IVC to allow for increased air flow rates, while, at very high load, an early IVC is once again preferred to reduce the effective compression ratio for knock control. The exhaust valve is accordingly controlled, to limit the valve overlap, and/or to increase the expansion work at low load.

The actual positions of the BB and L2 lines also depend on the selection of the intake lift profile, namely the SML or the EML. To reduce pumping losses, the EML is always specified when the computed air flow rate is below 100 kg/h. By analysing the results of the previous mathematical optimization, it was indeed found that for strategy #1 (max BTE), the SML is only selected below a specific BMEP limit (namely 6,5 bar), while it is always selected above 100 kg/h air flow rate in the strategy #2 (max OBTE). This can be easily explained by observing that the SML requires a lower boost level for the same load. For this reason, a lower E-Comp power is required, which improves the OBTE. Moreover, to better reproduce the optimization results, a different running line is selected for strategy #2, moving the boost sharing mainly on the LPC and reducing the E-Comp contribution.

Even if not ensuring to achieve the actual optimal calibration, the proposed rule-based methodology is quite refined to provide engine operations very close to the maximum BTE and OBTE, as confirmed in the following. In addition, the advantage of this RB strategy is related not only to its easy implementation in the used 1D software but also to its much faster execution compared to a set of multi-objective optimizations.

In the following to quantify the reliability of the two implemented calibration strategies, their outcomes are compared to the optimization results. The optimization outcomes are shown in the next figures with open symbols and label Opt and referring to the outcomes belonging to the Pareto frontier.

Figure 6-5 reports the comparisons of BTE and OBTE at 2000 rpm for the considered calibration strategies (#1 and #2). In both cases, a considerable agreement is realized along the BMEP sweep between Opt and RB procedures. *Figure 6-5* also shows the potentiality of the analysed engine architecture to reach a very high BTE level of about 50% at the higher load. In the latter conditions, lower OBTE is reached due to the relevant power request by E-Comp (see OBTE definition in eq. (6.2)). Indeed, OBTE assumes a maximum value of around 42% at medium loads, with a slight reduction at the highest BMEP levels.

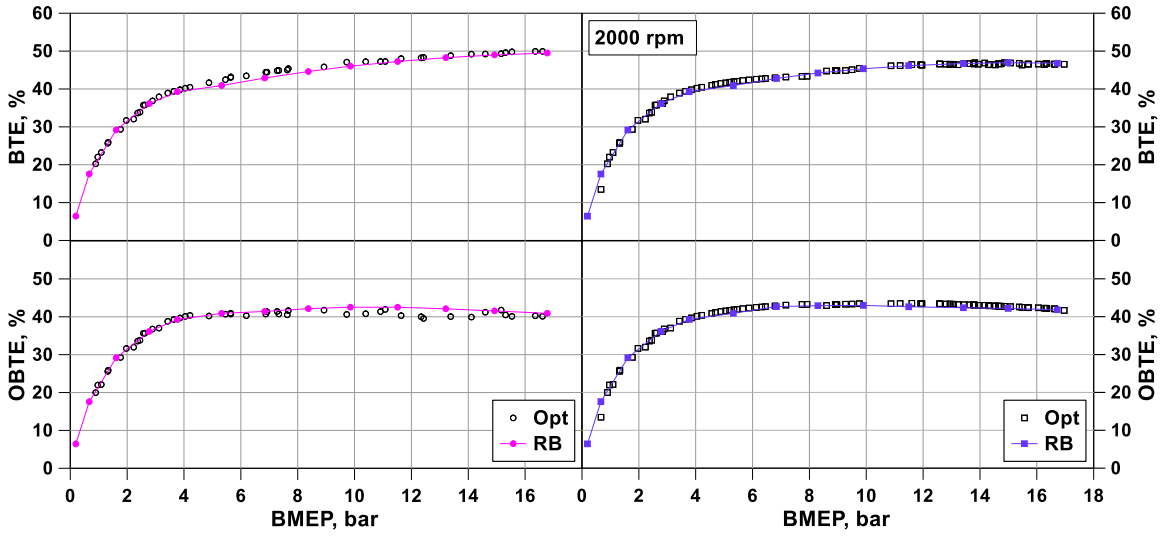

Figure 6-5 Brake thermal efficiency (BTE) and Overall brake thermal efficiency (OBTE) comparison in a BMEP sweep at 2000 rpm for strategies #1 (a) and #2 (b).

Quite satisfactory RB / Opt agreements are found for the most relevant engine calibration variables depicted in *Figure 6-6* and *Figure 6-7*. The first assessment regards the intake valve strategy and the intake / exhaust valve timings, which are plotted in *Figure 6-6.* Considering strategy #1, the Extreme Miller is mainly preferred all along the BMEP sweep, while in strategy #2, at medium / high loads the Standard Miller strategy is chosen.

From a general viewpoint, at both low and high loads, IVC is selected near to the most advanced timing setting. This option, as said, is preferred minimizing the pumping losses at low loads and mitigating the knock occurrence at high loads. In the medium BMEP range, especially for strategy #2, IVC is slightly delayed allowing for higher air flow rates, resulting in a better agreement with the Opt outcomes. EVC, indeed, exhibits an approximately constant trend with the load.

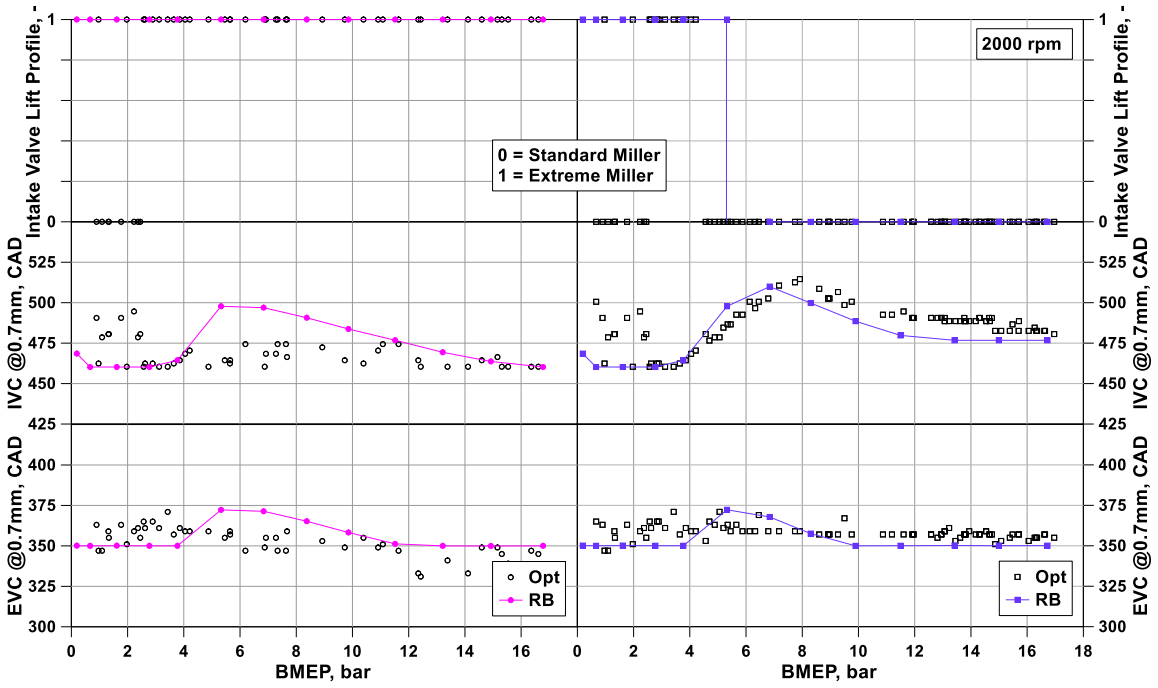

Figure 6-6 Selected intake valve lift profile, IVC, and EVC comparison in a BMEP sweep at 2000 rpm for strategies #1 (a) and #2 (b).

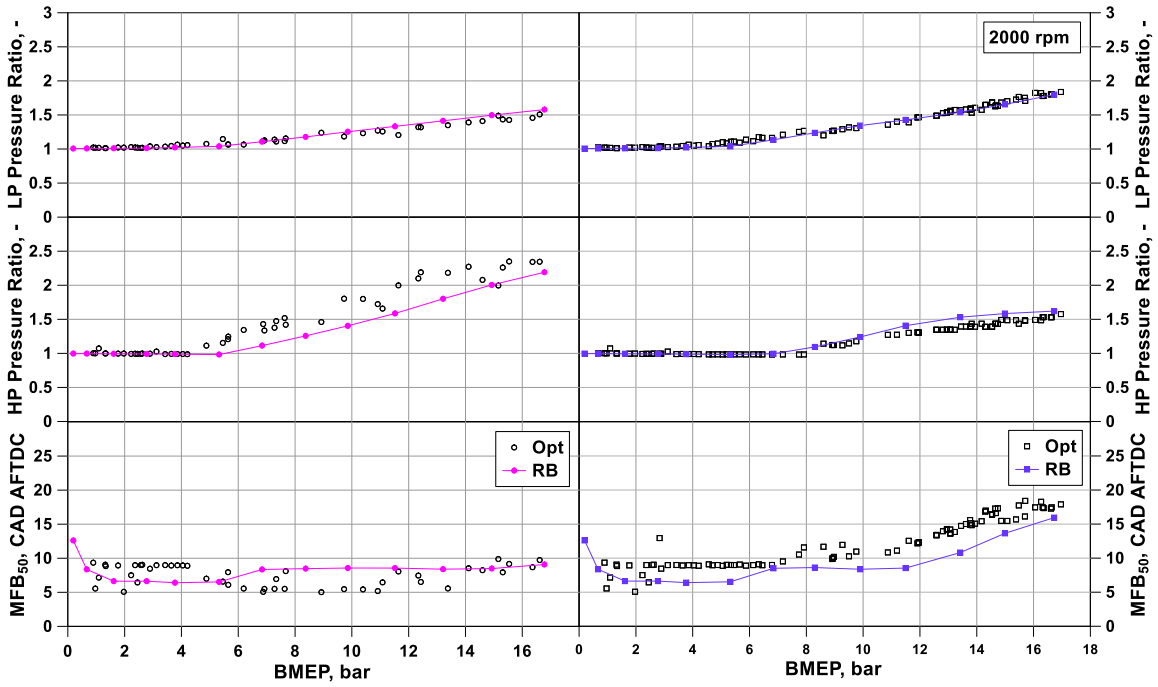

Figure 6-7 Low / High pressure ratios and MFB_{50} comparison in a BMEP sweep at 2000 rpm for strategies #1 (a) and #2 (b).

Figure 6-7 shows the sharing of the overall engine boosting between the two compressors, depicting the HP and the LP pressure ratios. As expected, strategy #1 favours a higher boosting by the E-Comp, instead of the LPC. Conversely, for strategy #2, the boosting is principally realized by the LPC, instead the E-Comp works by having a pressure ratio as low as possible. This choice involves an increased engine exhaust backpressure, but it results in a lower power absorbed by the E-Comp.

The results in *Figure 6-7* also show that HP and LP pressure ratios assume unit values below 5 bar BMEP, suggesting a throttle-based load control. Above 5 bar, indeed, both LP and HP boosting are progressively regulated by a partial closing of the LPT rack and by simultaneously increasing the E-Comp power.

It is worth to underline that the RB strategy #1 between 4-10 bar shows some discrepancies if compared to the optimal outcomes. More specifically, the RB approach determines a delayed IVC, which is compensated by a lower HP boost pressure. Nevertheless, this reflects in a slight BTE lowering compared to the optimizer output (less than 1%).

As a further assessment between RB and Opt methodologies, in *Figure 6-7* the BMEP-trends of 50% of the mass burned fraction (MFB_{50}) are reported, highlighting a satisfactory RB / Opt agreement. For this combustion parameter, the optimal value is usually around 6-10 CAD AFTDC. Indeed, in the case of later phasing, the combustion develops during the expansion stroke, leading to a less effective work exchange between the piston and the gas, while, in the case of too advanced MFB50, a relevant portion of the combustion process takes place during the compression stroke, increasing the compression work exerted by the piston on the fluid. An almost flat trend is obtained for strategy #1 in a wide load range (2-15 bar BMEP) with most of the points in the band 5-10 CAD AFTDC. A slightly delayed MFB_{50} at both higher and lower BMEP values is detected. At high loads, this is due to knock mitigation, while at low loads, it is because of the combustion lengthening and of the limitation on the maximum allowable spark advance. For strategy #2, MFB_{50} shows a different trend, with a more pronounced delay of the MFB_{50} at increasing loads (above 10 bar BMEP). This, of course, is the only possibility for knock control once the Standard Miller profile for the intake valves has been selected. This quite different behaviour is very well captured by the RB strategies.

Although not discussed here for sake of brevity, another outcome of the optimization is that a close-to-stoichiometric mixture is preferred in the pre-chamber whatever is the BMEP. A certain mixture leaning is required at high loads to limit the pressure peak in the PC.

To further prove the consistency of the RB calibration, *Figure 6-8.* and *Figure 6-9* present additional comparisons between RB and Opt strategies, referring to the engine speed of 3000 rpm. Once again, a satisfactory RB / Opt agreement for all the considered variables is reached all along the

BMEP sweep. *Figure 6-8.* shows that, for this higher speed, the optimal control involves more relevant modifications of intake valve lift profile and IVC / EVC timings at changing loads.

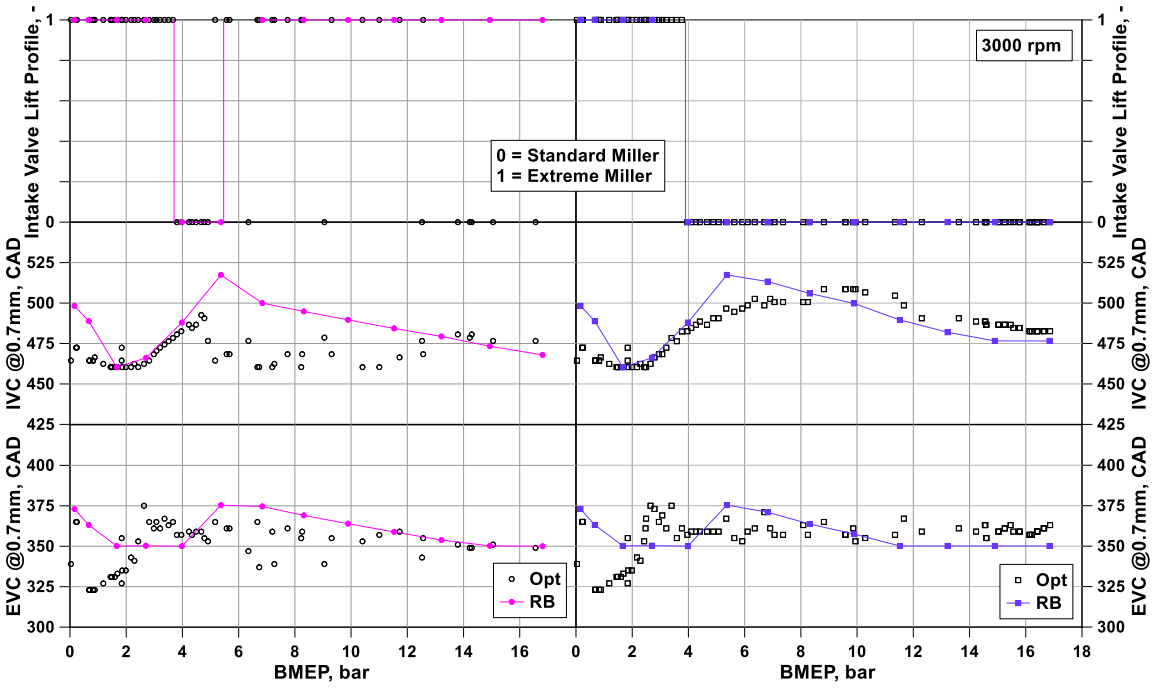

Figure 6-8 Intake Valve Lift profile, IVC, and EVC comparison in a BMEP sweep at 3000 rpm for strategies #1 (a) and #2 (b).

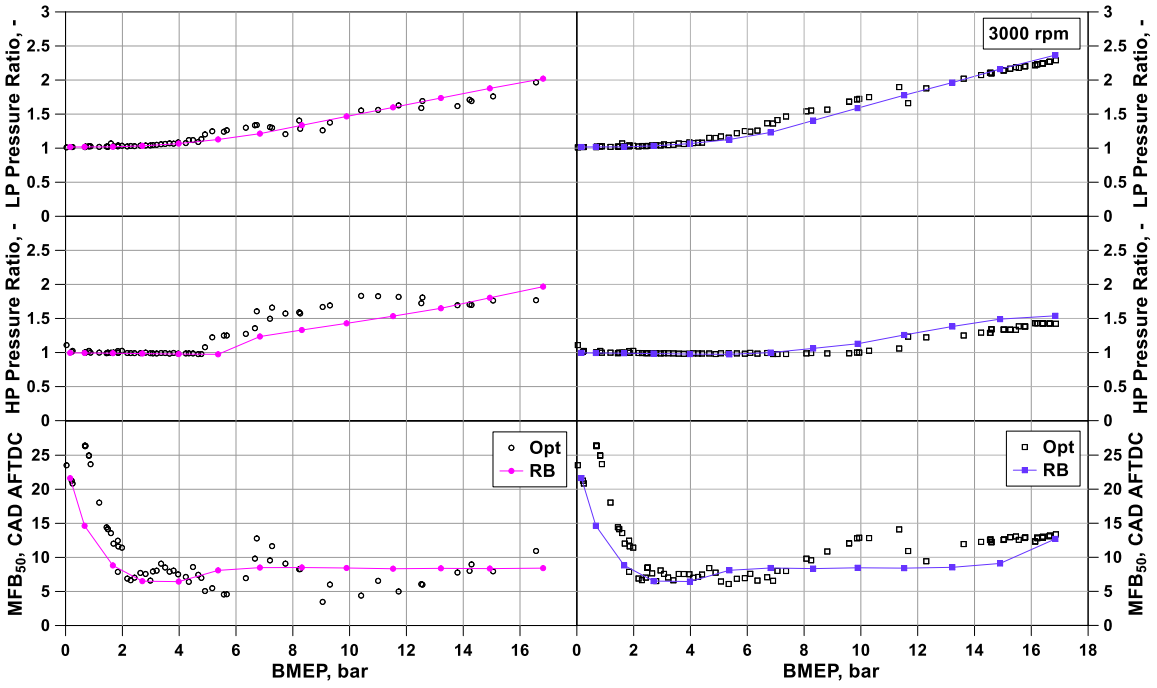

Figure 6-9 Low / High pressure ratios and MFB_{50} comparison in a BMEP sweep at 3000 rpm for strategies #1 (a) and #2 (b).

For strategy #1, differently from the previous speed, the Standard Miller is selected in a restricted low / medium load range (4-5,5 bar BMEP), to enhance the effective compression ratio, and hence the efficiency, in the light of a minor knock tendency at this speed. However, the Extreme Miller is

once again preferred as soon as the load increases (*Figure 6-8.*). For strategy #2, an earlier transition from the Extreme Miller to the Standard Miller at increasing the BMEP is detected if compared to the results at 2000 rpm. Once again, at medium loads, the IVC is delayed allowing for increased air flow rates. EVC trends appear almost load insensitive whatever is the calibration strategy and a modest discrepancy between RB and Opt procedures is detected especially at very low BMEPs (0-2 bar in *Figure 6-8.*). This is probably due to a more refined calibration given by the optimizer, which tends to reduce the valve overlap with the aim to limit the internal EGR even more than the logics of the RB approach. Referring to the results plotted in *Figure 6-9*, similar considerations to the ones already carried out for the case at 2000 rpm still hold.

Concerning the combustion phasing differences between 2000 and 3000 rpm, a greater delayed MFB_{50} is observed at low loads for the engine speed of 3000 rpm, mainly ascribed to a pronounced combustion lengthening of its initial stage, due to an excessively rich mixture in the pre-chamber at the spark event. This is due to the lower bound of the PC injection duration of 300 μs (see *Table 6.1*). At high loads, a less pronounced MFB_{50} delay occurs for strategy #2, due to the lower knock tendency at 3000 rpm.

Summarizing, the above-discussed results highlight that the RB calibration demonstrates to be extremely trustworthy for various load levels and for two different speeds, allowing to reach both efficiencies and control variables very close to the ones obtained by the optimizer-based methodology. In the light of the latter consideration, the developed RB calibration will be broadened to the full engine speed / load range in order to investigate the close-to-optimal engine performance in the whole operating domain, as reported hereinafter

6.4. Engine Performance Maps Discussion

According to the RB control strategy, the entire engine operating map is computed (consisting of 143 operating points - 11 rpm x 13 BMEP) for the two different calibration strategies above discussed. In *Figure 6-10* the BTE maps for calibration strategies #1 (a) and #2 (b) are shown. The maximum levels for both strategies occur at 2000 rpm, close to the full load region. The OBTE maps for the different strategies are shown in *Figure 6-11* For these, the maxima occur at medium speeds (2000-2500 rpm) and medium-high loads (8-14 bar BMEP). According to the selected optimization targets, a 3% higher peak BTE is obtained in strategy #1 (*Figure 6-10(a)*, while a 1% higher peak OBTE is obtained in strategy #2 (*Figure 6-11(b)*). The engine performance maps are computed following the RB control strategy previously described for the whole engine operating plane, composed of 143 operating points - 11 rpm x 13 BMEP.

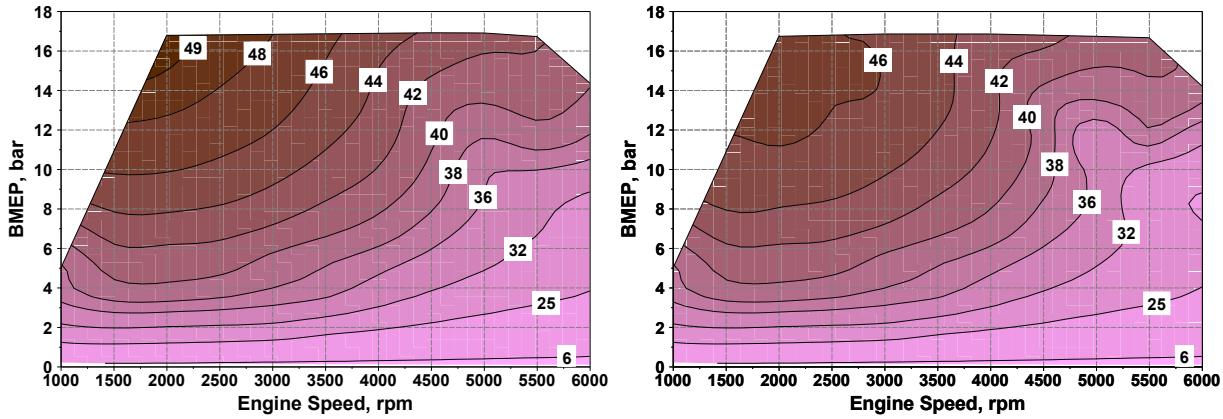

Figure 6-10 Map of BTE [%] for strategies #1 (a) and #2 (b).

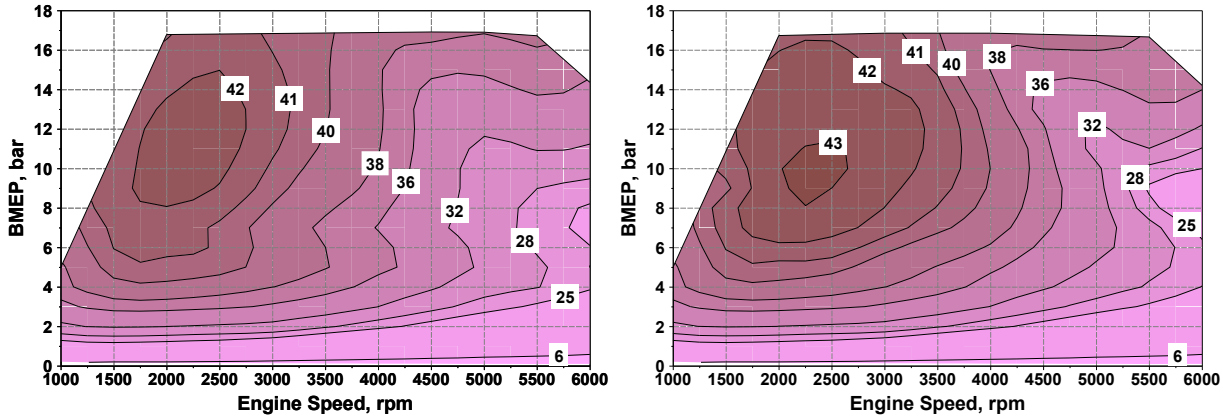

Figure 6-11 Map of OBTE [%] for strategies #1 (a) and #2 (b).

The gap between BTE and OBTE for strategy #1 is about 7% in the OBTE peak zone and gradually decreases at higher speeds and low loads. A similar behaviour characterizes strategy #2, having in the peak zone a gap of about 3-4%. This is due to the power absorbed by the E-Comp, whose maps are reported in *Figure 6-12*. For strategy #1, the E-Comp power gets to the upper bound of 10 kW, which is about the 8 % of the power rated by the engine, while for strategy #2, it only gets a maximum of about 7 kW.

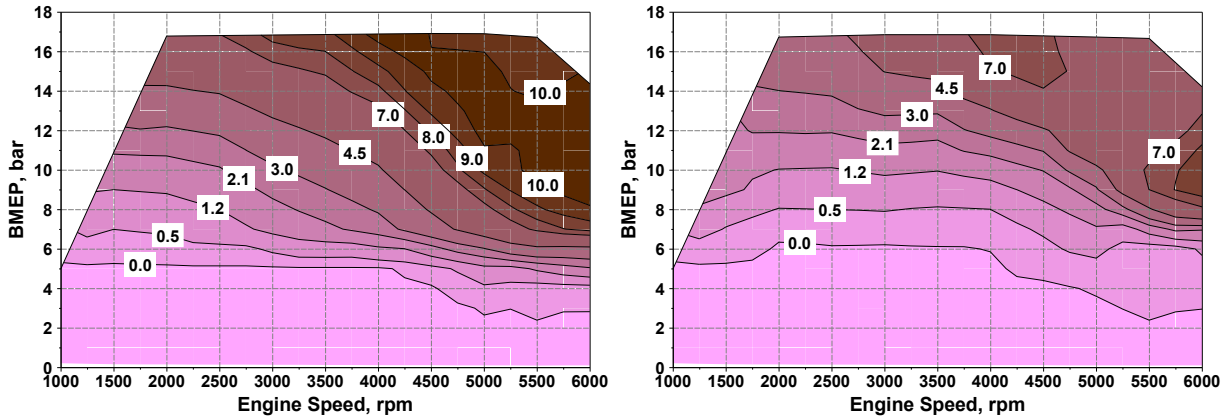

Figure 6-12 Map of E-Comp power consumption [kW] for strategies #1 (a) and #2 (b).

For the considered engine, featured by an ultra-lean air / fuel mixture, both strategies involve a very high plenum pressure, which is mandatory to achieve the load target. As an example, *Figure 6-13(*a) shows the boost pressure map for strategy #1, which attains the limit of 4.3 bar at the highest speeds and loads. The intake plenum pressure is conserved above 1.0 bar in most of the map (reduced pumping losses), and above 0.5 bar even in the area at lowest BMEP. The lambda target of 2 in the main chamber is reached in most of the operating domain, as shown in *Figure 6-13(b)*, excepting in the maximum power area. This is due to the attainment of the maximum boost pressure, which obliges to reduce the mixture leaning ($\lambda_{MC} < 2$) to get the load. Similar boost pressure and lambda maps are also found for strategy #2.

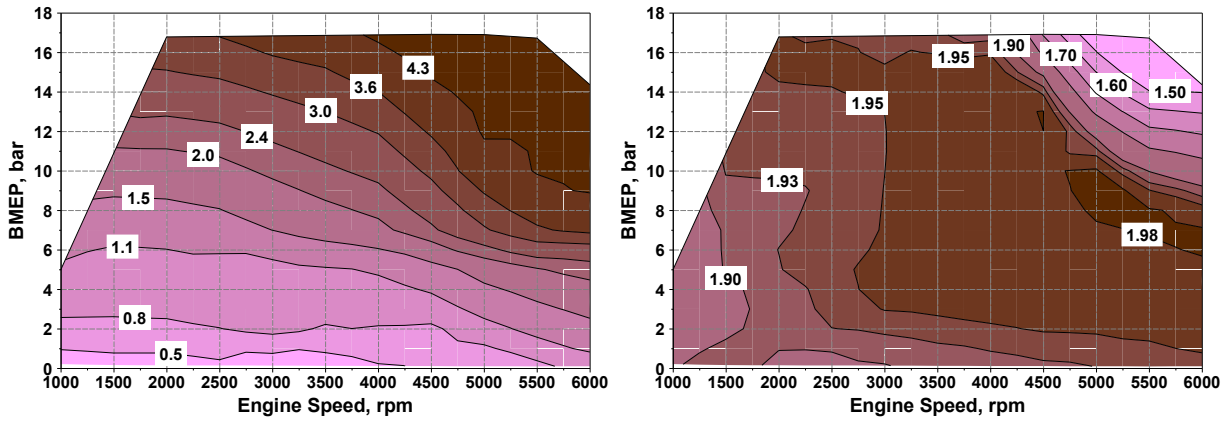

Figure 6-13 Map of intake plenum pressure [bar] (a) and Map of λ_{MC} [-] (b) for strategy #1.

The predicted Brake Specific emissions of NOx and HC are shown in *Figure 6-14(a)* and *Figure 6-14(b)*, respectively, still referring to strategy #1. With the aim to limit the temperature peaks in the burned zone of the combustion chamber, preventing the formation of the above pollutants, the ultra-lean combustion concept is used. The NOx production is very low in the most part of the operating map, except for the high speed and load zone. This is due to the lower mixture leaning in the above-mentioned zone, compared to the λ_{MC} =2 target (see λ_{MC} contours in *Figure 6-13*). Due to the higher burned temperature, if compared to the one in the MC, for this engine, the NOx production is prevailing in the pre-chamber. Although the large excess-air, here the HC production is not negligible over the whole engine domain (*Figure 6-14(b)*). This is due to the lean burning concept, which, compared to a conventional stoichiometric engine, reduces the in-cylinder temperatures, and consequently makes less effective the post-oxidation phenomenon. Looking to *Figure 6-14(b)*, the shape of the HC iso-contours is justified by a faster post-oxidation at increasing speed (less time for wall heat losses) and load (lower percent wall heat losses).

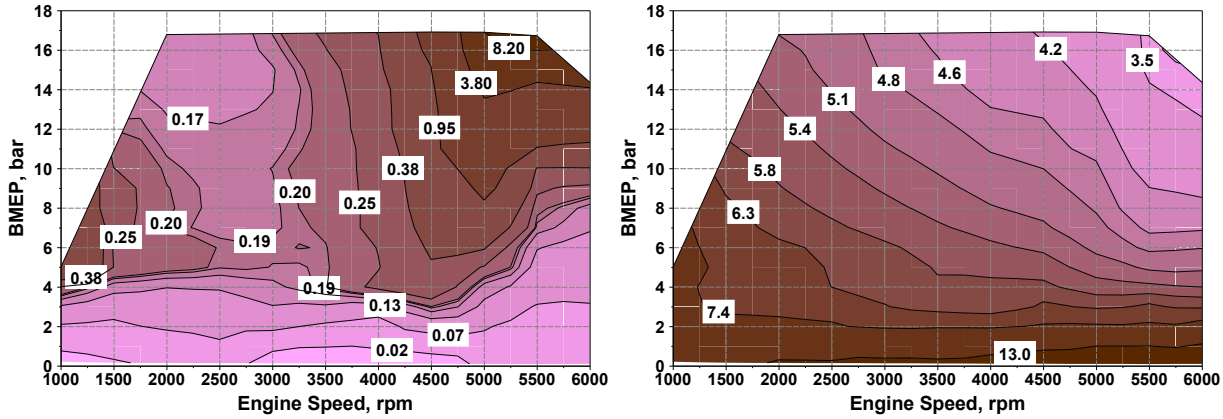

Figure 6-14 Map of brake specific NO_x emission [g/kWh] (a) and Map of brake specific HC emission [g/kWh] (b) for strategy #1.

6.5. Vehicle simulation outcomes

In the following subsections, the outcomes from vehicle simulations are presented. The vehicle analysed is a HEV architecture, in turn equipped with the multi-cylinder engine treated in section 5.2.4. The outcomes of the control strategy proposed in this thesis, i.e. ETESS, are processed and compared, in off-line and on-line variants, to PMP and ECMS methodologies, respectively.

6.5.1. HEV Architecture

The powertrain architecture of the tested C-class vehicle is a combined series / parallel hybrid power-unit, as represented in *Figure 6-15*. The powertrain includes the Multi-Cylinder PC engines described in the previous section, two Electric Motor / Generator units, a battery (Ba), three clutches (Cl_{1-3}), and two Gear-Boxes (GB_{1-2}). The main data of the vehicle and of the powertrain components are collected in

Table 6.4 [10],[11].

Thanks to the presence of three clutches, the powertrain can flexibly switch between series and parallel modes, excluding the mechanical connection with the components which are not used, to minimize the losses. In the series modality, the vehicle is moved by the EM, while in parallel mode, both thermal engine and EM are used to fulfil the power demand at the wheels. In this last case, the most common optimal control strategies involve a power-split between EM and ICE. In both series and parallel modes, the battery can be charged through the EG. The regenerative braking is realized by EM.

Table 6.4. Main characteristics of the tested HEV.

Vehicle	
Mass, kg	1730
Car aero drag, m^2	0.775
Tire rolling resistance coef., -	0.008
Wheel diameter, m	0.723
Axle ratio, -	4.4
Axle inertia, kgm^2	1.5
Electric Generator	
Max Power, kW	55
Max Torque, Nm	165
Inertia, kgm^2	0.10
Electric Motor	
Max Power, kW	50
Max Torque, Nm	240
Inertia, kgm^2	0.10
Battery	
Internal Resistance, Ohm	0.375
Voltage, Volt	400.0
Energy density, Wh/kg	170.0
Usable battery sizing, kWh	0.50
SoC limits, -	0.2 – 0.9
$Gear\text{-}Box_1$	
Gear 1 Ratio, -	2.72
Gear 2 Ratio, -	1.64
Gear 3 Ratio, -	0.99
Gear 4 Ratio, -	0.60
$Gear\text{-}Box_2$	
Gear 1 Ratio, -	2.67
Gear 2 Ratio, -	1.03

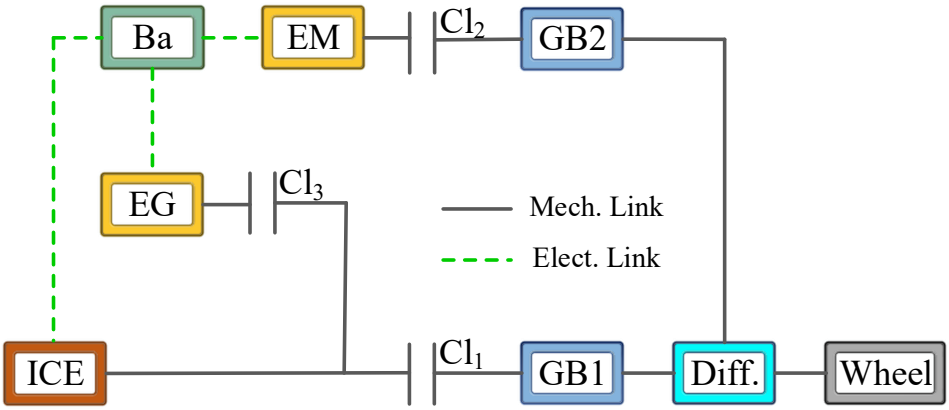

Figure 6-15 Powertrain schematic of the tested HEV.

The model-estimated Brake Specific Fuel Consumption maps of the Multi-Cylinder engine are plotted in *Figure 6-16(a)* and *Figure 6-16(b)*, for strategy #1 and #2, respectively, while the corresponding maps of the mechanical power required by its E-compressor are shown in *Figure 6-17(a)* and *Figure 6-17(b)*.

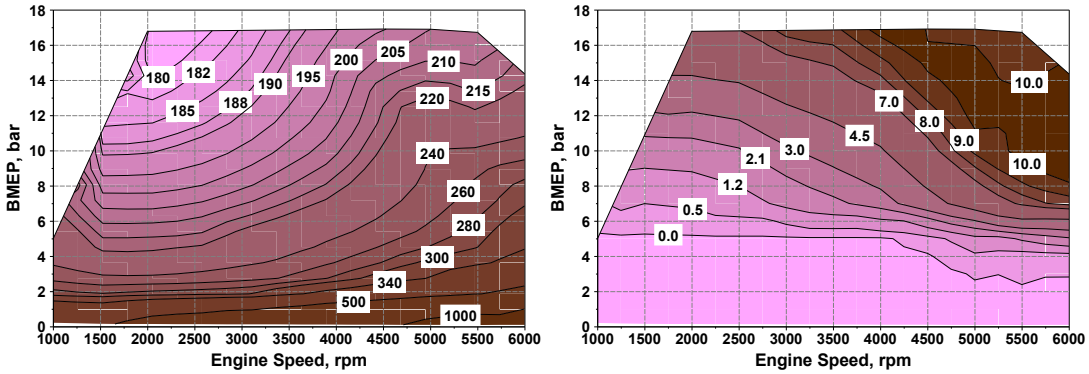

Figure 6-16 ICE BSFC map (left - g/kWh) and E-compressor power consumption map (right - kW), strategy 1.

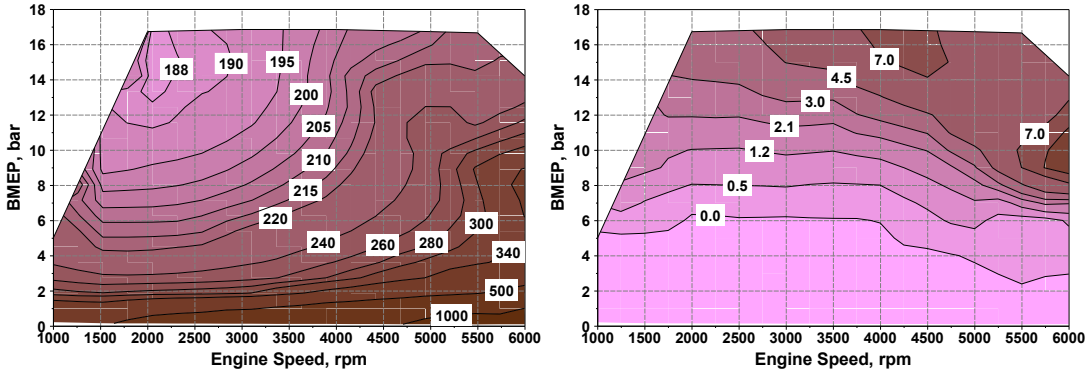

Figure 6-17 ICE BSFC map (left - g/kWh) and E-compressor power consumption map (right - kW), strategy 2.

The efficiency maps of EM and EG have been generated with an Electric Motor Map Creation Tool in Simcenter Amesim [12]. These maps, depicted in *Figure 6-18(a)* and *Figure 6-18(b)*, are representative of typical synchronous electric motors under 400 V. The efficiency maps and the maximum torque are modelled assuming a perfect symmetry of the performance for motor / brake operations. This means that the maps in *Figure 6-18(a)* and *Figure 6-18(b)* are also representative of efficiency with a negative torque, and the maximum absorbed torque is equal to the maximum delivered torque.

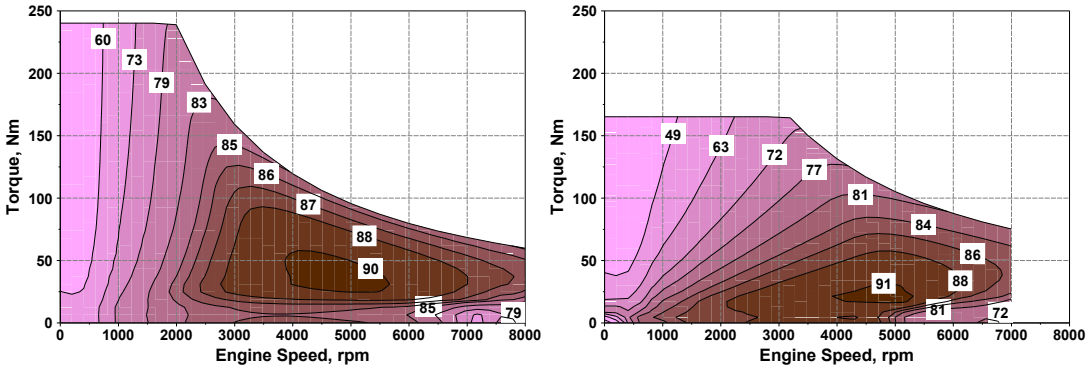

Figure 6-18 EM (left) and EG (right) efficiency maps (-).

6.5.2. Vehicle modeling

Concerning the vehicle and powertrain modeling, the simulation platform is an "in-house developed" software, implemented in Fortran language (UniNa Vehicle Simulation - UNVS) [11]. In this framework, the vehicle is characterized by the data listed in

Table 6.4 (mass, aerodynamic coefficient, etc.), while each component of the powertrain and of the vehicle is described by a lumped-parameter approach. The control is handled by a "backward-facing" (quasi-static) method [13]. The tractive demand at the wheels considers the inertial forces (related to vehicle and rotating parts), resistances (aerodynamic and rolling load), and road grade. The thermal unit and the electric motors are characterized by a quasi-steady map-based approach. In particular, for the ICE, the BSFC map is implemented, collecting the BSFC levels as a function of the engine rotational speed and Brake Mean Effective Pressure, while, for the electric units, the efficiency maps are considered, function of rotational speed and delivered / absorbed torque. For both thermal and electric units, the maximum and minimum torque curves are assigned. A linear interpolation method is used to extract BSFC, efficiency, maximum and minimum torque values from ICE and electric units performance maps. A simplified SoC model is employed to describe the battery behaviour, where Joule-losses are introduced by a constant internal resistance [14]. The gearboxes

are characterized by constant efficiencies of 0.97. The fuel consumption of the ICE at zero or negative load is estimated by a torque-dependent linear extrapolation method, following the observations in [15]. The ICE thermal transient is not modeled, resulting in a null fuel consumption penalization at a cold start. The consistency of the physics behind the adopted simulation platform has been verified in a previous work through the assessment with a commercial software, as detailed in [11]. Despite the above-mentioned simplifications, the adopted approach can be considered enough accurate to be employed for the illustration of the potential of the ETESS and for the estimation of HEV emissions.

6.5.3. ETESS outcomes

Preliminarily, the assessment between the ETESS and the PMP in off-line simulations is described, for the tested hybrid vehicle by considering different driving cycles. For each tested case, the constants λ^* (eq. (4.19)) and c_0 (eq. (4.26)) are tuned case-by-case aiming at obtaining the battery energy balance between the cycle start and end. In *Table 6.5*, all the tested configurations are reported, pointing out the driving cycles and the powertrain features. The driving cycles considered are six. Specifically, cases from #1 to #4 refer to common speed missions (standardized WLTC and Artemis variants), whereas cases #5 and #6 correspond to Real Driving Emissions compliant cycles provided by the European Commission's Joint Research Centre. For those two cases, the speed and altitude profiles are plotted in *Figure 6-19* and their main data are listed in *Table 6.6* (additional information on these two RDE-compliant cycles is available in the annex of [16]).

For the analyses presented in this section, the engine BSFC map applying strategy #1 is considered. For the RDC compliant cycles, the battery capacity is doubled. Without a resizing of the battery, the RDE-compliant cycles could not be performed without fully discharging the battery, hence without respecting the constraints of the optimization problem expressed by eq. (4.15).

Table 6.5. Simulation plan.

Case #	Driving Cycle	ICE	EM	EG	Ba
1	WLTC	Base	Base	Base	Base
2	Artemis Motorway	Base	Base	Base	Base
3	Artemis Road	Base	Base	Base	Base
4	Artemis Urban	Base	Base	Base	Base
5	RDE1	Base	Base	Base	Big
6	RDE2	Base	Base	Base	Big

Table 6.6. RDE-compliant cycles main data [16].

	RDE1	RDE2
Length, m	93’939	78’853
Duration, s	6’693	5’599
Mean Speed, km/h	56.2	56.3
Max Speed, km/h	126	129
Mean Accel., m/s^2	0.39	0.41
Max Accel., m/s^2	3.33	5.04
Mean Decel., m/s^2	-0.42	-0.43
Max Decel., m/s^2	-3.14	-3.38

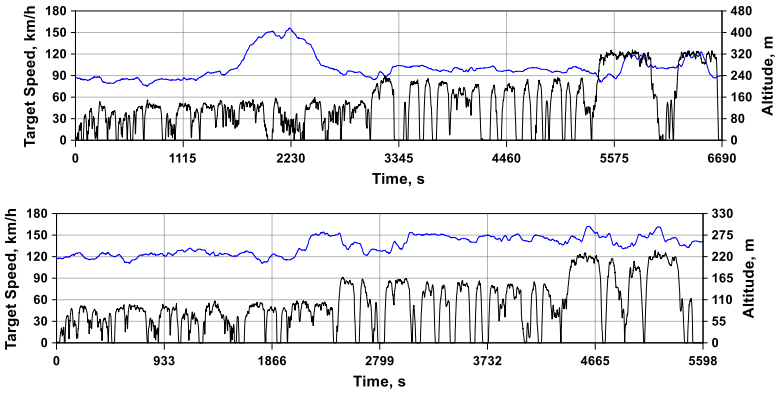

Figure 6-19 RDE-compliant cycles target speed and altitude profiles.

Detailed results will be presented for cases #1. As can be seen in *Figure 6-20*, ETESS and PMP provide almost superimposed results of EM (*Figure 6-20(c)*) and ICE (*Figure 6-20(b)*) powers, which reflects on the trends of fuel rate (*Figure 6-20(f)*), SoC (*Figure 6-20(e)*) and selected gear number (*Figure 6-20(g)*). The power split trend in *Figure 6-20(h)* (upper side) points out that the PMP switches between 0 and 1, even if a modulation between those extreme levels is potentially available. The ETESS profile is superimposed in most parts of the cycle. The bottom part of *Figure 6-20(h)* shows the ratio between the power of EG and ICE. It can be observed that the PMP chooses to realize a very limited battery charging through the EG, which determines a SoC profile similar to the ETESS one, for which the battery charging by the ICE is disabled.

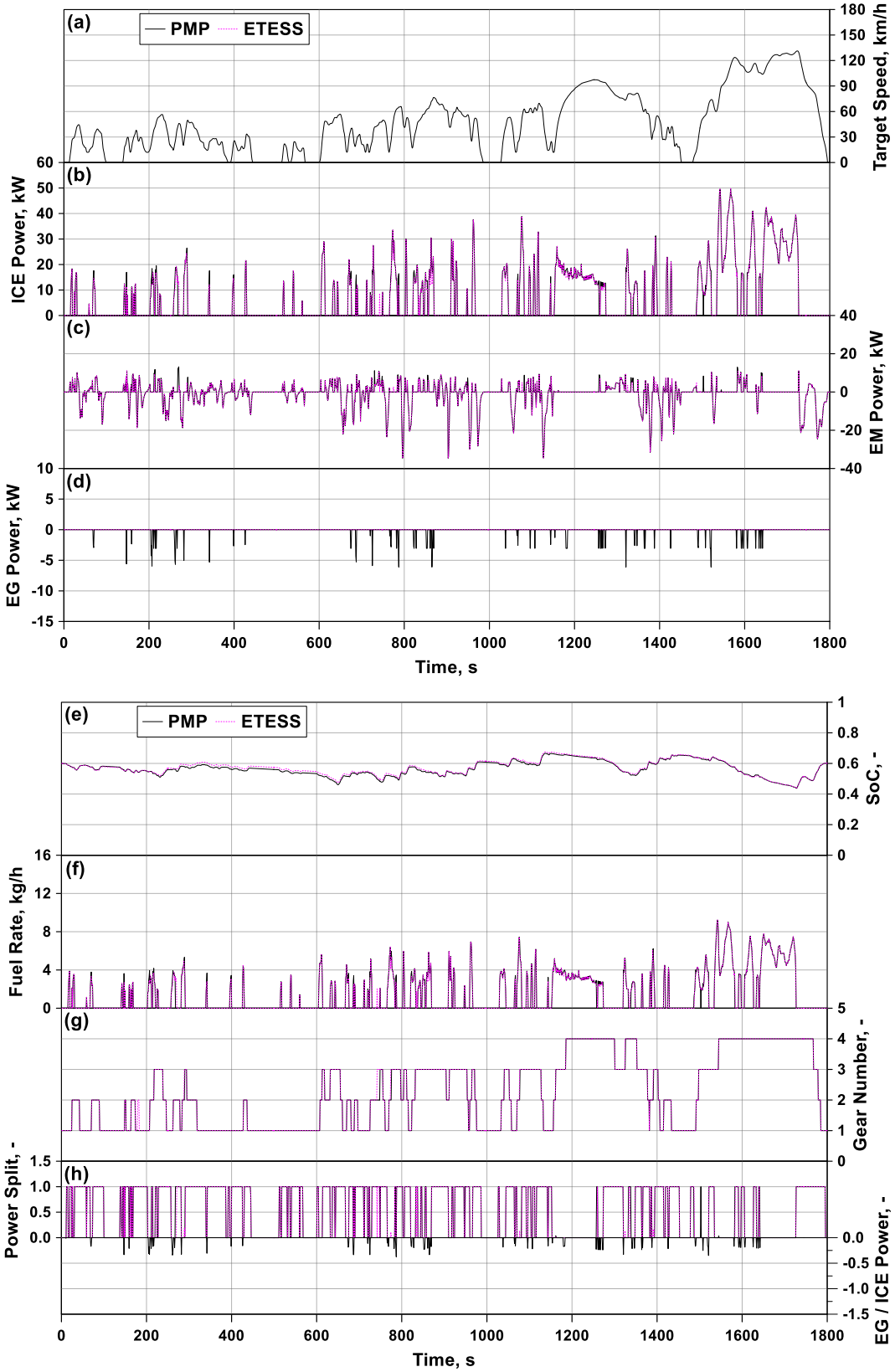

Figure 6-20 PMP / ETESS comparisons of ICE power (b), EM power (c), EG power (d), SoC (e), fuel rate (f), GB1 number (g) and vehicle mode (h) along the WLTC (vehicle speed – (a)) – case #1.

From an overall analysis of the instantaneous profiles for the two compared control strategies, it turns out their substantial coherence. A global comparison between ETESS and PMP is made by the

bar charts in *Figure 6-21*. The bars represent the consumed mass of fuel per kilometre for all the considered cases, and, over each couple of bars, is reported the fuel consumption percent difference (assuming as a reference the PMP level). The ETESS behaves similarly to PMP, with an average fuel consumption increase of about 0.2% and, in all cases below 0.6%. Greater differences emerge when the electric driving is limited (cases #4). Following in the ETESS / PMP comparison assessment, very similar fuel consumptions occur over substantially different driving cycles. This result appears relevant considering that those cycles differ in terms of both power demand, vehicle medium and maximum speed, vehicle medium and maximum acceleration / deceleration, duration, and length.

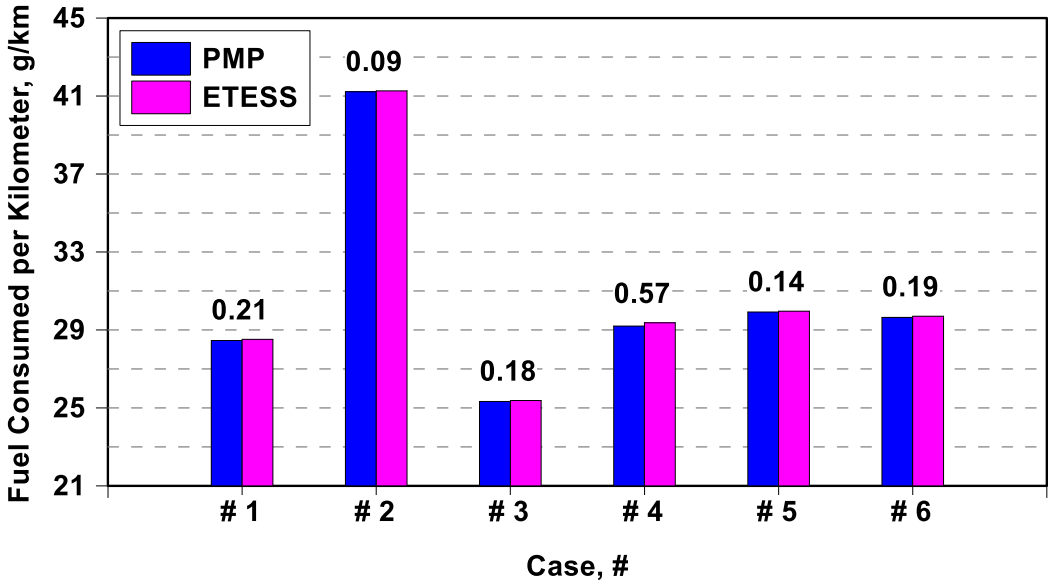

Figure 6-21 Assessment of kilometric consumed fuel in the cases of *Table 6.5* between off-line ETESS and PMP.

The PMP strategy allows achieving a lower fuel consumed, however with a difference with the ETESS smaller than 1%. This result also depends on the gridding process to access the maps. This is clarified by a parametric analysis on the gridding of the maps of EM and EG, whose results are reported in *Figure 6-22*. This last shows the kilometric fuel consumption for different gridding of the torque levels for EM and EG (whose number of breakpoints are represented in the figure by the notation n_{EM}xn_{EG}) and the simulation time normalized by the physical time. The setting with a grid of 29x19 is assumed as a reference for the definition of the fuel consumption percent difference reported on each bar. For sake of completeness, the values related to the ETESS are shown, as well. *Figure 6-22* underlines that, refining the grid, the fuel consumption slightly reduces, but the computational time increases exponentially, as expected. The lowest fuel consumption level is reached by the PMP with the finest grid (79x69 points) among the ones considered but with a simulation time about 10 times longer than the reference setting (29x19). Compared to the ETESS, the computational time is about three orders of magnitude higher, with only a slight increased fuel

consumption. Among the tested gridding, the overall difference between the best and worst PMP cases is about 1.3 %, proving the relevance of this aspect for the identification of the optimal strategy and fuel consumption. Analogous sensitivity analyses are repeated for all the other cases of *Table 6.5*, from which emerge that the differences between the gridding settings are less evident. As an example, the results of the analyses are shown for case #1 in *Figure 6-23*. In this case, the percent difference between the extreme PMP was reduced to about 0.1%.

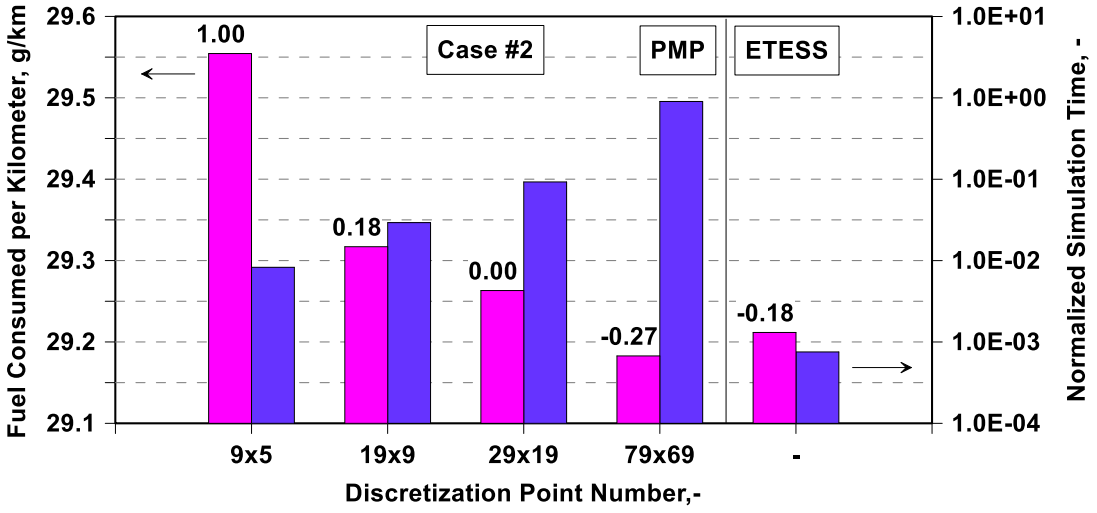

Figure 6-22 Assessment of kilometric consumed fuel and normalized simulation time in the case #2 of *Table 6.5*, between off-line PMP, for different map grid discretization, and ETESS.

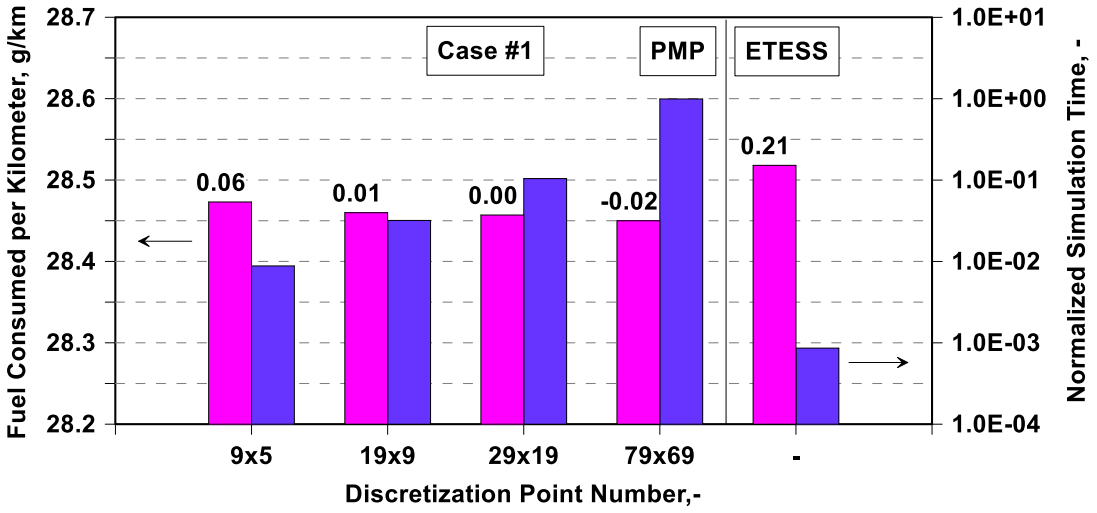

Figure 6-23 Assessment of kilometric consumed fuel and normalized simulation time in the case #1 of *Table 6.5*, between off-line PMP, for different map grid discretization, and ETESS.

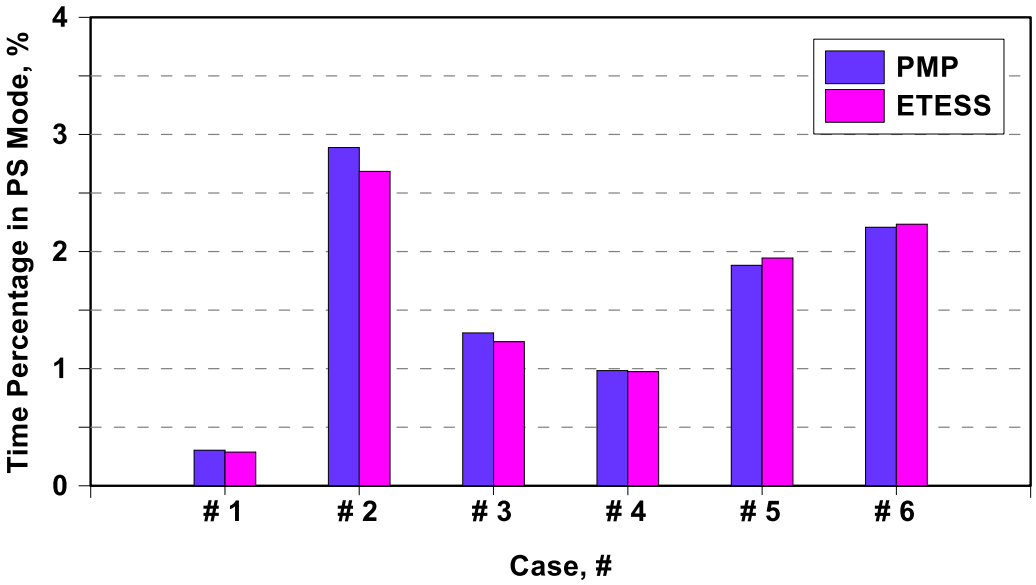

Figure 6-24 Assessment of time percentage in power-split mode in the cases of *Table 6.5* between off-line ETESS and PMP.

Coming back to the comparison between the considered cases of *Table 6.5*, the bar chart in *Figure 6-24* depicts the duration when a hybrid thermal / electric driving is chosen (PS greater than 0 and lower than 1) normalized by the total cycle duration. It can be noted that in all cases, a power-split is applied both from PMP and ETESS to a comparable extent.

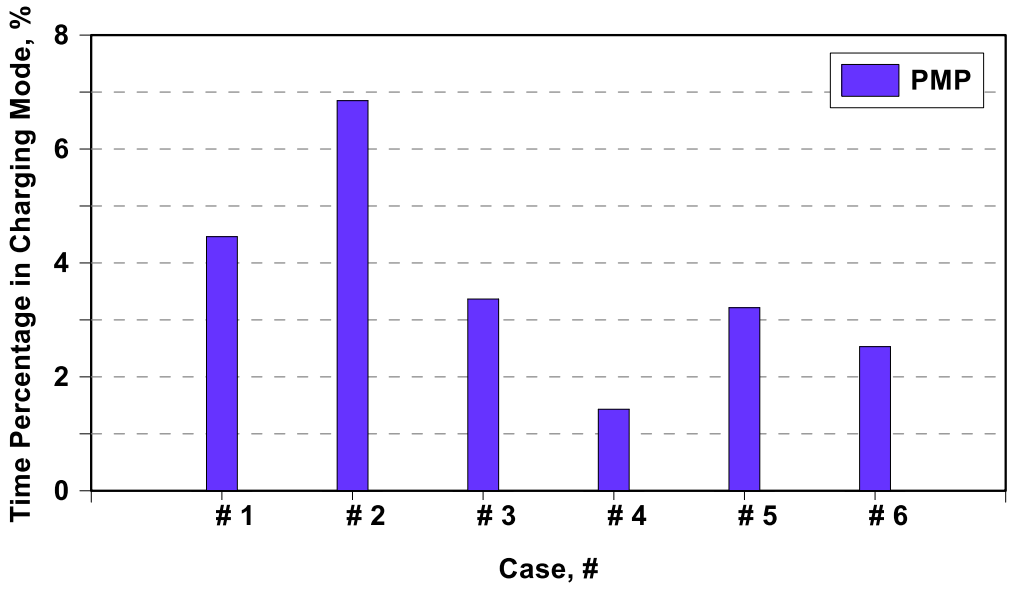

Figure 6-25 Time percentage in charging mode for PMP in the cases of *Table 6.5*.

The time percentage in charging mode is shown in *Figure 6-25* for the PMP strategy. It is worth recalling that the same plot for the ETESS would have been meaningless, not being allowed battery charging through the EG. *Figure 6-25* highlights that more burdensome cycles require more time in charging mode.

As a final consideration about off-line simulations discussed above, the ETESS gives fuel consumption performance very close to PMP ones in all tested cases, but with a shorter computational time (about two orders of magnitude lower). The ETESS executes three orders of magnitude faster than the physical system, demonstrating the potential for a real-time implementation on the vehicle.

The second part of the numerical activity concerns the verification of the robustness of the ETESS on-line version for different driving cycles (all the cases listed in *Table 6.5*), in comparison to a well-assessed on-line methodology such as the ECMS. The on-line variant of ETESS is tested establishing an adaptative correction for c_0 in eq. (4.26), achieved by using a PID controller. The latter minimizes the error between the current SoC and a predefined target of 0.55. The correction is applied starting from an initial value that is equal, for each case, to the one identified for the corresponding off-line simulation. A similar approach is adopted for the ECMS analyses, where the control adaptivity is realized by a PID controller acting on s_0 in eq. (4.22).

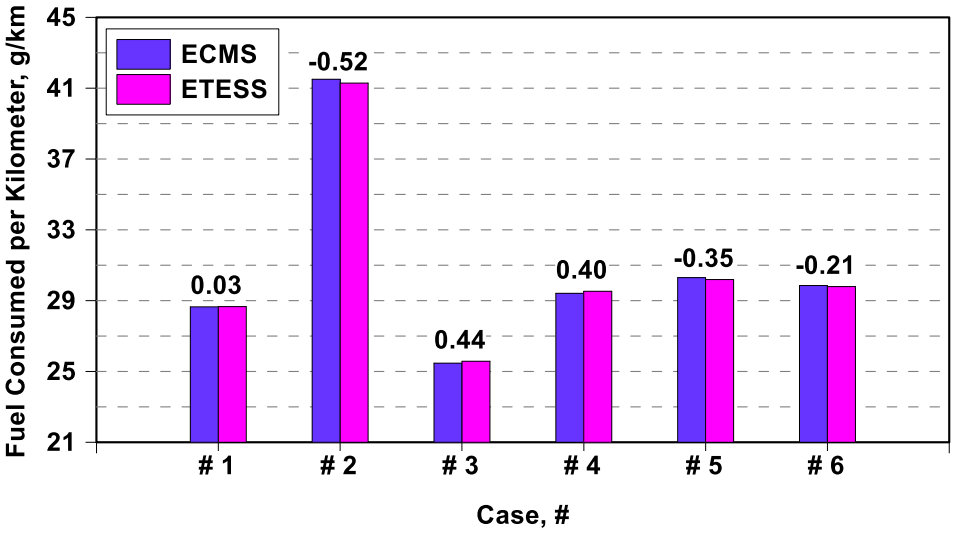

Figure 6-26 Assessment between on-line ETESS and ECMS of kilometric consumed fuel and percent difference in the cases of *Table 6.5*.

The on-line simulations consist of six simulations for each case, with different initial SoC and the same final target. The results of those analyses are arranged, according to the WLTP procedure [17],[18], to obtain a corrected kilometric fuel consumption. The results are reported in the bar chart in *Figure 6-26*. The ETESS returns values comparable to the ECMS ones, confirming the robustness of the methodology. A fuel consumption penalization of about 0.3 % arises on average. ETESS even lower levels in the cases #2. In the on-line ETESS variant, if compared to the ECMS, the advantages in the simulation time are confirmed, to a similar extent.

As a final consideration, the slightly different performance of ETESS compared to well-assessed methodologies (PMP and ECMS) appears acceptable because of its computational efficiency. The

near optimal results essentially arise from the theoretical background of the ECMS approach. The additional evidence that emerged by the proposed analyses is that a fine exploration of whatever power-split is not mandatory, since its evaluation in two relevant values (either 0 or 1) is enough to reach results near to optimum. Further, the ETESS computational efficiency proves the potential for a real-time implementation and for the handling of situational information, which are required for the control of connected vehicles. The strategy provides a certain robustness for different driving missions.

6.5.4. ETESS application to CO_2 and pollutant emission prediction

Once assessed the consistency of the ETESS strategy, it has been applied on the EAGLE HEV to compare the engine calibration strategy #1 and calibration strategy #2, presented in section 6.4, in terms of CO_2 and pollutant emissions along WLTC and RDE1 cycles. The results are presented in the form of bar charts and express the kilometric emission. Each couple of bars compares the results of the calibration strategy #1 (red) and strategy #2 (blue), reporting on the top the percent difference.

Starting from the CO_2 results, shown in *Figure 6-27* a first consideration is that the emissions are below the target imposed by the European Union for 2021 of 95 g/km, but above the one of 2025, equal to about 81 g/km, whatever is the ICE control strategy These results indicate that the HEV vehicle here analysed, even equipped with a very efficient thermal unit, is not enough to match the EU 2025 target and a plug-in HEV variant is mandatory to get this. The pollutant emission outcomes, as stated above, refer to engine-out values, although compared to the tailpipe reference standards imposed by the legislation. The potential abatement due to an after-treatment system is not explicitly considered. However, the comparison can help also to evaluate and design the most adequate Exhaust After-Treatment System (EATS) for the considered application.

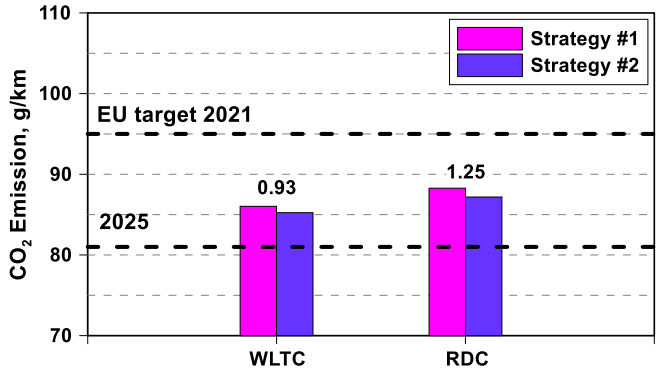

Figure 6-27 Strategies assessment of CO_2 emission and their percent difference along WLTC and RDC.

Looking at the values for the nitrogen oxides (*Figure 6-28(a)*), it can be seen that the emissions are within the bounds. The HC values (*Figure 6-28(b)*), for both the considered cycles and calibration strategies, are much higher than the limit imposed from the Euro 6d, highlighting the need for an oxidizing EATS for regulation compliance. Anyway, the technology of an oxidizing EATS at the current state-of-art is very robust, low-cost, and reliable, not representing a substantial challenge for a real on-vehicle application. The engine calibration, either strategy #1 or #2, does not seem to exert a substantial influence on the pollutant emissions. It is worth noting that the ETESS control strategy is not conceived to minimize the pollutant emissions, but the fuel consumption, and hence the CO_2 emissions.

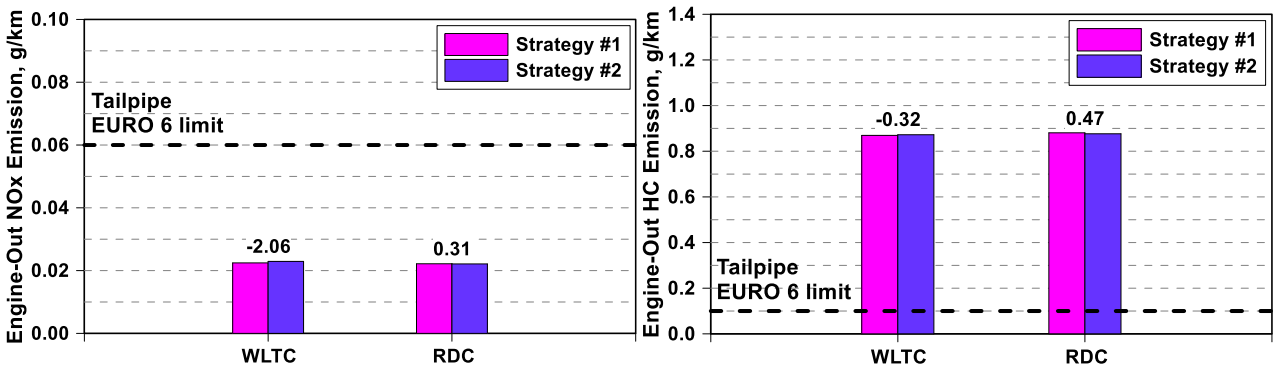

Figure 6-28 Strategies assessment of NO_x emission (a) and of HC emission (b) and their percent difference along WLTC and RDC.

The comparison presented underlines that strategy #2 allows slightly lower CO_2 emissions for both the considered driving cycles. To clarify this result, the instantaneous trends of some representative control and performance parameters are plotted in *Figure 6-29* with reference to the WLTC. The trends underline that the powertrain control is practically the same for both the ICE calibrations, resulting in almost superimposed traces of ICE power (b), EM power (c), and gear number (g). Some differences emerge for the trends of E-Comp power (d) and SoC (e), which reflect in slight misalignments of fuel consumption (f) and battery power (h) profiles. Note that a positive value of battery power corresponds to an energy flux drained from the battery.

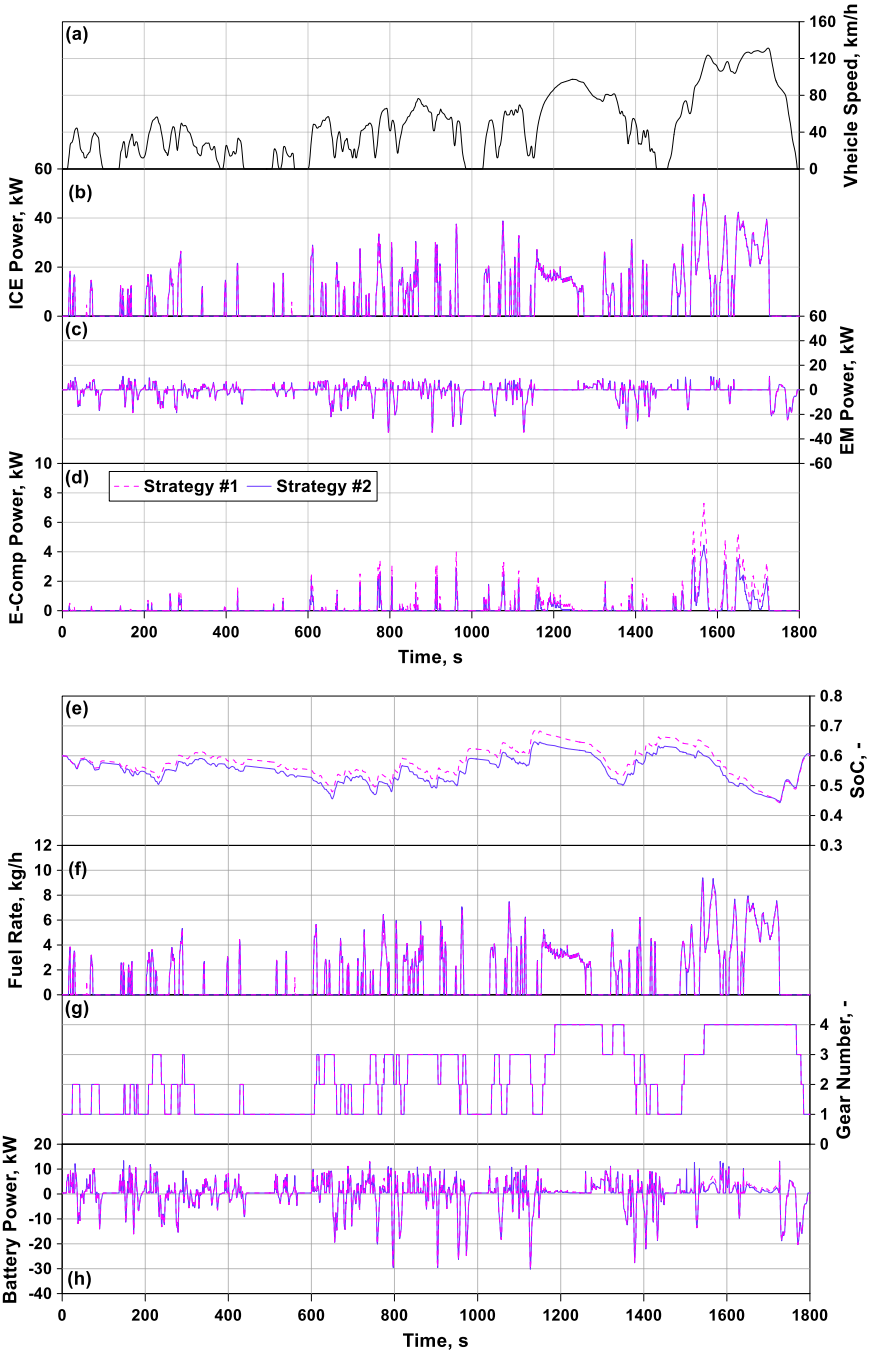

Figure 6-29 Instantaneous trends of vehicle speed (a), ICE power (b), EM power (c), E-Comp power (d), SoC (e), fuel rate (f), gear number (g), and battery power (h) along WLTC.

To better highlight the differences among the two engine calibrations, the plots of SoC, fuel rate, and battery power are re-proposed in *Figure 6-30* with a magnified time scale, in the most load-demanding portion of the driving cycle, namely between 1450-1750 s. During this period, the fuel rate is lower for the calibration strategy #1, if compared to the strategy #2 one, while the opposite occurs for the battery power consumption due to a higher E-Comp power absorption (*Figure 6-29(d)*). This reflects in a faster decrease of the SoC, which leads to a reduced electric driving in the first portion of the cycle, where the load demand is lower. For this reason, the ICE works for a

longer time in the operating conditions, namely at low load / speed, where its efficiency is well below its maximum level. On the contrary, the calibration strategy #2 allows a longer pure electric driving in the first portion of the cycle, avoiding the thermal engine operations with very reduced efficiency.

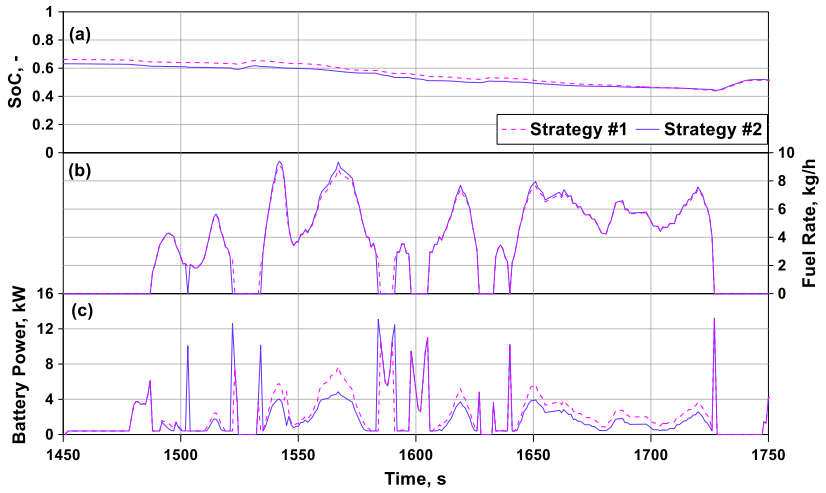

Figure 6-30 Instantaneous trends SoC (a), fuel rate (b), and battery power (c) along the last portion of WLTC.

A similar behaviour emerges for the RDC, as shown in *Figure 6-31*. This reports the vehicle speed profile (a) and the SoC trend (b). Note that the initial SoC level is chosen to get simultaneously the optimal control and battery energy balance along the cycle. Such a choice is a consequence of the simplified approach for the battery treatment, where the losses are not dependent on the instantaneous SoC level and on the possible stress when the extreme SoC bounds are attained.

Once again, during the most load-demanding portion of the cycle (after about 5400 s), the battery discharge for the calibration strategy #1 is faster, and this is compensated by a reduced use of electric driving in the first portion of the cycle. This occurrence globally penalizes strategy #1 in comparison with strategy #2.

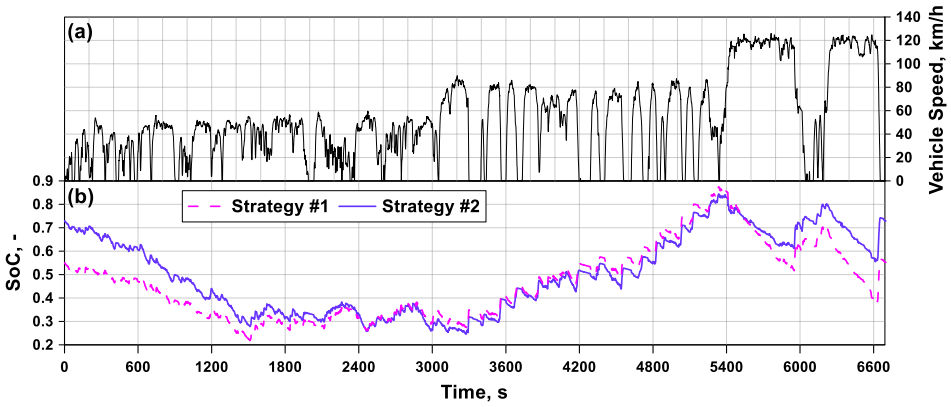

Figure 6-31 Instantaneous trends vehicle speed (a) and SoC (b) along the RDC.

Under a more general point of view, for a given battery capacity and vehicle mission, the engine calibration which reduces the energy drain from the battery, allows for a more efficient choice of the electric driving phase along the cycle. In the presented cases, however, a limited benefit has been estimated. An explanation of such reduced fuel consumption differences can be drawn analysing the time-evolution of the engine operating point. Referring to the RDC, the instantaneous engine operating points, sampled at each second, are shown in *Figure 6-32.* They are plotted over the map of OBTE difference between strategies #2 and #1. It can be observed that most of the samples are located in a speed range between 1500 and 2500 rpm and loads below 8/9 bar BMEP, where the OBTE difference is lower than 0.6% and the E-Comp power is small (*Figure 6-12*). Changes between the two calibrations only emerge outside the above operating area, where the percentage difference in terms of OBTE increases, contributing to reduce the fuel consumption of strategy #2. Similar considerations can be applied to the WLTC results. Different driving missions, more load demanding, are expected to bring out more relevant differences between the considered strategies.

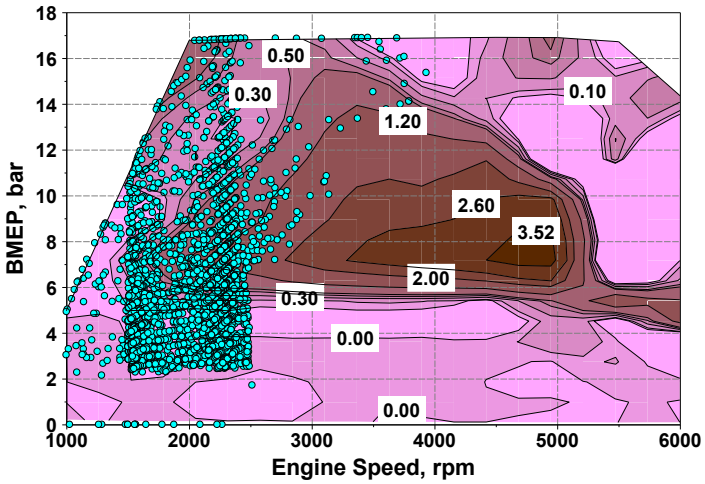

Figure 6-32 Instantaneous engine operating point along the RDC, over the OBTE difference between strategy #2 and #1.

Even if the advantage of strategy #2 cannot be considered yet a general result, due to the need for further verifications with different powertrain / vehicle types, it seems that a reduced battery consumption, even if the thermal engine will not give its maximum efficiency performance, is the path to improve the hybrid vehicle fuel economy. As stated above, further analyses will be performed in the next development of this activity to confirm the generality of this result.

References

[1] Sens, M.; Binder, E.; Benz, A.; Kramer, L.; at al. Pre-chamber ignition as a Key Technology for Highly Efficient SI Engines-New Approaches and Operating Strategies. 39th International Vienna Motor Symposium, Apr. 2018.

[2] Mueller, C., Morcinkowski, B., Schernus, C., Habermann, K., Uhlmann, T., "Development of a pre-chamber for spark ignition engines in vehicle applications," 4th International Conference on Ignition Systems for Gasoline Engines, Dec. 2018, doi: 10.5445/IR/1000088588.

[3] Serrano, D., Zaccardi, J.M., Müller, C., Libert, C. and Habermann, K., "Ultra-Lean Pre-Chamber Gasoline Engine for Future Hybrid Powertrains," SAE Technical Paper, 2019-24-0104, 2019, doi:10.4271/2019-24-0104.

[4] Millo, F.; Bernardi, M.G.; Delneri, D. Computational Analysis of Internal and External EGR Strategies Combined with Miller Cycle Concept for a Two Stage Turbocharged Medium Speed Marine Diesel Engine. SAE Int. J. Engines 2011, 4(1): 1319-1330, doi: 10.4271/2011-01-1142.

[5] Gottschalk, W., Lezius, U., Mathusall, L., "Investigations on the Potential of a Variable Miller Cycle for SI Knock Control" SAE Technical Paper 2013-01-1122, 2013, doi: 10.4271/2013-01-1122.

[6] Bozza, F.; De Bellis, V.; Tufano, D.; Malfi, E. et al. A Quasi-Dimensional Model of Pre-Chamber Spark-Ignition Engines 2019, SAE Technical Paper 2019-01-0470, doi:10.4271/2019-01-0470.

[7] Bozza, F.; De Bellis, V.; Tufano, D.; Malfi, E.; et al. "1D Numerical and Experimental Investigations of an Ultra lean Pre-Chamber Engine". SAE International Journal of Engines 2020, 03-13-02-0012, doi:10.4271/03-13-02-0012.

[8] Bozza, F.; De Bellis, V.; Malfi, E.; Teodosio, L., et al. "Optimal Calibration Strategy of a Hybrid Electric Vehicle equipped with an Ultra-Lean Pre-chamber SI engine for the minimization of CO_2 and pollutant emission," *Energies* 2020 13(15): 4008.

[9] Bozza F, Tufano D, Malfi E, Teodosio L. et al. Performance and Emissions of an Advanced Multi-Cylinder SI Engine Operating in Ultra-Lean Conditions. SAE Technical Paper 2019-24-0075, 2019. doi: 10.4271/2019-24-0075.

[10] Tufano D, De Bellis V, Malfi E. Development of an on-line energy management strategy for hybrid electric vehicle. Energy Procedia 2018; 148: 106-113. doi: 0.1016/j.egypro.2018.08.037.

[11] De Bellis V, Malfi E, Tufano D, Bozza F. Efficient Thermal Electric Skipping Strategy applied to the Control of Series/Parallel Hybrid Powertrain. SAE Technical Paper 2020-01-1193, 2020, doi: 10.4271/2020-01-1193.

[12] Dabadie J-C, Sciaretta A, Font G, Le Berr F, Automatic Generation of Online Optimal Energy Management Strategies for Hybrid Powertrain Simulation, SAE Technical Paper 2017-24-0173, 2017. doi: 10.4271/2017-24-0173.

[13] Wipke KB, Cuddy MR, Burch SD. ADVISOR 2.1: a user-friendly advanced powertrain simulation using a combined backward/forward approach. IEEE Transactions on Vehicular Technology 1999; 48: 1751-1761. doi: 10.1109/25.806767.

[14] Sciarretta A, Guzzella L. Control of hybrid electric vehicles. IEEE Control Systems Magazine 2007; 27(2):60-70. doi: 10.1109/MCS.2007.338280.

[15] Dekraker P, Barba D, Moskalik A, Butters K. Constructing Engine Maps for Full Vehicle Simulation Modeling. SAE Technical Paper 2018-01-1412, 2018. doi:10.4271/2018-01-1412.

[16] Valverde, V, et al. Joint Research Centre 2018 light-duty vehicles emissions testing - Contribution to the EU market surveillance: testing protocols and vehicle emissions performance EUR29897 EN, Publications Office of the European Union, Luxembourg, 2019, ISBN 978-92-76-12333-0, doi:10.2760/289100, JRC117625.

[17] Mock P, Kühlwein J, Tietge U, Franco V, Bandivadekar A, German J. The WLTP: How a new test procedure for cars will affect fuel consumption values in the EU. Working Paper 2014-9, https://theicct.org/publications/wltp-how-new-test-procedure-cars-will-affect-fuel-consumption-values-eu [last accessed 17 April 2020].

[18] Commission Regulation EU, 2018/1832 of 5 November 2018, Official Journal of the European Union L 301/1, https://eur-lex.europa.eu/legal-content/EN/TXT/PDF/?uri=CELEX:32018R1832&from=FR [last accessed 17 April 2020].

7. Conclusions

During the research activity here summarized, in a first stage, a conventional stoichiometric naturally aspirated small SI engine has been investigated. The well assessed and *in-house* developed turbulence and combustion models have been improved and widely validated. Pollutant emission models have been developed and embedded in the commercial simulation platform GT-Power, to predict NOx, CO and uHC. Starting from this conventional engine advanced solutions to improve engine efficiency have been investigated.

Firstly, an innovative SI engine, equipped with an active pre-chamber ignition system, able to work in ultra-lean conditions in its whole operating range, has been examined. Two variants of this single cylinder engine have been numerically investigated through a hierarchical simulation-level approach. Then, two large-bore engines, a single-cylinder, and a multi-cylinder, featured by different ignition systems, and operating in ultra-lean conditions, have been studied. Hence, an innovative 4-cylinder SI engine, equipped with an active pre-chamber, has been presented. To estimate the CO_2 and pollutant emissions along the different driving cycles, an HEV architecture was considered and investigated through a numerical methodology. In this context, an energy management strategy *in-house* developed is applied, which was conceived to reduce the fuel consumption.

For the above-mentioned purpose, 1D schematizations of the six presented engines were developed in a 0D/1D modelling environment (GT-Power). Concerning the conventional engine, a standard version of the fractal combustion model, with an improved correlation for the laminar flame speed, was used. The pre-chamber engine architecture required the development of a dedicated model, to properly describe the physics behind such a system. Starting from models suitable for conventional SI engines, the turbulence and combustion models were modified to handle all the phenomena occurring in a pre-chamber engine, such as mixture preparation, turbulence evolution, flame area enhancement, burn rate development, jet entrainment, etc.

The engine models were tuned and validated against 3D calculations and experimental data, selecting a single set of tuning constants for each engine, not dependent on the operating condition. The conventional engine was validated against more than 350 operating points, both with and without external EGR. Predicted parameters, such as combustion phasing or BSFC, presented an error within the band of ±5%. Concerning the pollutant emission prediction, validated in 33 operating points, the agreement was found to be satisfactory. The single cylinder pre-chamber engine was numerically verified in two versions. For the first variant, the experimental campaign was carried out on a prototype single-cylinder engine, fitted with either a conventional spark plug or a pre-chamber

ignition device. In this last case, both passive and active PC operations were considered, with different fuels, i.e. CNG and H_2. The second engine version, fuelled only with gasoline, was experimentally investigated in a single operating point, namely 13 bar BMEP and 3000 rpm, varying the air/fuel ratio from stoichiometric to ultra-lean values. For both PC single cylinder engines, the model validation concerned comparisons of pressure traces in PC and MC, and the global performance parameters. For the second PC engine variant, pollutant emissions were verified, as well. The outcomes demonstrated the reliability of enhanced turbulence and combustion models and their capability to correctly simulate variants of an engine architecture, adopting a unique engine-dependent set of tuning constants. These results strengthened the robustness of the used approaches, leading to the conclusion that the model, well-describing physic phenomena, was accurate enough and could be employed in a predictive way. Before this, the uHC emission model has been deeply tested with reference to two large-bore engines: a single cylinder engine with a dual fuel system and a six-cylinder engine equipped with pre-chamber devices. For both engines, the model validation concerned operating points at fixed engine speed and various loads. Two different geometrical configurations of the piston top land were considered for both engines, as well. The uHC model demonstrated a good reliability, with an averaged error of 7% and 10% for the single cylinder dual fuel engine and for the six-cylinder PC engine. The model allowed to distinguish the uHC contributions from accumulation / release from crevices and flame wall quenching, and their percent weight at changing load and top land geometry.

Based on the second investigated single cylinder PC engine, a 4-cylinder turbocharged SI engine has been numerically studied, to support the design process and the calibration of the real engine. After a verification against the outcomes of an automatic optimizer, two different Rule-Based calibration strategies were defined. The RB strategies aim to properly define the optimal setting of control parameters, mimicking the experimental calibration procedure at the test bench. The two RB strategies are characterized by different fuel and electric consumptions, the first one aims to exclusively maximize the brake thermal efficiency, while the second one additionally considers the electric energy absorbed by the E-compressor and drained from the battery. Hence, the RB approaches were utilized to compute two sets of engine maps, summarizing the calibration strategies following the maximum BTE and overall BTE, respectively.

Subsequently, since the 4-cylinder PC engine was designed to be embedded in a HEV, an energy management strategy for hybrid powertrains was developed during this research activity. This simplified control strategy, labelled as Efficient Thermal Electric Skipping Strategy – ETESS, is based on the alternative vehicle driving by thermal engine or electric unit, where the choice is realized

by the comparison of representative fuel rates in these two modalities. No power-split between the power units is applied, except in the cases where no unit is able to supply alone the power demand at the wheels. The ETESS was tested in a "backward facing" vehicle simulator and its outcomes put into evidence that it gives fuel consumption close to PMP strategy (consumed fuel per kilometre higher than PMP of about 0.4% on average), with a drastically reduced computational time. The ETESS was also extended to an on-line implementation, through the introduction of an adaptative equivalence factor, resulting in performance similar to the well-assessed ECMS, preserving the computational effort.

Finally, the ETESS strategy was applied in HEV simulations to compare the two calibration strategies of the 4-cylinder ultra-lean PC engine in terms of CO_2 and pollutant emissions along WLTC and RDE-compliant cycle. The comparisons underlined that the strategy maximizing the OBTE allowed slightly lower CO_2 emissions for both the considered driving cycles, because of a more extended pure electric driving during the low-speed portion of the driving cycles, allowed by a reduced electric consumption in the high-speed portion of the driving mission. The control strategies did not show a clear impact on pollutant emissions.

The outcomes from vehicle simulation showed that the HEV presents a kilometric CO_2 emission of 85 g/km along the WLTC. This value is below the target imposed by the EU for 2021 of 95 g/km but above the one of 2025, equal to about 81 g/km. These results indicate that the HEV vehicle here analysed, even equipped with a very efficient thermal unit, is not enough to match the EU 2025 target. A Plug-in HEV variant is mandatory to comply with the CO_2 EU 2025 limit.

Concerning the pollutant emissions, the model outcomes refer to engine-out values, not considering the potential abatement of EATS, and are compared to the tailpipe reference standards imposed by the legislation Euro 6d. From the comparisons emerged that, even not including an EATS abatement, the NO_x emissions are well below the legislation bounds (0.02 g/km against of 0.06 g/km). Concerning the uHC emissions, the predicted levels are much higher than the Euro 6d limit (0.87 g/km against 0.1 g/km), highlighting the need for an oxidizing EATS for regulation compliance. Anyway, as known, the technology of an oxidizing EATS is very robust, low-cost, and reliable, not representing a challenge for a real on-vehicle application.

As a last consideration, it is worth underlining that the presented methodologies, whether applied to a conventional or to an innovative engine, represent powerful and effective tools to forecast both engine and vehicle performance. These numerical procedures showed the potential to support and drive the development phase of a high-efficient engine and low-emission HEV.